© 2024 Mark R. Hirsbrunner

CRYSTALLINE-ELECTROMAGNETIC RESPONSES OF TOPOLOGICAL SEMIMETALS AND INSULATORS

BY

MARK R. HIRSBRUNNER

DISSERTATION

Submitted in partial fulfillment of the requirements
for the degree of Doctor of Philosophy in Physics
in the Graduate College of the
University of Illinois Urbana-Champaign, 2024

Urbana, Illinois

Doctoral Committee:

Associate Professor Barry Bradlyn, Chair
Professor Taylor L. Hughes, Director of Research
Professor Vidya Madhavan
Assistant Professor Jacob Covey

Abstract

Topological phases of quantum matter have been at the forefront of physics research for the past forty years, ever since the observation of the integer quantum Hall effect (IQHE) and, soon after, the discovery that its precise quantization arises from the topology of the groundstate wavefunction. The realization that the topology of the wavefunction can have meaningful physical consequences has been incredibly impactful, and topology is now a core aspect of nearly every field of physics. In the context of condensed matter physics, understanding the topology of the groundstate provides a means to further resolve distinct phases of matter beyond the Landau-Ginzburg paradigm of spontaneous symmetry breaking. Rather than being characterized by a local order parameter, topological quantum matter possesses robust *global* properties that are of fundamental theoretical and practical importance. These global properties are often well-described by topological effective actions, also known as topological response theories, that capture how the system responds to probe gauge fields. The paradigmatic example of this is the electromagnetic response of the IQHE, which is captured by the Abelian Chern-Simons action. These topological responses are an invaluable tool, as they both provide insight into experimental signatures of topological phases of matter and have significantly furthered our understand of quantum field theory.

In condensed matter physics, the geometry of the lattice plays a central role. The crystal lattice greatly reduces the symmetry of the system from the full Poincaré group to that of a space group, enabling the emergence of exotic phenomena that are otherwise prohibited. In topological phases of matter, these reduced symmetries allow the further resolution of topological phases into those that cannot be adiabatically deformed into one another while preserving certain symmetries. These symmetry protected topological phases (SPTs) are distinct from phases exhibiting topological order, which require no symmetry protection. Our understanding of SPTs protected by crystalline symmetries is currently quite robust, with the recent advent of topological quantum chemistry and the development of symmetry indicators for topological phases. In parallel to these developments, there has been a recent resurgence of interest in gauging crystalline symmetries. Crystalline gauge fields are a tool that allow us to formally treat lattice defects as fluxes of crystalline symmetries, placing them on the same footing as electromagnetic gauge fields that describe magnetic fluxes

(fluxes of $U(1)$ symmetry). As such, crystalline gauge fields enable the construction of topological effective actions that capture the coupling of electrons to the lattice geometry. These effective actions describe mixed crystalline-electromagnetic response theories in which fluxes of crystalline symmetries induce electric charge fluctuations, and, conversely, electromagnetic fluxes induces fluctuations of charges associated with crystalline symmetries (namely crystal momentum and orbital angular momentum).

In this thesis we utilize the tool of crystalline gauge fields to study the crystalline-electromagnetic response of a range of topological semimetals and insulators. In Chapter 2 we begin by developing a unifying framework based on translation gauge fields that allows us to study the translation-electromagnetic responses of topological semimetals in up to $D = 3$ dimensions. This framework not only illuminates relations between previously-known topological semimetals, but also allows us to identify a new class of quadrupolar nodal line semimetals. Within this framework, we exhaustively construct all topological effective actions that can be built by combining electromagnetic and translation gauge fields. In Chapter 3 we identify tight-binding lattice models that host each such action and confirm the predicted responses through microscopic and numerical calculations. We find that the coefficients of these responses are universally proportional to weighted momentum-energy multipole moments of the nodal points (or lines) of the semimetal.

In Chapter 4 we expand the study of translation-electromagnetic responses to higher order topological semimetals. To do so we construct a model Hamiltonian for a time-reversal symmetric Weyl semimetal with a quadrupolar arrangement of higher-order Weyl nodes. It is known that similar first order Weyl semimetals exhibit a translation-electromagnetic response in which charge is bound to screw dislocations and momentum is bound to magnetic flux, both in an amount proportional to the chirality-weighted quadrupole moment of the Weyl nodes in the momentum space. We show that the higher-order nature of the Weyl nodes in our model leads to the emergence of an additional translation-electromagnetic *surface* response with a coefficient proportional to the dipole moment of the surface Dirac nodes that emerge with open boundary conditions. We also find that the quadrupole moment of the crystal momentum, a previously unstudied quantity, provides a link between the bulk and surface translation-electromagnetic response coefficients.

Finally, we study in Chapter 5 the rotation-electromagnetic response of the insulator that emerges from a Dirac semimetal coupled to charge density wave order. Using analytic and numeric methods we show the following. First, when the CDW is lattice-commensurate, disclination-line defects of the lattice have a quantized charge per length. Second, when the CDW is inversion-symmetric, disclinations of the lattice have a quantized electric polarization. Third, when the CDW is lattice-commensurate and inversion-symmetric, disclinations are characterized by a "disclination filling anomaly" – a quantized difference in the total charge bound to disclination-lines of Dirac-CDW with open and periodic boundaries. We construct an effective response theory that captures the topological responses of the Dirac-CDW insulators in terms of a total

derivative term, denoted the $R \wedge F$ term. The $R \wedge F$ term describes the crystalline analog of the axion electrodynamics that are found in Weyl semimetal-CDW insulators. We also use the rotation-electromagnetic response theory to classify the strongly correlated topological phases of three-dimensional charge-ordered Dirac-semimetals.

To my parents, Alex and Theresa

Acknowledgments

I spent the better part of the last decade studying at the University of Illinois at Urbana-Champaign, both as an undergraduate and a graduate student, to become a physicist. Over those years, I grew immensely as both a scientist and a person, and here I attempt to thank the many people that touched my life in Urbana. First and foremost, I must thank my advisor, Prof. Taylor L. Hughes. I was first introduced to condensed matter physics as an undergraduate taking his class, which inspired me so much that it set the course of my career. Taylor generously invited me to join his group, first as an undergraduate and then again as a graduate student, after a brief stint in electrical engineering and a global pandemic. My development as a physicist would not have been possible without his support, and I am especially grateful for his funding of my research assistantships and for sending me to conferences and summer schools. Most importantly, Taylor consistently believed in me, pushed me when I needed it, and gave me room to develop my own style as a scientist. I am deeply indebted to him for his unwavering support over the years.

In addition to Taylor, I was fortunate to be mentored early on by my fellow graduate students Timothy M. Philip, Moon Jip Park, and Youngseok Kim. Their friendship and patience gave me the support I needed to get my bearings as a young researcher, and I would have been lost without them. There are also many more faculty members at the University of Illinois to which I am grateful: Matthew J. Gilbert for mentoring and supporting me as an undergraduate and young graduate student; Nadya Mason for providing my first opportunity to collaborate with an experimentalist, for welcoming me to group events as though I were her own student, for her enduring friendship; Vidya Madhavan for giving me the chance to help with some truly remarkable experiments, and for the warmth and humor she always brings along with her; Michael Stone and Eduardo Fradkin for building my foundation as a physicist with their excellent courses; and Fahad Mahmood for his friendship, his kindness, and for introducing me to Pakistani cuisine. I also thank Barry Bradlyn for chairing my prelim and thesis committees, and Jacob Covey and Vidya Madhavan for serving as members on those committees. I owe a special thanks to the heart of the physics department, Lance Cooper, whose bottomless well of kindness, respect, and generosity helped get me, and countless other students, through many hard times. I also could not have succeeded without the help of the incredibly friendly and

effective staff of the physics department, especially Janice Benner, Stephen Bullwinkel, Wendy Wimmer, Rebecca Wiltfong, and Ljubica Milutinovic. Beyond the University of Illinois, I also immensely benefited from the mentorship of Norman M. Tubman, who gave me the opportunity to participate in the Feynman Quantum Academy internship program, my first foray into the world of quantum computing. I am also grateful to Katherine Klymko and Daan Camps for taking me in as an intern at Lawrence Berkeley National Lab. Finally, I want to thank the professors I collaborated with at other universities: Boris Kozinsky, Jenny Hoffman, Fiona J. Burnell, and Dirk Morr.

In addition to those mentioned above, I owe a debt of gratitude to the many other scientists that I had the pleasure of working with during my graduate studies, each of which inspired me with their brilliance: Anuva Aishwarya, Jan Balewski, Bora Basa, Roel Van Beeumen, Johannes Blaschke, Diana Chamaki, Yueqing Chang, Jenny Coulter, Siva Darbha, Oleg Dubinkin, Lei Gioia, Jacopo Gliozzi, Alex Gray, Vincent Humbert, Milan Kornjaca, Fangli Liu, Yulia Maximenko, Julian May-Mann, J. Wayne Mullinax, Yizhi Shen, Ka Ho Wang, David B. Williams-Young, and Penghao Zhu. I would also like to thank the many friends that made my time in graduate school so enjoyable: Nina Bielinski, Rebecca Chan, Chu Chu, Andrew Dong, Veronika Dubinkin, Chelsea Gao, Ian George, Hart Goldman, Kimiko Gunji, Jennifer Gunji-Ballsrud, David Hayes, Sarah Hayes, Greg Hamilton, Vincent Hickl, Yoonseok Hwang, Abid Khan, Amanda Gatto Lamas, Diana Liao, Yingkai Liu, Yuhao Ma, Dmitry Manning-Coe, Logan Meredith, Jessica Montone, Rachel Nguyen, Matthew O'Brien, Junseok Oh, Sahaj Patel, Pranjal Raleganker, Louis Schatzki, Kristen Schumacher, Joseph Sklenar, Raman Sohal, Giuseppe De Tomasi, and Kealie Vogel.

Finally, and most importantly, I thank my family, Alex, Theresa, William, and Daniel Hirsbrunner, as well as my partner, Maggie Murphree, without whom none of this would have been possible.

The work in this thesis was supported by ARO MURI W911NF2020166 (awarded to Taylor L. Hughes).

Table of contents

Chapter 1

Introduction

Some of this chapter is adapted from Mark R. Hirsbrunner, Oleg Dubinkin, Fiona J. Burnell, and Taylor Hughes, arXiv preprint arXiv:2309.10840.

1.1 Topological quantum matter

Topological phases of matter are one of the most active and important areas of modern condensed matter physics. The field initiated with the experimental observation of the integer quantum Hall effect (IQHE), in which the Hall conductivity of a two-dimensional electron gas is precisely quantized to integer multiples of e^2/h in the presence of sufficiently strong magnetic fields [1]. Shortly after the discovery of the IQHE, it was shown that the Hall conductivity is a topological invariant of the bandstructure, explaining the integer quantization of the quantity [2]–[5]. Topological invariants are global properties of quantum systems that are insensitive to local details. In the case of the Hall conductivity, the invariant for non-interacting insulators the integral of the Berry curvature over the Brillouin zone (BZ),

$$\sigma_{xy} = \frac{e^2}{h} C, \quad C = -\frac{1}{2\pi} \int d^2k \mathcal{F}_{xy}, \quad \mathcal{F}_{xy} = -i \left[\left\langle \frac{\partial u}{\partial k_x} \middle| \frac{\partial u}{\partial k_y} \right\rangle - \left\langle \frac{\partial u}{\partial k_y} \middle| \frac{\partial u}{\partial k_x} \right\rangle \right], \tag{1.1}$$

where $|u\rangle$ are the Bloch states and C is the Chern number. It is straightforward to show that this integral is insensitive to generic variations in Bloch states, $|u\rangle \to |u\rangle + |\delta u\rangle$, and is thus a topological invariant. It is also manifestly global and involves all length scales in the problem, since it is an integral over momentum space. The non-local nature of topological phases places them outside the Landau-Ginzburg classification scheme, in which phases of matter are differentiated by patterns of spontaneous symmetry breaking and local order parameters. Put simply, topological phases of matter cannot be distinguished from another by

local properties.

The fractional quantum Hall effect (FQHE), in which the Hall conductance is quantized in rational fractions of e^2/h, was first observed just years after the initial discovery of the IQHE [6]. Despite their apparent similarity, FQHE and IQHE represent two drastically different classes of topological phases, topologically ordered phases and symmetry protected topological (SPT) phases, respectively. SPTs are phases that cannot be adiabatically deformed into trivial insulators while maintaining their symmetry and can exist with or without interactions [7]–[17]. Topologically ordered phases are inherently interacting and are characterized by the presence of anyonic excitations with fractional statistics and by special patterns of long-range entanglement [18]–[21]. Topological order also implies a groundstate degeneracy that is distinct from the trivial groundstate degeneracy of phases resulting from spontaneous symmetry breaking. The degenerate groundstates of a spontaneously broken symmetry state can be differentiated by local order parameters, while groundstates with topological order are related to each other by non-local operators such as non-contractible Wilson loops.

SPTs are universally characterized by topological invariants of the bandstructure. The IQHE is characterized by the Chern number, and its quantization is protected by $U(1)$ charge conservation symmetry [2]–[5]. Another important SPT is the one-dimensional Su-Schrieffer-Heeger (SSH) model [22], [23]. When chiral symmetry is enforced, the topological invariant characterizing the SSH model is the chiral winding number of the Hamiltonian [24]. In three spatial dimensions, time-reversal symmetric insulators are characterized by their axion Θ angle, which is quantized to 0 or π [25], [26]. As discussed above, the Hall conductance of two-dimensional topological insulators is proportional to the Chern number [2]–[5]. Similarly, the parity of the chiral winding number of the SSH chain is proportional to the electric polarization, and the theta angle of three-dimensional topological insulators is proportional to the magnetoelectric polarizability [25]–[28]. The Hall conductivity, polarization, and magnetoelectric polarizability are all examples of topological electromagnetic responses. The relation between topological invariants and quantized responses like these is quite general, and topological responses are, in fact, a key manifestation of electronic topology in solids.

These electromagnetic topological responses are obtained by coupling the electronic degrees of freedom of a system to a probe (non-dynamical) $U(1)$ electromagnetic gauge field and integrating out the electrons, which produces an effective action for probe field:

$$e^{-iS_{\text{eff}}[A_\mu]} = \int \mathcal{D}\psi\mathcal{D}\bar{\psi}e^{-iS[\psi,\bar{\psi},A_\mu]}. \tag{1.2}$$

Topological responses appear in the effective action as terms that are independent of the metric, i.e., they are functions only of the topology of the manifold, not the geometry. One such term is the Chern-Simons

action,

$$S_{\mathrm{CS}}[A_\mu] = \frac{C}{4\pi}\int A \wedge dA, \tag{1.3}$$

from which one can obtain the charge and current responses by taking functional derivatives with respect to A_μ,

$$\begin{aligned} j^0 &= \frac{\delta S_{\mathrm{CS}}[A_\mu]}{\delta A_0(x)} = \frac{C}{2\pi}B_z(x) \\ j^i &= \frac{\delta S_{\mathrm{CS}}[A_\mu]}{\delta A_i(x)} = \frac{C}{2\pi}\epsilon^{ij}E_j, \end{aligned} \tag{1.4}$$

The first line is the Středa effect, in which electric charge is bound to magnetic flux in systems with finite Hall conductivity, and the second line describes the Hall conductivity [29], [30]. This effective action faithfully captures the electromagnetic response of the IQHE, but it it not clear upon inspection that S_{CS} is gauge-invariant.

Applying a gauge transformation $A_\mu \to A_\mu + \partial_\mu\omega$, we find that the action changes by a surface term

$$S_{\mathrm{CS}}[A_\mu + \partial_\mu\omega] = S_{\mathrm{CS}}[A_\mu] + \frac{C}{4\pi}\int d(\omega \wedge dA). \tag{1.5}$$

This term vanishes if ω is chosen to be zero at the boundary or, if ω is finite, when there are no magnetic monopoles. Consider now placing the system on a sphere instead of a plane, and Wick rotate to imaginary time to compactify the time direction to a circle with circumference β. Place a magnetic monopole within the sphere, which by Dirac quantization must have flux

$$\int_{S_2} F_{12} = 2\pi n, \quad n \in \mathbb{Z}, \tag{1.6}$$

and take the field configuration to be static. The resulting effective action is

$$S_{\mathrm{CS}}[A_\mu] = \frac{C}{2\pi}\int_0^\beta d\tau \int_{S_2} d^2x\, A_0 F_{12}, \tag{1.7}$$

where the extra factor of two comes from an integration by parts. If we choose a large gauge transformation for which ω winds by 2π around the Euclidean time axis, $\omega(\tau, x_i) = 2\pi\tau/\beta$, then the value of A_0 shifts by $2\pi/\beta$, and the effective action changes by $\delta S = 2\pi C$. Because the action appears in the partition function as $\exp(-iS_{\mathrm{CS}})$, to ensure gauge invariance we need C to take integer values. The preceding calculation was, admittedly, quite convoluted. However, it shows that we can obtain the quantization of the Hall conductivity just by studying the gauge invariance of the Chern-Simons effective action! This demonstrates the power of topological responses for understanding the physics of topological quantum matter.

The topological electromagnetic responses of one- and three-dimensional insulators are captured by the effective actions

$$S_{1\mathrm{D}} = P \int dA \tag{1.8}$$

and

$$S_{3\mathrm{D}} = \frac{\Theta}{8\pi^2} \int dA \wedge dA, \tag{1.9}$$

both of which are manifestly gauge invariant. Their coefficients are instead quantized by symmetries, chiral and time-reversal for the one- and three-dimensional cases, respectively, rather than by enforcing gauge invariance. More general topological terms can be written down if one considers gauge fields for symmetries beyond $U(1)$ charge conservation. For example, the physics of the quantum spin Hall effect, a time-reversal symmetric topological insulator phase in two dimensions, can be understood by constructing a topological effective action that couples the electromagnetic gauge field to the gauge field for $U_s(1)$ spin conservation symmetry [31].

Interestingly, certain distinctive features of the electromagnetic responses of topological semimetals are described by response theories that are closely analogous to those of topologically insulating phases, but with unquantized coefficients that are determined by the momentum-space and energy locations of the point or line nodes [32]–[37]. For point-node semimetals, the relevant response coefficients are momentum-energy vectors determined as a sum of the momentum and energy locations of the point-nodes weighted by their chirality (or by their helicity, for Dirac semimetals), yielding a momentum-energy space dipole. For example, the low-energy, nodal contribution to the anomalous Hall effect tensor of a 3D Weyl semimetal is determined by the momentum components of this momentum-energy dipole vector. The quasi-topological response coefficients of topological semimetals are not strictly quantized since they can be continuously tuned with the nodal momenta. However, the forms of the responses share many features with topological insulators in one lower dimension, or perhaps more precisely, with weak topological insulators in the same dimension [38], [39]. Indeed, topological semimetals and weak topological insulators both require discrete translation symmetry to be protected and both are sensitive to translation defects such as dislocations [40].

This sensitivity to discrete translation symmetry points out an important flaw in our discuss so far — the topological insulators discussed above are all protected by local anti-unitary symmetries, but we have not yet considered crystalline symmetries. One of the major accomplishments in the field of topological quantum matter is the "ten-fold way", an exhaustive classification of topologically distinct phases in any dimension that are protected by time-reversal, charge-conjugation (particle-hole), and/or chiral symmetry, each of which is local and anti-unitary [7], [41], [42]. The importance of crystalline symmetries for topological classification was appreciated early on, with generalizations to inversion-, rotation-, and mirror-symmetric

systems following shortly afterward [39], [43]–[47]. Full classification of SPTs with crystalline symmetries is a challenging problem, but the tools needed to do so were developed over the next decade, culminating in the advent of topological quantum chemistry and the theory of symmetry indicators, which enabled the successful classification of topological phases protected by any magnetic or non-magnetic space group [48]–[57]. While the classification is now complete, a deep understanding of the many topological phases encompassed by this classification is an important area of active research.

Motivated in part by this progress in crystal topology, there has been a recent resurgence of interest in developing gauge theories of crystalline symmetries [58]–[67]. We saw above that topological response theories are a powerful tool for studying topological phases of matter. It therefore stands to reason that gauge theories of crystal symmetries are indispensable for understanding crystalline topological insulators. As with gauge fields of on-site symmetries, the physical content of crystalline gauge fields is encoded in their fluxes. For both on-site and crystalline symmetries, particles encircling fluxes of the symmetry are acted upon by an element of the symmetry group. For a magnetic flux, this group element is just a phase. For crystalline symmetry, the group element can be a translations, rotation, or any other element of the crystalline symmetry group. These crystal fluxes are actually well-known under a different name: lattice defects [68]. This connection to lattice defects shows that crystalline gauge fields are quite physical, despite appearing as an abstract mathematical construction. Crystalline gauge fields are a powerful tool, and there exists now a large body of work employing them to study the crystalline responses of topological quantum matter [62]–[64], [68]–[84]. In the following sections we provide detailed background information on lattice defects and crystalline gauge fields, and the remainder of this thesis is a collection of our work applying these techniques to study the translation- and rotation-electromagnetic responses of topological insulators and semimetals.

1.2 Topological lattice defects

Lattices are described by their space group, the set of symmetry operations that leaves the lattice invariant. There are 230 three-dimensional space groups and 17 two-dimensional ones, also known as the wallpaper groups. The elements of the space group are products of point group operations, like rotations and reflections, with translations, applied in that order. If all the elements of a space group, excepting translations, leave a single common point fixed, the group is called symmorphic. Non-symmorphic groups contain symmetry elements combining point group operations with partial translations by fractional primitive lattice vectors. Space groups can also be extended to include the time-reversal operation to form magnetic space groups, which are useful for describing crystals with spin ordering. In this thesis we only consider symmorphic

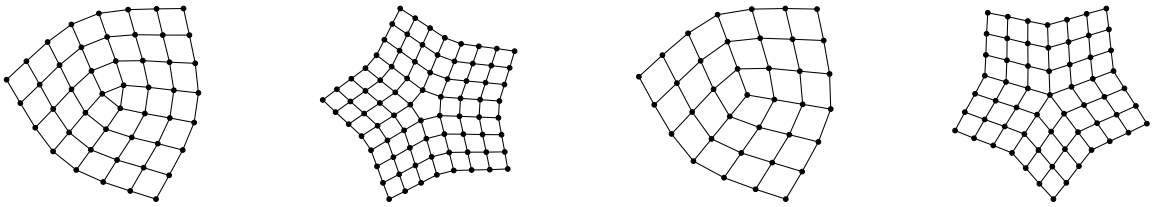

(a) (b) (c) (d)

Figure 1.1: Illustrations of isolated disclinations on the square lattice: (a) plaquette-centered with $\Theta_F = \pi/2$, (b) plaquette-centered with $\Theta_F = -\pi/2$, (c) vertex-centered with $\Theta_F = \pi/2$, and (d) vertex-centered with $-\pi/2$.

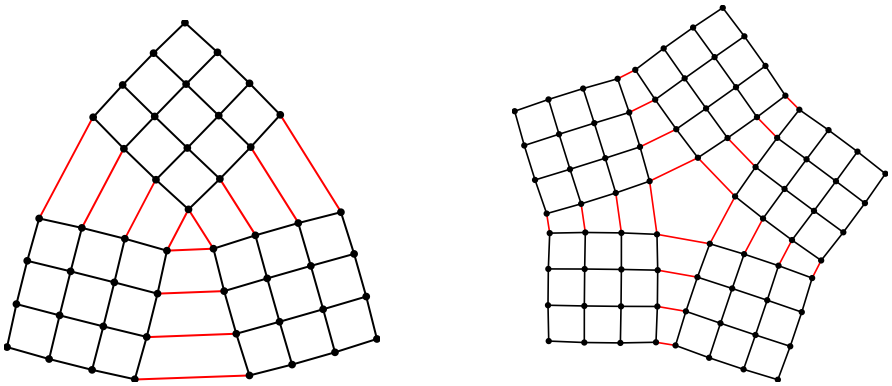

(a) (b)

Figure 1.2: Illustrations of a method for constructing plaquette-centered disclinations. For a systems with C_n rotation symmetry, a disclination with $\Theta_F = 2\pi m/n$ can be constructed by stitching together $n - m$ defect-free patches of the lattice. The illustrations depict (a) $\Theta_F = \pi/2$ and (b) $\Theta_F = -\pi/2$ plaquette-centered disclinations of a C_4 symmetric lattice, where the defect-free patches are shown in black and the connections between them in red.

non-magnetic space groups, and only work with defects of rotation and translation symmetries.

We first consider defects of n-fold rotation symmetry, C_n. Defects of rotations symmetry are called disclinations and can be formed via the insertion or removal of wedges of the lattice that subtend an angle $2\pi m/n$, such that the lattice is locally symmetric under rotations by $C_{n\pm m}$. Disclinations are characterized by their Frank angle Θ_F, the angle by which a vector rotates when it traverses a loop around the disclination core. Examples of $\Theta_F = \pi/2$ and $\Theta_F = -\pi/2$ disclinations on the square lattice are depicted in Fig. 1.1. For a given Frank angle, there are two distinct types of disclination, plaquette-centered (Fig. 1.1 a and b) and vertex-centered (Fig. 1.1 c and d), that are differentiated by the location of their rotation center. Before discussing the physical consequences of the differing locations of the rotation center, it is prudent to first discuss the construction of disclinations in more detail.

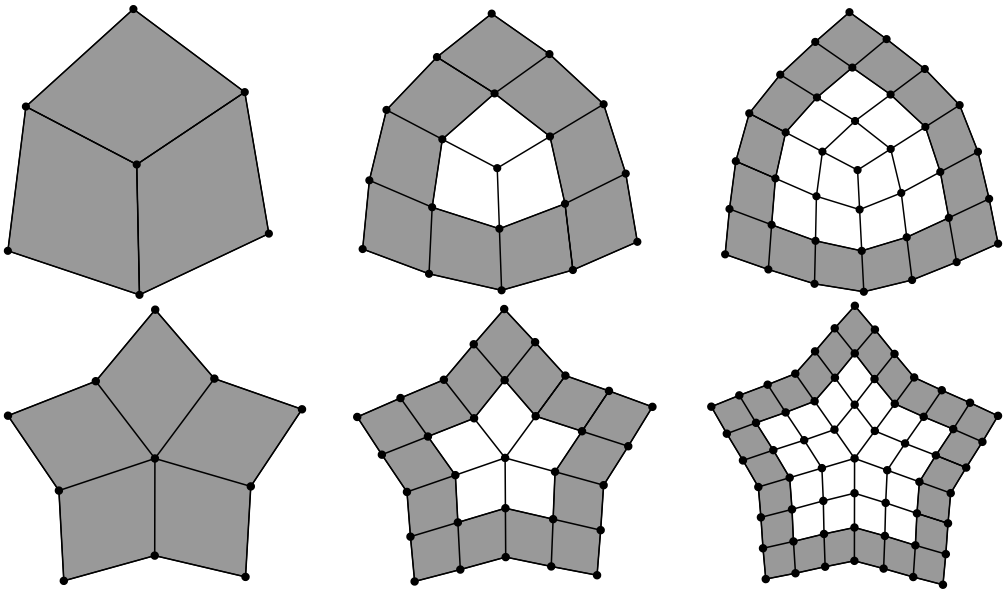

Figure 1.3: Illustrations depicting a method to iteratively build vertex-centered disclinations. For a disclination with $\Theta_F = 2\pi m/n$ on a C_n-symmetric lattice, the method begins by patterning $n - m$ plaquettes around a central vertex. The disclination is grown is placing additional rows of plaquettes along each face of the boundary and connecting the faces with $n - m$ additional plaquettes at the corners of the boundary. The illustrations depict from left to right growing the disclination layer by layer, with shading indicating the plaquettes added in each step. The top and bottom rows depict $\Theta_F = \pi/2$ and $\Theta_f = -\pi/2$ disclinations, respectively, on the square lattice.

Plaquette-centered disclinations of a C_n symmetric lattice with $\Theta_F = 2\pi m/n$ can be constructed by stitching together $n - m$ identical defect-free patches of the lattice, as depicted in Fig. 1.2. One corner of each patch is placed at a vertex of the central plaquette, forming an $n-m$-sided polygon. The edges of each section emanating from the central plaquette are stitched together to complete the disclination. Vertex-centered disclinations are constructed iteratively by building up plaquettes around the central vertex, as shown in Fig. 1.3. The first step is to place $n - m$ plaquettes around the central vertex. The disclination is built out by placing an additional plaquette onto each edge of the boundary, then placing an additional plaquettes at each of the $n - m$ corners to close the new outer ring of plaquettes. This process is iterated to grow the disclinated lattice. These algorithms are neither unique nor physically motivated, but they are useful tools for building explicit lattices onto which tight-binding Hamiltonians can be placed for numerical calculations.

We now consider the physical differences between plaquette and vertex-centered disclinations. Lattice defects are characterized by the holonomy of closed loops containing the defect core. In other words, encircling defects is equivalent to the application of a symmetry element of the space group, and distinct defects correspond to distinct symmetry elements. In practice, the holonomy can be calculated by traversing a closed loop, i.e. translating by $n_x\hat{x}$, followed by $n_y\hat{y}$, $-n_x\hat{x}$, and finally $-n_y\hat{y}$. The defect enclosed by such

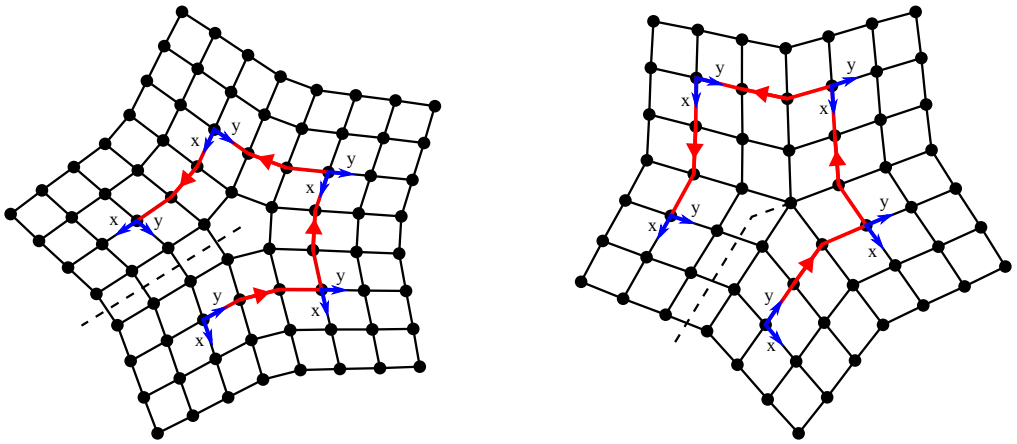

Figure 1.4: The holonomy of (a) plaquette- and (b) vertex-centered disclinations with $\Theta_F = -\pi/2$. The red arrow depicts the loop upon which the holonomy is calculated, $3\hat{y} \to -3\hat{x} \to -3\hat{y} \to 3\hat{x}$. The blue arrows and labels show the local frame of the coordinate system at each point along the path, from which the rotation of the local frame by $-\pi/2$ can be clearly seen. The loop around the plaquette-centered disclination fails to close by the vector $-3\hat{x}$, and the loop around the vertex-centered disclination fails to close by $-3\hat{x}+\hat{y}$. The vector by which the path fails to close is not universal and depends on the path chosen, but the difference in this vector between plaquette- and vertex-centered disclinations is path-independent. The dashed lines indicate a choice for the branch-cut across which the local Hilbert space is rotated.

a loop will be characterized by the angle by which the local frame has rotated (the Frank angle Θ_F) and the vector separating the starting and ending points of the loop. In Fig. 1.4 we show such loops encircling $-\pi/2$ plaquette and vertex-centered defects on the square lattice. Comparing the local frame at the start and end of each loop, it is clear that the Frank angle of the disclination is $-\pi/2$. Both loops fail to close, with the start and end points separated by the vectors $-3\hat{x}$ and $-3\hat{x}+\hat{y}$ for the plaquette and vertex-centered disclinations, respectively. The translation that is enacted by such a loop around a disclination is dependent on the path, meaning it is not a topological quantity and cannot be used to characterize the defect. However, the difference in the translation affected by the plaquette and vertex-centered disclinations is path-independent. This difference arises from the different location of the rotation center for each disclination.

The composite defect formed by two disclinations with opposite Frank angles has a zero net Frank angle, but a loop encircling it will generally not close, so the holonomy still includes a translation part. Such a defect is called a dislocation, a defect solely of translation symmetry. The simplest construction of a dislocation is obtained by joining a plaquette-centered disclination with a vertex-centered disclination of opposite Frank angle. Two versions of this construction are depicted in Fig. 1.5, the two combinations of a $\pm\pi/2$ plaquette-centered disclination with a $\mp\pi/2$ vertex-centered disclination. Also shown in Fig. 1.5 are loops around the dislocations, drawn in blue. In flat space these loops would close, and the vector separating the start and end of the loop is the Burgers vector that defines the dislocation. More general dislocations can be formed

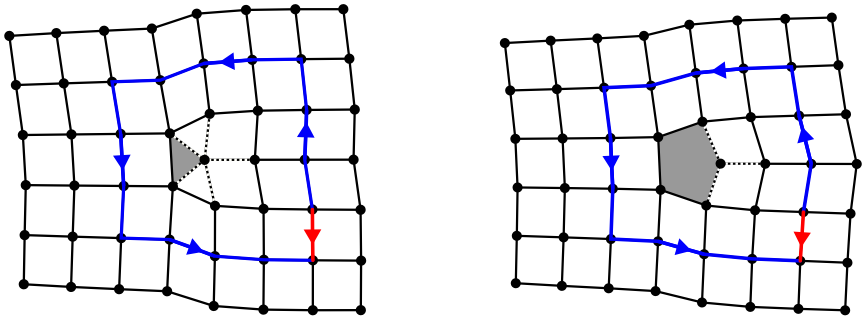

Figure 1.5: Depictions of two dislocations formed by combining (a) a $\Theta_F = \pi/2$ plaquette-centered disclination and a $\Theta_F = -\pi/2$ vertex-centered disclination and (b) a $\Theta_F = -\pi/2$ plaquette-centered disclination and a $\Theta_F = \pi/2$ vertex-centered disclination. The rotation parts of the individual disclinations cancel, leaving only the path-independent translation part of the composite defect. The blue path indicates a closed loop upon which the holonomy of the dislocation can be computed, and the red arrow is the Burgers vector of the dislocation that closes the loop. The shaded plaquettes indicate the plaquette-centered disclination, and the links connecting to the core of the vertex-centered disclination are indicated by dashed lines.

by combining different types of disclinations (plaquette-centered with plaquette-centered, vertex-centered with vertex-centered) and by placing the disclinations further apart. The Burgers vector of such disclination dipoles will scale linearly with the separation between the disclination centers, but the general form of the Burgers vector is complex. Only in the extreme case of zero separation between the disclinations do the translation parts properly cancel, permitting the description of plaquette and vertex-centered disclinations as differing by fusion with a dislocation. In this thesis we do not consider systems that are sensitive to both rotation and translation symmetry, so this subtlety will not arise here. We note that such systems do exist and their response to disclinations is an important question for future research.

Our discussion of defects has so far been limited to defects of rotation and translation symmetry in two dimensions. Fortunately, these defects generalize straightforwardly to three dimensions. Disclinations can be stacked to form disclination lines. Disclination lines are uncommon in real materials, but they provide an useful theoretical tool for understanding the role of rotation symmetry in topological phases. Dislocations are somewhat more complex in three dimensions, as we have to consider cases in which the Burgers vector either lies in the plane of the defect or is perpendicular to it. The former case is an edge dislocation and corresponds to the insertion of partial planes of sites into the lattice. The latter case are screw dislocations, in which the planes of the lattice are cut along a line extending from the axis of the defect and stitched back together such that each plane connects to a neighboring plane, rather than itself. The planes of the lattice wrap around the screw dislocation core like the threads of a screw, as implied by the name.

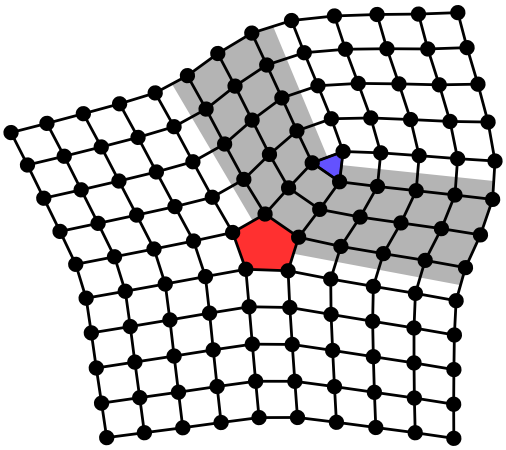

Figure 1.6: A lattice containing a dipole of plaquette-centered disclinations. The central plaquettes of the $\Theta_F = \pi/$ and $\Theta_F = -\pi/2$ disclinations are marked in blue and red, respectively. The gray shading indicates the additional lattice sites inserted by the disclination dipole, which form a dislocation with Burgers vector $3\hat{x} + 3\hat{y}$.

1.3 Tight-binding Hamiltonians on defected lattices

Much of this thesis is concerned with performing explicit calculations using model tight-binding Hamiltonians on defected lattices, so here we provide details on how to construct such Hamiltonians. For simplicity, we consider a Hamiltonian with only nearest-neighbor hopping elements,

$$\hat{\mathcal{H}} = \sum_{\vec{R}} H_0 c^\dagger_{\vec{R}}\, c_{\vec{R}} + H_x c^\dagger_{\vec{R}+\hat{x}}\, c_{\vec{R}} + H_y c^\dagger_{\vec{R}+\hat{y}}\, c_{\vec{R}} + \text{H.c.}, \tag{1.10}$$

where $\vec{R}$ enumerates lattice sites. For any lattice, defected or not, the first step of constructing the Hamiltonian is placing the onsite term H_0 on each lattice site. For a lattice with a disclination, the local frame cannot be chosen consistently across the entire lattice and there must exist a branch cut emanating from the disclination core across which the local frame rotates abruptly. Away from this branch cut, the local geometry determines the placement of hopping elements H_x and H_y on the links of the lattice. For links that connect across the branch cut, the hopping elements must be rotated accordingly. For example, consider the branch cuts depicted in Fig. 1.4. The local frame is rotated by $\pi/2$ on either side of the dashed line, so the hopping elements crossing that line must take the form

$$H_{\text{disc}} = H_x U_{\pi/2} = U_{\pi/2} H_y, \tag{1.11}$$

where $U_{\pi/2}$ is the unitary part of the rotation operator. This procedure is sufficient to place a tight-binding Hamiltonian on a plaquette-centered disclination, but there is an additional complication for vertex-centered

disclinations. Any hopping elements including the central vertex of a vertex-centered disclination are not determined by the bulk Hamiltonian. Any coupling that respects the rotation symmetry of the disclination is permissible, but often the central vertex is left disconnected from the rest of the lattice. These considerations generalize straightforwardly to Hamiltonians with hopping elements to further neighbors, and disclination lines can be treated in momentum space along their axis.

Placing a tight-binding Hamiltonian on a lattice with a dislocation is significantly simpler. Because the local frame can be consistently defined across the lattice in the absence of disclinations, the hopping elements connecting to the sites added by the dislocation are determined by the local geometry. The exception is that the hopping elements connecting to sites at the end of a dislocation are not determined by the bulk Hamiltonian and must be chosen according to additional, problem-specific considerations. Similar to disclination lines, screw dislocations can be treated in momentum space along the screw axis by modifying the hopping elements that span a branch cut extending from the screw axis. An electron traversing a loop containing a screw dislocation is translated along the screw axis by the Burgers vector $\vec{b}$. When translation symmetry is maintained along the screw axis, the crystal momentum along that axis is a good quantum number, and the electron wavefunction acquires a phase $e^{i\vec{k}\cdot\vec{b}}$. The dislocation can therefore be accounted for by multiplying any hopping elements crossing a branch cut extending from the screw axis by this phase factor. These generalized momentum-dependent Peierls factors are a powerful tool that we employ extensively in this thesis.

Treating edge dislocations with momentum-dependent Peierl factors is somewhat more subtle. Consider a lattice on a cylinder with infinite length and a circumference of N sites. We would like to add a dislocation to the lattice by inserting a semi-infinite row of sites while maintaining translation symmetry along the circumference of the cylinder. Unfortunately, it is not possible to do so except in three extreme cases: implementing all-to-all hoppings for the lattice sites other either side of the end of the dislocation, removing all hopping elements connecting across the end of the dislocation, or inserting an integer multiple of N dislocations. None of these is physically motivated, but we can implement a compromise that captures most of the essential physics by using momentum-dependent Peierls factors. Consider an electron with definite momentum k along the circumference of the cylinder. In the absence of a dislocation, it acquires a phase e^{ikN} upon traversing the circumference. Inserting a dislocation corresponds to locally increasing the circumference of the cylinder by the Burgers vector b, such that the phase acquired is instead $e^{ik(N+b)}$. This phase can be accounted for by multiplying hopping elements along the circumference by the phase $e^{ikb/N}$. This is equivalent to shifting the momentum to $k \to k(1 + b/N)$ on the portion of the cylinder threaded by the dislocation. Implementing this momentum shift allows us to treat the dislocation in momentum space, sidestepping the issue of implementing translation-invariant hopping elements at the end of the dislocation.

However, this technique does not account for the change in the number of electrons caused by the insertion of a dislocation. The implications of this shortcoming are an important topic for future research, but we do not consider it in this thesis.

1.4 Crystalline gauge fields

The tool we use in this thesis to capture the coupling between electrons and lattice geometry is crystalline gauge fields. In this section we review their formulation, focusing on analogies between them and conventional gauge fields. In an abstract sense, conventional gauge fields for on-site symmetries describe the twisted boundary conditions of each closed space-time loop. A clear example of this is the electromagnetic gauge field, A_μ. This field emerges from gauging global $U(1)$ charge conservation symmetry, so loop integrals of A_μ accordingly measure the winding of the phase of the wavefunction around the loop. This is simply the Aharanov-Bohm effect, in which electrons acquire a phase upon encircling a magnetic flux. In this example, the loop is taken around a defect of the gauge field. One can also consider threading the magnetic flux through the loop made by any periodic spatial direction, i.e. through the center of a torus. In that case the gauge field measures the phase electrons acquire upon traversing the periodic axis of space. This picture can be extended to other on-site symmetries. The general statement is that traversing space-time loops is equivalent to acting on the system with an element of the gauged symmetry group, G, and the flux of the gauge field, $\mathcal{A}$, through the loop can be identified with this symmetry operator,

$$\oint_\gamma \mathcal{A} = g \in G. \tag{1.12}$$

This statement is also true for crystalline symmetries, but gauging them is more subtle because they are both discrete and do not leave space-time invariant. We first consider gauging translation symmetry on lattices without disclinations. We discuss gauging rotation symmetry next, and then briefly summarize some difficulties of gauging both simultaneously.

Keeping the picture of loop integrals corresponding to symmetry operators in mind, it is convenient to begin by considering weak lattice deformations. The quantity of interest is

$$\mathfrak{e}_i^a = \delta_i^a - \frac{\partial u^a}{\partial x^i}, \tag{1.13}$$

where the Kronecker δ_i^a encodes the fixed reference lattice vectors, u^a is the lattice displacement, and $\frac{\partial u^a}{\partial x^i}$ is the distortion tensor [85]. Integrals of this quantity around closed loops captures the net Burgers vector,

b^a, of all the dislocations contained within the loop [85],

$$\oint \mathfrak{e}_i^a \, dx_i = \oint \frac{\partial u_a}{\partial x_i} dx^i = b^a. \tag{1.14}$$

We would like to identify the components of $\vec{b}$ as elements of the discrete translation symmetry group, T_{x_i}, which would allow us to define $\mathfrak{e}^a$ as the gauge fields for discrete translation symmetry. However, the vector defined above contains two contributions from the lattice geometry, integer multiples of primitive lattice vectors and generic contributions arising from local elastic deformation of the lattice sites. The stress and strain fields arising from such local elastic deformations can couple to electrons, but we are only interested in the coupling between electrons and topological lattice defects. By discarding the part of $\mathfrak{e}^a$ arising from local elastic deformations, we can treat $\mathfrak{e}^a$ as integer-valued gauge fields for discrete translation symmetry. The gauge freedom of these fields corresponds to arbitrary relabeling of lattice sites and arises from the local elastic deformations that we discard. In earlier work, e.g., Ref. [72], these translation gauge fields could have been called frame-fields, but the translation gauge fields encode only the translation part of geometric distortions, whereas the frame fields also carry rotational information.

These translation gauge fields are locally flat, $d\mathfrak{e}^a = 0$, and loop integrals of them describe the topology of the lattice. Integrals of translation gauge fields along non-contractible loops that encircle the entire lattice capture either the dimensions of the lattice,

$$\oint_{C_a} \mathfrak{e}^a = L_a, \tag{1.15}$$

or the shear of lattice when integrating the field $\mathfrak{a}$ along an axis other than a,

$$\oint_{C_a} \mathfrak{e}^b, \tag{1.16}$$

i.e. the displacement of the slice of the lattice at $x_a = 0$ from the slice of the lattice at $x_a = L_a$. Dislocations correspond to defects of the translation gauge field, and integrals of $\mathfrak{e}^a$ along loops containing such defects produce the net Burgers of all dislocations contained by the loop,

$$\oint \mathfrak{e}^a = b^a. \tag{1.17}$$

We can equivalently write this as a surface integral of the exterior derivative of the translation gauge field,

$$\int_S d\mathfrak{e}^a = b^a, \tag{1.18}$$

from which we can see that the dislocation density is analogous to the magnetic field arising from the $U(1)$ electromagnetic gauge field. By the same analogy, the equivalent of electric fields are time-dependent strains.

The analogy between dislocations and magnetic flux is what underlies the appearance of momentum-dependent Peierl factors in Hamiltonians placed on lattices containing dislocations, as discussed in the previous section. Conventional Peierls phases capture the $U(1)$ phase acquired by electrons as they encircle a magnetic field ($U(1)$ flux). Importantly, the acquired phase is proportional to the electric charge, because this is the coupling constant between electrons and the electromagnetic field. Translation gauge fields instead couple to electrons through the crystal momentum. The momentum dependence of the Peierls factors we use to account for dislocations arises from simple substitution in conventional Peierls factors of the electric charge with crystal momentum, and it is simply a manifestation of the electron being translated as it winds around the defect. In Appendix A.1, we show more explicitly how translation symmetry can be gauged under a teleparallel constraint of the underlying system geometry, which provides more clarity on why translation gauge fields are charged under crystal momentum.

It is clear that there are many ways in which $\mathfrak{e}_\mu^a$ can be treated on equal footing with the electromagnetic gauge field, but there are some important distinctions. First, the fields $\mathfrak{e}_j^a$ in Eq. (1.13) are not true gauge fields. This becomes important when considering the possible response actions: while the total charge of a system strictly conserved, momentum conservation is not similarly inviolable (see e.g. [86]–[88] for some interesting physical consequences of this distinction). Second, responses involving $\mathfrak{e}_\mu^a$ are predicated on the existence of translation symmetry. Thus, if the response is characterized by a boundary effect or a response to a flux, we must be careful to ensure that (at least approximate) translation symmetry is maintained in order to connect the coefficient of the response action to explicit model calculations. Indeed, some responses are not well-defined unless configurations that maintain translation symmetry are used. This is unlike the electromagnetic response for which $U(1)$ charge symmetry is maintained independent of the geometry and gauge field configuration. Other important distinctions have been discussed in recent literature that has begun putting the gauging of discrete spatial symmetries on firmer ground [58], [62], [89]. One important distinction is that the translation gauge fields correspond to a discrete gauge symmetry $\mathbb{Z}_{N_a}$, where N_a is the number of unit cells in the a-th direction. This discreteness can play an important role in the topological response properties [62], [63], but such details do not arise in this thesis.

Gauging rotation symmetry proceeds similarly to translation symmetry. Consider a lattice with C_n rotation symmetry about some axis. Defects of rotation symmetry are disclinations, around which the local coordinate frame rotates non-trivially. To account for the rotation of the local coordinates, we can introduce a $\mathbb{Z}_n$-valued gauge field ω. More specifically, if the rotation gauge field is non-zero on a particular link, $\omega_{ij} = m$ mod n, the local coordinate frames on the sites i and j are rotated from each other by the angle $2\pi m/n$.

The gauge freedom of this field corresponds to the freedom to arbitrarily choose the local coordinate frame at each site. The physical content of ω is again captured by integrals of it along closed loops. An integral around a defect of the field, $\oint \omega = m \neq 0$ corresponds to a disclination with Frank angle $\Theta_F = 2\pi m/n$. In dimensions $D >= 3$, it is possible to also consider integral of ω along non-contractible loops spanning the system, which indicate rotated boundary conditions, but it is unclear what the interpretation of such integrals is for $D = 2$.

Although rotation gauge fields appear more straightforward than translation gauge field, they are quite complex to implement alongside each other. Here we briefly consider the difficulty of doing so, following the treatment of the topic in Ref. [62]. This point is made most clear by explicitly treating them as discrete lattice gauge fields, rather than approximating them as continuous gauge fields as we do in the rest of this thesis. Consider a combined discrete gauge field for translations and rotations of a two-dimensional system with C_n rotation symmetry, $B_{ij} = (\vec{R}_{ij}, \Omega_{ij})$, defined on links of the lattice directed from site i to site j. The notation $\vec{R}_{ij}$ is simply a compact way to write the components of the translation gauge field, $\vec{R}_{ij} = (\mathfrak{e}^x_{ij}, \mathfrak{e}^y_{ij}, \mathfrak{e}^z_{ij})$. The composition of two elements of this field is given by

$$(\vec{R}_1, \Omega_1)(\vec{R}_2, \Omega_2) = (\vec{R}_1 + U(\Omega_1)\vec{R}_2, \Omega_1 + \Omega_2), \tag{1.19}$$

where $U(\Omega)$ is a rotation matrix. We see that the rotations combine straightforwardly, but composing translations involves rotating one of the two vectors. This is the central challenge of gauging both symmetries simultaneously.

A gauge transformation of this field is determined by the choice of the gauge variable on each lattice site, $(\vec{r}_i, \omega_i)$, under which the field transforms as

$$(\vec{R}_{ij}, \Omega_{ij}) \to \left(U(-\omega_i)\left(\vec{R}_{ij} + U(\Omega_{ij})\vec{r}_j - \vec{r}_i\right), -\omega_i + \Omega_{ij} + \omega_j\right). \tag{1.20}$$

The physical quantities of these gauge fields are the symmetry fluxes, which in the lattice description are given by

$$dA[ijk] = A_{ij} + A_{jk} - A_{ik}. \tag{1.21}$$

Fluxes of the rotation part of the gauge field are gauge invariant,

$$\begin{aligned} d\Omega'[ijk] &= \Omega'_{ij} + \Omega'_{jk} - \Omega'_{ik} \\ &= (-\omega_i + \Omega_{ij} + \omega_j) + (-\omega_j + \Omega_{jk} + \omega_k) - (-\omega_i + \Omega_{ik} + \omega_k) \\ &= \Omega_{ij} + \Omega_{jk} - \Omega_{ik} \\ &= d\Omega[ijk], \end{aligned} \tag{1.22}$$

but the same cannot be said for the translation part:

$$\begin{aligned} d\vec{R}'_{ij}[ijk] &= \vec{R}'_{ij} + \vec{R}'_{jk} - \vec{R}'_{ik} \\ &= U(-\omega_i)\left(\vec{R}_{ij} + U(\Omega_{ij})\vec{r}_j - \vec{r}_i\right) + U(-\omega_j)\left(\vec{R}_{jk} + U(\Omega_{jk})\vec{r}_k - \vec{r}_j\right) \\ &- U(-\omega_k)\left(\vec{R}_{ik} + U(\Omega_{ik})\vec{r}_k - \vec{r}_i\right). \end{aligned} \tag{1.23}$$

This only reduces to $d\vec{R}_{ij}$ in the case that both ω_i and Ω_{ij} vanish. This variation under a gauge transformation arises from the fact that we have not taken into account the local change of the coordinate frame along the loop $[ijk]$. The complicated change of $\vec{R}$ under gauge transformations makes it quite difficult to construct gauge invariant quantities from the field.

One natural approach to solving this problem is to modify the translation gauge fields such that the rotation of the local frame is accounted for when adding fields on different links. Consider the product of the crystalline gauge field along some path between two arbitrary sites 0 and n, $B_{01}B_{12}\dots B_{n-1,n}$. Expanding out this product yields

$$B_{01}B_{12}\dots B_{n-1,n} = \left(\sum_{k=0}^{n-1} U\left(C_{01} + C_{12} + \cdots + C_{k,k-1}\right)\vec{R}_{k,k-1}, \sum_{k=0}^{n-1} C_{k,k-1}\right). \tag{1.24}$$

Each translation component is rotated by the sum of all preceding rotation components in the sum. This product keeps track of all the rotations along the path from the arbitrary origin (0) to the point k, enabling the parallel transport of $\vec{R}$ between different sites on the lattice. Using this path to construct a modified translation gauge field

$$\vec{\mathcal{R}}^{(0)}_{k,k+1} = U(C_{01} + C_{12} + \cdots + C_{k-1,k})\vec{R}_{k,k+1}, \tag{1.25}$$

we can attempt to define a Burgers vector via the loop integral

$$\oint_\gamma \vec{\mathcal{R}}^{(0)}. \tag{1.26}$$

This becomes after a gauge transformation

$$\begin{aligned}
\oint_\gamma \vec{\mathcal{R}}^{(0)\prime} &= U(-\omega_0)\left(\vec{R}_{01} + U(\Omega_{01})\vec{r}_1 - \vec{r}_0\right) \\
&\quad + U(\Omega'_{01})U(-\omega_1)\left(\vec{R}_{12} + U(\Omega_{12})\vec{r}_2 - \vec{r}_1\right) \\
&\quad + \dots \\
&\quad + U(\Omega'_{01} + \dots + \Omega'_{n_1,n})U(-\omega_n)\left(\vec{R}_{n0} + U(\Omega_{n0})\vec{r}_0 - \vec{r}_n\right) \\
&= U(-\omega_0)\vec{R}_{01} + U(-\omega_0 + \Omega_{01})\vec{R}_{12} + \dots + U(-\omega_0 + \Omega_{01} + \dots + \Omega_{n-1,n})\vec{R}_{n0} \\
&\quad + U(-\omega_0 + \Omega_{01})\vec{r}_1 + U(-\omega_0 + \Omega_{01} + \Omega_{12})\vec{r}_1 + \dots + U(-\omega_0 + \Omega_{01} + \dots + \Omega_{n0})\vec{r}_0 \\
&\quad - U(-\omega_0)\vec{r}_0 - U(-\omega_0 + \Omega_{01})\vec{r}_1 - \dots - U(-\omega_0 + \Omega_{01} + \dots + \Omega_{n-1,n})\vec{r}_n \\
&= U(-\omega_0)\oint_\gamma \vec{\mathcal{R}}^{(0)},
\end{aligned} \tag{1.27}$$

assuming there are no disclinations such that $\oint_\gamma \Omega = 0$. This definition of the Burgers vector is independent of the translation part of the gauge transformation but rotates according to the change in the local frame at the origin. This is sensible, as rotating the local frame should rotate the Burgers vector.

One would hope that $d\vec{\mathcal{R}}^{(0)}$ would be a well-defined symmetry flux defining the dislocation density, since the loop integral of $\vec{\mathcal{R}}^{(0)}$ seems like a sensible definition of the Burgers vector. However, this quantity is non-local, origin-dependent, and not gauge invariant. It is clear that constructing a well-defined translation symmetry flux is a subtle challenge, but it is possible [62]. In this thesis we do not study systems that are sensitive to both translations and rotations in the same plane, so such a construction is not necessary. However, it is an important consideration for future work studying combined translation- and rotation-electromagnetic responses of three-dimensional systems.

1.5 Outline

So far we have reviewed the relevant history of topological quantum matter, the utility of effective response theories for studying topological phases, the types of topological lattice defects that exist in crystals, how to place tight-binding Hamiltonians on defected lattices, and how crystalline gauge fields can be used to capture lattice geometry. In the remainder of this thesis, we apply these tools to study the crystalline-electromagnetic response of a wide range of systems. We begin in Chapter 2 by developing a unified theory of topological response theories that can be built by combining electromagnetic and translation gauge fields. We identify topological semimetals that host each of these responses and calculate the response coefficients through a combination of the gradient expansion procedure, dimensional reduction, compactification, and

the Kubo formula. In Chapter 3 we verify these effective response theories through microscopic and numerical calculations employing tight-binding models. In Chapter 4 we apply the ideas developed in the previous two chapters to study the translation-electromagnetic responses of a higher order topological semimetal. Using a combination of analytic and numerical tools, we show that the higher order topological semimetal hosts both bulk and surface translation-electromagnetic responses, the coefficients of which are related by the bulk quadrupole moment of crystal momentum, a previously unstudied quantity. Finally, in Chapter 5 we turn to studying the rotation-electromagnetic response of a novel insulator that arises from coupling a Dirac semimetal to charge density wave (CDW) order. We show that the anomalous unquantized rotation-electromagnetic response of conventional Dirac semimetals is elevated to a quantized response in the resulting Dirac-CDW insulator. The rotation-electromagnetic response binds a quantized charge per length to disclination lines and leads to a disclination filling anomaly, a difference in the charge bound to disclination lines with open and periodic boundary conditions.

Chapter 2

Anomalous translation-electromagnetic responses in semimetals

This chapter is adapted from Mark R. Hirsbrunner, Oleg Dubinkin, Fiona J. Burnell, and Taylor Hughes, arXiv preprint arXiv:2309.10840.

2.1 Introduction

In this chapter we study the topological responses of 1D, 2D, and 3D topological semimetals coupled to electromagnetic and translation gauge (strain) fields. In addition to the well-studied case where the nodal points form a dipole in the BZ, we also study cases where the point-nodes have momentum-energy quadrupole or octupole patterns. Our approach allows us to make clear connections between a wide variety of response theories across dimensions, and clarifies relationships between many of the response theories we discuss. We find that the chirality-weighted momentum-energy *multipole* moments of the semimetals determine new types of quasi-topological responses to electromagnetic fields and strain. We are able to explicitly derive many of these responses from Kubo formula calculations (sometimes combined with dimensional reduction procedures [26]). We also extend our results to the responses of nodal line semimetals (NLSMs) and construct a new type of NLSM with an unusual crossed, cage-like nodal structure. In the next chapter we explicitly study these families of response theories using lattice model realizations.

This chapter is organized as follows. In Sec.2.2 we provide an overview of and intuition about the

response theories that we discuss in more detail in later sections, and in the following sections we derive a family of effective actions that describe mixed crystalline-electromagnetic responses coupling electromagnetic and translation gauge fields in various spatial dimensions. We begin in section 2.3 by deriving the effective response theories of 2D semimetals. We use these 2D responses as guides to derive the responses of 1D semimetals in section 2.4 and the responses of 3D nodal line semimetals in section 2.5. The anomalous nature of semimetals in 3D makes direct calculation of their responses quite subtle, so we next derive in section 2.6 the responses of 4D semimetals. In section 2.7 we both consider boundary responses of and apply compactification procedures to 4D semimetals to obtain response theories for 3D semimetals.

2.2 Overview of Response Theories

The systems we consider in this article all exhibit $U(1)$ charge conservation and discrete translation symmetry in at least one spatial direction. In the presence of these symmetries we can consider the responses to background field configurations of the electromagnetic gauge field A_μ and the collection of translation gauge fields $\mathfrak{e}^a_\mu$. For example, if the system exhibits translation symmetry in the x-direction, then we can consider coupling the system to the field $\mathfrak{e}^x_\mu$. Our goal is to study low-energy response theories of electrons coupled to translation and electromagnetic gauge fields.

Using this framework, our goal is to consider the low-energy responses of electrons to the background electromagnetic and translation gauge fields. Given a translation-invariant Bloch Hamiltonian H, the response theories we consider can, in principle, be derived from correlation functions of the electromagnetic current

$$j^\mu = e\frac{\partial H}{\partial k_\mu}, \tag{2.1}$$

and the crystal momentum current

$$\mathcal{J}^\mu_a = \hbar k_a \frac{\partial H}{\partial k_\mu}, \tag{2.2}$$

where the former couples to A_μ and the latter to $\mathfrak{e}^a_\mu$ (see App. A.1 for more details for the latter). Indeed, we take exactly this approach in Sections 2.3-2.7 to derive response actions for 2D and 3D systems. While our explicit derivations are important for precisely determining the coefficients of the response actions we study, it will be helpful to first motivate the overarching structure that connects a large subset of these response theories. We also note that alternative approaches to determining some of the response actions we discuss have been proposed in Refs. [63], [78], [79], and where the results overlap with ours, they agree.

To understand the connections between the response theories we study, it is useful to begin by reviewing the well-known dimensional hierarchy of response theories of strong topological insulators [26]. We show the

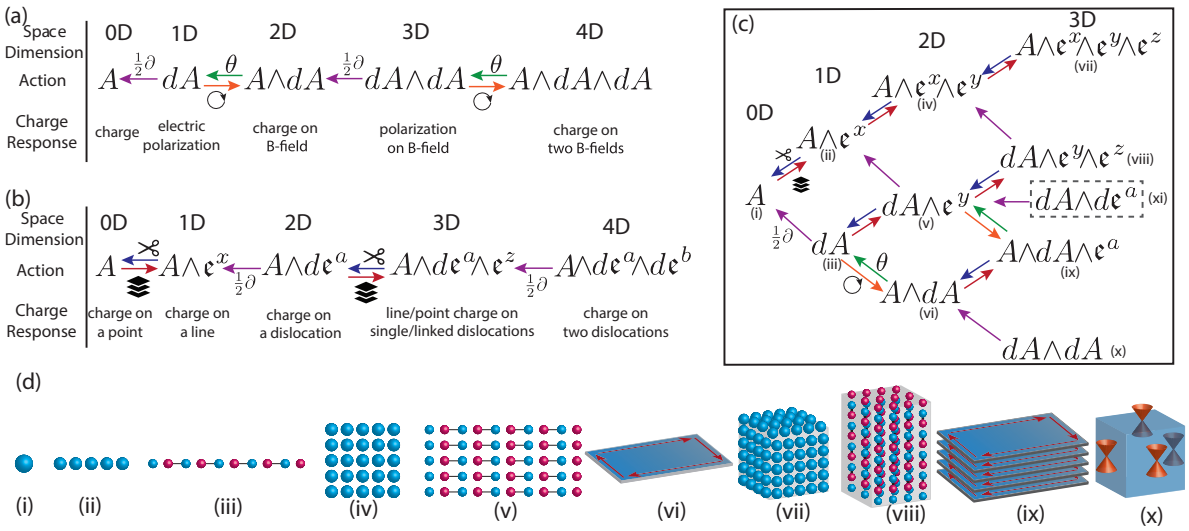

Figure 2.1: (a) A dimensional hierarchy of theories describing responses of strong topological insulators. The theories are related by dimensional reduction (θ symbol, green arrow) [26], taking the boundary response ($(1/2)\partial$ symbol, purple arrow), or adiabatic pumping ($\circlearrowleft$ symbol, red arrow) [5]. (b) A dimensional hierarchy of insulating systems with mixed crystalline-electromagnetic responses. The theories are related by stacking (layer symbol, dark red arrow) and cutting (scissor symbol, blue arrow). (c) A family tree of dimensional hierarchies establishing connections between responses of strong TIs and insulators with mixed crystalline-electromagnetic responses. (d) Illustrations representing the nature of the phases constituting the hierarchy depicted in (c). (i) A single isolated charge. (ii) A line of charges forming a lattice. (iii) An insulating chain having a quantized charge polarization. (iv) A two-dimensional lattice of charges. (v) A two-dimensional weak topological insulator where polarized chains are stacked transverse to their polarization. (vi) A two-dimensional Chern insulator having chiral edge states indicated by red arrows. (vii) A three-dimensional lattice of charges. (viii) A three-dimensional lattice built from a two-dimensional array of polarized chains; alternatively, a stack of two-dimensional weak topological insulators. (ix) A three-dimensional stack of Chern insulators forming a time-reversal breaking weak topological insulator. (x) A three-dimensional strong topological insulator with surface Dirac cones.

general structure in Fig. 2.1(a), where the response terms are built solely from the electromagnetic gauge field. Furthermore, Chern-Simons and θ-term response actions appear in even and odd spatial dimensions, respectively. There are a number of connections between the theories in different dimensions, and we will now review three of them. First, a Chern-Simons action in D spatial dimensions can be dimensionally reduced to a θ-term action in (D-1)-dimensions by compactifying one spatial direction [90], [91]. The (D-1)-dimensional system can also represent a TI if the value of θ is quantized to be $0 or \pi$ by a symmetry that protects the (D-1)-dimensional topological insulator [26]. Second, one can consider the reverse process in which quantized adiabatic pumping [5] in (D-1)-dimensions converts a θ-term action to a D-dimensional Chern-Simons action. Finally, a θ-term action for a (D-1)-dimensional topological insulator exhibits a half-quantized (D-2)-Chern-Simons response on boundaries where θ jumps by π. These general relationships are summarized in Fig. 2.1(a) where each type of relationship is color- and symbol-coordinated.

Next, consider the less familiar set of relationships in Fig. 2.1(b) between *gapped* theories with mixed

crystalline-electromagnetic responses arising from effective actions containing both A_μ and $\mathfrak{e}^a_\mu$ fields. We emphasize that the precise relationships we refer to in Fig. 2.1(b) are for gapped systems where the coefficients of the actions are quantized. In contrast, for the majority of this chapter we focus on the quasi-topological responses of *gapless* systems which take similar forms, but with non-quantized coefficients. Remarkably, many of the actions we discuss for insulators can be generalized to the non-quantized case. For semimetals, however, the dimensional relationships we point out are more akin to physical guides than a precise prescription for deriving matching coefficients in-between dimensions.

With this caveat in mind, let us consider the family of theories in Fig. 2.1(b). In 0D we can consider the response action for a gapped system of electrons, $S[A] = Q\int dtA_0$, which represents a system with charge $Q = eN_e$ where N_e is the (integer) number of electrons. Stacking these 0D systems in a discrete, translation-invariant lattice in the x-direction, generates a line of charges. Indeed, stacking produces the response for a translation invariant line-charge density which is captured by the next action in the sequence in Fig. 2.1(b), i.e., $Q\int A\wedge e^x = Q\int dxdt(A_0\mathfrak{e}^x_x - A_x\mathfrak{e}^x_0)$. In this action the first term represents the charge density along the line, while the second term represents a current generated if the lattice of charges is moving. The latter consequence becomes manifest in the weakly distorted lattice limit since the current is proportional to the displacement rate: $j\sim\mathfrak{e}^x_0\sim\frac{\partial u^x}{\partial t}$.

One can also imagine a reverse process in which a single unit cell is cut out of a translation-invariant line of charge at integer filling. Since the system is gapped and translation invariant, this results in a move in the opposite direction in Fig. 2.1(b), i.e., from $A\wedge\mathfrak{e}^x$ in 1D to A in 0D with the same *integer* coefficient Q. We can use this example to highlight our caveat about gapped vs. gapless systems mentioned above. That is, while it is reasonable to have a 1D gapless system with non-quantized (i.e., non-integer) charge (per unit cell) described by the 1D action, the cutting procedure will not work properly at non-integer filling since the result will be a 0D point with a fractional charge.

In comparison to the response sequence for strong TIs, we see that stacking is the analog of pumping for the translation gauge field [1]. While pumping adds an extra electromagnetic gauge field factor A, stacking adds an extra translation gauge field $\mathfrak{e}^{D+1}$, where D+1 is the stacking direction. As a result, given any action in the strong TI sequence, we can stack copies to get the response action of a primary weak TI (stacks of co-dimension-1 strong TIs, e.g., lines stacked into 2D) by adding a wedge product with $\mathfrak{e}^{D+1}$. We can push the stacking idea further to generate secondary weak TIs (stacks of co-dimension-2 strong TIs, e.g., lines stacked into 3D) by a wedge product with $\mathfrak{e}^{D+1}\wedge\mathfrak{e}^{D+2}$, and so on.

The stacking and cutting procedures are not the only relationships between the response theories in

[1] As mentioned, this analogy is precise only for gapped systems. For gapless systems the analogy predicts the correct form of the action, but does not uniquely determine the coefficient.

Fig. 2.1(b). Just as in the strong TI sequence, there exist connections between the boundary properties of some D-dimensional systems and the bulk response of a (D-1)-dimensional system. For example, the 2D response action in Fig. 2.1(b) represents the response of a stack of Su-Schrieffer-Heeger chains (SSH) [22], each with a quantized polarization of $e/2$. The boundary of such a 2D system is a line of charge on the edge, albeit with a density of $e/2$ electrons per unit cell on the edge line instead of the integer density obtained by stacking integer-filled 0D points. As such, the boundary of the 2D $A \wedge d\mathfrak{e}^x$ action represents a line-charge described by the action $A \wedge \mathfrak{e}^x$, but with a half-integer coefficient.

Combining the dimensional relationships in the sequences of both Fig. 2.1(a) and (b) allows us to construct family tree of related theories. We show this tree in Fig. 2.1(c), including response actions in 0, 1, 2, and 3 spatial dimensions. In 0D there is only an integer electron charge response that couples to A_0. For 1D, one can either stack charges to form a line of charge (upper branch), or consider an electrically polarized TI (lower branch) where the charge is split in half and moved to opposing ends of the chain while the interior remains neutral. In 2D one can stack line charges to get a plane of charge (top branch), stack 1D polarized TIs to get a weak TI (middle branch), or pump charge in a 1D TI to generate a 2D Chern insulator (bottom branch).

In 3D the set of responses is richer. Stacking plane charges generates a 3D volume of charges (top branch), stacking Chern insulators generates a 3D primary weak TI (second from bottom branch), and stacking 2D weak TIs generates a 3D secondary weak TI built from 1D polarized wires (second branch from top). The other well-known possibility is the magneto-electric response for a 3D strong TI [26], [27] (bottom branch). Although it is not shown, this theory is related to a 4D quantum Hall system via pumping (3D to 4D) or dimensional reduction (4D to 3D) [26]. The final option we consider, which is the middle branch enclosed by a dotted rectangle, is $\int dA \wedge d\mathfrak{e}^a$. This response theory has not been previously studied in detail. This theory is a total derivative, and yields a gapped boundary with an electric polarization (e.g., a stack of SSH chains on the boundary). This is reminiscent of an electric quadrupole (higher-order) response [92], [93], and we explore this connection further in Sec. 2.7.

While the above discussion centers on gapped systems, our primary focus is on gapless topological semimetals. Importantly, each of the actions in the family tree in Fig. 2.1(c) that contain a translation gauge field can also represent a contribution to the response of various types of metals or topological semimetals [32]–[36], [63], [77]–[79], [94]. This is because many semimetals can be generated by translation-invariant stacking of lower dimensional topological phases. Since the momentum k^a in the stacking direction is conserved, one can consider adding up the set of topological response terms for each gapped k^a. A semimetal represents a scenario where the coefficients of these topological terms at each k^a are quantized and have discrete jumps at k^a that contain a nodal point. For example, the 2D electric polarization response of a

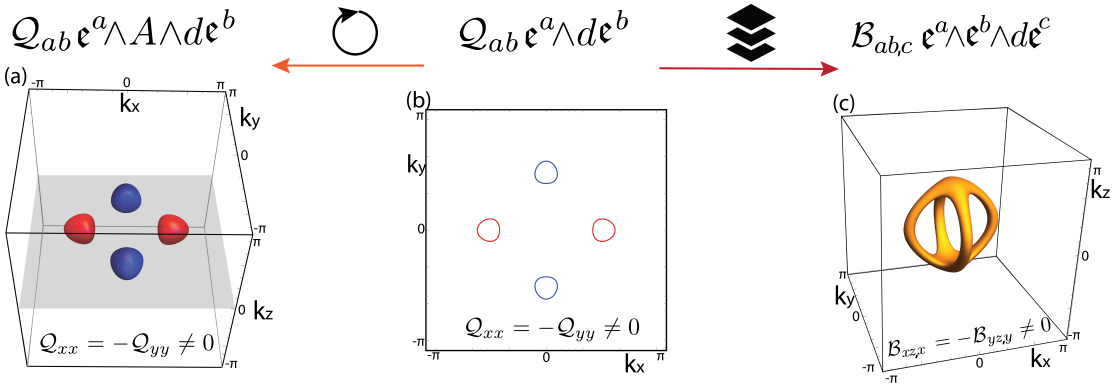

Figure 2.2: (a) Fermi-surfaces of a 3D time-reversal invariant Weyl semimetal with a quadrupole Weyl node configuration. Red and blue colors denote positive and negative Berry-curvature respectively. The associated action has a coefficient matrix $\mathcal{Q}_{ab}$ which is symmetric and proportional to the Weyl-node quadrupole moment. For this configuration the coefficients $\mathcal{Q}_{xx}$ and $\mathcal{Q}_{yy}$ are non-vanishing. (b) Similar to subfigure (a) except it is the Fermi surfaces for a 2D Dirac semimetal having four Dirac nodes in a quadrupole pattern. The action is described by a symmetric matrix of coefficients $\mathcal{Q}_{ab}$. (c) the Fermi surface of an unusual cage-like nodal line semimetal built from stacking the Dirac node quadrupole semimetal in subfigure (b). The action has a set of coefficients $\mathcal{B}_{ab,c}$ which is anti-symmetric in a and b. Heuristically the action in (b) can generate the action in (a) by adiabatic pumping, or can generate the action in (c) by stacking.

stack of 1D TIs becomes the response of a 2D Dirac semimetal if the wires forming the stack are coupled strongly enough to close the insulating gap [36]. In the presence of reflection symmetry, each momentum in the stacking direction has a quantized charge polarization that jumps when the momentum hits a gapless 2D Dirac point. Additionally, the 3D response of a stack of Chern insulators becomes the non-quantized anomalous Hall effect response of a time-reversal breaking Weyl semimetal, in which each fixed-k plane that does not intersect a Weyl point carries a quantized Chern number that jumps at a Weyl point [32]–[35]. While many of these response theories have been discussed in detail before, only a few works have highlighted the contributions from the translation gauge fields [63], [73], [77]–[79], [86], [94], [95]. As such, a large fraction of this chapter is devoted to explicit derivations of the response coefficients of the actions in Fig. 2.1(c) that have couplings to the translation gauge fields. We leave explicit calculations of the physical response phenomena in representative model systems to the next chapter.

Before moving on to more explicit derivations, we first provide here motivation for three additional response theories that lie outside the family tree in Fig. 2.1(c). As mentioned above, a remarkable feature of the response actions of point-node semimetals is that their coefficients are determined from the energy-momentum locations of the nodal points. Indeed, for the relevant response actions in Fig. 2.1(c), the coefficients are obtained as a chirality-weighted momentum dipole moment of the point-nodes (note that Dirac points do not have a chirality, nevertheless there is a signed quantity that plays the same role). Interestingly, recent work on rank-2 chiral fermions and Weyl semimetals with a chirality-weighted momentum *quadrupole*

moment [63], [77], [78], [94] has unveiled a new set of response theories. This category of theories contains actions that include factors of more than one translation gauge field of the same type (e.g., $\mathfrak{e}^a \wedge d\mathfrak{e}^b$, where $a = b$), and as such, does not appear in the family tree in Fig. 2.1(c). This also implies that the translation gauge field factors in these response theories cannot be obtained by the conventional stacking of lower dimensional systems that we discussed above, since stacking produces wedge products with distinct translation gauge fields.

In Fig. 2.2 we show three response theories that follow this pattern along with representative Fermi surfaces of systems hosting the response theories. Fig. 2.2(a) shows the Fermi surface structure of a 3D time-reversal invariant Weyl semimetal with a Weyl node quadrupole moment. The response action of this system is mixed between electromagnetic and translation gauge fields, and the inset in the Fermi-surface figure lists which coefficients $\mathcal{Q}_{ab}$ are non-vanishing. Some details of this response were discussed in Refs. [63], [77], [94], the former of which connects the response to rank-2 chiral fermions on the surface of the 3D Weyl semimetal. Fig. 2.2(b) shows the Fermi surface structure of a 2D Dirac semimetal with a Dirac node quadrupole structure. This response represents a momentum current response to a translation gauge field. Its form shares some similarities with the torsional Hall viscosity [72], [95]–[98], though we leave a precise connection to future work. Finally, in Fig. 2.2(c) we show the Fermi-surface for an unusual nodal line semimetal formed from stacking the Dirac node quadrupole semimetal of Fig. 2.2(b). While one may naively expect this system to host two independent Fermi rings, we instead find a new type of Fermi-surface structure in which the Fermi lines join at two crossings to form a cage. The symbols on the right-hand-side of Fig. 2.2 indicate the connections between these theories: (i) the response of the nodal line structure is a stacked version of the 2D Dirac node quadrupole semimetal response from Fig. 2.2(b), and (ii) one can heuristically consider the four-node Weyl response in Fig. 2.2(a) to be a dimensional extension of the response in Fig. 2.2(b) via pumping.

Hvaing described the forms of the various response actions of interest, in the following sections we determine their coefficients. All of the response actions in Fig. 2.1(c) that contain only electromagnetic gauge fields represent insulators, and their coefficients have been studied in detail (e.g., see Ref. [26]). The actions containing translation gauge fields can represent insulators or gapless systems, and the two can often be distinguished by the values of the coefficients. That is, for insulators we expect the coefficients to be quantized in some units (in even spatial dimensions they are quantized in the presence of some symmetry), while for topological semimetals we expect the coefficients to be a tunable function of the momentum and energy locations of the nodal points or lines. Our focus here is on 2D Dirac, 3D Weyl, and 3D nodal line semimetals. Interestingly, some of the response coefficients for metals/semimetals can take the same values allowed for an insulator, although this would typically require fine-tuning, or extra symmetry. For example,

a 1D system can have compensating particle and hole Fermi surfaces such that the total filling is an integer, as one would find in an insulator, yet the system is still gapless. In such a case we will show that the system has additional response terms that have coefficients that are incompatible with a gapped insulator.

It is important to acknowledge a key qualitative difference between these types of topological semimetals. Namely, we recall that 2D topological Dirac semimetals and 3D nodal line semimetals require symmetry (the composite $\mathcal{TI}$ symmetry) to guarantee the local stability of the gapless points/lines in momentum space. This is inherently different from the case of 3D Weyl semimetals, for which the nodes require no extra symmetry to protect their gaplessness. A Weyl node can be gapped out only by bringing another Weyl node of opposite chirality to the same point in the Brillouin zone. A similar story applies to (semi)metallic systems in 1D: each gapless point has a well-defined chirality defined as the sign of the Fermi velocity, and a gap can be opened only by overlapping Fermi points of opposite chiralities.

This distinction in symmetry protection is important for the response theories describing Dirac and Weyl semimetals as it reflects the well-known structure of anomalies in even and odd spatial dimensions. Furthermore, it will impact our strategy for deriving the response coefficients for these systems. As an example, the response properties of 2D Dirac semimetals can be determined straightforwardly from the Kubo formula if we first apply a symmetry-breaking perturbation that weakly gaps out the nodes. The resulting insulator response can then be taken to the semimetallic limit by tuning the perturbation to zero. Hence, the effective response action for such systems can be obtained by treating the system as an insulator and applying the Kubo formula, or more generally, a gradient expansion procedure. This method can be applied to 2D and 4D Dirac semimetals, and consequently 3D nodal line semimetals since they are just stacks of 2D Dirac semimetals. For such semimetals we actually have a choice of what symmetry to break, e.g., inversion or time-reversal. Which one we need to break depends on the nodal configuration and the action we are intending to generate. For example, in the case of a 2D Dirac semimetal with a pair of nodes, breaking time-reversal is well-studied and generates a quantum Hall response via a Chern-Simons term. However, breaking inversion symmetry is relatively less-studied and generates a mixed Chern-Simons response between electromagnetic and translational gauge fields. This is corroborated by the fact that the electromagnetic Chern-Simons action breaks time-reversal, while the mixed Chern-Simons term with these fields breaks inversion. We show that the mixed Chern-Simons term has a well-defined limit as the gap closes and inversion symmetry is restored, which leads to a non-trivial response action for the 2D Dirac semimetal.

Alternatively, the response of isolated chiral gapless points in 1D and 3D can be determined if they are viewed as theories that live on the boundary of a higher-dimensional topological insulator or topological semimetal. In the presence of gauge fields, the higher-dimensional bulk generates a current inflow to the boundary to compensate the anomalous response of the gapless boundary modes. From this perspective, one

expects that the effective response action of Weyl semimetals in odd spatial dimensions can be obtained by taking the boundary contribution of a higher-dimensional system. There are likely other methods that can be applied to derive these response actions in their intrinsic spatial dimension, e.g., via the subtle introduction of an auxiliary θ-field, but we choose our procedure since it reinforces the dimensional relationships discussed in the previous section and requires fewer formal tools.

Our strategy for deriving the general form of the coefficients of mixed crystalline-electromagnetic responses begins with deriving effective response actions in even spatial dimensions, i.e., 2D and 4D. We do so by identifying gradient expansion contributions (see Appendix A.2 for a brief review) that contain an appropriate effective action constructed out of translational ($\mathfrak{e}^\lambda$) and electromagnetic (A) gauge fields. The response of semimetals in odd spatial dimensions is then obtained by looking at the boundary of response theories defined in one higher dimension.

2.3 Effective responses of 2D semimetals

In this subsection we derive the coefficients of two 2D response actions that contain translation gauge fields, namely response action (v) from Fig. 2.1(c), and the response action in Fig. 2.2(b). We find that the coefficients of these actions are characterized by the dipole and quadrupole moments of the Berry curvature in the 2D Brillouin Zone, respectively. Specializing to 2D Dirac semimetals, we find the distribution of Berry curvature is sharply localized as $\pm\pi$-fluxes at the Dirac nodes. Hence, the coefficients become proportional to the dipole and quadrupole moment of the distribution of Dirac nodes.

Dirac node dipole semimetal

First consider a gapped $\mathcal{T}$-invariant system with broken $\mathcal{I}$ symmetry. Under these conditions the electromagnetic Chern-Simons term, which represents the Hall conductivity, vanishes. We can consider instead the mixed linear response of a momentum current to an electromagnetic field, or vice-versa. Using the Kubo formula, or applying the gradient expansion procedure described in App. A.2, we find the following contribution to the effective action (when the chemical potential lies in the insulating gap) (See also [88]):

$$S_{e,A} = -e \int d^3r \; \mathfrak{e}^\alpha_\mu \partial_\nu A_\rho \int \frac{d\omega d^2k}{(2\pi)^3} k_\alpha \Omega^{(3)}_{\mu\nu\rho}(\omega, k), \tag{2.3}$$

where

$$\Omega^{(3)}_{\mu\nu\rho}(\omega, k) = \mathrm{tr}\left(G_0 \frac{\partial G_0^{-1}}{\partial k_\mu} \frac{\partial G_0}{\partial k_\nu} \frac{\partial G_0^{-1}}{\partial k_\rho} \right), \tag{2.4}$$

and $G_0(k_\mu)$ is the single-particle Green function. To extract the coefficient of the $\mathfrak{e}^\alpha \wedge dA$ term, we contract $\Omega^{(3)}_{\mu\nu\rho}$ with the totally antisymmetric tensor $\frac{1}{3!}\varepsilon^{\mu\nu\rho}$. This gives the coefficient

$$c_\alpha = e\frac{\varepsilon^{\mu\nu\rho}}{3!}\int \frac{d\omega d^2k}{(2\pi)^3} k_\alpha \; \Omega^{(3)}_{\mu\nu\rho}(\omega, k) \tag{2.5}$$

of the response action

$$S_{e,A} = c_\alpha \int \mathfrak{e}^\alpha \wedge dA. \tag{2.6}$$

We note that Eq. 2.5 is very similar to the response coefficient of the standard electromagnetic Chern-Simons term, excepting from the factor of k_α in the integrand. As such, assuming $\alpha = x, y$, we use a well-established result to evaluate the frequency integral and obtain [99]:

$$\frac{\varepsilon^{\mu\nu\rho}}{24\pi^2}\int d\omega d^2k \; \Omega^{(3)}_{\mu\nu\rho}(\omega, k) = \frac{1}{2\pi}\int_{BZ} dk_x dk_y \; \mathcal{F}^{xy}(k_x, k_y), \tag{2.7}$$

where $\mathcal{F}^{xy}$ is the Berry curvature. Hence, we can rewrite c_α as an integral over the BZ by substituting this relationship into Eq. 2.5 to find:

$$c_\alpha = \frac{e}{(2\pi)^2}\int_{BZ} dk_x dk_y \; k_\alpha \mathcal{F}^{xy}(k_x, k_y). \tag{2.8}$$

We have thus arrived at the result that c_α is proportional to the α-th component of the dipole moment of the distribution of Berry curvature. This coefficient can be non-zero since it is allowed by broken $\mathcal{I}$ and preserved $\mathcal{T}$, i.e., $\mathcal{F}^{xy}(\mathbf{k}) = -\mathcal{F}^{xy}(-\mathbf{k})$. We also note that c_α is independent of the choice of zone center, and shifts of k in the integrand in general, because the Chern number (Hall conductivity) vanishes in the presence of $\mathcal{T}$.

In a gapped $\mathcal{T}$-invariant system, restoring $\mathcal{I}$-symmetry forces c_α to vanish, since $\mathcal{F}^{xy}(\mathbf{k}) = 0$. However, in gapless systems this need not be the case. To see this, we apply our result from Eq. 2.8 to a 2D Dirac semimetal by first introducing a weak perturbation $V_\mathcal{I}$ that breaks $\mathcal{I}$ and opens up a small gap, and then taking the limit $V_\mathcal{I} \to 0$, in which inversion symmetry is restored. In the gapped system the Berry curvature $\mathcal{F}^{xy}$ is distributed smoothly across the entire 2D BZ. In the gapless limit, the Berry curvature distribution develops sharp peaks of weight π localized at the positions of the Dirac points:

$$\mathcal{F}^{xy} = \sum_{a=1}^{N_D} \pi\chi_a \delta(\mathbf{k} - \mathbf{k}^a), \tag{2.9}$$

where a runs over all Dirac nodes at momenta $\mathbf{k}^a$, and $\chi_a = \pm 1$ is an integer indicating the sign of the

π-Berry phase around the Fermi surface of the a-th Dirac point at a small chemical potential above the node [36]. Ultimately, we find the effective response action of a Dirac node dipole semimetal is given by:

$$S_{DD} = \frac{e\mathcal{P}_\alpha}{4\pi}\int \mathfrak{e}^\alpha \wedge dA, \tag{2.10}$$

where

$$\mathcal{P}_\alpha = \sum_{a=1}^{N_D} \chi_a k_\alpha^a, \tag{2.11}$$

is the dipole moment of the Dirac nodes.

Note that if the Dirac nodes meet at the zone boundary, they can be gapped even in the presence of $\mathcal{TI}$ symmetry. The resulting insulating phase represents a weak TI with $\mathcal{P}_\alpha = G_\alpha$, where G_α are the components of a reciprocal lattice vector. In this case, the action in Eq. 2.10 describes a stack (i.e., a family of lattice lines/planes corresponding to G_a) of 1D polarized TI chains aligned perpendicular to G_a. To see this explicitly, we take $G_x = \frac{2\pi}{a_x}$, and set $e_\beta^\alpha = \delta_\beta^\alpha$ in Eq. 2.10 to obtain the action

$$\frac{e}{2}\int \frac{dx}{a_x}\left(\int dydtE_y\right) = N_x\frac{e}{2}\int dydtE_y, \tag{2.12}$$

where N_x is the number of unit cells in the x-direction. This action is just N_x copies of the usual θ-term action for 1D, electrically-polarized topological insulators ($\theta = \pi$) parallel to the y-direction, stacked along $\hat{x}$.

We shown that Eq. 2.10 is a quasi-topological contribution to the response of a 2D Dirac semimetal where the nodes have a dipolar configuration. However, there is another important subtlety that we must consider. Earlier work shows that the electromagnetic response of 2D Dirac semimetals with both $\mathcal{T}$ and $\mathcal{I}$ symmetry is an electric polarization proportional to the Dirac-node dipole moment [36]. Even more recently, connections have been made between mixed translation-electromagnetic responses and the electric polarization [89]. Since we have a clear derivation of the response term we can use our results to understand the precise connection between the electric polarization and the coefficient c_α of the $e^\alpha \wedge dA$ response action. Using the standard approach of Ref. [100], the polarization in 2D is

$$P_e^\alpha = \frac{e}{(2\pi)^2} i\int_{BZ} d^2\mathbf{k}\langle u_\mathbf{k}|\partial_{k_\alpha} u_\mathbf{k}\rangle \tag{2.13}$$

where $\mathcal{A}^\alpha(k) = i\langle u_\mathbf{k}|\partial_{k_\alpha} u_\mathbf{k}\rangle$ is the Berry connection. Hence, we find that the electric polarization P_e^α is

related to c_α by an integration by parts (See Appendix A.3):

$$\begin{aligned} P_e^\alpha &= \frac{e}{(2\pi^2)}\varepsilon^{\alpha\beta}\int d^2k\ k_\beta \mathcal{F}^{xy} + \frac{e}{2\pi}W^\alpha \\ &= \epsilon^{\alpha\beta}c_\beta + \frac{e}{2\pi}W^\alpha, \end{aligned} \tag{2.14}$$

where we set the lattice constants equal to unity and the Wilson loop

$$W^\alpha = \oint dk_\alpha \mathcal{A}^\alpha(k_\alpha, k_\beta = \pi), \tag{2.15}$$

is an integral of the Berry connection $\mathcal{A}^\alpha$ along the α-th momentum direction at a fixed, inversion-invariant transverse momentum $k_\beta = \pi$ at the boundary of the BZ.

From this explicit relationship there are some immediate conclusions. First, in the Dirac semimetal limit we reproduce the result of Ref. [36], where the polarization is proportional to the Dirac node dipole moment: $P_e^\alpha = \frac{e}{2(2\pi)}\varepsilon^{\alpha\beta}\mathcal{P}_\beta$. Second, if we have broken inversion symmetry (while $\mathcal{T}$ is still preserved), we see that the polarization and the coefficient c_α are not quantized, and *not equal* to each other. This scenario can be found in inversion-breaking insulators with a Berry curvature dipole moment. These insulators have a charge polarization and also possess a mixed translation-electromagnetic response. However, we find from this calculation and explicit numerical checks that they are generically inequivalent. Ultimately, this boils down to the fact that the Wilson loop at the boundary of the BZ requires a symmetry to be quantized, e.g., mirror or inversion. Otherwise, the Wilson loop gives a contribution that distinguishes the polarization and the mixed crystalline-electromagnetic responses. We leave a detailed discussion of this subtle distinction to future work.

To summarize, Eq. 2.10 captures the generic mixed crystalline-electromagnetic response of the bulk of a 2D system with $\mathcal{T}$-symmetry. In the limit of a Dirac semimetal, the coefficient of the response coincides with the electric polarization of the system. We note that in this limit there are other non-vanishing response terms since the system is gapless, but Eq. 2.10 represents a distinct contribution to the total response of the system to electromagnetic and translation gauge fields. We study an explicit model with this response term in Sec. 3.2.

Dirac node quadrupole semimetal

Here we discuss the response of quadrupole arrangements of 2D Dirac nodes, as shown in Fig. 2.2(b). If the Chern number and momentum dipole moment $\mathcal{P}_\alpha$ vanish, then the semimetal has a well-defined momentum quadrupole moment that is independent of the choice of zone center. Here we show that such systems are

described by the response action:

$$S_{DQ} = \frac{\hbar \mathcal{Q}_{\alpha\beta}}{8\pi} \int \mathfrak{e}^{\alpha} \wedge d\mathfrak{e}^{\beta}. \tag{2.16}$$

From the derivation in the previous subsection we anticipate that, in the limit of a Dirac semimetal band structure, the coefficient $\mathcal{Q}_{\alpha\beta}$ of this response action is related to the momentum quadrupole moment of the Dirac nodes. To confirm this statement, let us consider the linear response of a momentum current to a translation gauge field for a gapped system. From the Kubo formula, or gradient expansion, we find a coefficient of the $\mathfrak{e}^{\alpha} \wedge d\mathfrak{e}^{\beta}$ term:

$$\mathcal{Q}_{\alpha\beta} \equiv \frac{1}{2} \frac{\varepsilon_{\mu\nu\rho}}{3!} \int \frac{d\omega d^2k}{(2\pi)^3} k_\alpha k_\beta \ \Omega^{(3)}_{\mu\nu\rho}(\omega, k). \tag{2.17}$$

We can use the relationship mentioned in Eq. 2.7 to carry out the frequency integral to obtain the coefficient of Eq. 2.16:

$$\mathcal{Q}_{\alpha\beta} = \frac{1}{\pi} \int_{BZ} dk_x dk_y \ k_\alpha k_\beta \mathcal{F}^{xy}(k_x, k_y). \tag{2.18}$$

To apply this to the Dirac node quadrupole semimetal shown in Fig. 2.2(b), we evaluate the response by first introducing a symmetry-breaking mass term and study the topological response of the resulting gapped system. The mass term breaks $\mathcal{T}$ but produces a vanishing total Chern number. In the example at hand, this is accomplished by adding a k-independent term that opens a local mass of the same sign for each of the four Dirac points in Fig. 2.2b. Such a mass term preserves $\mathcal{I}$, which in the gapped system automatically guarantees a vanishing dipole moment of the Berry curvature. This, together with the vanishing Chern number, is necessary so that the momentum quadrupole moment is well-defined and independent of the choice of zone center. For this scenario, in the limit that the perturbative mass goes to zero,

$$\mathcal{Q}_{\alpha\beta} = \sum_{a=1}^{N_D} \chi_a k^a_\alpha k^a_\beta, \tag{2.19}$$

which is the Dirac node quadrupole moment. In Sec. 3.3 we explicitly study a model with this Berry curvature configuration and non-vanishing $\mathcal{Q}_{\alpha\beta}$. We find that while the Dirac node dipole moment captures the electric polarization (see Appendix A.3), the Dirac node quadrupole moment captures a momentum polarization (see Appendix A.4), this time, without the subtlety of an additional Wilson loop contribution. For comparison, the surface charge theorem relates the bulk electric polarization to a boundary charge, and the bulk momentum polarization generates a boundary momentum.

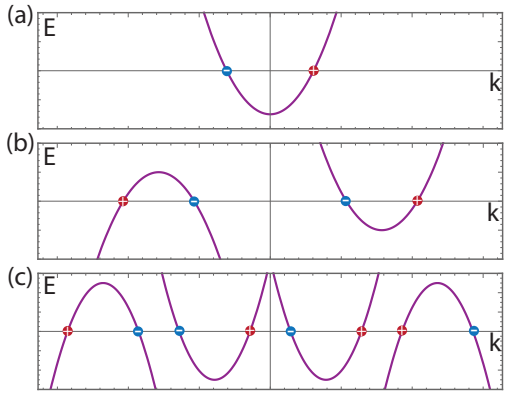

Figure 2.3: (a) One-dimensional band structure of an ordinary metal. The pair of gapless points is marked by the sign of their respective chiralities, highlighting the momentum-space dipole characterizing the response of the system. (b) Band structure of a 1D metal characterized by a momentum quadrupole moment. The system has an integer (vanishing in this case) charge filling, but a non-zero momentum. (c) Band structure of a 1D metal characterized by a momentum octupole moment. The system has an integer (vanishing) filling, a vanishing momentum, but a non-vanishing expectation value for the square of the momentum. See Appendix A.5.

2.4 Effective responses of 1D (semi)metals

Having derived the responses of 2D systems coupled to electromagnetic and translation gauge fields, here we use Figs. 2.1(b) and 2.2 as guides to generate related responses in 1D and 3D. To calculate 1D responses we consider boundary response of the 2D systems (this section), and we obtain responses of 3D nodal line semimetals by stacking 2D responses (next section). We note that in the following discussion we treat translation as a continuous symmetry (as in Appendix A.1, as this perspective is useful for obtaining the correct response actions from our diagram calculations). One can see Ref. [63], for example, for a discussion that treats the subtleties associated to having a discrete translation symmetry.

It is well-known that chiral modes in 1D are anomalous, i.e., charge is not conserved in the presence of an electric field. This anomaly is resolved in 1D lattice models by fermion doubling, i.e., for every right-moving chiral mode there is a corresponding left-moving mode that compensates the anomaly. While it is true that the electromagnetic charge anomaly is resolved with such a lattice dispersion, the doubled system can still be anomalous in a different sense if we have translation symmetry (see Ref. [63] for a similar discussion).

To be specific, in the presence of translation symmetry we can consider the momentum current in Eq. 2.2: $\mathcal{J}^\mu_x = \hbar k_x j^\mu$, where j^μ is the particle number current. At low energies, current-carrying excitations lie in the vicinity of Fermi points $k_x^{F,\alpha}$ and carry corresponding particle currents $j^\mu_{(\alpha)}$. The total contribution to momentum current from these low-lying modes is:

$$\mathcal{J}^\mu_x = \sum_\alpha \hbar k_x^{F,\alpha} j^\mu_{(\alpha)}. \tag{2.20}$$

In the simplest case of a nearest-neighbor lattice model with a single, partially-filled band, there are two Fermi points: $k^F \equiv k_x^{F,R} = -k_x^{F,L}$, with $j_R^\mu = (\rho_R, v_F\rho_R)$ and $j_L^\mu = (\rho_L, -v_F\rho_L)$, where ρ is the number density. Interestingly, the momentum current in this scenario is

$$\mathcal{J}_x^\mu = \hbar k^F (j_R^\mu - j_L^\mu), \tag{2.21}$$

which, up to a factor of $\hbar k^F$, is just the axial current!

Importantly, even though this lattice model does not have an electromagnetic charge anomaly, $\partial_\mu(ej_L^\mu + ej_R^\mu) = 0$, it does have an axial anomaly:

$$\partial_\mu(j_R^\mu - j_L^\mu) = \frac{eE^x}{\pi\hbar}. \tag{2.22}$$

Taking this point of view, we can reformulate the axial anomaly in this system as a mixed crystalline-electromagnetic anomaly where an electric field E_x violates conservation of the k_x momentum current,

$$\partial_\mu \mathcal{J}_x^\mu = \frac{e\hbar k^F}{\pi\hbar} E^x. \tag{2.23}$$

More generally the anomaly is proportional to the momentum dipole moment of the Fermi points, which replaces a factor of $2k_F$ in Eq. 2.23 (see App. A.5).

There is a conjugate effect that occurs in an applied strain field, which can be implemented as a translation electric field $\mathcal{E}_x^x = \partial_x \mathfrak{e}_0^x - \partial_t \mathfrak{e}_x^x$. Naively, such a non-vanishing field will generate violations to the conservation law for the usual electromagnetic current according to

$$\partial_\mu(ej^\mu) = \frac{ek^F}{\pi}\mathcal{E}_x^x, \tag{2.24}$$

(again see App. A.5 for a more general expression in terms of the momentum dipole). However, this equation is not quite correct for an isolated system with a fixed number of electrons, and hence, we must be careful when considering time-dependent changes to $\mathfrak{e}_x^x$.

To gain some intuition for Eq. 2.24, consider increasing the system size by one lattice constant a during a time T by adding an extra site to the system: $\int dxdt\ \mathcal{E}_x^x = a$ (one can also think of threading a dislocation into the hole of a 1D periodic system). From the anomaly equation we find that the amount of charge in the system changes by $ek^F a/\pi$, as one would expect for adding a unit cell to a translation-invariant system with a uniform charge density $\rho = ek_F/\pi$. However, there is a subtlety that we can illustrate by considering a system with a fixed number of electrons $N_e = k^F L_x/\pi$ that we strain by uniformly increasing the lattice

constant. Assuming a uniform system, the anomalous conservation law in this case becomes

$$\partial_t \rho = \partial_t \left(\frac{e k^F}{\pi} \mathfrak{e}_x^x \right). \tag{2.25}$$

Crucially, we note that if we increase the system size with fixed particle number, then k^F will decrease. Indeed, in the small deformation limit the momenta are proportional to $(\mathfrak{e}_x^x)^{-1}$ since their finite size quantization depends inversely on the system size. Using this result, the conservation law becomes:

$$\partial_t \rho = \frac{e}{\pi} \left(\mathfrak{e}_x^x \partial_t k^F + k^F \partial_t \mathfrak{e}_x^x \right) = \frac{e k^F}{\pi} (-\partial_t \mathfrak{e}_x^x + \partial_t \mathfrak{e}_x^x) = 0 \tag{2.26}$$

where we used $\partial_t (\mathfrak{e}_x^x)^{-1} = -(\mathfrak{e}_x^x)^{-2} \partial_t \mathfrak{e}_x^x$.

The outcome $\partial_t \rho = 0$ is the result one would expect by stretching the system uniformly while keeping the number of particles fixed. To clarify, at a fixed particle number we know the total charge cannot change, however it perhaps seems counter-intuitive that the *density* does not decrease if we stretch the system. The reason is that the quantity ρ above, which is defined as $\frac{\delta S}{\delta A_0}$, is not a scalar density. Indeed, for general geometries the scalar charge density is defined as

$$\bar{\rho} = \frac{1}{\mathfrak{e}_x^x} \frac{\delta S}{\delta A_0}, \tag{2.27}$$

where the $\mathfrak{e}_x^x$ is essentially playing the role of the determinant of a spatial metric. To calculate the total charge we then use

$$Q = \int dx \, \mathfrak{e}_x^x \bar{\rho} = \int dx \, \rho. \tag{2.28}$$

The scalar charge density $\bar{\rho}$ decreases as the system is stretched since $\partial_t \bar{\rho} \propto \partial_t \mathcal{P}_x$, which decreases as the system size increases at fixed electron number.

The effective response action of the 1D system can be derived as a boundary effective action of an appropriate 2D theory. In fact, we have already seen such a 2D system when studying the 2D Dirac semimetal with Dirac nodes arranged in a dipolar fashion. The bulk response for this 2D system with a weak inversion-breaking gap is Eq. 2.10. As mentioned above, this bulk theory implies that the system has an electric polarization. From the surface-charge theorem for polarization we expect that the boundary will have a charge density equal the polarization component normal to the boundary. The contribution to the buondary effective action from Eq. 2.10 is:

$$S_\partial = \frac{e}{4\pi} \mathcal{P}_\alpha \int \mathfrak{e}^\alpha \wedge A. \tag{2.29}$$

From this we can extract the boundary charge density: $\rho_\partial = \frac{e}{2}\frac{\mathcal{P}_\partial}{2\pi}\mathfrak{e}_\partial^\partial$ where $\mathcal{P}_\partial$ is the component along the boundary, and $\mathfrak{e}_\partial^\partial$ is the diagonal translation gauge field component along the boundary that is simply equal to unity in non-deformed geometries.

While the form of this action is what we expect for a 1D metal, the coefficient is half the size it should be. The reason is that on the edge of the 2D Dirac semimetal, the momentum-space projections of the bulk Dirac nodes in the edge BZ represent points where the edge-filling changes by $\pm e/2$, [36] not $\pm e$ as would be the case for a 1D Fermi-point in a metal. Hence for a metal we expect a result twice as large (we will see a similar result in Sec. 2.7 when comparing the boundary response of a 4D system to that of a 3D Weyl semimetal). Thus the action for the 1D system is

$$S_{1D,D} = \frac{e}{2\pi}\mathcal{P}_\alpha \int \mathfrak{e}^\alpha \wedge A. \tag{2.30}$$

From this form we can identify $\mathcal{P}_\alpha = (-\Delta\mu/\hbar, \Delta k_x)$ such that $\frac{\mathcal{P}_x}{2\pi}$ is simply the filling fraction of the 1D metal and $\frac{\mathcal{P}_t}{2\pi}$ measures the imbalance of left- and right-moving excitations in the system ($\Delta\mu = \mu_R - \mu_L$).

Introducing a charge current vector

$$j^\mu = \frac{e}{2\pi}\varepsilon^{\mu\nu}\mathcal{P}_\nu = \frac{e}{2\pi}\left(\Delta k_x, \Delta\mu/\hbar\right)^T \tag{2.31}$$

we can recast Eq. 2.31 in the most familiar form: $S_{1D,D} = \int dtdx\ j^\mu A_\mu$. Thus, we have now generated the action (ii) from Fig. 2.1(c). Let us also note that the edge states of the Dirac semimetal can be flat, while the 1D context we mentioned above has a dispersion. However, the key feature of both cases is that as momentum is swept across the 1D BZ (1D surface BZ for the 2D case) the filling of the states changes in discrete jumps at either the Fermi points in 1D, or the (surface-projected) Dirac points in 2D. It is this change in the filling that is captured by the quantity $\mathcal{P}_x$, and it does not depend on the dispersion in a crucial way.

With this example in mind, we can ask what the analogous 1D boundary system is for the Berry curvature quadrupole action Eq. 2.16. We mentioned that this bulk response represents a momentum polarization, which implies that the boundary should have a momentum density parallel to the edge. Indeed, we expect that such a 1D system will have a vanishing Fermi-point dipole moment (i.e., the filling is integer), but a quadrupole moment that is non-vanishing (see Fig. 2.3(b)).

From the point of view of the translation gauge fields, such band structures are chiral since either the right movers or left movers carry larger momentum charge. To see this, consider a 1D Fermi surface with right-movers at momenta $\pm K_F$, and left-movers at momenta $\pm Q_F$. Let us further restrict our attention to

currents for which the net number of right-movers (and of left-movers) is zero, e.g. $\rho_R(K_F)+\rho_R(-K_F)=0$. Defining $\delta\rho_R = (\rho_R(K_F) - \rho_R(-K_F))$, and $\delta\rho_L = (\rho_L(Q_F) - \rho_L(-Q_F))$, we see that the momentum gauge field couples to

$$\mathcal{J}^\mu_x = K_F\delta\rho_R + Q_F\delta\rho_L \ . \tag{2.32}$$

Thus we see that for $K_F \neq Q_F$ (as in Fig. 2.3(b)), the momentum gauge field couples differently to right- and left- moving density fluctuations. In the extreme limit that $Q_F = 0$, the momentum gauge theory is fully chiral.

More generally, in a 1D system with a Fermi-point quadrupole given by (c.f. Eq. 2.19)

$$\mathcal{Q}_{xx} = \sum_{a=1}^{N_F} = \mathrm{sgn}(v_{Fa})(k_x^{(a)})^2, \tag{2.33}$$

and fixed electric charge, this chiral coupling leads to an anomaly in the presence of a non-vanishing translation gauge field:

$$\partial_\mu \mathcal{J}^\mu_x = \frac{\hbar\mathcal{Q}_{xx}}{4\pi}\mathcal{E}^x_x. \tag{2.34}$$

This anomaly implies that if we turn on a translation gauge field (e.g., via strain) then we will generate momentum as shown in App. A.5 [2].

The response theory describing such a 1D system is similar to that describing the chiral boundary of a Chern-Simons theory. Indeed, if we start from Eq. 2.16 and derive the boundary response (and compensate for a similar factor of two as mentioned above in the momentum-dipole case) we arrive at an effective action:

$$S = -\frac{\hbar}{4\pi}\int dtdx \ \left(\mathcal{Q}_{xx}\mathfrak{e}^x_x\mathfrak{e}^x_t + \mathcal{Q}_{xt}\mathfrak{e}^x_x\mathfrak{e}^t_t\right). \tag{2.35}$$

In this effective action the momentum quadrupole moment of the Fermi points $\mathcal{Q}_{xx}$ encodes the ground state momentum density (see Appendix A.5). The quantity $\mathcal{Q}_{xt}$ is the mixed Fermi-point quadrupole moment in momentum and energy, but we leave a detailed discussion of such mixed moments to future work.

The arguments of this section can be extended to look at higher moments of the chirality-weighted Fermi momenta, which are proportional to the ground state expectation values of higher and higher powers of momenta. To describe these properties, and related response phenomena, we can introduce gauge fields $\mathfrak{e}^{abc\ldots}$ that couple to higher monomials of momentum, $k_ak_bk_c\ldots$. For example, the fields that couple to zero powers or one power of momentum are the electromagnetic A and translation gauge fields $k_x\mathfrak{e}^x$ respectively,

[2] As shown in the Appendix, this anomaly has two contributions. One comes from the low-energy currents that contribute with a factor of $1/2\pi$ and a second from a change of system-size for a ground state carrying a non-vanishing momentum density with a factor of $-1/4\pi$.

and we could introduce a coupling $k_a k_b \mathfrak{e}^{ab}$ to the set of 1-form gauge fields $\mathfrak{e}^{ab}$, e.g., $k_x^2 \mathfrak{e}^{xx}$. We describe the hierarchical anomalies associated to these gauge fields in Appendix A.5.

2.5 Effective responses of 3D nodal line semimetals

Next we use our 2D results from Sec. 2.3 to generate the responses of two types of nodal line semimetals in 3D. To generate the two types we imagine stacking either the action in Eq. 2.10 or in Eq. 2.16. The action resulting from stacking the former has been discussed in Refs. [37], [78]; the second is, to the best of our knowledge, new. From our arguments for gapped systems in Sec. 2.2, we expect that the form of the actions we obtain from stacking contain an extra wedge product with the translation gauge field in the stacking direction. To be explicit, suppose we are stacking up 2D semimetals (that are parallel to the xy-plane) into the z-direction. By stacking decoupled planes of the responses in either Eq. 2.10 or Eq. 2.16, we expect to find

$$S = \frac{e\mathcal{P}_\alpha}{4\pi a_z} \int \mathfrak{e}^z \wedge \mathfrak{e}^\alpha \wedge dA, \tag{2.36}$$

or

$$S = \frac{\hbar \mathcal{Q}_{\alpha\beta}}{8\pi a_z} \int \mathfrak{e}^z \wedge \mathfrak{e}^\alpha \wedge d\mathfrak{e}^\beta, \tag{2.37}$$

respectively, where $\alpha, \beta = x, y$. The forms of these actions match action (viii) in Fig. 2.1(c) and the action in Fig. 2.2(c), respectively. We note that the stacked, decoupled systems simply inherit the response coefficient of the 2D system.

We want to consider more general configurations of systems with stacked and coupled planes, perhaps stacked in several directions. As we have seen, if the layers we stack are decoupled, then each layer contributes the same amount. This contribution (for a stack in the z-direction) is captured by the integral $\frac{1}{a_z}\int \mathfrak{e}^z = N_z$ where N_z is the number of layers. However, if the layers are coupled, then each fixed-k_z plane can have a different amount of Dirac node dipole moment ($\mathcal{P}_\alpha(k_z)$) or Dirac node quadrupole moment ($\mathcal{Q}_{\alpha\beta}(k_z)$), respectively. The total coefficient is determined by the sum over all values of k_z. One can also have stacks in any direction, not just the z-direction. Hence, in this more generic scenario the actions become

$$S_{DD3} = e\mathcal{B}_{\alpha\beta} \int \mathfrak{e}^\alpha \wedge \mathfrak{e}^\beta \wedge dA, \tag{2.38}$$

and

$$S_{DQ3} = \hbar \mathcal{B}_{\alpha\beta,\gamma} \int \mathfrak{e}^\alpha \wedge \mathfrak{e}^\beta \wedge d\mathfrak{e}^\gamma, \tag{2.39}$$

with coefficients

$$\mathcal{B}_{\alpha\beta} = \frac{1}{4(2\pi)^3}\epsilon^{\alpha\beta\sigma}\int d^3k\ k_\delta \mathcal{F}^{\sigma\delta} \tag{2.40}$$

and

$$\mathcal{B}_{\alpha\beta,\gamma} = \frac{1}{6(2\pi)^3}\epsilon^{\alpha\beta\sigma}\int d^3k\ k_\gamma k_\delta \mathcal{F}^{\sigma\delta}. \tag{2.41}$$

where $\mathcal{F}^{\mu\nu}$ is the Berry curvature of the $k_\mu k_\nu$-plane. These forms of the coefficients capture scenarios with more complicated nodal line geometries. Indeed, as previously shown in Ref. [37], the coefficient $\mathcal{B}_{\alpha\beta}$ is determined by the line nodes that have non-vanishing area when projected into the $\alpha\beta$-plane. Additionally, for nodal line semimetals with $\mathcal{TI}$ symmetry the coefficient is proportional to the charge polarization in the direction normal to the $\alpha\beta$-plane [37]. We can see this explicitly by integrating Eq. 2.40 by parts with the same caveats mentioned in Sec. 2.3 surrounding Eq. 2.14.

Analogously, the coefficient $\mathcal{B}_{\alpha\beta,\gamma}$ can represent a kind of "momentum"-polarization where the polarization is again normal to the $\alpha\beta$-plane, and the charge that is polarized is the momentum along the γ-direction. We can see this heuristically by integrating by parts using the derivatives in the $\mathcal{F}^{\sigma\delta}$ to find

$$\mathcal{B}_{\alpha\beta,\gamma} \sim -\frac{1}{2(2\pi)^3}\int d^3k \left(\epsilon^{\alpha\beta\sigma}k_\gamma \mathcal{A}^\sigma - \epsilon^{\alpha\beta\gamma}k_i\mathcal{A}^i\right) \tag{2.42}$$

where we have used the $\sim$ symbol to indicate that there are boundary terms we have dropped that can be important if the line nodes span the Brillouin zone. We can see from this from the that that the coefficient for the case when α, β, γ are not all different, e.g. $\mathcal{B}_{xz,x}$, is proportional to the polarization in the y-direction (i.e. normal to the xz-plane) weighted by the momentum in the x-direction.

We note that for $\mathcal{B}_{\alpha\beta}$ to be well-defined, the Chern number in each plane must vanish. In addition to this constraint, $\mathcal{B}_{\alpha\beta} = 0$ is a necessary constraint for $\mathcal{B}_{\alpha\beta,\gamma}$ to be well defined. These hierarchical requirements are analogous to the usual requirements for the ordinary (magnetic) dipole and (magnetic) quadrupole moments of the electromagnetic field to be independent of the choice of origin. Here the role of the magnetic field distribution is being played by $\mathcal{F}^{\sigma\rho}(k)$, and, for example, the constraint on the vanishing Chern number eliminates the possibility of magnetic monopoles (i.e., Weyl points).

2.6 Effective responses of 4D semimetals

Our next goal is to determine the coefficients for the response actions of 3D Weyl point-node semimetals. However, because the Weyl nodes in 3D exhibit an anomaly, the responses are subtle to calculate intrinsically in 3D. Instead, to accomplish our goal we first carry out more straightforward calculations of the responses

of 4D semimetals and return to 3D either by considering the boundary of a 4D system or by compactifying and shrinking one dimension of the bulk. Hence, as a step toward 3D semimetals, in this section we provide the derivation for effective response actions of semimetals in 4D.

The first action we consider is of the form

$$S = c_\alpha \int \mathfrak{e}^\alpha \wedge dA \wedge dA, \tag{2.43}$$

where for our purposes $\alpha = x, y, z, w$. Collecting all terms in the gradient expansion that have this field content we obtain:

$$S = \frac{e^2}{\hbar} \int d^5 r \; \mathfrak{e}^\alpha_\mu \partial_\nu A_\rho \partial_\sigma A_\tau \times \int \frac{d\omega d^4 k}{(2\pi)^5} k_\alpha \Omega^{(5)}_{\mu\nu\rho\sigma\tau}(\omega, k), \tag{2.44}$$

where

$$\Omega^{(5)}_{\mu\nu\rho\sigma\tau}(\omega, k) = \mathrm{tr}\left(G_0 \frac{\partial G_0^{-1}}{\partial k_\mu} \frac{\partial G_0}{\partial k_\nu} \frac{\partial G_0^{-1}}{\partial k_\rho} \frac{\partial G_0}{\partial k_\sigma} \frac{\partial G_0^{-1}}{\partial k_\tau} \right), \tag{2.45}$$

and $G_0(\omega, k)$ is the single-particle Green function. To determine the coefficient c_α we project this coefficient onto the totally antisymmetric part and then, just as in Eq. 2.7, we can carry out the frequency integral [99] to obtain the simpler expression

$$\int \frac{d\omega d^4 k}{2\pi} \frac{\varepsilon_{\mu\nu\rho\sigma\tau}}{5!} k_\alpha \Omega^{(5)}_{\mu\nu\rho\sigma\tau}(\omega, k) = \frac{1}{16} \int_{BZ} d^4\mathbf{k} \; k_\alpha \varepsilon_{ijkl} \mathcal{F}^{ij} \mathcal{F}^{kl}. \tag{2.46}$$

Hence, the response coefficient takes the form

$$c_\alpha = \frac{e^2}{\hbar} \frac{1}{16(2\pi)^4} \int_{BZ} d^4 k \; k_\alpha \varepsilon_{ijkl} \mathcal{F}^{ij} \mathcal{F}^{kl} = \frac{e^2 \mathcal{P}_\alpha}{16\pi^2 \hbar}, \tag{2.47}$$

where we introduced

$$\mathcal{P}_\alpha = \frac{1}{16\pi^2} \int_{BZ} d^4\mathbf{k} \; k_\alpha \varepsilon_{ijkl} \mathcal{F}^{ij} \mathcal{F}^{kl}. \tag{2.48}$$

As we see from this calculation, similar to 2D, the 4D response theories can be characterized by the distribution of the quantity $\varepsilon_{ijkl} \mathcal{F}^{ij} \mathcal{F}^{kl}$ across the 4D Brillouin zone. For our focus, let us consider the case where the 4D system is a semimetal with a set of isolated Dirac points (linearly dispersing band touchings where four bands meet). Without symmetry, these Dirac points are locally unstable in momentum space to the opening of a gap. If we open up an infinitesimally small energy gap, the quantity $\varepsilon_{ijkl} \mathcal{F}^{ij} \mathcal{F}^{kl}$ becomes well-defined across the entire BZ and its distribution takes the following form in the massless limit:

$$\varepsilon_{ijkl} \mathcal{F}^{ij} \mathcal{F}^{kl} = \sum_{a=1}^{N_D} 16\pi^2 \chi_a \delta(\mathbf{k} - \mathbf{k}_a). \tag{2.49}$$

If we substitute this into Eq. 2.48 then we immediately see that $\mathcal{P}_\alpha$ becomes the momentum space dipole of the set of 4D Dirac nodes. Let us also comment that if we integrate Eq. 2.48 by parts we see that $\mathcal{P}_\alpha$ can also be interpreted as a set of magneto-electric polarizabilities [26], [27]. Just as in the case of the polarization of a 2D Dirac semimetal, the integration by parts will generate a boundary term that captures the magneto-electric polarizability coming from the 3D boundaries of the 4D BZ. Hence, the connection between the total magneto-electric polarizability and the mixed translation-electromagnetic response is only exact in the symmetric limit when the boundary term is quantized.

In summary, a 4D response of a system characterized by a dipolar distribution of the $\varepsilon_{ijkl}\mathcal{F}^{ij}\mathcal{F}^{kl}$ quantity reads:

$$S = \frac{e^2\mathcal{P}_\alpha}{16\pi^2\hbar}\int \mathfrak{e}^\alpha \wedge dA \wedge dA. \tag{2.50}$$

Similar to 2D, if the dipolar response vanishes we can obtain a momentum quadrupole response coefficient for the action:

$$S = \frac{e\mathcal{Q}_{\alpha\beta}}{16\pi^2}\int \mathfrak{e}^\alpha \wedge d\mathfrak{e}^\beta \wedge dA, \tag{2.51}$$

where $\mathcal{Q}_{\alpha\beta}$ is a symmetric matrix determined by the momentum space quadrupole moment of the 4D Dirac nodes. Finally, if both the dipolar and quadrupolar responses vanish we can consider an octupolar distribution that will give the response coefficient for the action:

$$S = \frac{\hbar\mathcal{O}_{\alpha\beta\gamma}}{48\pi^2}\int \mathfrak{e}^\alpha \wedge d\mathfrak{e}^\beta \wedge d\mathfrak{e}^\gamma, \tag{2.52}$$

where $\mathcal{O}_{\alpha\beta\gamma}$ is determined by the momentum space octupole moment of the 4D Dirac nodes. We will leave the discussion of octupolar configurations of Dirac and Weyl nodes to future work. We also mention that, similar to 2D, for these responses to be independent of the choice of BZ origin we require that the second Chern number of the 4D system vanishes. Alternatively, if the second Chern number is non-vanishing, then the boundary of the system will contain a non-vanishing chirality of Weyl nodes. As such, the anomalous charge response of the chiral boundary will not allow us to uniquely determine the momentum response on the boundary.

Before moving on to 3D, let us briefly present some physical intuition about the response in Eq. 2.50. Consider a 4D time-reversal and inversion invariant system having two Dirac nodes separated in the k_z-direction. To simplify the discussion, let us also assume the system has mirror symmetry M_z. The assumed symmetries imply that each fixed-k_z volume can be treated as an independent 3D insulator having 3D inversion symmetry, and hence the magneto-electric polarizability of these 3D insulator subspaces is quantized [26], [44], [101]. Now, if we sweep through k_z then each bulk 4D Dirac point crossing changes the magneto-electric

polarizability of the fixed-k_z volume by a half-integer (i.e., changes the related axion angle by π) [26]. Since the magneto-electric polarizability jumps between its quantized values as we pass through the two bulk Dirac nodes, the k_z Brillouin zone splits into two intervals: (i) an interval with a vanishing magneto-electric polarizability, and (ii) an interval with a non-vanishing quantized magneto-electric polarizability. Indeed, we could have anticipated this result from the form of the action Eq. 2.50 when $\alpha = z$, i.e., the action represents stacks of 3D topological insulators that each have a non-vanishing magneto-electric polarizability.

2.7 Effective responses of 3D semimetals

From this discussion we see that, in the presence of symmetry, the 4D bulk Dirac node dipole moment determines the magneto-electric polarizability of these 4D topological semimetals via Eq. 2.50. In this section we connect this result to 3D semimetals in two ways. First, we consider the 3D boundary of the 4D system, and second we consider the compactification of one spatial dimension.

Let us begin by considering the boundary response action from Eq. 2.50. For the model system described at the end of the previous section we know the system has a k_z-dependent magneto-electric polarizability. Consider a boundary in the fourth spatial direction w. Since the magneto-electric polarizability is changing from inside to outside of the boundary, the boundary itself will have a non-vanishing Hall conductivity. For our example system, each fixed-k_z slice of this boundary will have a Hall conductivity σ_{xy}, which is quantized, but possibly vanishing. Additionally, since the bulk 4D Dirac nodes are separated in the k_z direction, they will project to gapless points in the 3D surface BZ (on surfaces that have at least one direction perpendicular to the z-direction) where the Hall conductivity discretely jumps by $\Delta\sigma_{xy} = \pm\frac{e^2}{2h}$.

From this phenomenology, i.e., discrete Hall conductivity jumps as we sweep through k_z we expect that the boundary response of Eq. 2.50 captures the same response as a Weyl semimetal that has a non-vanishing momentum space dipole moment of the Weyl nodes in the z-direction. Indeed the generic boundary contribution from Eq. 2.50 has the form:

$$S_{WD} = \frac{e^2\mathcal{P}_\alpha}{8\pi^2\hbar}\int \mathfrak{e}^\alpha \wedge dA \wedge A \tag{2.53}$$

which was proposed by Ref. [35] to describe the response of Weyl semimetals, though in the more conventional form using an axion field and without the translation gauge field. Here $\mathcal{P}_\alpha$, $\alpha = x, y, z$ is the momentum dipole of the Weyl nodes in the α-th direction. This action is represented as (ix) in Fig. 2.1(c). We note that the coefficient in Eq. 2.53 is twice as large as the actual boundary term derived from Eq. 2.50. This is because when k_i passes through a single Weyl point we have $\epsilon_{ijk}\Delta\sigma_{jk} = \pm\frac{e^2}{h}$, where the surface the response

of the 4D system has jumps of half the size. This is analogous to the fact that a 1D metal has an integer jump in the filling as we pass through a Fermi point, whereas the surface of a 2D Dirac semimetal has a boundary "filling" that jumps by a half-integer as we pass through a gapless point in the surface BZ.

We can repeat this analysis for Eq. 2.51. The coefficient of this term is proportional to the momentum space quadrupole moment of the nodal points. Unfortunately the phenomenology of this term is not as easy to analyze in 4D because it is not generated from a lower dimensional system in a clear way [3]. By analogy with the previous case, the bulk 4D Dirac nodes will project to a quadrupole of 3D Weyl nodes on the surface. We can extract the form of the 3D action we want by taking the boundary term generated from Eq. 2.51. Then accounting for the factor of two as in the previous case, we arrive at:

$$S_{WQ} = \frac{e\mathcal{Q}_{\alpha\beta}}{8\pi^2} \int \mathfrak{e}^\alpha \wedge d\mathfrak{e}^\beta \wedge A. \tag{2.54}$$

(Note that since $\mathcal{Q}_{\alpha\beta}$ is symmetric, the related contribution of the form $e\mathcal{Q}_{\alpha\beta}/8\pi^2 \int \mathfrak{e}^\alpha \wedge \mathfrak{e}^\beta \wedge dA$ vanishes). This action is the same as that shown in Fig. 2.2(a). It produces a mixed crystalline-electromagnetic response and represents a rank-2 vector charge response when certain mirror symmetries are preserved [77]. Its response coefficient is determined by the momentum space quadrupole moment of the Weyl nodes.

Finally, we come to the action (x) in Fig. 2.1(c). Let us briefly sketch some salient features of this response, while we leave a detailed discussion to future work. We can arrive at this action using a formal compactification of the action in Eq. 2.50 [26]. First we can integrate that action by parts to arrive at

$$\frac{e^2\mathcal{P}_\alpha}{16\pi^2\hbar} \int A \wedge d\mathfrak{e}^\alpha \wedge dA, \tag{2.55}$$

where we have ignored the boundary term. We now want to dimensionally reduce the fourth spatial direction w, which we accomplish by choosing periodic boundary conditions in w and letting the size of the system in this direction shrink toward zero. In this limit any derivatives with respect to w are (formally in our case) dropped [4]. The resulting non-vanishing contribution is

$$\frac{e^2\mathcal{P}_\alpha}{8\pi^2\hbar} \oint A_w dw \int d\mathfrak{e}^\alpha \wedge dA, \tag{2.56}$$

where the integral and exterior derivative in the second factor are over only the remaining four spacetime

[3] Even though there is a $\mathfrak{e}^\alpha$ wedge product with a lower-dimensional action, it is not transverse to the lower-dimensional action since $\mathcal{Q}_{\alpha\beta}$ is symmetric. For example, there will be terms where, say, $\mathfrak{e}^x$ couples to $d\mathfrak{e}^x$, which cannot be interpreted as a conventional stacked action.

[4] Alternatively we can assume the fields A_w, e^α_w are locked to their ground state values and thus have vanishing derivatives in all directions.

dimensions. We can now make the definition

$$\Theta \equiv 2\pi \frac{e}{h} \int A_w dw, \tag{2.57}$$

to arrive at action (x) from Fig. 2.1(c):

$$\frac{e\mathcal{P}_\alpha}{8\pi^2} \int \Theta d\mathfrak{e}^\alpha \wedge dA. \tag{2.58}$$

To illustrate some of the phenomenology of this action let us assume that $\mathcal{P}_z \neq 0$. Additionally let us assume that we maintain time-reversal and inversion symmetry. As such, $\Theta = 0, \pi$. To begin, we see that the action in Eq. 2.58 is a total derivative if Θ and $\mathcal{P}_\alpha$ are space-time independent. The resulting pure boundary term is just proportional to the response of a 2D weak TI (or 2D Dirac semimetal), i.e., Eq. 2.6. Depending on the symmetry of the surfaces, this implies that we expect the surface to be gapped except for possibly isolated Dirac points. Since the boundary terms appear as $\mathfrak{e}^z \wedge dA$ we expect that surfaces normal to $\hat{x}$ ($\hat{y}$) will harbor a y-polarization (x-polarization), i.e., the polarization is tangent to the surface.

Importantly, the sign of the polarization depends on the interpolation of Θ between its non-trivial bulk value of $\Theta = \pi$ and the trivial vacuum value $\Theta = 0$ outside the system. For neighboring surfaces where the effective sign of the polarization changes we anticipate hinge charges where surfaces intersect since the polarizations are converging or diverging from the hinges. Thus, the response of this system is similar to a stack of 2D planes of quadrupole moment having component $q_{xy} \neq 0$. In this scenario, coupled quadrupole planes could lead to either a higher order weak topological insulator with a quadrupole moment, or a higher order topological semimetal with boundary (and possibly bulk) Dirac nodes [102], [103]. To make further progress it would be advantageous to have a microscopic derivation of the coefficient in Eq. 2.58 intrinsically in 3D. Hence, we will leave further discussion of this action to future work.

2.8 Discussion

In this chapter we presented a framework of explicit connections between a wide-ranging family of topological response theories from 0D to 3D. Using this framework, we showed how the coefficients for these response theories, most of which are well-known in insulators, can be obtained for topological semimetals. This allowed us to provide careful derivations and characterizations of mixed crystalline-electromagnetic responses of semimetallic and insulating systems in various spatial dimensions. In the next chapter we provide an extensive set of microscopic lattice calculations and numerical confirmations affirming that our predicted field theory responses do indeed arise in tight-binding lattice models.

With the advent of topological quantum chemistry [48]–[53], thousands of crystalline topological in-

sulators and semimetals have been identified, but many open questions persist about how to probe their topological features. The work in this chapter provides insight into how the topology in some of these materials may be probed and characterized, i.e., by combining geometric/strain distortions and electromagnetic responses.

There is a growing body of work studying the mixed crystalline-electromagnetic responses of Weyl semimetals with dipole and quadrupole arrangements of nodes [63], [73]–[80], [82], [86], [94], [104]–[112], that indicate a broad interest in these topics. Our work serves two major purposes in the context of this previous literature: (i) we identified several aspects of mixed crystalline-electromagnetic responses that have not yet been addressed in earlier work, and (ii) we synthesized aspects of the existing literature to present a unified description of these responses in terms of the momentum-space multipole moments of the nodal configurations, and to provide new intuition in previously studied responses. While prior work has examined the mixed crystalline-electromagnetic response of two-dimensional Dirac node dipole semimetals [36], [89], we have advanced this understanding by identifying a Wilson loop correction the response coefficient that raises a subtle question about the connection between the charge polarization and the mixed-crystalline-electromagnetic response. Additionally, the Dirac node quadrupole semimetal has not been previously discussed, making our work the first study of its properties and mixed crystalline-electromagnetic responses. Furthermore, our model of a nodal line quadrupole semimetal and its corresponding response theory are new to the literature as well.

The results of this work point in many possible directions for future work. First, finding experimental realizations of the proposed topological responses in solid state or metamaterial systems is an exciting prospect. Rank-2 chiral fermions, which have an anomaly compensated by the bulk response of a Weyl quadrupole semimetal [77], were realized in a recent experiment on non-Hermitian topo-electric circuit metamaterials [113]. In that platform, the mixed crystalline-electromagnetic response generates a momentum-resolved non-Hermitian skin effect that was observed in the experiment. Topo-electric circuits, along with other metamaterials and solid state platforms are promising arenas in which the many mixed crystalline-electromagnetic responses we discuss in this paper could be realized. Other extensions of this work include the consideration of additional crystalline gauge fields as was done in, e.g., Refs. [61]–[64], [83], [84]. Some of us are also working on extending the nodal, higher-multipole responses to interacting systems and non-equilibrium systems where, in the latter, one can have mixed energy-momentum multipole moments. Studying the leading nodal dipole moments has already led to a rich set of phenomena, and the higher moments provide a large hierarchy of phenomena that can be explored in current experiments.

Chapter 3

Microscopic and numerical calculations of translation-electromagnetic responses

This chapter is adapted from Mark R. Hirsbrunner, Oleg Dubinkin, Fiona J. Burnell, and Taylor Hughes, arXiv preprint arXiv:2309.10840.

3.1 Introduction

In this chapter we provide a series of model examples that manifest the responses described in the previous chapter by the actions in Figs. 2.1(c) and 2.2. Using these models we numerically calculate the various charge and momentum responses to electromagnetic and translation gauge fields, providing an independent verification of the coefficients derived in the previous chapter. Some of the models and responses we discuss below have appeared elsewhere in the literature, while others are have not. We carry out this analysis in the same order as the previous chapter, i.e., point-node Dirac semimetals in 2D, nodal line semimetals in 3D, and then point-node Weyl semimetals in 3D. Comparable calculations for 1D systems were carried out analytically in Sec. 2.4, so we do not perform additional numerical studies for 1D systems here. Additional discussion of 1D systems can be found in App. A.5.

This chapter is organized as follows. In Secs. 3.2 and 3.3 we study Dirac node dipole and quadrupole models in $D = 2$. In Secs. 3.4 and 3.5 we study nodal line semimetals generated by stacking Dirac node dipole and quadrupole semimetals in 3D. Finally, in Secs. 3.6 and 3.7 we study 3D Weyl semimetals with

dipole and quadrupole node arrangements.

3.2 2D Dirac node dipole semimetal and insulator

We begin with the time-reversal invariant 2D systems discussed in Sec. 2.3 that exhibit a mixed crystalline-electromagnetic response. Since $\mathcal{T}$ is preserved, the usual Chern-Simons response of the electromagnetic field vanishes. Instead, the response action derived in the Sec. 3.2 takes the form of a mutual Chern-Simons term [89]:

$$S[\mathfrak{e}^\lambda_\nu, A_\mu] = \frac{e}{4\pi}\mathcal{P}_\lambda \int \mathfrak{e}^\lambda \wedge dA. \tag{3.1}$$

Unlike the purely electromagnetic polarization response action considered in Ref. [36], this formulation of the low-energy response theory also includes bulk electromagnetic responses to the translation gauge fields. For example, by taking a functional derivative with respect to A_μ we have

$$\begin{aligned} \rho &= -\frac{e}{4\pi}\mathcal{P}_\lambda \varepsilon^{ij}\partial_i \mathfrak{e}^\lambda_j, \\ j^x &= \frac{e}{4\pi}\mathcal{P}_\lambda(\partial_t \mathfrak{e}^\lambda_y - \partial_y \mathfrak{e}^\lambda_t), \\ j^y &= -\frac{e}{4\pi}\mathcal{P}_\lambda(\partial_t \mathfrak{e}^\lambda_x - \partial_x \mathfrak{e}^\lambda_t). \end{aligned} \tag{3.2}$$

We see that the first equation predicts an electric charge density localized on a dislocation in the bulk of the lattice, which is exactly the phenomenology we expect for a weak topological insulator [40] or a 2D Dirac semimetal. The action (3.1) also predicts a bulk momentum response to the electromagnetic field when varied with respect to $\mathfrak{e}^\mu$,

$$\begin{aligned} \mathcal{J}^t_\lambda &= -\frac{e}{4\pi}\mathcal{P}_\lambda B_z, \\ \mathcal{J}^i_\lambda &= -\frac{e}{4\pi}\mathcal{P}_\lambda \varepsilon^{ij} E_j, \end{aligned} \tag{3.3}$$

where E_i and B_i are the components of electric and magnetic fields respectively. In the inversion-symmetric limit and in the absence of lattice defects and deformations, for which the crystalline gauge fields reduce to $\mathfrak{e}^\lambda_\mu = \delta^\lambda_\mu$, Eq. (3.2) simply reproduces the boundary charge and current responses of an ordinary 2D Dirac semimetal or weak topological insulator, which harbors a non-vanishing electric polarization. However, as we mentioned in Sec. 2.3, and comment further on below, we do not expect the coefficient of this action to match the electric polarization when inversion is strongly broken.

While the electric polarization and magnetization responses of Dirac semimetals were discussed in detail in Ref. [36], the momentum responses in Eq. 3.3, and the charge responses to translation fluxes (i.e., dislocations)

in Eq. 3.2 are less familiar. We therefore explicitly calculate these responses using a minimal tight-binding model. For simplicity, we employ a two-band Bloch Hamiltonian that can model both 2D Dirac semimetals and weak topological insulators:

$$H(\mathbf{k}) = V_{\mathcal{I}}\sigma^x + \sin(k_y a_y)\sigma^y + (m - \cos(k_x a_x) - \cos(k_y a_y))\sigma^z. \tag{3.4}$$

When $V_{\mathcal{I}} = 0$, H has both inversion symmetry, $\mathcal{I} = \sigma^z$, and (spinless) time-reversal symmetry, $\mathcal{T} = K$. In this symmetric regime, m can be chosen to produce a semimetal with Dirac points located at, for example, $(k_x, k_y) = (\pm\pi/(2a_x), 0)$, when $m = 1$. In the semimetal phase, turning on $V_{\mathcal{I}}\sigma^x$, which breaks inversion while preserving $\mathcal{T}$, generates a mass term that opens a gap at the Dirac points. The signs of the Berry curvature localized near the two now-gapped Dirac points are opposite, as shown in Fig. 3.1(a), with the sign at a particular point determined by the sign of the perturbation $V_{\mathcal{I}}$. Hence the total Berry curvature of the occupied band integrated over the entire BZ, equivalent to the Chern number, is zero, and the Berry curvature dipole is well-defined.

To confirm our analytic calculations of the response coefficients we first calculate the momentum density localized around an out-of-plane magnetic flux Φ_z using the tight-binding model Eq. (3.4). In order to determine the k_x momentum density in the lattice model, we must introduce magnetic flux in a fashion that preserves translation symmetry in the $\hat{x}$-direction. We show the configuration that we employ in Fig. 3.1(b). This configuration keeps the crystal momentum k_x as a good quantum number and allows us to compute the value of $\mathcal{J}_x^t$ as the probability density of the occupied single particle states weighted by their momentum $\hbar k_x$. The results of the numerical calculations are presented in Fig. 3.1(c,d), where we study how the excess k_x momentum density bound to magnetic flux behaves as a function of both the magnetic flux Φ_z at fixed Berry curvature dipole $\mathcal{P}_x$, and and as a function of $\mathcal{P}_x$ at fixed Φ_x. Our numerical results match our analytic calculations precisely.

We can interpret this result by noting that the momentum current in Eq. 3.3 can be obtained in the semiclassical limit by considering the momentum current carried by electron wavepackets subject to an anomalous velocity [114], [115]. The equation of motion of an electron wavepacket with momentum $\mathbf{k}$ formed from a single band is

$$v^i(\mathbf{k}) = \frac{\partial \mathcal{E}}{\hbar \partial k_i} + \frac{e}{\hbar}\epsilon^{ij}E_j\mathcal{F}^{xy}(\mathbf{k}), \tag{3.5}$$

where $v^i(\mathbf{k})$ is the wavepacket velocity, $\mathcal{E}(\mathbf{k})$ is the energy spectrum of the band, E_j is the electric field, and $\frac{e}{\hbar}\epsilon^{ij}E_j\mathcal{F}^{xy}(\mathbf{k})$ is the anomalous velocity. The momentum current of the occupied states is obtained by adding up the contributions $\hbar k_\mu v^i(\mathbf{k})$ in the BZ and contains a term arising from the anomalous velocity

given by

$$\begin{aligned}\mathcal{J}^i_\lambda &= -\frac{e}{(2\pi)^2}\epsilon^{ij}E_j\int dk_x dk_y\, k_\lambda \mathcal{F}^{xy}(k_x,k_y)\\ &= -\frac{e}{4\pi}\mathcal{P}_\lambda\epsilon^{ij}E_j.\end{aligned} \tag{3.6}$$

We can also numerically probe our response equations by studying the charge response to the deformation of the lattice. To do so, we introduce a translation flux to rows of plaquettes located near $y = N_y/4$ and $y = 3N_y/4$, analogous to the magnetic flux configuration we just considered. This effectively inserts two rows of dislocations such that if one encircles a plaquette containing translation flux, the Burgers vector is in the x-direction. This creates opposite translational magnetic fields $\mathcal{B}^x_z = \partial_x \mathfrak{e}^x_y - \partial_y \mathfrak{e}^x_x$ penetrating the two rows of plaquettes. We again choose this geometry since it is compatible with translation symmetry in the x-direction. In our lattice model we insert the translation flux by explicitly adding generalized Peierls' factors that are k_x-dependent, i.e., $\exp\left(ik_x \int \mathfrak{e}^x_i dx^i\right)$ such that the colored regions in Fig. 3.1(b) contain non-vanishing translation flux. The resulting electron charge density localized on the translation magnetic flux has a dependence on both the $\mathcal{B}^x_z$ field strength and the Berry curvature dipole moment $\mathcal{P}_x$ as shown in Fig. 3.1(e),(f). This again matches the expectation from our analytic response equations.

We emphasize that the effective action (3.2) describes the *mutual bulk* response between the electromagnetic and the momentum currents in semimetallic and insulating systems with vanishing Chern number. We showed in Sec. 2.3 that one must be careful when comparing this response to the charge polarization. In particular, our numerics show that, even in the presence of significant inversion-breaking, the bulk momentum density response to a magnetic flux tracks the value of the coefficient c_α from Eq. 2.8 as demonstrated in Fig. 3.1 (d). In contrast, as shown in Sec. 2.3, the expression for the electric polarization, Eq. 2.14, contains an additional term that is proportional to the value of a Wilson loop along the boundary of the BZ. This value is not quantized when inversion symmetry is broken, and, for large values of $V_{\mathcal{I}}$, this contribution becomes significant enough that the polarization response clearly deviates from the result one would expect from a naive interpretation of Eq. 3.2. However, the mutual response between the electromagnetic and translation gauge fields described by this action remains valid. This subtlety is not the focus of our current article, so we leave further discussions to future work.

3.3 2D Dirac quadrupole semimetal

Next, we consider the class of 2D semimetallic phases characterized by the quadrupole moment of the Berry curvature introduced in Sec. 2.3. We know from Sec. 2.3 that the low-energy effective response action for

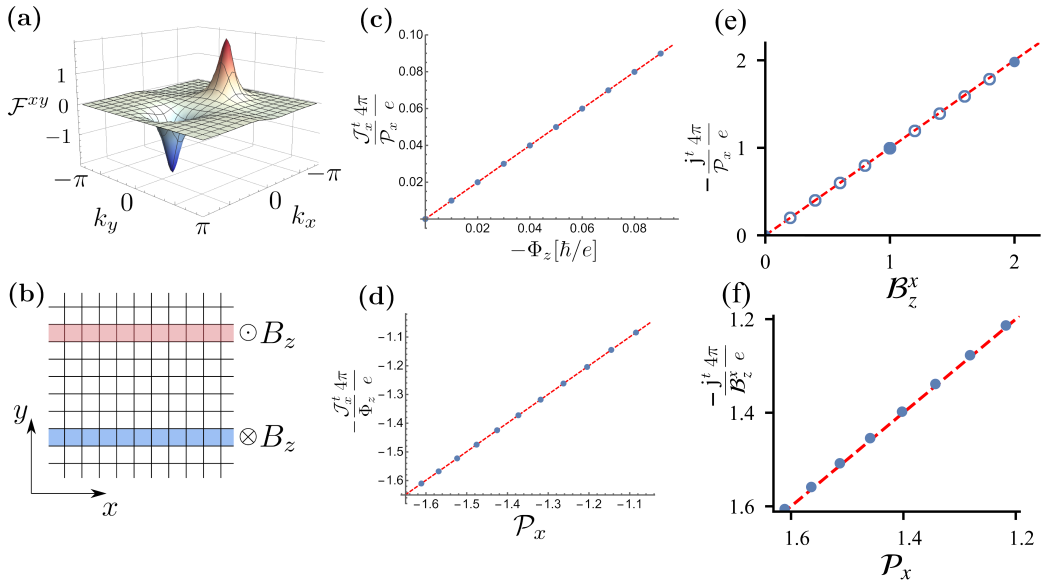

Figure 3.1: (a) Plot of the Berry curvature across the 2D Brillouin zone for the Dirac node dipole semimetal model (3.4) for $m = 1.1$ with an added inversion-breaking perturbation with $V_{\mathcal{I}} = -0.5$. We use this model to probe the k_x momentum density response. For that we consider a completely periodic system and insert the magnetic flux Φ_z thorough two lines of plaquettes such that the translational symmetry along the $\hat{x}$-direction is preserved, as shown in panel (b). (c) shows the k_x momentum density localized around one line of plaquettes penetrated by the magnetic field B_z as a function of magnetic flux. (d) shows the k_x momentum density as a function of Berry curvature dipole moment $\mathcal{P}_x$ defined in Eq. (2.8) which we tune in our model by varying the parameter m between $m = 1.0$ and $m = 1.5$. In (e) and (f) we show analogous calculations for the charge density response to a translation flux with Burgers vector in the x-direction as a function of (e) translation flux at fixed Berry curvature dipole, and (f) Berry curvature dipole at fixed translation flux. The open circles in (e) represent Burgers' vector choices that are not integer multiples of a lattice constant. The red dashed lines in (c)-(f) are guides to the eye indicating a slope of 1.

this system takes the form:

$$S = \frac{\hbar}{8\pi}\mathcal{Q}_{\alpha\beta}\int \mathfrak{e}^{\alpha}\wedge d\mathfrak{e}^{\beta}. \tag{3.7}$$

This action generates a momentum current response

$$\mathcal{J}^{\mu}_{\alpha} = -\frac{\hbar}{4\pi}\mathcal{Q}_{\alpha\beta}\varepsilon^{\mu\nu\sigma}\partial_{\nu}\mathfrak{e}^{\beta}_{\sigma} \tag{3.8}$$

These currents describe both a bulk momentum polarization (e.g., yielding momentum on the boundary where $\mathcal{Q}_{\alpha\beta}$ changes), and a bulk energy-momentum response to translation gauge fields. We note that this response is exactly analogous to that of the Dirac node dipole semimetal discussed above if we replace the electromagnetic field with a translation gauge field.

To illustrate and explicitly confirm the responses numerically we use the following 2-band square lattice Bloch Hamiltonian with next-nearest-neighbor hopping terms:

$$H(\mathbf{k}) = V_{\mathcal{T}}\sigma^{x} + \sin(k_x a)\sin(k_y a)\sigma^{y} + (m - \cos(k_x a) - \cos(k_y a))\sigma^{z}. \tag{3.9}$$

This model has an inversion symmetry (i.e., C_2^z symmetry) that is realized trivially on-site with $\mathcal{I} = \mathbb{I}$, mirror symmetry along the $k_x = k_y$ axis, and, when $V_{\mathcal{T}} = 0$, time-reversal symmetry $\mathcal{T} = \sigma^z K$. This model can be tuned to a semimetal phase as well, for example, setting $m = 1$ we find four gapless Dirac points located at $(k_x, k_y) = (\pm\pi/2a, 0)$ and $(k_x, k_y) = (0, \pm\pi/2a)$.

To confirm the response action is correct, we first need to calculate the Dirac-node quadrupole moment. To see that the Berry curvature quadrupole moment is well-defined, we first note that the choice of $V_{\mathcal{T}}$ as a mass perturbation forces $\mathcal{P}_{\alpha}$ to vanish. We also need the Chern number to vanish, which is guaranteed by the mirror symmetry. With these symmetries, the Berry curvature peaks at Dirac points that are related by inversion symmetry have the same sign, while the peaks related by mirror symmetry carry opposite signs, resulting in a quadrupolar distribution of the Berry curvature, as in Fig. 3.2(b). Since the Chern number and $\mathcal{P}_{\alpha}$ both vanish, the quadrupolar distribution is well-defined and signals the presence of a well-defined elastic response in this model (see also Ref. [98]). The diagonal elements of the Dirac-node quadrupole moment of our model are equal and opposite, $\mathcal{Q}_{xx} = -\mathcal{Q}_{yy}$, and the off-diagonal elements are zero. Since the sign of the Berry curvature flux for 2D Dirac points with $\mathcal{TI}$-symmetry is ambiguous, we once again treat our system in the insulating regime with non-zero $V_{\mathcal{T}}$ first and then recover the semimetallic case by taking the limit $V_{\mathcal{T}} \to 0$.

Using this model, let us first focus on the momentum polarization response and highlight the difference with the 2D Dirac node dipole semimetal case from Section 3.2. If the bulk has a momentum polarization

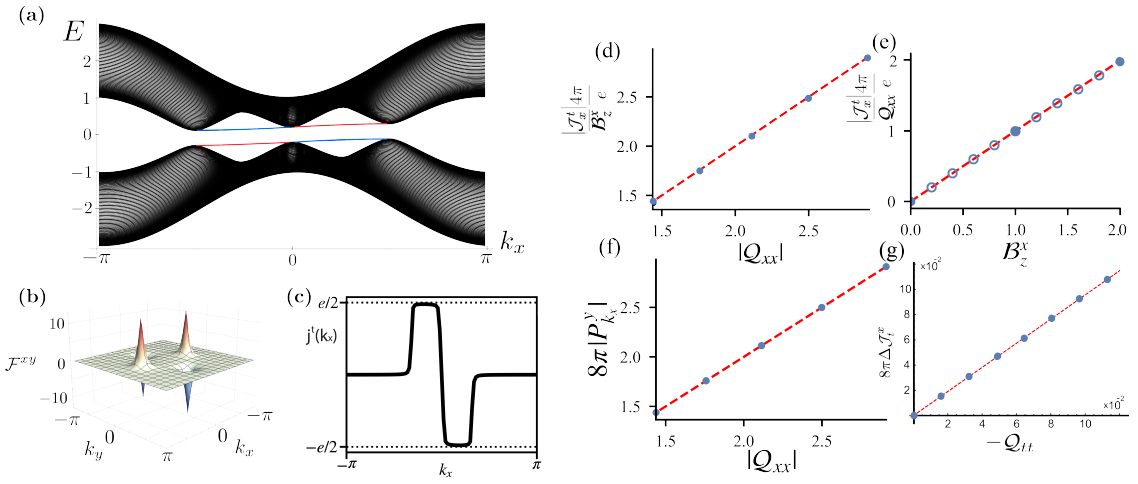

Figure 3.2: (a) Spectrum of the 2D Dirac node quadrupole semimetal (3.9) in a ribbon geometry (y-direction open, x-direction periodic) for $m = 1$, the $\mathcal{T}$-breaking perturbation set to $V_{\mathcal{T}} = -0.2$, and the energy tilt in Eq. 3.11 $\epsilon = 0.1$. At half filling, the ground state of the model is momentum-polarized: occupied states localized near $y = 1$, which are indicated by the blue color, carry a positive value of the k_x momentum, while the occupied states near $y = N_y$ have a negative value of k_x. (b) Berry curvature distribution across the Brillouin zone for a small gapping perturbation $V_{\mathcal{T}} = -0.2$. (c) The boundary charge distribution as a function of momentum. (d), (e) k_x momentum bound to a row of dislocations (c.f. Fig. 3.1(b)) as a function of $\mathcal{Q}_{xx}$ at fixed $\mathcal{B}^x_z$ in (d) and as a function of $\mathcal{B}^x_z$ at fixed $\mathcal{Q}_{xx}$ in (e). (f) Plot of momentum polarization $P^y_{k_x}$ obtained from computing k_x-momentum bound to an edge normal to $\hat{y}$. (g) As a consequence of non-zero ϵ we see that the velocities of single-particle states in (a)localized on opposite edges have the same sign, while the energy and k_x momentum charges are exact opposite. This leads to boundary energy currents as illustrated in panel (g) as a function of $\mathcal{Q}_{tt}$.

we expect translation-symmetric edges to have a bound momentum density. We will first make a general argument for the existence of the boundary momentum and then confirm the results numerically for our model. Let us suppose our system has a boundary normal to the y-direction. We expect such a boundary will carry k_x momentum if $\mathcal{Q}_{xx} \neq 0$. To show this, let us make a gauge transformation on the fields in Eq. 3.7: $\mathfrak{e}^a_\mu \to \mathfrak{e}^a_\mu + \partial_\mu \lambda^a$ for some vector function λ^a. Since there is a boundary, the response action is not gauge invariant and we find the variation $\delta_\lambda S = -\frac{\hbar \mathcal{Q}_{ab}}{8\pi} \lambda^a (\partial_0 \mathfrak{e}^b_x - \partial_x \mathfrak{e}^b_0)$. Our system has no translation-twisting of the boundaries, i.e., $\mathfrak{e}^y_x = \mathfrak{e}^x_y = 0$, so we find the variation reduces to $\delta_\lambda S = -\frac{\hbar \mathcal{Q}_{xx}}{8\pi} \lambda^x (\partial_0 \mathfrak{e}^x_x - \partial_x \mathfrak{e}^x_0)$. This variation can be canceled by adding an action of the form Eq. 2.35. That is, we expect to have 1D degrees of freedom on the boundary that harbor a non-vanishing k_x-momentum density captured by an effective 1D quadrupole moment $\mathcal{Q}_{xx}$ that matches the value of the 2D quadrupole moment. Interestingly, we note that the coefficient of Eq. 2.35 is twice that of the variation we need to cancel. Hence, the edge of our system has a fractional momentum density, i.e., a 1D system with the same $\mathcal{Q}_{xx}$ would have twice as much momentum. This is analogous to the fractional boundary charge density one finds from the half-quantized electric charge polarization.

We confirm this response numerically by studying the model (3.9) on a lattice in a ribbon geometry that is open in the $\hat{y}$-direction and periodic in $\hat{x}$. Figure 3.2 (a) shows the resulting band structure, for which a gap is opened by a non-vanishing $V_{\mathcal{T}}$ and the occupied states have two symmetrically positioned sets of flat band states: one in an interval having $k_x < 0$ and the other in an interval having $k_x > 0$. The occupied boundary states with $k_x < 0$ (red) are localized near the top ($y = N_y$) boundary, while the occupied boundary states with $k_x > 0$ (blue) are localized near the bottom ($y = 1$) boundary. At half filling we find that the excess/deficit charge near the boundary depends on k_x as shown in Fig. 3.2(c). We see that the states at positive and negative k_x are imbalanced, indicating a non-vanishing k_x momentum density on the edge. Indeed, each state between the Dirac nodes contributes an amount to the total edge momentum equal to k_x weighted by a factor of $\pm 1/2$, since the particle density on the edge at each k_x in this range is $\pm 1/2$. Because states at opposite k_x have opposite excess/deficit probability density, the total sum is non-vanishing and depends on $\mathcal{Q}_{xx}$ as shown in Fig. 3.2(f). We find that the bulk momentum polarization $P^y_{k_x} = \frac{\hbar \mathcal{Q}_{xx}}{8\pi}$ matches the numerically calculated boundary momentum density, as expected for a generalized surface charge theorem [1]. To further probe the response equations, we subject the Dirac node quadrupole semimetal to the same linear array of dislocations employed in the previous section (c.f. Fig. 3.1(b)). From Eq. 3.8, we expect to find momentum density localized on dislocations. Since our geometry preserves translation

[1] We comment that even though the Chern-Simons term for the translation gauge fields shares some properties with the electromagnetic Chern-Simons term, there is a key distinction: The translation gauge fields have a constant background. This allows the Dirac node quadrupole system to have a static momentum polarization, whereas the electromagnetic Chern Simons term in a Chern insulator would predict generating an electric polarization as one tunes the vector potential.

in the $\hat{x}$-direction, we can compute the amount of k_x momentum bound to dislocations, similar to how we computed the amount of charge bound to dislocations in the previous section. We show our results in Fig. 3.2(d)(e) where we first plot momentum density as a function of $\mathcal{Q}_{xx}$ for fixed translation flux $\mathcal{B}^x_z$, and then plot momentum density as a function of $\mathcal{B}^x_z$ for fixed $\mathcal{Q}_{xx}$. Both results match the analytic value from the response action.

Finally, let us briefly consider a case when the mixed energy-momentum quadrupole moment $\mathcal{Q}_{ta}$ is non-vanishing. In this scenario the effective action (3.7) implies the existence of a bulk orbital *momentum magnetization* of

$$M^z_{k_\mu} = -\frac{\hbar}{8\pi}\mathcal{Q}_{t\mu}, \tag{3.10}$$

that will manifest as boundary momentum currents, even in equilibrium (note we assume $\mathfrak{e}^t_t = 1$). To generate a non-vanishing $\mathcal{Q}_{t\mu}$ in our model (3.9), we turn on an additional perturbation

$$\Delta H(\mathbf{k}) = \epsilon \sin(k_x)\mathbb{I}_{2\times 2}. \tag{3.11}$$

When $m = 1$ and $V_{\mathcal{T}} \to 0_-$, this induces $\mathcal{Q}_{tx} = -\pi\epsilon$ and $\mathcal{Q}_{tt} = \epsilon^2$, leading to momentum k_x magnetization, $M^z_{k_x} = -\frac{\hbar}{8\pi}\mathcal{Q}_{tx}$, and bulk energy magnetization, $M^z_{k_t} = -\frac{\hbar}{8\pi}\mathcal{Q}_{tt}$, following from Eq. (3.10). In Fig. 3.2(g) we plot the boundary energy current response $\Delta\mathcal{J}^x_t$ as a function of $\mathcal{Q}_{tt}$. We calculate this quantity by summing the particle current $\frac{1}{\hbar}\frac{\partial H}{\partial k_x}$ weighted by the energy $\epsilon(k)$ of each state. The slope of the plot confirms the coefficients predicted in Eq. (3.10).

3.4 3D nodal line dipole semimetal

Heuristically we can consider nodal 3D semimetals as arising from stacks of 2D Dirac node dipole semimetals. Furthermore, similar to the 2D case, with inversion symmetry the bulk response action

$$S[\mathfrak{e}^\lambda, A] = e\mathcal{B}_{\mu\nu}\int \mathfrak{e}^\mu \wedge \mathfrak{e}^\nu \wedge dA \tag{3.12}$$

can be interpreted as a charge magnetization M_i and electric polarization P^i_e:

$$e\mathcal{B}_{ta} = M^i\mathfrak{e}^a_i, \quad e\mathcal{B}_{ab} = \varepsilon_{ijk}P^k_e\mathfrak{e}^a_i\mathfrak{e}^b_j \tag{3.13}$$

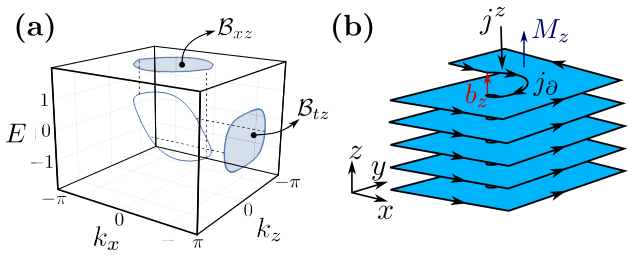

Figure 3.3: (a) Fermi line of a 3D NLSM (3.17) with $V_{\mathcal{I}} = 0$, $m = 2$ that is tiled in the energy-momentum space $\{k_z, k_x, E\}$ by the perturbation (3.19) where we set $\epsilon = 1$. The projections of this curve onto the $\{k_x, k_z\}$ and $\{k_z, E\}$ planes give the exact values of the $\mathcal{B}_{xz}$ and $\mathcal{B}_{tz}$ coefficients respectively. (b) A screw dislocation characterized by a Burgers' vector $b^z = a_z$ creates an internal boundary carrying a current circulating around the magnetization vector M_z. Note that the currents' direction is perpendicular to the Burgers' vector and the Magnetization vector M_z, as predicted by Eq. 3.20.

where we have taken functional derivatives of Eq. 3.12 with respect to the magnetic and electric fields respectively, and used $\mathfrak{e}_t^t = 1$. For an unmodified geometry we recover the results of Ref. [37], i.e.,

$$e\mathcal{B}_{ta} = M^a, \;\; e\mathcal{B}_{ab} = \varepsilon_{abk} P_e^k. \tag{3.14}$$

Microscopically, the coefficient $\mathcal{B}_{ab}$, where $a, b = 1, 2, 3$, is proportional to the area of the line nodes that project onto surfaces normal to the ab-plane as illustrated in Fig. 3.3(a).

The bulk action also implies a non-vanishing momentum response to electromagnetic fields:

$$\mathcal{J}_\lambda^\mu = 2e\mathcal{B}_{\lambda\eta}\varepsilon^{\mu\nu\rho\sigma}\mathfrak{e}_\nu^\eta \partial_\rho A_\sigma, \tag{3.15}$$

and a conjugate electromagnetic response to translation gauge fields:

$$j^\mu = 2e\mathcal{B}_{\lambda\eta}\varepsilon^{\mu\nu\rho\sigma}\mathfrak{e}_\nu^\lambda \partial_\rho \mathfrak{e}_\sigma^\eta. \tag{3.16}$$

To illustrate how these responses manifest in an explicit model, we can construct a Hamiltonian for a 3D nodal line dipole semimetal by stacking copies of the 2D Dirac node dipole semimetal in Eq. (3.4) in the $\hat{z}$-direction. When there is no hopping between the 2D layers, such a system will have two lines of gapless states spanning the BZ along the k_z direction, located at $(k_x, k_y) = (\pm K, 0)$ (for our model). Adding hopping terms in the $\hat{z}$-direction leads to a Bloch Hamiltonian:

$$H(\mathbf{k}) = V_{\mathcal{I}}\sigma^x + \sin(k_y a_y)\sigma^y + (m - \cos(k_x a_x) - \cos(k_y a_y) - \cos(k_z a_z))\sigma^z. \tag{3.17}$$

Taking $V_{\mathcal{I}} \to 0$ and $m = 2$, we find a single loop of gapless states located in the $k_y = 0$ plane, described by

the equation $\cos(k_x a_x) + \cos(k_z a_z) = 1$. The stack of 2D Dirac node dipole semimetals will naturally endow the 3D nodal line system with electric polarization (and/or magnetization). Correspondingly, this model has a single non-zero component of the antisymmetric tensor $\mathcal{B}_{xz}$ defined in Eq. (2.40), which encodes a charge polarization in the $\hat{y}$-direction. From Eq. 3.15, a non-vanishing $\mathcal{B}_{xz}$ also implies a k_x momentum line-density localized on a magnetic flux tube oriented in the $\hat{z}$-direction:

$$\mathcal{J}_x^t = 2e\mathcal{B}_{xz}\varepsilon^{tzij}\mathfrak{e}_z^z B_z = 2e\mathcal{B}_{xz}B^z, \tag{3.18}$$

similar to a stack of decoupled 2D Dirac semimetallic layers (in the last equality we replaced $\mathfrak{e}_z^z = 1$). This is the 3D analog of the response shown in Figs. 3.1(c) and (d) for the 2D Dirac semimetal.

We can see an example of a charge response if we tilt the nodal line to introduce a non-zero value of $\mathcal{B}_{tz}$ as illustrated in Fig. 3.3(a). In our model we can tilt the node by adding an extra dispersion

$$\Delta H(\mathbf{k}) = \epsilon \sin(k_x a_x)\mathbb{I}_{2\times 2}, \tag{3.19}$$

to the Hamiltonian. This term breaks $\mathcal{T}$ and induces a net magnetization $M_z = e\mathcal{B}_{tz}$, setting up the corresponding circulating boundary currents in the system [37].

Now, when $\mathcal{B}_{tz}$ is non-vanishing, Eq. 3.16 implies that a screw dislocation with Burgers vector $b^z\hat{z}$ hosts a bound electromagnetic current. Indeed, if we assume the screw dislocation is located at $(x, y) = (0, 0)$ and runs along the z-axis we find

$$j^z = -2e\mathcal{B}_{tz}\varepsilon^{tzjk}\mathfrak{e}_t^t\partial_j\mathfrak{e}_k^z = -2e\mathcal{B}_{tz}b^z\delta(x)\delta(y), \tag{3.20}$$

where we used $\mathfrak{e}_t^t = 1$ and $\nabla \times \mathfrak{e}^z = b^z\delta(x)\delta(y)$.

We can illustrate the origin of this current by considering the magnetization M_z (and associated boundary currents) induced by $\mathcal{B}_{tz}$. A screw dislocation with Burgers vector $b^z\hat{z}$ can be constructed by cutting a seam into layers normal to $\hat{z}$ and re-gluing them along the seams with neighboring layers above or below. When cut, the boundary current associated to M_z will appear, and after re-gluing this current will be routed vertically along the screw-dislocation line, i.e., along the z-direction as shown in Fig. 3.3 (b). The magnetization M_z gives rise to a surface bound current $j_\partial = M_z$ circulating around the $\hat{z}$-axis in each layer. The effective number of current loops winding around the dislocation line per unit length is equal to the Burgers vector b^z. Thus the total current in the $\hat{z}$-direction is:

$$j^z = -b^z j_\partial = -2e\mathcal{B}_{tz}b^z, \tag{3.21}$$

which reproduces the result obtained from the response action. Furthermore, we can understand the sign of the current from Fig. 3.3(b) where we see that the current on the dislocation has an opposite orientation to the current generated by M_z. Another interesting consequence of Eq. (3.12) is the topological piezoelectric effect discussed in Ref. [88].

3.5 3D nodal line quadrupole semimetal

In Sec. 2.5, we derived the effective response action:

$$S[\mathfrak{e}^\lambda] = \hbar \mathcal{B}_{\lambda\eta,\alpha} \int \mathfrak{e}^\lambda \wedge \mathfrak{e}^\eta \wedge d\mathfrak{e}^\alpha. \tag{3.22}$$

for the nodal line quadrupole semimetal. The response action implies the energy-momentum currents:

$$\mathcal{J}^\mu_\lambda = 2\hbar \left(\mathcal{B}_{\lambda\eta,\alpha} - \mathcal{B}_{\eta\alpha,\lambda}\right) \varepsilon^{\mu\nu\rho\sigma} \mathfrak{e}^\eta_\nu \partial_\rho \mathfrak{e}^\alpha_\sigma, \tag{3.23}$$

where we have used that $\mathcal{B}_{\lambda\eta,\alpha}$ is anti-symmetric under exchange of the first two indices.

In analogy with the 2D Dirac node dipole and Dirac node quadrupole semimetals, we expect that most of the responses from the Dirac nodal line dipole semimetal in Sec. 3.4 can be translated to describe some of the responses of this action if we replace charge currents and densities with momentum currents and densities etc. Indeed, we showed in Eq. 2.42 that when λ and η are both spatial indices, $\mathcal{B}_{\lambda\eta,\lambda}$ implies a momentum polarization in a direction perpendicular to λ and η, and carrying momentum parallel to λ. By analogy, the mixed temporal-spatial components $\mathcal{B}_{it,j}$ describe a momentum magnetization in the i-th direction carrying momentum in the j-th direction. The momentum magnetization is further responsible for generating bound-currents on screw-dislocations, i.e., the momentum magnetization will have circulating boundary momentum currents and a momentum current along screw dislocations similar to the charge bound currents on dislocations shown in Section 3.4.

To be more explicit, we can illustrate the momentum polarization in a model by showing the analog of the surface charge theorem, i.e., momentum polarization will yield surface momentum densities. To obtain a Hamiltonian for the nodal line quadrupole semimetal, we begin by stacking 2D Dirac node quadrupole semimetals (see Fig. 3.2 (b)) along the $\hat{z}$-direction. When the planes are completely decoupled, this construction produces a set of four straight Fermi lines stretching in the k_z-direction. If we couple the two-dimensional planes, then we arrive at the following Bloch Hamiltonian:

$$H(\mathbf{k}) = V_{\mathcal{T}}\sigma^x + \sin(k_x a)\sin(k_y a)\sigma^y + (m - \cos(k_x a) - \cos(k_y a) - \cos(k_z a_z))\sigma^z. \tag{3.24}$$

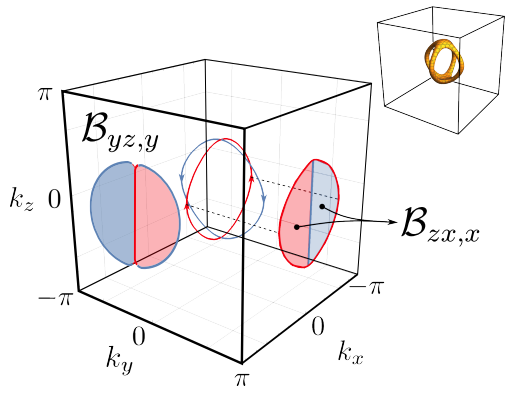

Figure 3.4: Fermi Lines of the model (3.24) with $m = 2$ and $V_{\mathcal{T}} \to 0_-$. Resolving this structure as a pair of loops with *fixed orientation* we can project them onto the $k_x k_z$ or $k_y k_z$ surfaces to determine the momentum polarization. The colored regions of the projected nodes indicate flat drumhead states that would appear in open boundary conditions on one boundary (red) or the opposing boundary (blue). By looking at the relative positions of the two areas bounded by the projected loops in the surface BZ, we see that one surface will have one sign of the k_x or k_y momentum, and the other surface will have the other. For example, for the $k_x k_z$ surface BZ the the projections indicate a dipole moment of k_x momentum polarized along the y direction captured by the response coefficient $\mathcal{B}_{zx,x}$. Inset: Cage-like nodal Fermi surface in the model (3.24) with $E_F = 0.2$.

For a wide range of parameters this model has a pair of nodal line loops that form a cage structure as shown in Figs. 2.2 and 3.4 with $m = 2$ and $V_{\mathcal{T}} = 0$. In general, the local gaplessness of the nodal loops can be protected by the product $\mathcal{TI}$. The cage structure created by the joined, intersecting loops can be split apart by, for example, breaking mirror symmetry along the $k_x = k_y$ axis while preserving $\mathcal{TI}$. However, even in this case the nodal loops still produce a non-vanishing contribution to the response coefficient $\mathcal{B}_{\alpha\beta,\gamma}$. Hence, the response is more general than the specific cage-like nodal configuration. Calculating the response coefficient for the action in the limit $V_{\mathcal{T}} \to 0_-$, we find that $\mathcal{B}_{xz,x} = -\mathcal{B}_{zx,x}$, $\mathcal{B}_{yz,y} = -\mathcal{B}_{yz,y}$ are non-vanishing, as shown in Fig. 3.4.

Using this model we can illustrate the origin of the boundary momentum resulting from the bulk momentum polarization. The discussion is analogous to the calculation of the boundary momentum of the 2D Dirac node quadrupole semimetal in Sec. 3.3. Indeed, the analogy is clear since the cage nodal structure is just arising from a family of 2D Dirac node quadrupoles parameterized by k_z. To specify an unambiguous momentum polarization we turn on a small $\mathcal{T}$-breaking perturbation $V_{\mathcal{T}}$. After doing this, and as shown in Fig. 3.4, we see that the two nodal loop segments that lie in the $k_y = 0$ plane (one for $k_x > 0$ and one for $k_x < 0$) carry the same Berry flux in the k_z-direction (red arrows in Fig. 3.4). Similarly, the two loop segments in the $k_x = 0$ plane carry the same Berry flux (blue arrows), which is opposite to that carried by the $k_y = 0$ segments. Consequently, the loop segment in the $k_y = 0$, $k_x > 0$ half-plane must connect with a loop segment in the $k_x = 0$ plane in order to form a closed nodal loop with a consistent helicity/flux sign.

To clarify the consequences of this nodal configuration let us consider the k_xk_z plane in Fig. 3.4. We can calculate a Berry-Zak phase [116] in the k_y direction parameterized by (k_x, k_z), and for our model we find a Berry phase of magnitude π inside the projected nodal region in the k_xk_z plane. When $V_{\mathcal{T}}$ is turned on, the sign of the π Berry-Zak phases are no longer ambiguous, and are opposite for the projected areas at $k_x > 0$ and $k_x < 0$. If we calculate the total polarization in the y-direction when summed over all k_x and k_z it will vanish. However, the polarization weighted by the k_x momentum will be non-zero. The occupied drumhead surface states in the k_xk_z surface-BZ (see Fig. 3.4 and c.f. Fig. 3.2(a,b,c)) will have an imbalanced k_x momentum, but, when combined with the bulk charge density, a vanishing charge (c.f. Fig. 3.2(c)). This is a reflection of the surface charge theorem for a vanishing charge polarization, and non-vanishing momentum polarization. We numerically calculated the magnitude of the bound surface momentum, finding it to be in agreement with the value predicted by the response action, $2\hbar\mathcal{B}_{xz,x}$. We see from this picture that to have a non-zero response $\mathcal{B}_{xz,x}$, we want two oppositely oriented nodal loops with identical, non-vanishing areas when projected in the k_xk_z-plane, but positioned so that the sums of all k_x inside each nodal loop are different from each other, e.g., in our model they are opposite values.

As an additional explicit example of a non-vanishing response allowed in our model we can consider the momentum density

$$\mathcal{J}^0_x = 2\hbar\mathcal{B}_{xz,x}\epsilon^{ijk}(2\mathfrak{e}^z_i\partial_j\mathfrak{e}^x_k - \mathfrak{e}^x_i\partial_j\mathfrak{e}^z_k) \tag{3.25}$$

generated by a geometric deformation. To generate a non-vanishing response let us consider an xz-planar interface. Since we must preserve translation symmetry along x to calculate k_x momentum, and we want to preserve translation in z for convenience, we have the following terms:

$$\mathcal{J}^0_x = 2\hbar\mathcal{B}_{xz,x}\left(2\mathfrak{e}^z_x\partial_y\mathfrak{e}^x_z - 2\mathfrak{e}^z_z\partial_y\mathfrak{e}^x_x - \mathfrak{e}^x_x\partial_y\mathfrak{e}^z_z + \mathfrak{e}^x_z\partial_y\mathfrak{e}^z_x\right). \tag{3.26}$$

If we cut the system at $y = 0$, both sides of the interface will carry a surface k_x-momentum density $\mathcal{J}^0_{x,surf} = \pm 2\hbar\mathcal{B}_{xz,x}$, since the system has a k_x momentum polarization along $\hat{y}$ with this magnitude. Since each interface carries an opposite sign of the momentum density, if we glue them back together there will be no momentum at the interface. Now, for $y > 0$ let us perturb away from the background translation gauge field configuration to $\mathfrak{e}^a_i = (1+\epsilon^a)\delta^a_i$ where $\epsilon^a = (\epsilon^x,\, 0,\, \epsilon^z)$ is a small deformation. The momentum density response to leading order in ϵ^a is

$$\mathcal{J}^0_x = 2\hbar\mathcal{B}_{xz,x}\left[-2\epsilon^x\delta(y) - \epsilon^z\delta(y)\right], \tag{3.27}$$

which we see is localized at the interface $y = 0$.

We can interpret this response by noting that changing $\mathfrak{e}^x_x$ or $\mathfrak{e}^z_z$ effectively changes the area of one side of

the interface ($y > 0$) relative to the other ($y < 0$). Since the total k_x momentum on both sides of the interface should be unchanged by this deformation (we maintain translation symmetry in x during the process), then increasing the area for $y > 0$ must lower the momentum *density*. Indeed, the surface k_x momentum density on $\hat{y}$ surfaces must be inversely proportional to L_x and L_z. Finally, since we are considering k_x-momentum density, the quantization of which depends on L_x^{-1}, $\mathcal{J}_x^0$ actually depends on L_x^{-2}, hence the difference between the coefficients of ϵ^x and ϵ^z in Eq. 3.27.

3.6 3D Weyl node dipole semimetal

The electromagnetic and geometric response of time-reversal breaking 3D Weyl semimetals have been discussed extensively in the literature [35], [36], [63], [73]–[80], [82], [86], [95], [104]–[112], [117], [118]. Here we focus on a few particular consequences of the mixed crystalline-electromagnetic response and on establishing agreement between the response field theory and microscopic lattice model calculations. Recall that the response action for a 3D Weyl semimetal with a non-vanishing Weyl-node dipole moment $\mathcal{P}_\lambda$ is

$$S[\mathfrak{e}_\nu^\lambda, A_\mu] = \frac{e^2\mathcal{P}_\lambda}{8\pi^2\hbar}\int \mathfrak{e}^\lambda \wedge A \wedge dA. \tag{3.28}$$

This response implies the following bulk electromagnetic and momentum currents:

$$j^\mu = -\frac{e^2\mathcal{P}_\lambda}{4\pi^2\hbar}\varepsilon^{\mu\nu\rho\sigma}\mathfrak{e}_\nu^\lambda\partial_\rho A_\sigma + \frac{e^2\mathcal{P}_\lambda}{8\pi^2\hbar}\varepsilon^{\mu\nu\rho\sigma}A_\nu\partial_\rho\mathfrak{e}_\sigma^\lambda\ , \tag{3.29}$$

$$\mathcal{J}_\lambda^\mu = \frac{e^2\mathcal{P}_\lambda}{8\pi^2\hbar}\epsilon^{\mu\nu\rho\sigma}A_\nu\partial_\rho A_\sigma. \tag{3.30}$$

In the presence of dislocations the translational flux is non-vanishing, and hence the bulk electromagnetic current is anomalous:

$$\partial_\mu j^\mu = -\frac{e^2\mathcal{P}_\lambda}{8\pi^2\hbar}\varepsilon^{\mu\nu\sigma\rho}\partial_\mu\mathfrak{e}_\nu^\lambda\partial_\sigma A_\rho. \tag{3.31}$$

This reflects the fact that the action Eq. 3.28 is not gauge-invariant in the presence of dislocations. Indeed, in our explicit tight-binding model calculations below we find the spectrum on a single screw dislocation line contains a pair of chiral modes of the same chirality (one near each bulk Weyl node momentum as shown in Fig. 3.6(b)). These modes are responsible for the anomalous current on dislocation lines, as was first described by Ref. [40].

To verify the electromagnetic response to the applied crystalline gauge field we consider a simple 2-band

model of a 3D Weyl semimetal with a pair of gapless nodes:

$$H(\mathbf{k}) = \sin(k_z a_z)\sigma^x + \sin(k_y a_y)\sigma^y + (2 - m - \cos(k_x a_x) - \cos(k_y a_y) - \cos(k_z a_z))\sigma^z. \tag{3.32}$$

The Weyl node with the positive chirality $\chi = +1$ is located at $\mathbf{k} = (\arccos(-m), 0, 0)$ and the node with $\chi = -1$ is at $\mathbf{k} = (-\arccos(-m), 0, 0)$. The Weyl node dipole moment therefore has only one non-zero component $\mathcal{P}_x = 2\arccos(-m)$ and the resulting response action is

$$S[\mathfrak{e}^\lambda_\nu, A_\mu] = \frac{e^2\mathcal{P}_x}{8\pi^2\hbar}\int d^4x \epsilon^{\mu\nu\rho\sigma}\mathfrak{e}^x_\mu A_\nu \partial_\rho A_\sigma. \tag{3.33}$$

Let us first consider the response arising from the constant background translation fields $\mathfrak{e}^x_x = 1$ and $\mathfrak{e}^x_y = b^x/L_y$, which describe a twist such that a particle traversing the lattice in the y-direction translates by b^x in the x-direction. We note that such a configuration is volume preserving since $\det(\mathbf{e}) = 1$, where the matrix $\mathbf{e}$ has matrix elements $e_{ij} = \mathfrak{e}^j_i$. When $b^x = 0$ the response action is

$$\frac{e^2\mathcal{P}_x}{8\pi^2\hbar}\int \mathfrak{e}^x_x dx \int dt dy dz \epsilon^{x\nu\rho\sigma} A_\nu \partial_\rho A_\sigma. \tag{3.34}$$

Using the relation $\int dx \mathfrak{e}^x_x = L_x$ we find an anomalous Hall effect in the yz-plane such that $\sigma_{yz} = \frac{e^2}{h}\frac{\mathcal{P}_x L_x}{2\pi}$, which is the standard result [34], [35]. Now, if we turn on b^x we will still have the same σ_{yz}, but we will also have the additional term

$$\frac{e^2\mathcal{P}_x}{8\pi^2\hbar}\int \mathfrak{e}^x_y dy \int dt dx dz \epsilon^{y\nu\rho\sigma} A_\nu \partial_\rho A_\sigma. \tag{3.35}$$

Because of the different index on the ϵ-symbol, this term represents an anomalous Hall effect in the xz-plane with $\sigma_{zx} = \frac{e^2}{h}\frac{\mathcal{P}_x b_x}{2\pi}$. We can find a simple interpretation for this effect: when we turn on $\mathfrak{e}^x_y$, the minimal coupling $k_x \to k_x, k_y \to k_y + k_x\mathfrak{e}^x_y$ shifts the bulk Weyl nodes, $(\pm\mathcal{P}_x/2, 0, 0) \to (\pm\mathcal{P}_x/2, \pm\mathcal{P}_x b_x/(2L_y), 0)$. Hence an effective $\mathcal{P}_y = \frac{\mathcal{P}_x b_x}{L_y}$ is generated when the Weyl momenta are sheared. Indeed, we expect that, at least for uniform, traceless translation gauge field deformations, the response phenomena can be simply interpreted as transformations of the Weyl node dipole $\mathcal{P}_i \to \mathfrak{e}^j_i \mathcal{P}_j$. We show an explicit example of this in the first and third surface-BZ panels of Fig. 3.5(a) where the bulk nodes and their connected Fermi arcs have been rotated in the deformed geometry relative to the undeformed geometry. We note that if the deformation is not volume-preserving, then we must be careful when considering what is held fixed while volume is changing in order to interpret the resulting phenomena.

In addition to these cases of fixed background translation fields, let us consider varying those fields in space. We are interested in the electromagnetic response to applied translational *magnetic* fields $\mathcal{B}^a_i =$

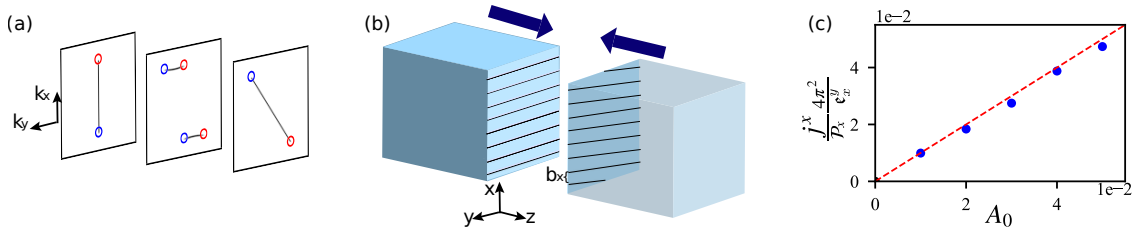

Figure 3.5: (a) The three panels show numerically calculated Fermi arcs in (left) the surface BZ with un-deformed geometry, (right) the surface BZ with $\mathfrak{e}^x_y$ non-vanishing, and (center) the arcs localized at the interface formed by gluing the two sides of the interface together. The colored circles in the first and third panels represent the surface BZ projections of the bulk Weyl nodes on either side of the interface. The color is a guide to show the connectivity/orientation of the Fermi arcs, not the chirality of the bulk nodes. On both sides of the interface the bulk nodes have the same chirality, but since they are effectively projected onto surfaces having opposite normal vectors they generate Fermi arcs having opposite chirality. (b) Illustrations of (left) the un-deformed geometry and (right) the deformed geometry with $\mathfrak{e}^x_y$ non-vanishing. (c) The numerically calculated current localized at the interface between un-deformed and deformed geometries as a function of the chemical potential shift A_0.

$\epsilon^{ijk}\partial_j \mathfrak{e}^a_k$. Since the nodes in our model are separated in k_x, we will consider geometries where the Burgers vector of the translation magnetic field also points along the x-direction, $\mathcal{B}^x_i \neq 0$.

First let us consider a system containing a domain wall as a function of z, such that at $z = 0$ the field $\mathfrak{e}^x_y$ jumps from 0 to b_x/L_y. For $z < 0$ we have bulk Weyl nodes that project onto the z-surface at $(\pm\mathcal{P}_x/2, 0)$, while for $z > 0$ the bulk Weyl nodes have been transformed and sit at $(\pm\mathcal{P}_x/2, \pm\mathcal{P}_x b_x/(2L_y))$. We show the numerically calculated Fermi arcs for our un-deformed and deformed models in the left and right surface BZ panels of Fig. 3.5(a).

Now let us glue the $z < 0$ and $z > 0$ sides to each other to make a domain-wall interface. We schematically illustrate the interface geometry in Fig. 3.5(b). Since the normal vector on each side of the interface is opposite, we expect the Fermi arcs for $z < 0$ to have the opposite chirality to their corresponding arcs for $z > 0$. Indeed, as shown in the center surface BZ panel of Fig. 3.5(a), the Fermi arcs on both sides can hybridize because of their opposite chiralities and form new arcs in the 2D subsystem of the interface. These new Fermi arcs encode the fact that the Hall conductivity σ_{xz} is varying at this interface. These effects are all manifestations of the fact that the Weyl node dipole moment $\mathcal{P}_i$ is changing at the interface, and hence we expect Fermi arcs to be trapped generically at interfaces of this type. We note that a similar strain geometry, and the corresponding Weyl node configuration, was discussed in [87].

From Eq. 3.29 we see that applying a uniform, non-vanishing A_0 to the system described above should generate a charge current in the x-direction. We can see the microscopic origin of this current as follows. If we increase A_0, each linearly-dispersing point on the Fermi arc will have an excess charge density $\delta n(\mathbf{k}) = \frac{eA_0}{2\pi\hbar|v_F(\mathbf{k})|}$ where $v_F(\mathbf{k})$ is the Fermi velocity of the Fermi arc located at $\mathbf{k}$ in the surface-BZ. Hence, the contribution to the current of such a point on the Fermi arc is $j^x(\mathbf{k}) = e v_F(\mathbf{k})\delta n(\mathbf{k})$. For our model and

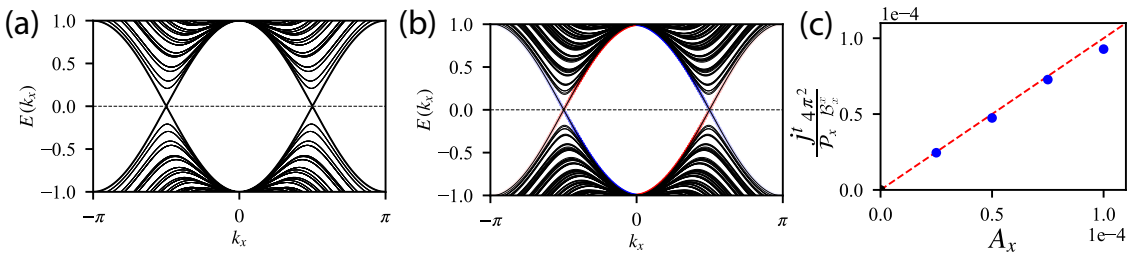

Figure 3.6: (a) The bulk spectrum of a Weyl semimetal with two nodes on the k_x-axis (b) The spectrum of the same Weyl semimetal with periodic boundary conditions and two screw dislocations with opposite Burgers vectors threaded along the x-direction. Red and blue coloration indicates on which dislocation the chiral modes are localized. Each dislocation has a net positive (red) or negative (blue) chirality. (c) Numerical calculation of the charge density bound to a screw dislocation as A_x is tuned. The red dashed lined corresponds to the theoretical prediction.

geometry, the contributions to the j^x current that are linear in the deformations of $\mathfrak{e}_i^a$ arise from the Fermi arcs stretching between $(K,0) \to (K, K\mathfrak{e}_y^x)$ and $(-K,0) \to (-K, -K\mathfrak{e}_y^x)$. Each of these arcs has a fixed value $k_x = \pm K$ and each arc has an opposite Fermi velocity. Hence

$$j^x = ev_F(K,k_y)\delta n \frac{K\mathfrak{e}_y^x}{2\pi} + ev_F(-K,k_y)\delta n \frac{K\mathfrak{e}_y^x}{2\pi} = \frac{e^2\mathcal{P}_x\mathfrak{e}_y^x A_0}{4\pi^2\hbar}\mathrm{sgn}(v_F), \tag{3.36}$$

where $K\mathfrak{e}_y^x/2\pi$ counts the density of states on the Fermi arc in the k_y direction, $\mathrm{sgn}(v_F)$ is sign of the velocity on the $k_x = +K$ arc, and $\mathcal{P}_x = 2K^2$ is the un-deformed value. This result matches the prediction from the response theory and matches the numerical results in Fig. 3.5(c) [2].

We can also study a system with a pair of screw dislocation lines. We explicitly insert two screw dislocations at positions $(y,z) = (N_y/4, 0)$ and $(y,z) = (3N_y/4, 0)$, running parallel to the $\hat{x}$-axis with Burgers vectors $b^x = +1$ and $b^x = -1$, respectively. In Fig. 3.6(a) we show the energy spectrum of a Weyl semimetal with Weyl nodes on the k_x-axis with periodic boundary conditions and no dislocations. In Fig. 3.6(b) we show the spectrum of the same system after two screw dislocations have been inserted as described above. The blue/red coloration indicates on which dislocation the states are localized. We see that near each Weyl point the right-moving modes are on the red dislocation while the left-moving modes are on the blue dislocation, as described by Eq. (3.29). Hence, each dislocation has a net chirality.

To test the response equation we apply a non-vanishing A_x and numerically calculate the charge density localized on a single dislocation. We can carry out a microscopic calculation of the charge bound to a dislocation as a function of A_x. Let us assume a nodal configuration with a positive node at $\mathbf{k} = (\mathcal{P}_x/2, 0, 0)$ and a negative node at $(-\mathcal{P}_x/2, 0, 0)$. In the presence of a dislocation with Burgers vector b^x, each $k_y k_z$-plane

[2] While the coefficient of the response in Eq. 3.29 is half the size of our numerical and analytic result, our calculations inherently determine the *covariant* anomaly of the interface Fermi arc states which receives inflow from the bulk term in Eq. 3.29, i.e., inflow from a boundary term of the same magnitude, hence doubling the result [96], [119]–[121].

sees an effective magnetic flux $\Phi(k_x) = \frac{b^x k_x}{2\pi}\Phi_0$, where $\Phi_0 = h/e$. Hence each $k_y k_z$-plane with a non-vanishing Chern number contributes to the charge as

$$\Delta Q = \frac{eL_x}{2\pi}\int_{BZ} C(k_x)\frac{k_x b^x}{2\pi}dk_x = 0, \tag{3.37}$$

where $C(k_x)$ is the Chern number of each $k_y k_z$-plane parameterized by k_x. If we turn on a non-vanishing A_x ($k_x \to k_x + \frac{e}{\hbar}A_x$) and re-calculate the bound charge we find

$$\begin{aligned}\Delta Q|_{A_x} &= -\frac{L_x}{2\pi}\int_{-\frac{\mathcal{P}_x}{2}-\frac{e}{\hbar}A_x}^{\frac{\mathcal{P}_x}{2}-\frac{e}{\hbar}A_x}\frac{k_x b^x}{2\pi}dk_x \\ &= \frac{e^2\mathcal{P}_x b^x L_x}{4\pi^2\hbar}A_x.\end{aligned} \tag{3.38}$$

This result is exactly what is found in our numerics shown in Fig. 3.6(c). Both of these results match the analytic prediction in Eq. 3.29 after including an extra factor of two which takes into account the bulk and boundary inflow to the boundary [96], [119]–[121].

3.7 3D Weyl node quadrupole semimetal

Finally, we will discuss some aspects of the crystalline response of 3D Weyl semimetals with gapless Weyl nodes forming a quadrupole pattern. Some of these responses were recently discussed in Refs. [63], [77], [94], and here we consider some of the responses in more microscopic detail and compare directly with lattice model calculations.

Recall from Sec. 2.7 the response action

$$S_{WQ} = \frac{e\mathcal{Q}_{\alpha\beta}}{8\pi^2}\int \mathfrak{e}^\alpha \wedge d\mathfrak{e}^\beta \wedge A. \tag{3.39}$$

The bulk linear response implied by Eq. (2.54) is

$$\mathcal{J}^\mu_\alpha = \frac{e}{8\pi^2}\varepsilon^{\mu\nu\rho\sigma}\mathcal{Q}_{\alpha\beta}\mathfrak{e}^\beta_\nu\partial_\rho A_\sigma - \frac{e}{4\pi^2}\varepsilon^{\mu\nu\rho\sigma}\mathcal{Q}_{\alpha\beta}A_\nu\partial_\rho\mathfrak{e}^\beta_\sigma, \tag{3.40}$$

$$j^\mu = -\frac{e}{8\pi^2}\epsilon^{\mu\nu\rho\sigma}Q_{\alpha\beta}\mathfrak{e}^\alpha_\nu\partial_\rho\mathfrak{e}^\beta_\sigma. \tag{3.41}$$

We also note that both of these currents can be anomalous when subjected to certain gauge field configura-

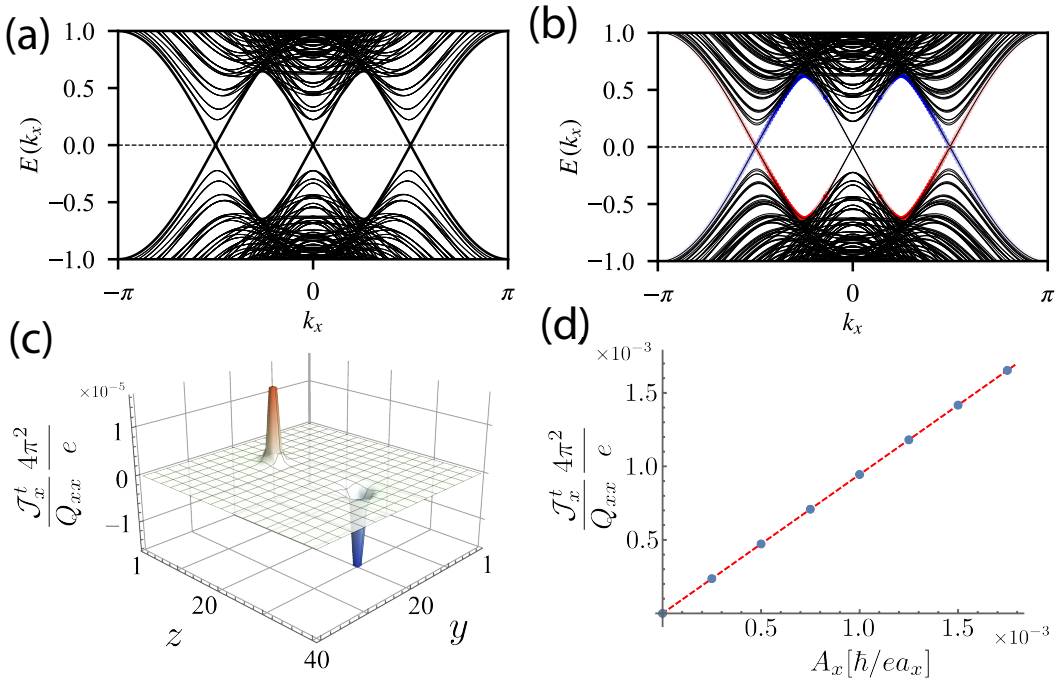

Figure 3.7: (a) The bulk spectrum of a Weyl semimetal with two nodes of one chirality on the k_x-axis and two nodes of the opposite chirality on the k_y-axis. (b) The spectrum of the same Weyl semimetal with periodic boundary conditions and two screw dislocations with opposite Burgers vectors threaded along the x-direction. Red and blue coloration indicates on which dislocation the chiral modes are localized. Each dislocation has a no net chirality, and the Weyl nodes on the k_y-axis do not form chiral modes. (c) The spatially-resolved k_x momentum density response of a Weyl node quadrupole semimetal to a pair of screw dislocations with opposite Burgers' vectors $b_x = \pm a_x$ located at $(y, z) = (20a_y, (20 \pm 10)a_z)$ with the background gauge field $A_x = 2.5 \times 10^{-4}\hbar/ea_x$ and $\mathcal{Q}_{xx} = \pi^2/(2a_x^2)$. (d) Numerically calculated dependence of the k_x momentum density localized on a screw dislocation with Burgers' vector $b_x = 1$ as a function of the background gauge field A_x, using the same model as in (c).

tions:

$$\partial_\mu \mathcal{J}^\mu_\alpha = -\frac{e}{8\pi^2}\varepsilon^{\mu\nu\rho\sigma}\mathcal{Q}_{\alpha\beta}\partial_\mu \mathfrak{e}^\beta_\nu \partial_\rho A_\sigma, \tag{3.42}$$

$$\partial_\mu j^\mu = -\frac{e}{8\pi^2}\epsilon^{\mu\nu\rho\sigma}Q_{\alpha\beta}\partial_\mu \mathfrak{e}^\alpha_\nu \partial_\rho \mathfrak{e}^\beta_\sigma. \tag{3.43}$$

Now let us consider several different phenomena associated to these response equations in the context of a lattice model introduced in Ref. [77]:

$$H(\mathbf{k}) = \sin k_x \sin k_y \Gamma^x + \sin k_z \Gamma^y + (m + t(\cos k_x + \cos k_y + \cos k_z))\,\Gamma^z. \tag{3.44}$$

Without any geometric deformations, the semimetal phase of our model with a Weyl node quadrupole has two nodes of one chirality at $\mathbf{k} = (\pm K, 0, 0)$ and two of the opposite chirality at $(0, \pm K, 0)$. Thus the gapped, 2D $k_y k_z$ planes parameterized by k_x will have a non-vanishing Chern number C for $-K < k_x < 0$ and a non-vanishing Chern number $-C$ for $0 < k_x < K$ where $C = \pm 1$. Similar statements can be made about the $k_x k_z$ planes. Without loss of generality let us choose the nodes on the k_x-axis to have positive chirality such that $\mathcal{Q}_{xx} > 0$ and $C = +1$. For our model this also implies that $\mathcal{Q}_{yy} < 0$ and the non-vanishing $k_x k_z$ Chern number planes have a negative Chern number for $k_y < 0$ and positive Chern number for $k_y > 0$. For example, in our model we can generate a configuration with this structure using $m = -2$, $t = 1$.

We study the momentum density bound to magnetic flux lines and charge density bound to screw dislocations. These two responses, some aspects of which were first described in Ref. [77] (see also Refs. [63], [94]), are the most straightforward because they are essentially bulk responses and do not generate anomalous currents, i.e., the RHS of the anomalous conservation laws above will vanish. Our model has $\mathcal{Q}_{xx} = -\mathcal{Q}_{yy} \neq 0$, and the responses generated by these two coefficients give two separate sets of terms in the response action. Hence, for simplicity we consider only the $\mathcal{Q}_{xx}$ responses for now.

Let us first microscopically calculate the expected response to inserting a magnetic flux or a screw dislocation and compare with the response theory. First, consider inserting a thin magnetic flux line along the x-direction having flux Φ localized at, say $(y, z) = (0, 0)$. This flux will generate a Hall effect from each of the non-trivial $k_y k_z$ Chern planes. The total charge bound to the flux line will vanish because there are equal and opposite contributions from $k_x < 0$ and $k_x > 0$. However, threading the flux will build up a non-vanishing k_x-momentum since planes with opposite k_x-momentum have opposite Chern number. The total momentum (spatial integral of momentum density) driven to the flux line by the Hall effect at each k_x momentum is

$$\Delta P_x = -\frac{\Phi}{\Phi_0}\frac{L_x}{2\pi}\int_{-\pi}^{\pi} C(k_x)\hbar k_x dk_x = \frac{\Phi}{\Phi_0}\frac{\hbar K^2 L_x}{2\pi}, \tag{3.45}$$

where the Chern number $C(k_x)$ is the piecewise-constant function across the k_x BZ described above , and $\Phi_0 = h/e$ is the quantum of magnetic flux. Using the fact that $\mathcal{Q}_{xx} = 2K^2$ and dividing by the volume we find the momentum density

$$\mathcal{J}^0_x = \frac{e\mathcal{Q}_{xx}}{8\pi^2} B_x. \tag{3.46}$$

This is the same result coming from the first term in Eq. 3.40 when $\mathfrak{e}^x_x = 1$.

Next let us calculate the charge response to inserting dislocations. Consider a screw dislocation with Burgers vector component b^x associated to a translation gauge field configuration $\mathcal{B}^x_x \equiv \partial_y \mathfrak{e}^x_z - \partial_z \mathfrak{e}^x_y = b^x \delta(y)\delta(z)$. From Eqs. 3.40 and 3.41 we see that both the momentum and charge currents have responses to dislocations, and we will first calculate the charge response. Heuristically the dislocation is like a $U(1)$ gauge flux that couples to momentum instead of electric charge, so the dislocation couples to k_x momentum because it has a non-vanishing b^x. Hence each $k_y k_z$-plane having non-vanishing Chern number (and non-vanishing k_x) will generate a Hall response, but with a magnitude proportional to its k_x charge. Indeed, each plane sees an effective flux $\Phi(k_x) = \frac{k_x b^x}{2\pi}\Phi_0$. Hence, the total charge bound to the dislocation will be

$$\Delta Q = \frac{eL_x}{2\pi}\int_{-\pi}^{\pi} \frac{k_x b_x}{2\pi} C(k_x) dk_x = -\frac{eb_x \mathcal{Q}_{xx}}{8\pi^2} L_x. \tag{3.47}$$

This matches Eq. 3.41, again after setting $\mathfrak{e}^x_x = 1$ (see also Refs. [63], [77], [94]).

Now we consider the momentum response to a dislocation, i.e., a momentum density bound to the dislocation when A_x is non-vanishing (this comes from the second term in Eq. 3.40). First we can compute the amount of momentum bound to a dislocation when $A_x = 0$ by adding the contributions of each Chern plane:

$$\begin{aligned}
\Delta P_x &= \frac{L_x}{2\pi}\int_{-\pi}^{\pi} \frac{k_x b_x}{2\pi} C(k_x)\hbar k_x dk_x \\
&= \frac{L_x b_x \hbar}{4\pi^2}\left(\int_0^K k_x^2 dk_x - \int_{-K}^0 k_x^2 dk_x\right) \\
&= 0.
\end{aligned} \tag{3.48}$$

We note that this calculation is similar to Eq. 3.47 except with an additional factor of the "momentum-charge" $\hbar k_x$ in the integrand. Now if we turn on an A_x such that $k_x \to k_x + \frac{e}{\hbar}A_x$, we can repeat the calculation to find

$$\begin{aligned}
\Delta P_x|_{A_x} &= \frac{L_x b_x \hbar}{4\pi^2}\left(\int_{-\frac{eA_x}{\hbar}}^{K-\frac{eA_x}{\hbar}} k_x^2 dk_x - \int_{-K-\frac{eA_x}{\hbar}}^{-\frac{eA_x}{\hbar}} k_x^2 dk_x\right) \\
&= -\frac{eL_x b_x 2K^2}{4\pi^2} A_x.
\end{aligned} \tag{3.49}$$

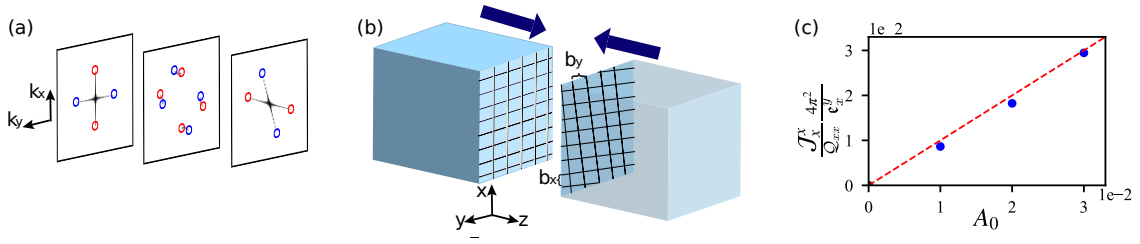

Figure 3.8: (a) The three panels show numerically calculated Fermi arcs in (left) the surface BZ of the un-deformed geometry, (right) the surface BZ of the deformed geometry with $\mathfrak{e}_y^x$ and e_x^y are non-vanishing, and (center) the BZ of the interface formed gluing the deformed and un-deformed geometries together. See the caption in Fig. 3.5 for comments about the color guides on the open circles representing the surface BZ projections of the bulk Weyl nodes. (b) Illustrations of (left) un-deformed and (right) deformed geometries. (c) The numerically calculated momentum current localized at interface between deformed and un-deformed geometries as a function of the chemical potential shift A_0.

The final result yields

$$\mathcal{J}_x^0 = -\frac{e\mathcal{Q}_{xx}A_x}{4\pi^2}\mathcal{B}_x^x, \tag{3.50}$$

which matches Eq. 3.40 and our numerical calculations in Figs. 3.7(c) and (d). For the numerics we inserted a pair of screw dislocations with burgers vectors $b^x = \pm a_x$ in the presence of a constant background gauge potential A_x. The resulting k_x momentum density of the ground state as a function of the y and z lattice coordinates is shown in Fig. 3.7 (c). Furthermore, the dependence of this momentum density on A_x reproduces the expected response coefficient, as shown in Fig. 3.7 (d).

Next let us consider an interface between an un-deformed geometry and a geometry with a non-vanishing background $\mathfrak{e}_x^y$ and $\mathfrak{e}_y^x$ as shown in Fig. 3.8(b). To be explicit, let the interface between the two geometries occur as a function of z at $z = 0$. On the surface of the un-deformed system we numerically calculated the characteristic (rank-2) Fermi arc structure as shown in the left surface-BZ panel in Fig. 3.8(a). For our deformed geometry we show the modified bulk Weyl node quadrupole and Fermi arcs when $\mathfrak{e}_x^y = \mathfrak{e}_y^x \neq 0$ in the right surface-BZ panel in Fig. 3.8(a).

From these figures we see that the Weyl node quadrupole moment $\mathcal{Q}_{ab}^{(R)}$ on the deformed side is modified from the quadrupole moment $\mathcal{Q}_{ab}^{(L)}$ on the un-deformed side. Explicitly, we can compute:

$$\begin{aligned}
\mathcal{Q}_{xx}^{(R)} &= (\mathfrak{e}_x^x)^2\mathcal{Q}_{xx}^{(L)} + 2\mathfrak{e}_x^x\mathfrak{e}_x^y\mathcal{Q}_{xy}^{(L)} + (\mathfrak{e}_x^y)^2\mathcal{Q}_{yy}^{(L)} \\
\mathcal{Q}_{xy}^{(R)} &= \mathfrak{e}_x^x\mathfrak{e}_y^x\mathcal{Q}_{xx}^{(L)} + \mathfrak{e}_x^y\mathfrak{e}_y^y\mathcal{Q}_{yy}^{(L)} + (\mathfrak{e}_x^x\mathfrak{e}_y^y + \mathfrak{e}_x^y\mathfrak{e}_y^x)\mathcal{Q}_{xy}^{(L)} \\
\mathcal{Q}_{yy}^{(R)} &= (\mathfrak{e}_y^x)^2\mathcal{Q}_{xx}^{(L)} + 2\mathfrak{e}_y^x\mathfrak{e}_y^y\mathcal{Q}_{xy}^{(L)} + (\mathfrak{e}_y^y)^2\mathcal{Q}_{yy}^{(L)},
\end{aligned} \tag{3.51}$$

i.e., $\mathcal{Q}_{ij}^{(R)} = \mathfrak{e}_i^a Q_{ab}^{(L)}\mathfrak{e}_j^b$. For our model and geometry we can make the simplifications $\mathfrak{e}_x^x = 1 = \mathfrak{e}_y^y, \mathfrak{e}_x^y =$

$\mathfrak{e}_y^x$, $\mathcal{Q}_{xy}^{(L)} = 0$, and $\mathcal{Q}_{xx}^{(L)} = 2K^2 = -\mathcal{Q}_{yy}^{(L)}$. Substituting these relations into Eq. 3.51 yields

$$\mathcal{Q}_{xx}^{(R)} = -\mathcal{Q}_{yy}^{(R)} = 2K^2(1 - (\mathfrak{e}_x^y)^2), \tag{3.52}$$

and $Q_{xy}^{(R)} = 0$. Alternatively, we can see this result from the locations of the deformed Weyl nodes which will sit at $(K, K\mathfrak{e}_y^x, 0)_+$, $(-K, -K\mathfrak{e}_y^x, 0)_+$, $(K\mathfrak{e}_x^y, K, 0)_-$, and $(-K\mathfrak{e}_x^y, -K, 0)_-$ (where the subscripts $\pm$ encode the chirality for our choice of model parameters).

Since the Weyl node quadrupole moments on the two sides of the interface are different, we expect gluing the two sides together will leave behind a signature at the interface. Indeed, from the middle surface-BZ panel in Fig. 3.8(a) we see gapless Fermi arcs that remain at the interface and stretch between the unmodified and modified projected locations of the bulk Weyl nodes. From Eqs. 3.40, 3.41 we see there should be responses

$$\mathcal{J}_x^x = -\frac{e}{4\pi^2}\mathcal{Q}_{xx}A_0\partial_z\mathfrak{e}_y^x,, \quad \mathcal{J}_y^y = -\frac{e}{4\pi^2}\mathcal{Q}_{yy}A_0\partial_z\mathfrak{e}_x^y, \tag{3.53}$$

$$j^0 = \frac{e}{8\pi^2}\left(\mathcal{Q}_{xx}\mathfrak{e}_x^x\partial_z\mathfrak{e}_y^x - \mathcal{Q}_{yy}\mathfrak{e}_y^y\partial_z\mathfrak{e}_x^y\right) = \frac{e\mathcal{Q}_{xx}}{4\pi^2}\partial_z\mathfrak{e}_x^y, \tag{3.54}$$

where in the last equality we substituted in the relations that are specific to our model and interface geometry, which we stated above.

We confirmed the momentum and charge responses numerically, in particular the $\mathcal{J}_x^x$ response shown in Fig. 3.8(c), and we also provide microscopic analytic arguments here. The momentum currents both follow the same logic, so let us consider only $\mathcal{J}_x^x$ for now. From the center surface-BZ panel in Fig. 3.8(a) we see remnant Fermi arcs. If we increase A_0, each linearly-dispersing point on the Fermi arc will have an excess charge density $\delta n(\mathbf{k}) = \frac{eA_0}{2\pi\hbar|v_F(\mathbf{k})|}$ where $v_F(\mathbf{k})$ is the Fermi velocity at the Fermi arc located at $\mathbf{k}$ in the surface-BZ. Hence, the contribution to the k_x momentum current of such a point on the Fermi arc is $\mathcal{J}_x^x(\mathbf{k}) = \hbar k_x v_F(\mathbf{k})\delta n(\mathbf{k})$. For our model and geometry, the contributions to the $\mathcal{J}_x^x$ current that are linear in the deformations of $\mathfrak{e}_i^a$ arise from the Fermi arcs stretching between $(K, 0) \to (K, K\mathfrak{e}_y^x)$ and $(-K, 0) \to (-K, -K\mathfrak{e}_y^x)$. Each of these arcs has a fixed value $k_x = \pm K$ and each arc has an opposite Fermi velocity. Hence

$$\begin{aligned}\mathcal{J}_x^x &= \hbar K v_F(K, k_y)\delta n\frac{K\mathfrak{e}_y^x}{2\pi} + \hbar(-K)v_F(-K, k_y)\delta n\frac{K\mathfrak{e}_y^x}{2\pi} \\ &= \frac{e\mathcal{Q}_{xx}^{(L)}\mathfrak{e}_y^x A_0}{4\pi^2}\mathrm{sgn}(v_F),\end{aligned} \tag{3.55}$$

where $K\mathfrak{e}_y^x/2\pi$ counts the density of states on the Fermi arc in the k_y direction, $\mathrm{sgn}(v_F)$ is sign of the velocity on the $k_x = +K$ arc, and the un-deformed $\mathcal{Q}_{xx}^{(L)} = 2K^2$. This result matches the prediction from the response theory and matches the numerical results in Fig. 3.8(c).

The calculation of the charge density j^0 at the interface is simpler since it comes from the bulk response to a translation magnetic field. At the interface there is a non-vanishing $\mathcal{B}_x^x = -\partial_z \mathfrak{e}_y^x$ and $\mathcal{B}_y^y = \partial_z \mathfrak{e}_x^y$. Since the $k_y k_z$-planes and $k_x k_z$-planes have non-vanishing Chern numbers, they yield a density response similar to what we found on the dislocation line in Eq. 3.47. Each k_x state sees an effective magnetic flux $\Phi(k_x) = -\frac{k_x b^x}{2\pi}\Phi_0$, and similarly for each k_y state $\Phi(k_y) = \frac{k_y b^y}{2\pi}\Phi_0$, where $b^x = \int dy \mathfrak{e}_y^x|_{z>0}$ and $b^y = \int dx \mathfrak{e}_x^y|_{z>0}$ are the Burgers vectors obtained when integrating across the entire periodic y- and x-directions respectively. Hence the total charge at the interface is

$$\begin{aligned}\Delta Q &= -\frac{2eL_x}{2\pi}\int_0^K \frac{k_x b^x}{2\pi} dk_x + \frac{2eL_y}{2\pi}\int_0^K \frac{k_y b^y}{2\pi} dk_y \\ &= \frac{e}{8\pi^2}\left(-\mathcal{Q}_{xx} b^x L_x + \mathcal{Q}_{yy} b^y L_y\right) \\ &= -\frac{e\mathcal{Q}_{xx} b^x L_x}{4\pi^2},\end{aligned} \tag{3.56}$$

where the leading factors of two in the first line account for identical contributions from the interval $k_x \in [-K, 0]$, and in the last equation we used $\mathcal{Q}_{xx} = -\mathcal{Q}_{yy}$ and $L_x b^x = L_y b^y$ since $\mathfrak{e}_x^y = \mathfrak{e}_y^x$. This final result matches Eq. 3.41.

Chapter 4

Anomalous translation-electromagnetic responses in higher order semimetals

This chapter is adapted from Mark R. Hirsbrunner, Alexander D. Gray, and Taylor Hughes, Phys. Rev. B 109, 075169 (2024). *©2024 American Physical Society.*

4.1 Introduction

Topological semimetals (TSMs) possess quasi-topological terms in their bulk electromagnetic responses that are governed by the configuration of their nodal points or lines in momentum space [117], [122]–[128]. In particular, the responses of point node TSMs are proportional to the chirality-weighted momentum space multipole moments of the nodal points, i.e., monomials of their momentum-space location weighted by their chirality or helicity. For example, in the simplest case of a time-reversal breaking Weyl semimetal (WSM) with two nodes, the magnitude of the bulk anomalous Hall conductivity is proportional to the dipole moment of the Weyl nodes in momentum space [33]–[36]. Additionally, these bulk responses are often necessary to compensate for anomalous surface states, such as chiral Fermi arcs in time-reversal breaking WSMs [34].

In recent years the field of TSMs has grown to include higher order TSMs (HOTSMs) that are characterized by spectral features and other phenomena on surfaces of codimension $n > 1$. The nodal points of HOTSMs differ from conventional TSMs in that they are attached to both surface and hinge Fermi arcs. Heuristically such a node separates gapped momentum space planes that differ in both Chern number *and*

some form of 2D higher order topology. The family of HOTSMs is quite diverse, including higher order analogs of Dirac and Weyl semimetals [102], [103], [129]–[141], nodal line semimetals [142], nodal superconductors [143]–[146], non-Hermitian TSMs [147]–[150], and periodically driven Floquet TSMs [151]–[155]. In some instances, HOTSMs possess additional boundary states and/or electromagnetic responses beyond first-order TSMs. For example, second order WSMs exhibit both surface Fermi arcs and hinge states that generate competing surface and hinge responses [137] in which the bulk charge bound to a magnetic flux (via the anomalous Hall effect) is constrained by the charge bound to hinges parallel to the flux. Similarly, conventional type-I Dirac semimetals (DSMs) have a bulk spin-Hall-like response determined by the momentum-space dipole moment of the Dirac nodes [36], while some higher order DSMs also possess a bulk electric quadrupole moment that generates a surface polarization response [102].

In parallel to these developments of HOTSMs, recent studies have shown that TSMs can exhibit mixed crystalline-electromagnetic responses in addition to purely electromagnetic responses. These mixed crystalline-electromagnetic responses are often probed by subjecting systems to dislocation and disclination defects [68]. TSMs typically possess interesting response phenomena to such defects because the TSM nodal surfaces are protected by translation symmetry and, in some cases, rotation symmetries [63], [73]–[82], [156]. For example, time-reversal symmetric WSMs with a quadrupole arrangement of Weyl nodes in momentum space have electric charge bound to screw dislocations and crystal momentum bound to magnetic flux [63], [77], [156].

Motivated by these unusual electromagnetic responses, here we take the first steps toward understanding the translation-electromagnetic responses of higher order TSMs. In Section 4.2 we introduce a model of a TSM with a quadrupole arrangement of higher order Weyl nodes and characterize its topological features. In Section 4.3 we show that this model possesses a rank-2 mixed translation-electromagnetic response similar to that found in Refs. [63], [77] for quadrupolar arrangements of first-order Weyl nodes. Furthermore, we demonstrate that the higher order nature of the Weyl nodes in our model leads to an additional *surface* translation-electromagnetic response arising from the presence of a dipole of surface Dirac nodes. In Section 4.4 we show that this model can possess a bulk quadrupole moment of equilibrium crystal momentum. We show that the magnitude of this quadrupole moment of momentum is determined by both the momentum-space quadrupole moment of the bulk Weyl nodes and the momentum-space dipole moment of the surface Dirac nodes. This result is a generalization of the notion of characterizing TSMs via multipole moments of the nodal point distribution to the broad class of HOTSMs. In Section 4.5 we conclude with a discussion of future directions for this work.

4.2 Model

In this section we construct a model of a time-reversal symmetric Weyl semimetal in which higher order Weyl nodes are arranged in a quadrupole pattern. We discuss bulk indicators of the topology of this model and the associated bulk, surface, and hinge spectra. Consider the following Bloch Hamiltonian,

$$\begin{aligned} H(\mathbf{k}) = &\sin(k_x)\sin(k_y)\Gamma_1 + \sin(k_z)\Gamma_2 + (m + \cos(k_x) + \beta\cos(k_z))\,\Gamma_3 \\ &+ (m + \cos(k_y) + \beta\cos(k_z))\,\Gamma_4 + i\gamma\Gamma_1\Gamma_2, \end{aligned} \tag{4.1}$$

where Γ_i is a set of five anti-commuting 4×4 matrices. We use the basis $\Gamma_0 = \sigma_2 \otimes \sigma_0$, $\Gamma_1 = \sigma_1 \otimes \sigma_1$, $\Gamma_2 = \sigma_1 \otimes \sigma_2$, $\Gamma_3 = \sigma_1 \otimes \sigma_3$, and $\Gamma_4 = \sigma_3 \otimes \sigma_0$, where σ_i are the Pauli matrices. This Hamiltonian possesses a range of symmetries: spinless time-reversal symmetry (TRS), $\mathcal{T} = \mathcal{K}\mathbb{I}$, two-fold rotation symmetry about each axis, $C_{2x} = C_{2y} = \Gamma_1\Gamma_2$, $C_{2z} = \mathbb{I}$, mirror symmetry about the $x = y$ and $x = -y$ planes, $M_{1,1} = M_{1,-1} = (\Gamma_3 - \Gamma_4)\Gamma_0/\sqrt{2}$, the product of four-fold rotation and reflection along the z-axis, $C_{4z}M_z = (\Gamma_3 + \Gamma_4)/\sqrt{2}$, and the product of inversion and chiral symmetry, $P\Xi = \Gamma_2$ [1].

We first consider the bulk energy spectrum of $H(\mathbf{k})$ in the special case $m + \beta = -1$ and $\gamma = 0$, for which a quadratic band crossing (QBC) appears at Γ, as shown in Fig. 4.1a. While m and β can be tuned to generate QBCs at other high-symmetry points of the BZ, we only consider parameter ranges that place the QBC at Γ. Departing from this starting point by tuning γ away from zero splits the QBC into four Weyl nodes that move apart along the k_x and k_y axes. We show the finite-γ spectrum in Fig. 4.1b which clearly depicts the Weyl nodes on the ΓX and ΓY lines.

To identify the bulk topology, we recall that Weyl nodes act as quantized sources of Berry curvature. As such, the Chern number of any surface in momentum space that encloses a single Weyl node is $C = \pm 1$, where the sign is determined by the chirality χ of the node. Consequently, we can foliate the Brillouin zone into families of fixed momentum planes, and planes that are separated by a Weyl node must have Chern numbers differing by χ. This planar family picture is very convenient and we denote the Hamiltonian restricted to two-dimensional momentum planes normal to the k_i axis as $H(\mathbf{k}; k_i)$. In Fig. 4.1c we plot the Chern numbers of $H(\mathbf{k}, k_i)$ for $i = x, y, z$ as functions of k_i with $m = -0.3$, $\beta = -0.7$ and $\gamma = 0.5$. The discrete jumps in Chern number at the Weyl nodes indicate that the chiralities of the nodes on the k_x and k_y axes are negative and positive, respectively.

The fixed-momentum planes having non-vanishing Chern number generate chiral edge modes along open

[1] Chiral symmetry is typically only realized approximately in material systems, with the exception of superconductors. Breaking the chiral symmetry of our model releases the bulk Weyl nodes, surface Dirac nodes, and hinge modes from being pinned to zero energy. This shift could introduce additional Fermi surface contributions to the translation-electromagnetic responses we study here, but otherwise does not affect our conclusions.

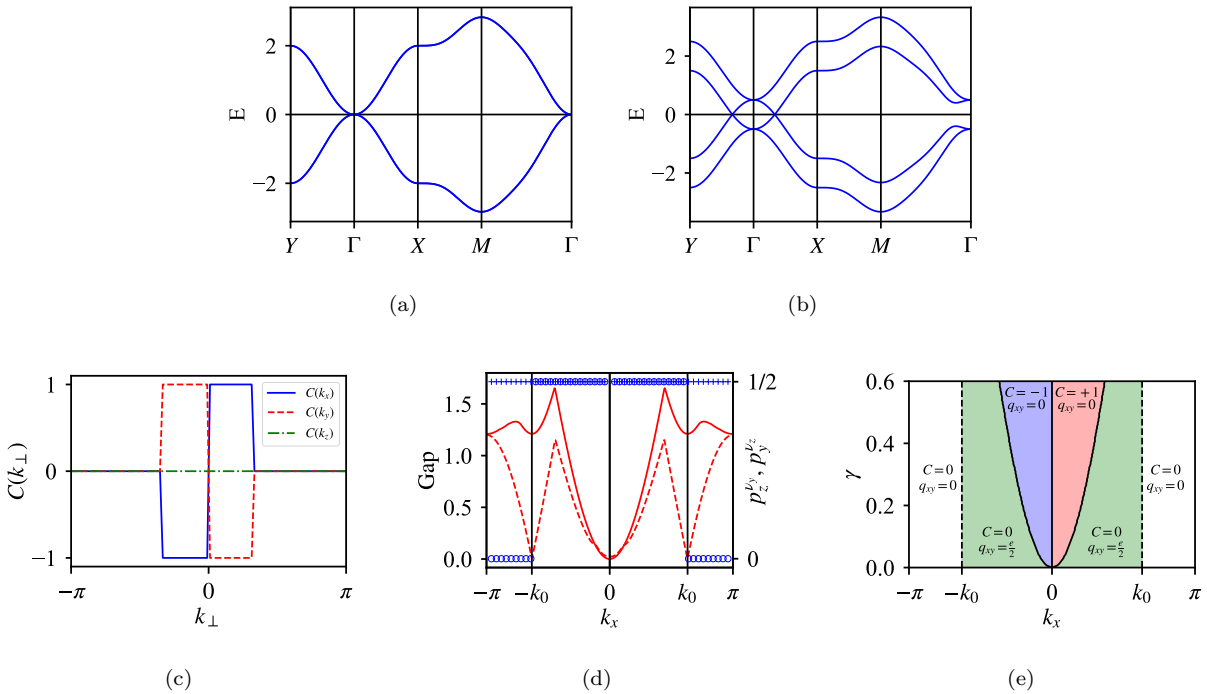

Figure 4.1: (a) The band structure of $H(\mathbf{k})$ along high-symmetry lines in the $k_z = 0$ plane with $m = -0.3$, $\beta = -0.7$, and $\gamma = 0$. The band structure possesses a QBC at Γ and is otherwise gapped. (b) The band structure of $H(\mathbf{k})$ with $m = -0.3$, $\beta = -0.7$, and $\gamma = 0.5$. The finite value of γ splits the QBC into four Weyl nodes, two on the k_x axis and two on the k_y axis. (c) The Chern number of $H(\mathbf{k}; k_x)$ (solid blue), $H(\mathbf{k}; k_y)$ (dashed red), and $H(\mathbf{k}; k_z)$ (dot-dashed green) as functions of the perpendicular momentum with $= m - 0.3$, $\beta = -0.7$, and $\gamma = 0.5$. The changes in the Chern number as the perpendicular momenta are tuned through Weyl nodes indicates that the nodes along k_x and k_y are of negative and positive chirality, respectively. (d) The nested Wilson loops $p_z^{v_y}$ (blue crosses) and $p_y^{v_z}$ (blue circles), bulk gap (solid red line), and surface gap (dashed red line) of $H(\mathbf{k}; k_x)$ with $m = -0.3$, $\beta = -0.7$, and $\gamma = 0.0$. (e) The finite-γ phase diagram of $H(\mathbf{k}; k_x)$ with $m = -0.3$, and $\beta = -0.7$. The solid and dashed black lines indicate bulk and surface gap closings of $H(\mathbf{k}; k_x)$, respectively. The light green region is adiabatically connected to the $\gamma = 0$ QI phase and therefore has $C = 0$ and $q_{xy} = e/2$. The red and blue regions are Chern insulator phases with $C = \pm 1$, and the white regions are trivial.

boundaries. The collection of these edge states comprise the surface Fermi arcs that connect projections of the Weyl nodes in the surface BZ. In Fig. 4.2a we plot the surface spectrum of $H(\mathbf{k})$ with open boundary conditions along the z-direction. At zero energy there are a pair of intersecting Fermi arcs, which we depict in blue, on the surface normal to the z-direction, with one nodal arc on the k_x-axis and another arc on the k_y-axis. At energies above or below $E = 0$ the Fermi arcs form portions of a hyperbola that originate at the positive chirality nodes, nearly meet at the origin, and then turn in opposite directions to eventually terminate at the negative chirality nodes. Indeed, the dispersion around Γ is that of a saddle point $E = k_x k_y$, hence this model is another realization of a surface rank-2 chiral fermion [77]. For comparison, in Fig. 4.2b we plot the surface spectrum with open boundaries in the x-direction with $m = -0.3$, $\beta = -0.7$, and $\gamma = 0.5$. We find that the Fermi arcs that appear on the x-normal surface originate at Γ and terminate at the positive- and negative-momentum projections of the Weyl nodes on the k_y-axis. On a y-normal surface the relative chirality of the nodes switches, but the Fermi arcs are identical because of the mirror and rotational symmetries of $H(\mathbf{k})$.

We can characterize arrangements of Weyl nodes by calculating the momentum-space multipole moments of the nodes weighted by the node chiralities. In particular, we define the Weyl dipole P_i and Weyl quadrupole Q_{ij} moments as

$$P_a = \sum_n \chi^n k_a^n, \quad Q_{ab} = \sum_n \chi^n k_a^n k_b^n, \tag{4.2}$$

where n indexes the nodes. The Weyl dipole moment of $H(\mathbf{k})$, which is proportional to the anomalous Hall conductivity, vanishes as required by TRS. In contrast, we find that the diagonal quadrupole moments Q_{xx} and Q_{yy} are non-vanishing, and the mirror symmetries along the $x = y$ and $x = -y$ axes require them to have the same magnitude and opposite sign. We consider these moments because, as mentioned above, the dipole moment is directly related to the anomalous Hall coefficient, and recent works have shown that the quadrupole moment characterizes translation-electromagnetic responses, e.g., screw dislocations bind electric charge, and magnetic flux binds crystal momentum [63], [77]. Below we show that the Weyl nodes in our model are, in fact, higher order Weyl nodes, and investigate the translation-electromagnetic responses that arise from quadrupole arrangements of higher order Weyl nodes.

We have mentioned that first order Weyl nodes represent a transition (as a function of momentum) between insulator phases on planes of the foliated BZ where the Chern number differs by the Weyl chirality. In contrast, higher order Weyl nodes separate insulators that differ by both a Chern number and some type of 2D higher order topology. In our case the higher order topology is that of a quadrupole insulator (QI) [55], [60], [92], [93], [136], [157]–[161]. Depending on the symmetry, such QI phases can be either bulk obstructed or boundary obstructed [162]–[166], and they are characterized by a quantized bulk electric quadrupole

moment $q_{xy} = e/2$ and a quantized, vanishing bulk charge polarization. The bulk electric quadrupole moment is defined as $q_{xy} = p_x^\partial + p_y^\partial - Q_{corner} \mod 1$, where p_x^∂ and p_y^∂ are the electric polarizations on $\hat{y}$- and $\hat{x}$-normal surfaces, respectively, and Q_{corner} is the charge localized on a corner where two such surfaces meet. One typical manifestation of a bulk electric quadrupole moment q_{xy} is a set of corner charges in systems with open boundary conditions in both the x- and y-directions. For our model these corner charges are accompanied by a set of four mid gap corner modes, the occupation of which determines the pattern of signs of the corner charges.

To show that the Weyl nodes in our model are higher order we need a procedure to diagnose the QI topology. One approach is to study the pair of Berry phases $(p_x^{\nu_y}, p_y^{\nu_x})$ of the hybrid Wannier bands $v_y(k_x)$ and $v_x(k_y)$ [92], [93]. These Berry phases, which are referred to as nested Wilson loops, indicate the QI phase with non-vanishing q_{xy} when they are both non-trivial, i.e., when $(p_x^{\nu_y}, p_y^{\nu_x}) = (1/2, 1/2)$. The symmetry restrictions required to quantize the nested Wilson loops are more stringent than those required to enforce a non-vanishing, quantized quadrupole moment, so this approach can be applied only in a reduced parameter region of our model. Typically, a pair of mirror symmetries is needed to quantize the nested Wilson loops, but our putative QI insulator Hamiltonians $H(\mathbf{k}, k_x)$ and $H(\mathbf{k}, k_y)$ instead possess pairs of mirror *times time-reversal* symmetries. These symmetries are represented by $M_{x/y}\mathcal{T} = \mathbb{I}_{4\times4}$ and $M_z\mathcal{T} = \Gamma_1\Gamma_2$, and descend from the the $C_{2x/y}$, C_{2z}, and $\mathcal{T}$ symmetries of $H(\mathbf{k})$. These mirror times time-reversal symmetries quantize the bulk quadrupole moment but do not quantize the nested Wilson loops.

We can make progress by noting that these symmetries are elevated to conventional mirror symmetries in the limit $\gamma = 0$. Hence the $\gamma = 0$ limit permits the computation of the bulk quadrupole moment via the nested Wilson loops. We present the results of this computation in Fig. 4.1d where we plot the bulk gap, surface gap, and nested Wilson loops of $H(\mathbf{k}, k_x)$ with $m = -0.3$, $\beta = -0.7$, and $\gamma = 0$ as a function of k_x. We find that the bulk gap closes at $k_x = 0$, corresponding to the QBC at Γ. Interestingly, the surface gap closes at a pair of momenta $k_x = \pm k_0$, far away from the location of the bulk gap closing. For $0 < |k_x| < |k_0|$, both nested Wilson loops are quantized to $1/2$, confirming the presence of a non-trivial QI phase for each fixed-k_x plane in this interval. One of the two nested Wilson loops changes values at the surface gap closing at $|k_x| = k_0$, leaving the region $|k_x| > k_0$ with only a single non-trivial nested Wilson loop, indicating a phase with vanishing quadrupole moment for all fixed-k_x planes in this interval.

While we can only calculate the quantized nested Wilson loops for $\gamma = 0$, we can go beyond the $\gamma \neq 0$ case by using an adiabatic argument. As long as the crystal symmetries that quantize q_{xy} and the x, y components of the (bulk) polarization are maintained, the bulk quadrupole moment can change only at bulk or surface gap closing points. Thus, knowing the results for $\gamma = 0$, we can determine the bulk quadrupole moment at finite γ via a straightforward adiabatic argument. At any momentum k_x for which $H(\mathbf{k}, k_x)$

realizes the $\gamma = 0$ QI phase, the Hamiltonian will remain in the QI phase at finite γ as long as there are no intervening bulk or surface gap closings, and the quantizing symmetry is maintained. We plot the locations of the bulk and surface gap closings of $H(\mathbf{k}, k_x)$ in Fig. 4.1e as a function of k_x and γ with $m = -0.3$ and $\beta = -0.7$. The splitting of the QBC into Weyl nodes nucleates a pair of $C = -1$ and $C = +1$ Chern insulator phases on opposite sides of $k_x = 0$, indicated in blue and red, respectively. The locations of the surface gap closings do not depend on γ, so the QI remains intact for $k_{\text{Weyl}} < |k_x| < k_0$, where k_{Weyl} is the location of the Weyl node on the k_x axis. Similar results obtain when we consider the 2D, fixed-momentum phases as a function of k_y instead of k_x. This confirms that the Weyl nodes in this system separate Chern insulator phases from QI phases and are higher order Weyl nodes.

The surface gap closings that bound the QI phases of $H(\mathbf{k}, k_x)$ appear as a pair of surface Dirac cones at opposite values of k_x on the $k_z = \pi$ boundary of the y-normal surface BZ. An analogous pair of surface Dirac cones appears on x-normal surface BZs owing to the rotation and mirror symmetries of $H(\mathbf{k})$. We plot the x-normal surface spectrum with $m = -0.3$, $\beta = -0.7$, and $\gamma = -0.5$ in Fig. 4.2b, in which the surface Dirac cone at positive k_y is visible and depicted in red. With open boundary conditions along both the y- and z-directions, the hinge spectrum of $H(\mathbf{k})$, shown in Fig. 4.2c, exhibits a pair of mid-gap flat bands in the hinge BZ spanning between the projections of the bulk Weyl nodes and the surface Dirac nodes. These mid-gap hinge arcs originate from the mid-gap corner modes of the QI phase. We find identical results for hinges parallel to $\hat{y}$ as ensured by the mirror and rotation symmetries of $H(\mathbf{k})$. In the next section we study the mixed crystalline-electromagnetic responses that arise from such quadrupole arrangements of higher order Weyl nodes, with $H(\mathbf{k})$ serving as an explicit realization. Additionally, in Sec. 4.4 we study some further consequences of the mid-gap hinge states.

4.3 Translation-Electromagnetic Responses

It was recently shown that semimetals hosting a quadrupole configuration of Weyl nodes exhibit a mixed translation-electromagnetic response that binds crystal momentum to magnetic flux and electric charge to screw dislocations [63], [77]. Here we confirm that the Hamiltonian Eq. (4.1) also exhibits this response. Furthermore, we show that the higher order nature of our model's Weyl nodes leads to an additional *surface* translation-electromagnetic response. This surface response manifests as crystal momentum bound to magnetic flux and electric charge bound to dislocations.

The translation-electromagnetic response of topological semimetals hosting a Weyl quadrupole is captured by the effective action

$$S[A, \mathfrak{e}] = -\frac{e}{8\pi^2} \int d^4x \, \epsilon^{\mu\nu\rho\sigma} Q_{ab} \mathfrak{e}^a_\mu A_\nu \partial_\rho \mathfrak{e}^b_\sigma, \tag{4.3}$$

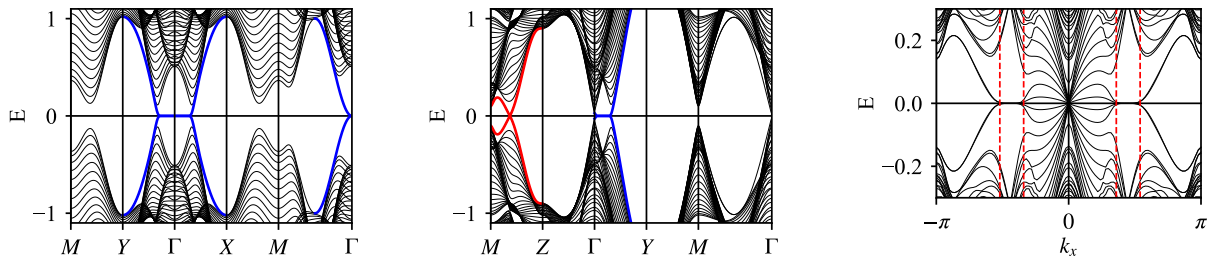

(a) (b) (c)

Figure 4.2: The (a) z- and (b) x-normal surface band structures of Eq. 4.1 along high-symmetry lines with $m = -0.3$, $\beta = -0.7$ and $\gamma = 0.5$, using 30 lattice sites in the open direction. The z-normal surface has a cross of Fermi arcs connecting the projections of the Weyl nodes on both the k_x and k_y axes. The x-normal surface possesses Fermi arcs between the projections of the Weyl nodes on the $\Gamma - Y$ line and a pair of Dirac cones on the BZ boundary. Bands containing Fermi arcs are drawn in blue and the surface Dirac cones are indicated with red. The spectrum of the y-normal surface is identical to the x-normal surface. (c) The spectrum of $H(\mathbf{k})$ with open boundary conditions along the y- and z-directions, 25 lattice sites along each open direction, $m = -0.3$, $\beta = -0.7$, and $\gamma = 0.5$. The zero-energy modes arise from the quadrupole phases of $H(\mathbf{k}; k_x)$ and are localized to the hinges. The dashed red lines indicate the bounds of the zero-energy hinge modes. The hinge spectrum along the y-direction is identical.

where Q_{ab} is the quadrupole moment of the Weyl nodes, A_μ is the electromagnetic gauge field, and $\mathfrak{e}_\mu$ are the translation gauge fields [58], [62], [72], [79], [89], [110]. For our model we simplify this action by noting that only the diagonal elements of the quadrupole moment of Q_{ab} are non-vanishing $Q_{xx} = -Q_{yy} \equiv \bar{Q}$.

One response encoded by this action is the binding of momentum density to magnetic flux that points along the x- or y-directions,

$$\mathcal{J}^0_a = \frac{e\bar{Q}}{8\pi^2} B_a \left(\delta_{ax} - \delta_{ay}\right), \tag{4.4}$$

where the bound momentum points along the magnetic field and the momentum density of the electrons is defined as

$$\mathcal{J}^0_a = \frac{1}{e} \int \frac{d^3\mathbf{k}}{(2\pi)^3} \, k_a j^0(\mathbf{k}), \tag{4.5}$$

where we have assumed $\mathfrak{e}^a_b = \delta^a_b$. If the lattice is distorted and off-diagonal elements of the translation gauge field are present, Eq. (4.4) is modified such that the momentum density does not align directly with the magnetic field. There is also a conjugate response wherein charge is bound to screw dislocations that have Burgers vectors in the xy-plane,

$$j^0 = \frac{e\bar{Q}}{8\pi^2} \left(\mathcal{B}^x_x - \mathcal{B}^y_y\right), \tag{4.6}$$

where we have set $\mathfrak{e}^x_x = \mathfrak{e}^y_y = \mathfrak{e}^z_z = 1$, $\partial_x \mathfrak{e}^x_y = \partial_x \mathfrak{e}^x_z = 0$, and allow $\partial_z \mathfrak{e}^x_y$ and $\partial_y \mathfrak{e}^x_z$ to be finite. In these two response equations B_a are the components of the magnetic field and $\mathcal{B}^a_a = \epsilon^{abc} \partial_b \mathfrak{e}^a_c$ denotes the torsional magnetic field induced by a screw dislocation along the a-axis.

This translation-electromagnetic response can be straightforwardly understood as a consequence of the arrangement of non-trivial Chern insulator phases on planes in the foliated BZ. For simplicity, let us first consider planes normal to k_x and denote the locations of the Weyl nodes away from $k_x = 0$ on the k_x-axis as $\pm k_0$. As shown in Fig. 4.1c, the Chern number of $H(\mathbf{k}; k_x)$ is $C = -1$ for $-k_0 < k_x < 0$, $C = 1$ for $0 < k_x < k_0$, and $C = 0$ elsewhere. Consider inserting a magnetic flux Φ in the yz-plane. Let us assume that this flux line preserves translation symmetry along $\hat{x}$. Then the net response of the system to the magnetic flux is the response of $H(\mathbf{k}, k_x)$ summed over k_x. The trivial phases of $H(\mathbf{k}, k_x)$ are inert to the flux, but the Chern insulator phases bind charge $q = C\Phi/\Phi_0$ to the flux, where Φ_0 is the quantum of magnetic flux [29]. The charge density bound to the flux by the $C = 1$ and $C = -1$ phases of $H(\mathbf{k}, k_x)$ are opposite, so no net charge is accumulated. However, the crystal momentum-per-length bound to the flux is non-vanishing:

$$\int dydz\, \mathcal{J}^0_x = \frac{e\bar{Q}}{8\pi^2}\Phi. \tag{4.7}$$

The dual response of charge bound to a screw dislocation along the $\hat{x}$-direction can be understood through similar reasoning. As with the Aharonov-Bohm effect for electrons near a magnetic flux line, electrons encircling a screw dislocation acquire a phase. In the magnetic flux case the phase is proportional to a product of the charge and flux, $\varphi \propto e\Phi$. In the torsional flux case, the phase is the dot product of the crystal momentum of the electron (translation charge) and the Burgers vector of the dislocation (torsional flux), $\varphi = \mathbf{k} \cdot \mathbf{b}$, where $\mathbf{b} = (b_x, 0, 0)$ in this case. Since the phase acquired upon encircling the screw dislocation is proportional to k_x, the $C = 1$ and $C = -1$ phases of $H(\mathbf{k}, k_x)$ bind *equal* charge (in both sign and magnitude) to the defect, yielding no bound crystal momentum density. However, there is a non-vanishing bound charge-per-length:

$$\int dydz\, j_0(\mathbf{r}) = \frac{eQ_{xx}}{8\pi^2} b_x. \tag{4.8}$$

The response to threading magnetic flux or screw dislocations along other directions can be interpreted similarly. That is, one can determine the arrangement of the Chern insulator phases perpendicular to the chosen direction $\hat{n}$ by projecting the Weyl nodes onto that axis in momentum space. Then one can apply the flux insertion method above to determine the response. As an additional example, this model has the interesting characteristic that for $\hat{n} = \hat{x} \pm \hat{y}$ and $\hat{n} = \hat{z}$, the response is zero because the Weyl nodes project onto the given axes in opposite-chirality pairs, yielding $C = 0$ for all momenta.

Since our model $H(\mathbf{k})$ has Weyl nodes arranged in a quadrupolar pattern we expect to find it has the responses encoded by Eq. 4.3. Here we verify that $H(\mathbf{k})$ exhibits the translation-electromagnetic response described above by numerically calculating both the electric charge density bound to screw dislocations and

the momentum density bound to magnetic fluxes. We consider a system with periodic boundary conditions in all directions and choose a configuration to preserve translation symmetry along $\hat{x}$, which is necessary to permit calculation of the crystal momentum density along $\hat{x}$. As such, we treat the x-direction in momentum space with $N_k = 40$, and use a lattice of dimension $N_y \times N_z = 40 \times 40$ in the y-and z-directions. We insert oppositely-signed flux lines, either electromagnetic or torsional, along $\hat{x}$ at sites $(y, z) = (20, 10)$ and $(20, 30)$. Torsional flux is defined analogously to magnetic flux, $\Phi_T^a = \int dS_b \mathcal{B}_b^a$, and screw dislocations are sources of torsional flux equal to the burgers vector of the screw dislocation.

To generate the fluxes we include the magnetic flux Φ via a Peierls phase, i.e., multiplying all hopping terms that cross the line connecting the two flux lines by the phase $\exp(2\pi i \Phi/\Phi_0)$. Because the translation gauge fields couple to momentum rather than charge, the torsional magnetic field of a screw dislocation is accounted for by modifying the Peierls phases used for the magnetic flux to be a product of the crystal momentum along $\hat{x}$ and the torsional flux of the dislocation, $k_x \Phi_x^T$ [72], [95], [96]. The modified Peierls phase captures the phase acquired by an electron having crystal momentum k_x encircling the screw dislocation and translating by Φ_x^T sites in the $\hat{x}$-direction.

Using this setup, we calculate the momentum density bound to magnetic flux as a function of the flux as shown in Fig. 4.3a. Similarly, in Fig. 4.3d we plot the charge bound to a screw dislocation as a function of the torsional flux. Both plots demonstrate the expected linear relationship between charge/momentum and flux with slope $e\bar{Q}/8\pi^2$, corroborating that the Hamiltonian $H(\mathbf{k})$ possesses the response predicted by the effective action in Eq. (4.3). Let us comment about the data points represented by open circles in Fig. 4.3d. In order to be commensurate with the lattice, torsional flux Φ^T should take integer values equivalent to the Burgers vector of the screw dislocation. The open circle data points are non-integer torsional fluxes that can be inserted via our momentum-dependent Peierls factors, but the interpretation in terms of an elastic lattice defect is less clear.

Now that we have confirmed the expected bulk responses we can move on to identify the surface responses. Indeed, as a consequence of our Weyl nodes being higher order, we expect that even regions of the surface BZ that do not harbor gapless surface states may contribute to surface responses. Indeed, since the $\hat{x}$- and $\hat{y}$-normal surfaces of the model Hamiltonian host a pair of Dirac nodes we expect to find a 2D surface response analogous to a 2D Dirac semimetal. As such, these surfaces possess a translation-electromagnetic response similar to that of the bulk described by the effective action [36]:

$$S[A, \mathfrak{e}] = \frac{e\mathcal{P}_a}{4\pi} \int d^3x \epsilon^{\mu\nu\rho} \mathfrak{e}_\mu^a \partial_\nu A_\rho. \tag{4.9}$$

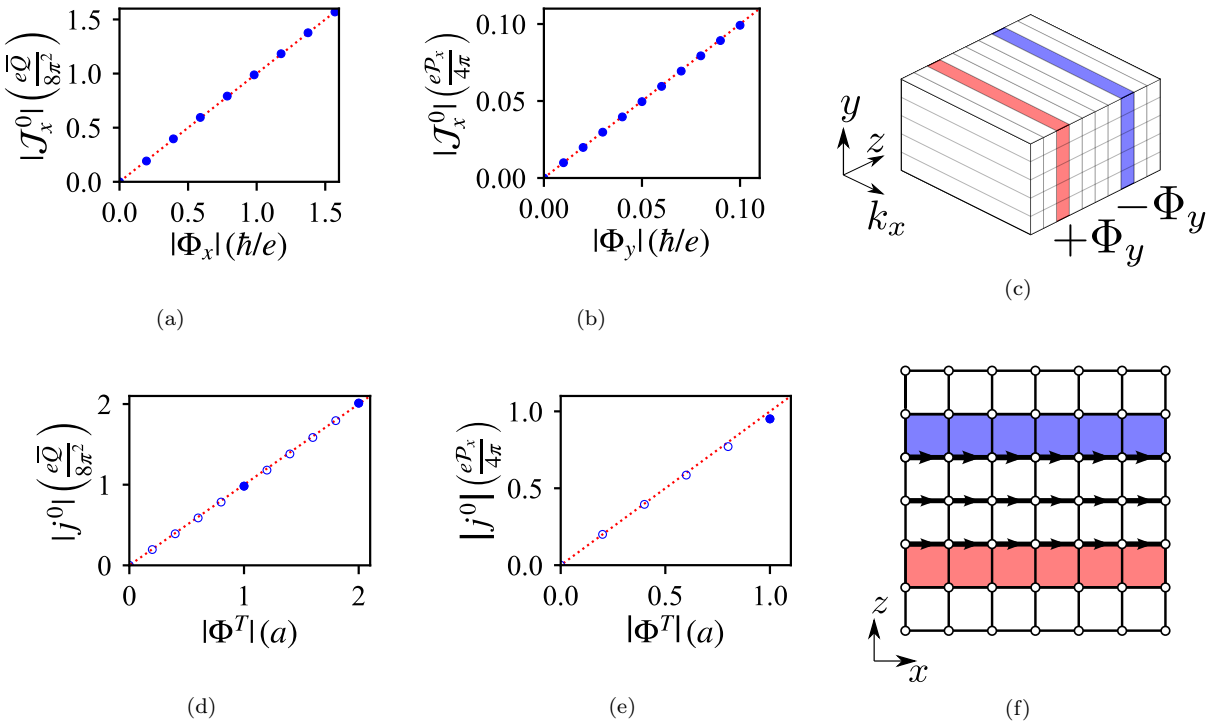

Figure 4.3: (a) The crystal momentum bound to magnetic flux by Eq. (4.1) on a lattice of dimension $N_y \times N_z = 40 \times 40$, and $N_{k_x} = 40$. (b) The surface crystal momentum density $\mathcal{J}_x^0$ bound to magnetic flux along the y-direction for a system size of $N_y \times N_z = 30 \times 30$ and $N_{k_x} = 40$. (c) The magnetic flux geometry we use to calculate the momentum and charge density response on x- and y-normal surfaces. Red (blue) coloration indicates either magnetic or dislocation flux pointing along the $+y$-direction ($-y$-direction). (d) The electric charge bound to a screw dislocation with $N_y \times N_z = 40 \times 40$, and $N_{k_x} = 40$. Empty and filled circles indicate fractional and integer torsional fluxes. (e) The surface electric charge density bound to dislocation flux for a system size of $N_y \times N_z = 40 \times 40$ and $N_{k_x} = 100$. Here Φ_{tot}^D is the total dislocation flux integrated along the x-direction, corresponding to the difference in system size along the x-direction between the strained and unstrained regions in units of the unstrained lattice constant. Empty and filled circles indicate fractional and integer dislocation fluxes. (f) The torsional flux geometry used to calculate the surface charge response. The red (blue) plaquettes correspond to positive (negative) torsional flux and the black arrows indicate the hoppings that acquire a momentum-dependent Peierls phase due to the strain of the lattice. All results presented here are calculated using the parameters $m = \beta = -0.5$ and $\gamma = 0.5$. The red dotted lines in (a), (b), (d), and (e) each have a slope of one and indicate the analytic result.

Here the response coefficient is the Berry curvature dipole moment, given by [36], [89], [156]

$$\mathcal{P}_a = \frac{1}{\pi}\int_{\mathrm{BZ}} d^2\mathbf{k} k_a \mathcal{F}(\mathbf{k}), \tag{4.10}$$

where $\mathcal{F}$ is the Berry curvature and the integration is restricted to the surface BZ. When the surface has time-reversal and inversion symmetry, this action implies that the system has a charge polarization $p^a = \frac{e}{4\pi}\epsilon^{ab}\mathcal{P}_b$[36] (which resides on the surface of our 3D system).

To illustrate a particular response let us focus on the response of the y-normal surface, for which $\mathcal{P}_x \neq 0$ and $\mathcal{P}_z = 0$ (the x-normal surface has an analogous response by symmetry). The translation-electromagnetic response captured by the effective action Eq. (4.9) binds momentum density to magnetic flux,

$$\mathcal{J}_x^0 = -\frac{e}{4\pi}\mathcal{P}_x B_y, \tag{4.11}$$

and binds electric charge to dislocations,

$$\begin{aligned} j^0 &= -\frac{e}{4\pi}\mathcal{P}_x\left(\partial_x \mathfrak{e}_z^x - \partial_z \mathfrak{e}_x^x\right) \\ j^0 &= -\frac{e}{4\pi}\mathcal{P}_x \mathcal{B}_y^x. \end{aligned} \tag{4.12}$$

Here we verify that the surfaces of our model have these responses via direct numerical calculation. We consider a system with open boundary conditions in the $\hat{y}$-direction and periodic boundary conditions in the $\hat{x}$- and $\hat{z}$-directions. We treat the $\hat{x}$-direction in momentum space and calculate the momentum density bound to magnetic flux (using $N_k = 40$ momentum points), and the charge bound to dislocations (using $N_k = 100$ momentum points). The other two directions we leave in position space and use a lattice of dimension $N_y \times N_z = 30 \times 30$ and $N_y \times N_z = 40 \times 40$ for each of the calculations respectively. To avoid difficulties arising from the divergent Berry curvature distribution of Dirac nodes, we also include an inversion-breaking perturbation $H' = -\nu\frac{i}{2}\Gamma_2\Gamma_3$ with $\nu = 0.5$.

To calculate the k_x momentum density on a $\hat{y}$-normal surface it is necessary to maintain translation symmetry along $\hat{x}$. To do so we introduce the magnetic field via two strips of magnetic flux lines extending in the x-direction, each with opposite field orientations $\pm B_y\hat{y}$. For the $N_y \times N_z = 40 \times 40$ lattice these strips are located at $z_1 = 10$ and $z_2 = 30$, while for the $N_y \times N_z = 30 \times 30$ lattice they are located at $z_1 = 8$ and $z_2 = 23$. The geometry of this magnetic field configuration is depicted in Fig. 4.3c. We include torsional flux in an analogous translation symmetry-preserving manner by using the generalized, momentum-dependent Peierls factors mentioned above for the bulk response. We can think of this torsional magnetic field as a non-vanishing strain configuration between the z_1 and z_2 planes that immediately relaxes back to the

unstrained lattice outside this interval. This configuration induces opposite torsional magnetic fields $\mathcal{B}_y^x$ at the boundaries of the strained region. We schematically depict this geometry in Fig. 4.3f, where the red (blue) plaquettes contain positive (negative) dislocation fluxes, and the black arrows indicate hopping terms to which we apply the momentum-dependent Peierls phases.

Because we are interested in a surface response, we must use a layer-resolved Berry curvature to calculate the response coefficient $\mathcal{P}_\alpha$ for just the top (or bottom) surface of the system. The layer-resolved Berry curvature can be obtained by combining the projector onto the occupied subspace, defined as

$$P(\mathbf{k}) = \sum_{\epsilon_i(\mathbf{k})<0} |u_i(\mathbf{k})\rangle \langle u_i(\mathbf{k})| \tag{4.13}$$

where $H(\mathbf{k})|u_i(\mathbf{k})\rangle = \epsilon_i(\mathbf{k})|u_i(\mathbf{k})\rangle$, and the projector onto the n^{th} layer of the lattice, P_n, via the formula [27]

$$\mathcal{F}_n^{ab}(\mathbf{k}) = \text{Tr}\left[P(\mathbf{k})\partial_{k_a}P(\mathbf{k})P_n\partial_{k_b}P(\mathbf{k})\right]. \tag{4.14}$$

Using this formalism, the surface response coefficient is given by the momentum-space dipole moment of the layer-resolved Berry curvature summed over half the sites in the open direction:

$$\mathcal{P}_x = \frac{1}{\pi}\sum_{n=1}^{N_y/2}\int_{\text{BZ}} dk_x dk_z\, k_x \mathcal{F}_n^{xz}(k_x,k_z). \tag{4.15}$$

The momentum and charge bound to the surface by dislocations and magnetic flux are calculated in a similar manner, i.e., layer contributions are summed over half of the sites in the open direction,

$$j^0 = \sum_{n=1}^{N_y/2} j^0(n), \quad \mathcal{J}_x^0 = \sum_{n=1}^{N_y/2}\mathcal{J}_x^0(n). \tag{4.16}$$

After carrying out these calculations, we show the x-momentum density bound to a strip of magnetic flux lines as a function of the magnetic flux in Fig. 4.3b and plot the charge density bound to a strip of dislocations as a function of torsional flux in Fig. 4.3e. The momentum density bound to magnetic flux is linear in the magnetic flux with the correct proportionality constant $e\mathcal{P}_x/4\pi$. Here the value of $\mathcal{P}_x$ is determined by directly calculating Eq. 4.15, which determines the slopes of the dashed lines in Figs. 4.3b and 4.3e. For a small torsional flux value, $\Phi^T = 1$, the charge density bound to dislocations matches the prediction of the effective action, but this relation becomes non-linear at higher values of Φ^T because of stronger lattice effects. As mentioned above for the bulk calculations, the open circles in Fig. 4.3e represent non-integral dislocation fluxes that are mathematically obtainable via our momentum-dependent Peierls factors, though

their physical interpretation as a lattice defect is not clear.

4.4 Momentum-Weighted Quadrupole Moment

As one final physical phenomenon associated to our system of a quadrupole of higher order Weyl nodes, let us consider what is happening at the hinges. Because some regions of momentum-space harbor higher order topology in our model, we expect to find hinge modes and/or fractional charge per unit length along the hinge. Indeed, the hinge phenomena in our system are associated with the momentum planes that harbor a 2D QI. At half-filling, the sign of the electric quadrupole moment of these planes is ambiguous when the symmetries protecting the topology are enforced, i.e., the value $q_{xy} = e/2$ is equivalent to $q_{xy} = -e/2$. In the case of the QI phases of $H(\mathbf{k}; k_x)$ and $H(\mathbf{k}; k_y)$, the relevant quantizing symmetries are the pair of mirror times time-reversal symmetries. To choose the sign of the quadrupole moment we want to weakly break both of these symmetries, but preserve the product, i.e., preserve C_2 symmetry so that no electric dipole moment is allowed. Operationally, for a system with open boundaries, the symmetry breaking provides a prescription of how to fill the low-energy hinge states that is consistent with the sign of the quadrupole moment. Interestingly, our model has two distinct possible choices of symmetry breaking that we discuss below.

One possible choice of symmetry breaking is the perturbations $H'(\mathbf{k}) = \delta \sin\big(k_{x/y}\big)\Gamma_0$, which accomplish the required symmetry breaking for $H(\mathbf{k}; k_{x/y})$ respectively. Since Γ_0 is odd under time-reversal, this term is time-reversal invariant, but it breaks both mirror symmetries since $\sin\big(k_{x/y}\big)$ is odd under mirror $M_{x/y}$. As a consequence, this perturbation endows the positive- and negative-momentum intervals of the QI phases with the same sign of quadrupole moment. Hence the positive and negative momentum intervals add together to yield a finite bulk electric quadrupole moment (per xz cross sectional area),

$$\begin{aligned} Q_{xz}^{\text{bulk}} &= L_y \int \frac{dk_y}{2\pi} q_{xz}(k_y) \\ &= \pm \frac{eL_y}{2\pi} \left(k_{\text{Dirac}} - k_{\text{Weyl}}\right), \end{aligned} \tag{4.17}$$

where the sign is determined by the sign of δ. The analogous quantity in the yz plane is defined as

$$\begin{aligned} Q_{yz}^{\text{bulk}} &= L_x \int \frac{dk_x}{2\pi} q_{yz}(k_x) \\ &= \mp \frac{eL_x}{2\pi} \left(k_{\text{Dirac}} - k_{\text{Weyl}}\right). \end{aligned} \tag{4.18}$$

The magnitude of the bulk electric quadrupole is determined solely by the separation between the projections onto the hinge BZ of the bulk Weyl nodes and surface Dirac nodes, k_{Weyl} and k_{Dirac}, as these control the

portion of the BZ that is occupied by the QI phase.

Next we consider a second possible symmetry breaking perturbation $H''(\mathbf{k}) = \delta\Gamma_0$. This term preserves the mirror symmetries but breaks time-reversal symmetry. It has the effect of endowing the positive- and negative-momentum intervals of QI phases with *opposite* quadrupole moments. The resulting bulk electric quadrupole moment vanishes, since it receives equal and opposite contributions from each momentum interval. Instead the system realizes quadrupole moments of *crystal momentum* density that have not previously been considered,

$$\begin{aligned} K^y_{xz} &= \frac{L_y}{e}\int \frac{dk_y}{2\pi} k_y q_{xz}(k_y), \\ K^x_{yz} &= \frac{L_x}{e}\int \frac{dk_x}{2\pi} k_x q_{yz}(k_x). \end{aligned} \tag{4.19}$$

The bulk crystal momentum quadrupole moment density manifests as momentum density bound to hinges, as shown in Fig. 4.4, where the momentum points along the hinges. Similar to the bulk electric quadrupole moment, the magnitude of the bulk crystal-momentum quadrupole moment is determined by the locations of the bulk Weyl and surface Dirac nodes,

$$K^y_{xz} = \pm\frac{L_y}{4\pi}\left(k^2_{\text{Dirac}} - k^2_{\text{Weyl}}\right), \tag{4.20}$$

where the overall sign is again determined by the sign of δ. It is interesting to note that this quantity can be concisely expressed in terms of the Weyl quadrupole moment $\bar{Q}$ and the surface Dirac dipole moment $\mathcal{P}_x$,

$$K^y_{xz} = \pm\frac{L_y}{\pi}\left(\mathcal{P}^2_y - 2\bar{Q}\right), \tag{4.21}$$

and therefore acts as a link between the bulk and surface translation-electromagnetic responses. This is analogous to the response of higher order Weyl dipole systems, in which the extent of the Fermi arcs on the surface and the arcs on the hinge must satisfy a sum rule [137].

We note that the bulk quadrupole moment of crystal momentum density is well-defined only when the bulk electric quadrupole moment vanishes, as its value can otherwise be arbitrarily changed by shifts of the BZ origin $\mathbf{k} \to \mathbf{k} + \mathbf{k}'$. This is exactly what happens when we choose the H'' perturbation since the total bulk quadrupole moment vanishes. The invariance of the bulk quadrupole moment of crystal momentum under shifts of the BZ can also be seen from the definition in Eq. (4.21). The Weyl quadrupole moments Q_{xx} and Q_{yy} are invariant under such shifts because the C_{2z} symmetry of the Hamiltonian forces the Weyl dipole moments in the k_x-k_y plane to vanish, and the surface Dirac dipole moments $\mathcal{P}_{x/y}$ are invariant because the product of the $M_{1,\pm1}$ and C_4M_z symmetries form a surface M_z symmetry that forces the surface Chern number to vanish.

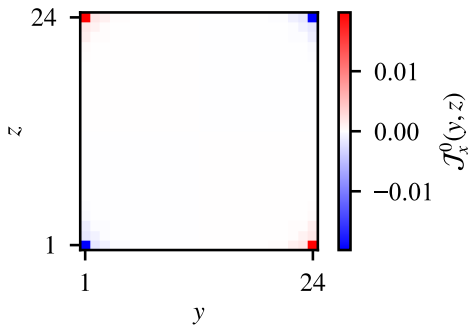

Figure 4.4: The position-resolved momentum density of $H(\mathbf{k}) + H''(\mathbf{k})$ with open boundary conditions along the y- and z- directions, $m = -0.3$, $\beta = -0.7$, $\gamma = 0.5$, and $\delta = 10^{-4}$.

4.5 Discussion

In this work we made the first steps towards understanding the interplay between higher order topology and translation-electromagnetic responses. By constructing and analyzing an explicit model, we showed that elevating a quadrupole arrangement of Weyl nodes, which is known to exhibit a bulk translation-electromagnetic response, to higher order Weyl nodes produces an additional translation-electromagnetic *surface* response. We further demonstrated that the surface response originates from the higher order QI phases of the Hamiltonian in the foliated BZ. We additionally found that adding symmetry breaking perturbations can produce bulk quadrupole moments of either electric charge or crystal momentum, depending on the particular perturbation chosen.

These results motivate a number of different directions for future research. Of primary importance is identifying promising material platforms in which these translation-electromagnetic responses can be observed. The response we predict in this work requires the system to possess both a bulk Weyl quadrupole moment and a surface Dirac dipole moment. As for the crystal symmetry ingredients, for the Weyl quadrupole moment to be well defined, the Weyl dipole moments in the plane of the quadrupole must vanish, which can be guaranteed by mirror symmetry or a set of C_2 symmetries (time reversal symmetry would also suffice, although that would prevent observation of the momentum quadrupole). The surface Dirac dipole moment similarly requires the surface Chern number to be zero, which can be enforced by the presence of a surface mirror symmetry or a time reversal symmetry (as long as the bulk is not a 3D topological insulator). These symmetries, along with the possible breaking of TRS either by magnetic ordering or an applied magnetic field, are necessary to observe the translation-electromagnetic response. Combining these symmetry requirements with the tools provided by topological quantum chemistry may provide a route to identifying materials that host this translation-electromagnetic response [48], [53].

There are a number of systems that are likely to host similar types of mixed responses and warrant further study. Higher order analogs of two-dimensional Dirac quadrupole semimetals and three-dimensional nodal line semimetals [156] are particularly promising, as are higher order nodal superconductors [143]–[146] and higher order non-Hermitian TSMs [147]–[150]. Furthermore, there are promising metamaterial platforms in which one could generate our model. Both Weyl points [167] and higher order quadrupole topology [168]–[170] have each been demonstrated separately in experiment, so combining the two is plausibly achievable. In these systems it may even be possible to extract information about the crystal momentum, as was recently accomplished in a topoelectric circuit experiment studying higher rank surface states [113].

Interestingly, our model also presents a platform in which to study quantum oscillations, as the combination of surface Fermi arcs and zero-energy hinge arcs may provide unusual circuits for electrons to traverse [171]. The properties of these systems in strong magnetic fields may also be a fruitful line of pursuit as the zeroth Landau level of the bulk Weyl nodes must coordinate with the zeroth Landau level of the surface Dirac fermions. We leave these studies to future work.

Chapter 5

Axionic rotation-electromagnetic response in charge-ordered Dirac semimetals

This chapter is adapted from Julian May-Mann, Mark R. Hirsbrunner, Lei Gioia, and Taylor Hughes, arXiv preprint arXiv:2403.00055.

5.1 Introduction

In this chapter we turn our attention to systems that are sensitive to defects of rotation symmetry. This works builds upon significant recent progress in understanding topological phases protected by rotation symmetry, including classification of two-dimensional topological crystalline insulators, unquantized quasi-topological response theories of three-dimensional type-I Dirac semimetals, and rotation-electromagnetic responses of three-dimensional topological crystalline insulators [61]–[63], [83], [84]. Specifically, we study the rotation-electromagnetic responses that can arise in insulators resulting from the gapping out of three-dimensional Dirac semimetals (DSMs) by charge density wave (CDW)order. The mixed rotation-electromagnetic response theory we discover is analogous to the purely electromagnetic response theory hosted by three-dimensional inversion-symmetry Weyl semimetals (WSMs) that are gapped out by CDW order [25], [73], [172]–[174]. These systems exhibit axion electrodynamics that is described by a 3D Θ term, the coefficient of which is quantized to 0 or π when the combined WSM and CDW system has inversion symmetry [26], [27], [44], [175]–[177]. In addition to axion electrodynamics, the inversion-symmetric Weyl-CDW insulator also exhibits

a quantized 3D anomalous Hall response [32], [38], [178]. Importantly, the $\Theta = 0$ and $\Theta = \pi$ Weyl-CDW insulators can be distinguished when inversion-symmetric open boundaries are present by their total Hall conductances, which differ by e^2/h [174].

DSMs can similarly be gapped out via a CDW to produce a Dirac-CDW insulator [179]. The resulting insulator can be understood by treating the DSM as two copies of a WSM related by time-reversal symmetry [180], [181]. This intuition reveals that the Dirac-CDW insulator cannot display a quantized 3D Hall response, as the 3D Hall response is odd under time-reversal symmetry. This intuition further shows that the Dirac-CDW insulator also has trivial axion electrodynamics (i.e., a vanishing 3D Θ term) since Θ is defined $\mod (2\pi)$. Despite the absence of these effects, there is more to the story of the Dirac-CDW insulator topological responses. In this work, we consider the crystalline-electromagnetic (CEM) responses of Dirac-CDW insulators, specifically those that describe how charge fluctuations are induced by rotation symmetry defects (i.e. disclinations) [62], [63], [68], [182]–[185].

Dirac-CDW insulators possess a natural sensitivity to disclination defects, which are line-like fluxes of rotation symmetry, because they are protected by rotation symmetry. However, the exact nature of the CEM response to disclinations depends on: (i) if the CDW is in/commensurate with the lattice and (ii) if the Dirac-CDW insulator has inversion symmetry. When the CDW is commensurate with the lattice, the Dirac-CDW insulator has residual discrete translation symmetry determined by the CDW period. We show that disclination loops in the 3D Dirac-CDW insulator bind a quantized charge per length in this case. The charge per length is determined by a combination of the Frank angle of the disclination and the length of the CDW period. This response can be considered as a CEM analog of the 3D Hall effect, as the former describes how charge per length is bound to disclination lines, while the latter describes how charge per length is bound to magnetic flux lines. In fact, the disclination response is essentially a layered version of the 2D discrete Wen-Zee response that describes how charge is bound to point-like disclinations of 2D lattices [59]–[62], [64], [84], [185]–[189]. Hence, we refer to this response of the 3D Dirac-CDW insulator as the 3D discrete Wen-Zee (dWZ) response. Furthermore, we show that the 3D dWZ response is captured in the effective response theory by a layered version of the 2D Wen-Zee term.

Just like the case for Weyl-CDW insulators, we find that there are two distinct classes of Dirac-CDW insulators when inversion symmetry is preserved. The difference between the two classes of insulators manifests as a difference in the parity of charge bound to disclination lines that terminate on the open boundaries of a system. In analogy to axion electrodynamics, we find that the effective response theories for the two classes of Dirac-CDW insulators differ by a quantized total derivative term. This term, called the $R \wedge F$ term, was previously discussed in Ref. [83]. Similar to the 3D Θ term that describes axion electrodynamics, the $R \wedge F$ term is a total derivative term that leads to anomalous boundary physics that

we discuss in detail below.

We show that it is generically possible to define a "disclination filling anomaly" when the CDW is commensurate and preserves the inversion symmetry of the DSM [161], [162]. A disclination filling anomaly occurs when it is impossible to change from periodic to (gapped) open boundary conditions while preserving both inversion symmetry and conserving charge on the disclination line. Alternatively put, we show that when the disclination filling anomaly is present, disclination lines of an inversion-symmetric insulator must bind different amounts of charge for open and periodic boundary conditions. This difference in charge is quantized and cannot be removed by inversion-preserving boundary effects. This serves to further classify crystalline insulators by considering filling anomalies in the presence of topological defects such as a disclination.

The rest of this paper is organized as follows: in Section 5.2 we provide an overview of Dirac semimetals, including lattice models, protecting crystalline symmetries, and their unquantized quasi-topological responses. In Section 5.4 we describe how adding a CDW to the DSM model can give rise to correlated topological crystalline insulators. In Section 5.3 we discuss relevant topological response terms, such as the discrete Wen-Zee and $R \wedge F$ terms. Equipped with this knowledge, in Section 5.5 we analytically and numerically demonstrate the topological crystalline-electromagnetic responses of Dirac-CDW insulators. Finally, in Section 5.6 we conclude with a discussion and outlook, and include technical details in the appendices.

5.2 Dirac semimetals: lattice model, topology, and responses

In this section we review the relevant properties of DSMs, paying particular attention to the symmetries that protect DSMs. We also discuss the anomalous responses of the gapless DSM in the presence of probe gauge fields. We demonstrate that these anomalous responses physically manifest as charge bound to disclination defects of the lattice.

Lattice model

In this subsection we briefly review the band theory of DSMs. DSMs are classified into two groups: type-I DSMs whose low-energy gapless features are protected by separate symmorphic and translation symmetries; and type-II DSMs wherein the Dirac nodes arise from non-symmorphic symmetry-enforcement of band crossings with four-dimensional irreducible representations at high-symmetry points at the Brillouin zone edge [123], [180], [181], [190]. We consider only symmorphic DSMs, utilizing a minimal model hosting a pair of Dirac nodes that are protected by time-reversal, inversion, rotation, and translation symmetry. Such DSMs are known to possess unquantized anomalous responses that we review in another section below [36], [63].

Our starting point for the symmorphic DSM is the following Bloch Hamiltonian of spin-1/2 fermions on an orthorhombic lattice [181],

$$\begin{aligned}\mathcal{H}_{\mathrm{DSM}}(\boldsymbol{k}) &= \sin(k_x a_x)\Gamma_1 + \sin(k_y a_y)\Gamma_2 \\ &+ [\cos(k_z a_z) - \cos(\mathcal{K} a_z)]\Gamma_3 \\ &- b_{xy}[2 - \cos(k_x a_x) - \cos(k_y a_y)]\Gamma_3,\end{aligned} \tag{5.1}$$

where $a_{x,y,z}$ are the lattice constants in the x, y, and z directions, respectively. The Γ_a matrices are defined as

$$\Gamma_1 = \sigma^x s^z, \quad \Gamma_2 = -\sigma^y, \quad \Gamma_3 = \sigma^z, \Gamma_4 = \sigma^x s^x, \quad \Gamma_5 = \sigma^x s^y, \tag{5.2}$$

where $\boldsymbol{\sigma}$ and $\boldsymbol{s}$ are Pauli matrices acting on the sublattice and spin degrees of freedom, respectively (this identification is not important for our discussion). Here and throughout this chapter we leave any 2×2 identity matrices implicit, (i.e., $\Gamma_2 = -\sigma^y s^0$, and $\Gamma_3 = \sigma^z s^0$, where s^0 is the 2×2 identity in spin space).

The (doubly-degenerate) energy bands of this model are given by

$$E_{\pm}(\boldsymbol{k}) = \pm \left[\sin^2(k_x a_x) + \sin^2(k_y a_y) + (\cos(k_z a_z) - \cos(\mathcal{K} a_z) - b_{xy}[2 - \cos(k_x a_x) - \cos(k_y a_y)])^2\right]^{1/2}. \tag{5.3}$$

From this equation we see that the parameter $\mathcal{K}$ determines the location of the Dirac nodes at which the bands become four-fold degenerate: $\boldsymbol{k}_{\mathrm{DN}} \equiv (0, 0, \mathcal{K})$, $E_{\pm}(\boldsymbol{k}_{\mathrm{DN}}) = E_{\pm}(-\boldsymbol{k}_{\mathrm{DN}}) = 0$. Intuitively, $\mathcal{K}$ can be varied to parameterize a process wherein two pairs of doubly-degenerate bands are inverted. At $\mathcal{K} = 0$ the bands are not inverted and have a quadratic band touching at $\boldsymbol{k} = 0$. At $\mathcal{K} = \pi$ the bands are fully inverted and have a quadratic band touching at $\boldsymbol{k} = (0, 0, \pi)$. For other values of $\mathcal{K}$, the two pairs of bands are partially inverted and have linear crossings at $\boldsymbol{k} = (0, 0, \pm\mathcal{K})$. The parameter b_{xy} determines the gap away from the high symmetry line $k_x = k_y = 0$. As expected, the continuum Hamiltonian near the four-fold degenerate nodal points takes on the Dirac-form

$$\mathcal{H}_{\mathrm{DSM}}(\pm\boldsymbol{k}_{\mathrm{DN}} + \boldsymbol{q}) \approx q_x a_x \Gamma_1 + q_y a_y \Gamma_2 \pm q_z a_z \sin(\mathcal{K} a_x)\Gamma_3. \tag{5.4}$$

Here and throughout we take the system to be half-filled, i.e., two electrons per unit cell, such that the chemical potential intersects the Dirac points.

Symmetries

For generic values of $\mathcal{K}$, the Hamiltonian in Eq. 5.1 consists of two doubly degenerate bands that meet at a pair of four-fold degenerate Dirac nodes. The four-fold degeneracies are stabilized by the combination of: four-fold rotation symmetry around the z-axis, C_{4z}; translation symmetry in the z-direction, T^z; charge conservation symmetry, U(1); time-reversal symmetry, $\mathcal{T}$; and inversion symmetry, $\mathcal{I}$.

The gaplessness of the Dirac nodes is protected by the combination of C_{4z} rotation symmetry, T^z translation symmetry, and U(1) charge conservation symmetry. The C_{4z} operator is given by

$$U_4 = \exp\left(i\frac{\pi}{2}[\tfrac{1}{2}\sigma^z s^z - s^z]\right), \tag{5.5}$$

where $(U_4)^4 = -1$, since we have spin-1/2 fermions. This symmetry prohibits mass terms $\propto \Gamma_4$ and $\propto \Gamma_5$. The T^z translation symmetry prevents the Dirac node at $+\boldsymbol{k}_{\mathrm{DN}}$ from hybridizing with the Dirac node at $-\boldsymbol{k}_{\mathrm{DN}}$. The U(1) charge symmetry precludes the appearance of superconducting pairing terms.

The two-fold degeneracy of the bands of Eq. 5.1 away from the Dirac nodes is ensured by the combination of time-reversal and inversion symmetry: time-reversal symmetry guarantees that a state with momentum $\boldsymbol{k}$ is accompanied by a degenerate state at $-\boldsymbol{k}$ with opposite spin ($\boldsymbol{\sigma}$) projection. Similarly, inversion symmetry guarantees that a state with momentum $\boldsymbol{k}$ is always accompanied by a degenerate state at $-\boldsymbol{k}$ with the *same* spin ($\boldsymbol{s}$) projection. The combination of time-reversal and inversion symmetries therefore guarantees that all states are at least two-fold degenerate. Furthermore, time-reversal and inversion symmetry also protect the four-fold degeneracy of the Dirac nodes at $\boldsymbol{k} = \pm\boldsymbol{k}_{\mathrm{DN}}$, and prevent the DSM phase from being deformed into a Weyl semimetal phase. For example, adding a time-reversal breaking term, such as a magnetic Zeeman term $\propto s^z$, will split a Dirac nodes into one positive-chirality and one negative-chirality Weyl node. If inversion symmetry is preserved, then this splitting of Dirac nodes must occur in pairs, and if there is a positive chirality Weyl node at $\boldsymbol{k}$, there will be a negative chirality Weyl node at $-\boldsymbol{k}$. This may be understood via the requirement that the Berry curvature satisfies $\boldsymbol{\Omega}(\boldsymbol{k}) = -\boldsymbol{\Omega}(-\boldsymbol{k})$ because of inversion symmetry. This Dirac node splitting procedure results in a magnetic Weyl semimetal that possesses an anomalous Hall conductivity. Alternatively, if inversion symmetry is broken and time-reversal symmetry is preserved, we may arrive at a time-reversal invariant Weyl semimetal, where a positive chirality Weyl node at $\boldsymbol{k}$, is accompanied by a second positive chirality Weyl node at $-\boldsymbol{k}$. This naturally arises as a consequence of time-reversal symmetry which implies $\boldsymbol{\Omega}(\boldsymbol{k}) = \boldsymbol{\Omega}(-\boldsymbol{k})$. Analogous to the magnetic WSM case, such a material is known to possess an unquantized momentum anomaly response that describes non-trivial charge responses to dislocations, as discussed in previous chapters [63], [77], [156], [191] .

The time-reversal operator is given by $\mathcal{T} = -is^y\kappa$, where κ is the complex conjugation operator ($\mathcal{T}^2 = -1$

for spin-1/2 fermions). For the lattice model in Eq. 5.1 there are multiple inequivalent choices of inversion symmetry, which correspond to different choices of inversion center. The different inversion centers are related by translations of half of a lattice vector. Since we consider breaking translation symmetry in the z-direction, we pay special attention to the two inversion centers that differ by a half-translation in the z-direction:

$$\mathcal{I}_s = \sigma^z, \mathcal{I}_b = e^{ik_z a_z}\sigma^z. \tag{5.6}$$

We call $\mathcal{I}_s$ "site-centered" inversion symmetry since it sends $\boldsymbol{r} = (r_x, r_y, r_z) \to (-r_x, -r_y, -r_z)$ and leaves the site $(0,0,0)$ invariant. Similarly, we call $\mathcal{I}_b$ "bond-centered" inversion symmetry since it sends $(r_x, r_y, r_z) \to (-r_x, -r_y, -r_z + a_z)$ and leaves the bond $(0,0,a_z/2)$ invariant. There are other choices of inversion symmetry that differ by half a translation in either the x or y-directions from those above. However, these other inversion symmetry definitions are unimportant for our analysis.

The distinction between the site- and bond-centered inversion symmetries has important implications when considering systems with open boundary conditions. Namely, for a system of length $L_z = a_z N_z$ in the z-direction (i.e., N_z lattice sites along the z-direction) and open boundary conditions, site-centered inversion symmetry necessitates that N_z is odd, while bond-centered inversion symmetry necessitates that N_z is even. We discuss the interplay between inversion symmetry and CDWs in Sec. 5.4 below.

Anomalous topological response

As shown in Ref. [63], the DSM in Eq. 5.1 possesses an anomalous topological response to fluxes of C_{4z} rotation symmetry (disclination line defects). This response can be expressed in terms of probe (non-dynamic) gauge fields for the U(1) charge symmetry (A_μ) and C_{4z} rotation symmetry (ω_μ) as

$$\mathcal{L}_{\text{anom}} = \frac{\nu}{2\pi^2} G_z \epsilon^{ijk} \omega_i \partial_j A_k, \tag{5.7}$$

where i,j,k run over t,x,y, the "fillinf" is given by $\nu = 2\mathcal{K}/2\pi$, and $G_z = 2\pi/a_z$ is the reciprocal lattice vector along the z direction. The origin of such a term may be understood via the lowest Landau level (LLL) picture wherein a uniform magnetic flux is applied in the z-direction: such a system possesses two LLLs with different C_{4z} charges, giving rise to a filling-type anomaly that protects the bands from gapping out [63]. We also note that Eq. 5.7 is not manifestly gauge invariant for arbitrary values of ν, but gauge invariance is restored by the gapless degrees of freedom at the nodes of the DSM.

Fluxes of the rotation gauge field, ω, encode disclinations with a Frank-vector $\propto \hat{z}$. In 3D lattices, the disclinations are line-defects that extend parallel to their Frank-vector. We implicitly take all disclinations to

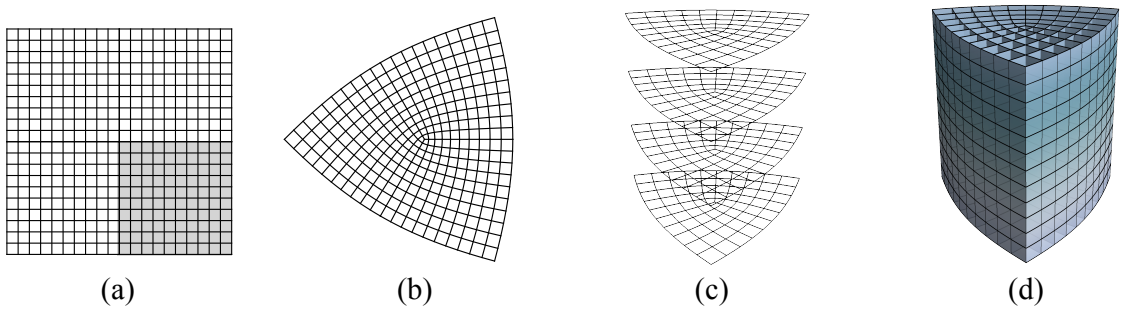

Figure 5.1: (a) A lattice with C_{4z} symmetry and no disclinations. Upon cutting out the greyed-out quadrant and re-gluing, we arrive at (b) a disclinated lattice. (c) A stack of disclinations of 2D layers forms a disclination line of a 3D crystal, as shown in (d).

stretch along the z-direction in this chapter. One can think of disclination lines as stacks of 2D disclinations in the xy-planes, as shown in Fig. 5.1. At the level of gauge field configurations, considering disclinations that stretch along only the z-direction amounts to the condition that $\oint_{C_{xz}} \omega = \oint_{C_{yz}} \omega = 0$, where the loop integrals are over curves C_{ab} in the ab-plane that do not intersect the cores of any disclinations.

While the (discrete) gauge field ω is formally characterized only by its holonomies, previous works [64], [83] have shown that it is possible to treat ω as a continuous gauge field with all fluxes quantized, i.e. $\oint \omega \in [0, \frac{\pi}{2}, \pi, \frac{3\pi}{2})$. This flux quantization can be thought of as arising from a Higgs mechanism, similar to the electromagnetic flux quantization in superconductors, where angular momentum is the analogy of electric charge. Here and throughout, we treat ω as smoothly varying, but with quantized fluxes.

The response theory in Eq. 5.7 implies that disclinations in a DSM bind a charge per length determined by ν. To demonstrate this, let us take a functional derivative of the action generated by Eq. 5.7 with respect to A_0. The contribution to the charge density from the DSM anomalous response is

$$\rho_{\text{anom}} = \frac{\nu}{2\pi^2} G_z [\partial_x \omega_y - \partial_y \omega_x]. \tag{5.8}$$

For a thin-core disclination parallel to the z-axis, $\partial_x \omega_y - \partial_y \omega_x = \Theta_F \delta(x)\delta(y)$, where $\Theta_F = 2\pi s/4$ is the Frank angle and $s \in \mathbb{Z}$. For a system of length $L_z = a_z N_z$ with $N_z \in \mathbb{Z}$, the disclination binds a total charge

$$Q_{\text{disc}} = \frac{\Theta_F}{\pi} \nu N_z + \delta Q. \tag{5.9}$$

Here we assume that the system is charge neutral in the absence of any disclinations, which amounts to adding negatively-charge background ions to each site of the lattice. In addition to the topological contribution $\propto \Theta_F$, we have included an additional contribution to the disclination charge, δQ. This contribution is $\mathcal{O}(1)$ and arises from the gapless particles that are necessary to restore the gauge invariance of the anomalous DSM

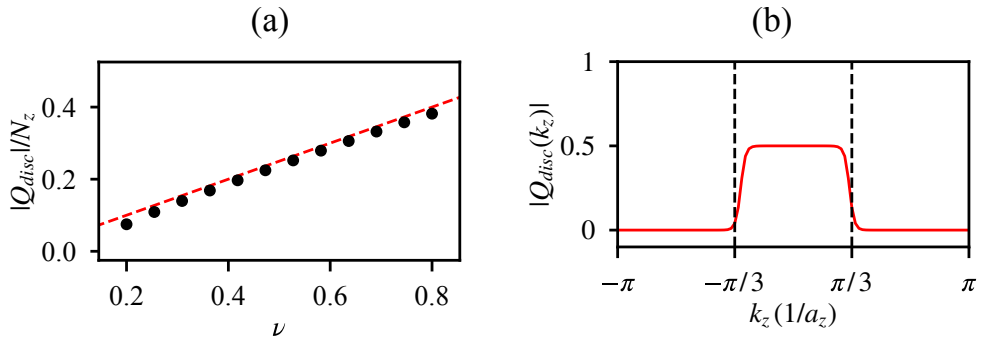

Figure 5.2: (a) The numerically computed charge per layer bound to a $\Theta_F = \pi/2$ disclination as a function of ν for the Hamiltonian Eq. 5.1 with $b_{xy} = 1$ (black circles). The dashed line for comparison has slope $\frac{1}{\pi}\Theta_F\nu$ and vanishing intercept, indicating the theoretical prediction. The disclinated lattice is constructed as in Ref. [83] for $N_x = N_y = 39$ lattice sites in the xy-plane, and 250 momentum points along the k_z axis. (b) The bound charge resolved in k_z (momentum parallel to the disclination line) for $\mathcal{K} = \pi/3$. The deviations from 0 and 1/2 near $k_z = \pm\frac{\pi}{3}\frac{1}{a_z}$ are the result of finite size effects and the small size of the gap near the Dirac nodes.

response [63]. In Fig. 5.2(a) we plot the disclination charge as a function of ν using the DSM tight-binding model in Eq. 5.1 and find that the disclination charge follows the predicted trend, $Q_{\text{disc}}/N_z \approx \frac{\Theta_F}{\pi}\nu$.

A useful way of understanding the disclination response of the DSM is to treat the momentum k_z of Eq. 5.1 as a tunable parameter, such that gapped planes with fixed k_z are trivial 2D insulators for $|k_z| > \mathcal{K}$ and quantum spin Hall (QSH) insulators for $|k_z| < \mathcal{K}$ [31], [192]. The Dirac nodes at $|k_z| = \mathcal{K}$ mark the band crossings that connect the topologically distinct two-dimensional insulators. In this way, the DSM with $\mathcal{K} \neq 0, \pi$ can be viewed as an intermediate phase between a trivial insulator ($\mathcal{K} = 0$), and a weak 3D topological insulator ($\mathcal{K} = \pi$) [36], [39]. As we discuss in Sec. 5.3, disclinations of the 2D QSH insulator bind charge Θ_F/π. For a system of length $L_z = a_z N_z$, the momentum k_z is discretized in steps of size $2\pi/N_z$. Each k_z slice binds charge Θ_F/π to a disclination if $|k_z| < \mathcal{K}$, and charge 0 if $|k_z| > \mathcal{K}$, as shown in Fig. 5.2(b). The disclination therefore binds a total charge

$$Q_{\text{disc}} = \sum_{k_z=-\kappa}^{\kappa} \frac{\Theta_F}{\pi} \approx \frac{\Theta_F}{\pi} 2\mathcal{K}\frac{N_z}{2\pi} = \frac{\Theta_F}{\pi}\nu N_z. \tag{5.10}$$

If we add in the extra $\mathcal{O}(1)$ contribution, δQ, that arises from the gapless modes at $k_z = \pm\mathcal{K}$, we arrive at Eq. 5.9.

5.3 Topological crystalline-electromagnetic responses of crystalline insulators

In preparation for our discussion of the topological crystalline-electromagnetic responses of the Dirac-CDW insulator in Sec. 5.5, we first discuss the crystalline-electromagnetic responses that are relevant for insulators with C_{4z} rotation as well as T_z discrete translation and/or inversion symmetries. These responses are similar to the anomalous response of the DSM discussed in Sec. 5.2. However, unlike the DSM responses, the topological responses of insulators are quantized because of gauge invariance and symmetry (DSMs can have unquantzed responses since the there are low energy gapless degrees of freedom that restore gauge invariance). We mainly consider insulators composed of spin-1/2 fermions with TRS, which is the relevant case for DSMs. Similar responses also exist for spinless fermions and systems without TRS, but the quantization of the responses is different [83], [185].

For spin-1/2 systems with TRS and C_{4z} rotation symmetry, we show here that crystalline-electromagnetic responses provde: a $\mathbb{Z}_4$ classification when the system possesses T^z discrete translation symmetry; a $\mathbb{Z}_2$ classification when the system has additional inversion symmetry; and a $\mathbb{Z}_4 \times \mathbb{Z}_2$ classification when the system has both T^z discrete translation and inversion symmetries. We also show that the $\mathbb{Z}_4$ index indicates that disclinations with Frank angle Θ_F bind a charge per length of $2n\frac{\Theta_F}{2\pi a_z}$ ($n \in \mathbb{Z}_4$) for a system with discrete translation $r_z \to r_z + a_z$ and periodic boundaries in the z-direction. The effective response theory for the insulator with a non-trivial $\mathbb{Z}_4$ index also contains a 3D discrete Wen-Zee (dWZ) term. The $\mathbb{Z}_2$ index corresponds to the charge parity of a disclination when inversion-symmetric open boundary conditions are present. Insulators with different $\mathbb{Z}_2$ indices have effective response theories that differ by a quantized total derivative term that was referred to as the $R \wedge F$ term in Ref. [83]. When the insulator has both T^z discrete translation and inversion symmetry, the $\mathbb{Z}_2$ index can be equivalently understood as the presence or absence of a filling anomaly [161], [162] of the 1D disclination lines, which we define more formally in Sec. 5.3.

We note that here we are discussing only the topological crystalline-electromagnetic responses of insulators in various symmetry classes. This is not an exhaustive list of all topological responses. Notably, we are ignoring any purely electromagnetic responses in the section.

The discrete Wen-Zee response

To begin, we consider the dWZ response in 2D and 3D. The dWZ response of a 2D system describes the binding of a quantized charge to disclinations [59]–[62], [64], [84], [185]–[189]. The 3D dWZ response is essentially a layered version of the 2D dWZ response and describes how disclination lines bind a quantized

charge per length.

The discrete Wen-Zee response in 2D

The 2D dWZ response corresponds to the following topological term in the effective field theory,

$$\mathcal{L}_{\text{2D-WZ}} = \frac{\mathcal{S}_{\text{2D}}}{2\pi}\epsilon^{ijk}\omega_i\partial_j A_k, \tag{5.11}$$

where i, j, k run over t, x, y. Here, fluxes of ω (which are point-like in 2D) are disclinations of the 2D lattice. For spin-1/2 fermions with TRS, $\mathcal{S}_{\text{2D}}$ is quantized to be an even integer [1] and defined mod (8) in the case of insulators with C_4 symmetry [2]. Therefore the allowed inequivalent values are $\mathcal{S}_{\text{2D}} = 0$, 2, 4, or 6 for insulators with time-reversal and C_4 symmetry.

A representative 2D insulator with $\mathcal{S}_{\text{2D}} = 2$ is realized by the following 4-band Hamiltonian,

$$\mathcal{H}_{\text{QSH}}(k_x, k_y) = \sin(k_x)\Gamma_1 + \sin(k_y)\Gamma_2 - [m - \cos(k_x) - \cos(k_y)]\Gamma_3, \tag{5.12}$$

with the C_4 rotation operator given by Eq. 5.5, and TRS given by $\mathcal{T} = -is^y\kappa$. This Hamiltonian is a QSH insulator for $0 < |m| < 2$ and a trivial insulator for $2 < |m|$ [31], [192]. The QSH insulator has a 2D dWZ response with $\mathcal{S}_{\text{2D}} = 2$, while the 2D dWZ response vanishes ($\mathcal{S}_{\text{2D}} = 0$) in the trivial phase[3] [64]. We note that Eq. 5.12 can be related to Eq. 5.1 by fixing $b_{xy} = 1$ and setting $M = 2 + \cos(k_z) - \cos(Q)$.

The 2D dWZ response indicates that a disclination with Frank angle Θ_F binds charge

$$Q_{\text{disc}} = \mathcal{S}_{\text{2D}}\frac{\Theta_F}{2\pi} \mod (2), \tag{5.13}$$

where we have added additional negative background charges such that the system is charge neutral in the absence of disclinations. The mod(2) ambiguity in defining Q_{disc} arises from the fact that it is possible to add a Kramers pair of particles to the disclination core without changing any topological properties for spin-1/2 insulators with TRS. Since Θ_F is a multiple of $\pi/2$, the disclination charge is always trivial if $\mathcal{S}_{\text{2D}} = 8$. This is why $\mathcal{S}_{\text{2D}}$ is defined mod(8) as noted before.

[1] For insulators composed of spinless fermions with TRS or spin-1/2 fermions without TRS, $\mathcal{S}_{\text{2D}}$ is quantized as an integer. For insulators composed of spinless fermions without TRS, $\mathcal{S}_{\text{2D}} = C/2 \mod (1)$ where C is the Chern number.

[2] For spin-1/2 fermions with TRS, $\mathcal{S}_{\text{2D}}$ is defined mod $(2n)$ in C_n symmetric insulators. For spinless fermions either with or without TRS, or spin-1/2 fermions without TRS, $\mathcal{S}_{\text{2D}}$ is defined mod (n) in C_n symmetric insulators

[3] In Ref. [61], a trivial insulator has a non-zero discrete shift. This difference arises because Ref. [61] considers the charge contribution from only the electrons. Here we are considering the contribution from the electrons, and the contribution from the background ions, which are effectively a trivial insulator composed of negative charges.

The discrete Wen-Zee response in 3D

For insulators with T^z discrete translation, $z \to z + a_z$, the 2D dWZ response can be extended to 3D as a layered response. The 3D layered response is expressed by the following topological term in the effective response theory,

$$\mathcal{L}_{\text{3D-WZ}} = \mathcal{S}_{\text{3D}} \frac{G_z}{4\pi^2} \epsilon^{ijk} \omega_i \partial_j A_k, \tag{5.14}$$

where $G_z = \frac{2\pi}{a_z}$ is the reciprocal lattice vector along the z-direction. Here, as in Sec. 5.2, flux-lines of ω are disclination lines with Frank-vector $\propto \hat{z}$. Again, we take all disclination lines to extend along the z-direction. This response is a layered version of the 2D dWZ response with 2D layer per lattice period, a_z. The coefficient $\mathcal{S}_{\text{3D}}$, which we call the 3D discrete shift, is defined $\mod (8)$ and quantized as an even integer for spin-1/2 fermions with TRS and C_{4z} rotation symmetry, i.e. $\mathcal{S}_{\text{3D}} = 0$, 2, 4, or 6. Because of the this, the value of $\mathcal{S}_{\text{3D}}$ defines a $\mathbb{Z}_4$ index for insulators in this symmetry class.

This quantization of $\mathcal{S}_{\text{3D}}$ is directly inherited from the quantization of $\mathcal{S}_{\text{2D}}$. The 3D dWZ term, Eq. 5.14, has the same form as the unquantized anomaly of the DSM, Eq. 5.7. However, the coefficient of the 3D dWZ term, $\mathcal{S}_{\text{3D}}$, is quantized, while the coefficient of the DSM anomaly equation, ν, is not (recall that ν is not quantized due to the gaplessness of the DSM).

The 3D dWZ response physically manifests as a quantized charge per length bound to disclination lines, as illustrated in Fig. 5.3a. If we take a system of length $L_z = a_z N_z$ that includes a disclination line with Frank angle Θ_F, Eq. 5.14 indicates that the total charge on the disclination line is

$$Q_{\text{disc}} = \frac{\Theta_F}{2\pi} \mathcal{S}_{\text{3D}} N_z \mod (2N_z). \tag{5.15}$$

Here we have again implicitly added negatively charged background ions such that the system is charge neutral without any disclinations. The $\mod (2N_z)$ ambiguity arises from the fact that it is possible to change the disclination charge by embedding a 1D insulator in the disclination core without changing any topological properties of the system. Due to the Kramers degeneracy and the Lieb-Schultz-Mattis theorem [193], the charge per unit length must be an even integer for translation invariant spin-1/2 1D insulators with TRS. From the $\mod (2N_z)$ ambiguity and the fact that the Frank angles of disclinations of a C_{4z} symmetric insulators are quantized in units of $\pi/2$, we also find that $\mathcal{S}_{\text{3D}} = 8$ leads to a trivial charge of the disclination, confirming our earlier assertion that $\mathcal{S}_{\text{3D}}$ is defined $\mod (8)$.

Without T^z discrete translation symmetry, the charge per length of a disclination line is not a well-defined quantity, as it is possible to add local charges to arbitrary points along the disclination. An important consequence of this is that the charge per length of a disclination is not a topological, quantized quantity for

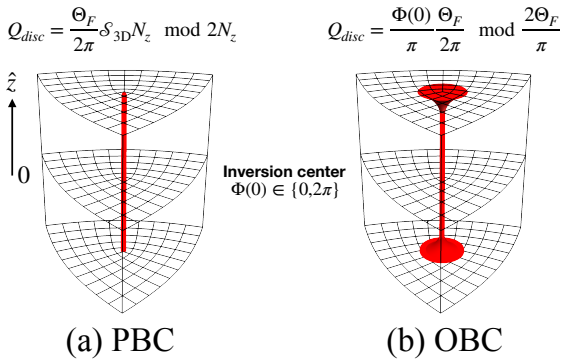

Figure 5.3: (a) The total charge per length, Q_{disc}/N_z, of an insulator with a disclination with Frank angle Θ_F is proportional to $\mathcal{S}_{3D}$, the coefficient of the dWZ term. (b) The disclination charge parity, Q_{disc} mod $(2\Theta_F/\pi)$, of a Θ_F-disclination of an inversion-symmetric insulator with open boundary conditions is determined by $\Phi(0) = \{0, 2\pi\}$, the value of the coefficient of the $R \wedge F$ term at the inversion center.

insulators with incommensurate CDWs, as it is possible to shift the charge per length of a disclination by an arbitrary amount. However, for systems that are finite in the z-direction, the *total* charge on a disclination line Q_{disc} is still a quantized multiple of Θ_F/π. This can be understood by treating the z-coordinate as an internal degree of freedom of an effectively 2D system with TRS and C_{4z} rotation symmetry. A disclination line of the finite 3D system is also a disclination of the effective 2D system, and the total charge bound to the disclination is therefore quantized according to the 2D dWZ response (Eq. 5.11).

The $R \wedge F$ Term

It was shown in Ref. [83] that the effective response theory of 3D crystalline insulators with rotation symmetry around a fixed axis can contain the topological term

$$\mathcal{L}_{R\wedge F} = \epsilon^{\mu\nu\lambda\eta}\frac{\Phi}{4\pi^2}\partial_\mu\omega_\nu\partial_\lambda A_\eta, \tag{5.16}$$

where μ, ν, λ, η run over t, x, y, z, and Φ is generally a function of position and time. We denote this response as the $R \wedge F$ term, since it couples the lattice curvature $R_{\mu\nu} = \partial_\mu\omega_\nu - \partial_\nu\omega_\mu$ to the electromagnetic field strength $F_{\mu\nu} = \partial_\mu A_\nu - \partial_\nu A_\mu$ [83]. The $R \wedge F$ term has a similar form to the Θ term, $F \wedge F$, that describes axion electrodynamics exhibited by 3D topological insulators [25], [26]. Like the Θ term, the $R \wedge F$ term has a periodic coefficient and is a total derivative when the coefficient is constant. For spin-1/2 insulators with TRS, Φ is 4π periodic. In general, the periodicity of Φ depends on the spin of the fermions and the presence of TRS, as discussed in Ref. [83].

The charge response associated with the $R \wedge F$ term is

$$j^\mu = \epsilon^{\mu\nu\lambda\eta} \frac{1}{4\pi^2} \partial_\nu \Phi \partial_\lambda \omega_\eta. \tag{5.17}$$

Fixing ω to the configuration of a disclination line, $\partial_x \omega_y - \partial_y \omega_x = \Theta_F \delta(x)\delta(y)$, the charge response simplifies to

$$\begin{aligned} \rho_{\text{disc}} &= \frac{\Theta_F}{4\pi^2} \partial_z \Phi \delta(x)\delta(y), \\ j^z_{\text{disc}} &= -\frac{\Theta_F}{4\pi^2} \partial_t \Phi \delta(x)\delta(y). \end{aligned} \tag{5.18}$$

The first lines indicates that spatial fluctuations of Φ along disclination lines bind charge. The second line indicates that temporal fluctuations along disclination lines drive a current. Together, these two responses indicate a charge polarization in the z-direction proportional to Θ_F localized on the disclination line.

Adiabatically increasing Φ homogeneously by an amount $\delta\Phi$ over some time T (i.e., $\Phi(t) = \Phi_0 + \delta\Phi \frac{t}{T}$) changes the polarization on the disclination line, P^z_{disc}, as

$$\Delta P^z_{\text{disc}} = \int_0^T dt \partial_t P^z_{\text{disc}} = \int_0^T dt j^z_{\text{disc}} = \frac{\delta\Phi}{2\pi} \frac{\Theta_F}{2\pi}. \tag{5.19}$$

We therefore find that if the effective response theories of two insulators *differ* by an $R \wedge F$ term with a constant coefficient $\delta\Phi$, the polarization of disclination lines will *differ* by $\frac{\delta\Phi}{2\pi} \frac{\Theta_F}{2\pi}$ between the two insulators. [4]

The $R \wedge F$ term with discrete translation symmetry

Here we turn our attention to the connection between the $R \wedge F$ term and the 3D dWZ response. We consider a system with T^z discrete translation, $z \to z + a_z$, and suppress any dependence on x and y here, since the disclination responses in Eq. 5.18 primarily involve the dependence of Φ on z and t. The coefficient of the $R \wedge F$ term can be non-constant for a system with T^z discrete translation symmetry, as $\Phi(z) = \Phi(z + a_z)$ mod (4π) has non-constant solutions. The solutions are characterized by their winding across a single unit-cell period $\int_0^{a_z} dz \partial_z \Phi(z)$, which is an integer multiple of 4π. Examples of different winding configurations are shown in Fig. 5.4.

With this in mind we can compute the total charge bound to a disclination for a periodic system of length

[4] Note that two systems can have a well-defined difference in polarization even if the systems do not have a well-defined polarization individually. For example, a system with a net charge does not have a well-defined polarization, as the polarization will depend on the choice of origin. However, the difference in polarization between two systems with the same net charge is independent of the choice of origin.

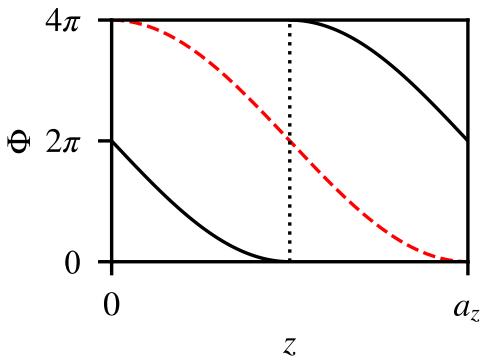

Figure 5.4: Two examples of how Φ can wind across the unit cell. Both lines wind by -4π across the unit cell, but one has $\Phi(0) = 0$ (red dashed) and the other has $\Phi(0) = 2\pi$ (black solid).

$L_z = a_z N_z$:

$$\begin{aligned} Q_{\text{disc}} &= \frac{\Theta_F}{2\pi} \int_0^{L_z} \partial_z \frac{\Phi(z)}{2\pi} dz \mod (2N_z) \\ &= \frac{\Theta_F}{2\pi} N_z \int_0^{a_z} \partial_z \frac{\Phi(z)}{2\pi} dz \mod (2N_z), \end{aligned} \tag{5.20}$$

where the $\mod (2N_z)$ ambiguity again arises from the fact that it is possible to change the disclination charge per length by embedding a 1D insulator in the disclination core. Comparing to Eq. 5.15, we find a relation for the dWZ response coefficient:

$$\mathcal{S}_{\text{3D}} = \frac{1}{2\pi} \int_0^{a_z} dz \partial_z \Phi(z), \tag{5.21}$$

from which we see that the winding of Φ over one period, a_z, generates a 3D dWZ response.

We can make the connection between the $R \wedge F$ and 3D dWZ terms more concrete by setting

$$\Phi(z) = \Phi_0 + \mathcal{S}_{\text{3D}} G_z z, \tag{5.22}$$

where Φ_0 is an arbitrary constant. This solution preserves T^z discrete translation symmetry when $G_z = 2\pi/a_z$. Plugging this value of $\Phi(z)$ into Eq. 5.16 leads to the 3D dWZ term in Eq. 5.14, after an integration by parts. Because of the $\mod (2N_z)$ ambiguity, the $R \wedge F$ term identifies a $\mathbb{Z}_4$ classification of insulators with T^z discrete translation symmetry, exactly as discussed in Sec. 5.3.

Although it is not manifest in Eq. 5.22, it is important to note that the coefficient of the $R \wedge F$ term, Φ, is a 4π-periodic variable. Importantly, when Φ has a winding there is no discontinuity between $z = 0$ and $z = L_z$, since $\mathcal{S}_{\text{3D}}$ is an even integer and $\mathcal{S}_{\text{3D}} G_z L_z = \mathcal{S}_{\text{3D}} 2\pi N_z = 0 \mod (4\pi)$. The expression for $\Phi(z)$

given in Eq. 5.22 is therefore smooth everywhere with $\partial_z \Phi(z) = \mathcal{S}_{3\mathrm{D}} G_z$. The same would be true if we replaced the linear interpolation in Eq. 5.22 with a more complicated function like those shown in Fig. 5.4.

$R \wedge F$ term with inversion symmetry

We can now consider the $R \wedge F$ term for a system with inversion symmetry. We again take Φ to be independent of the x and y coordinates but allow for Φ to depend on z. We show here that the $R \wedge F$ term resolves a $\mathbb{Z}_2$ distinction between inversion-symmetric insulators. Inversion symmetry requires that $\Phi(z) = -\Phi(-z)$ mod (4π), i.e., Φ must be an odd function of z. Here we take the inversion center to be in the $z = 0$ plane. It is also possible to have an inversion center at $z = a_z/2$, but the difference between the two inversion centers can be accounted for by a redefinition of the coordinate system. In continuum effective field theory, such a coordinate change is innocuous. However, such a change is not innocuous for lattice systems, as the discrete lattice sites lead to a unique choice of origin (modulo lattice translations). At $z = 0$, inversion symmetry requires that $\Phi(0) = -\Phi(0)$. Since Φ is 4π periodic, $\Phi(0) = 0$ or $\Phi(0) = 2\pi$ are both allowed values satisfying this condition. The choice of these values defines two classes (i.e., a $\mathbb{Z}_2$ classification) of inversion-symmetric insulators. Alternatively expressed, the response theories of insulators with different $\mathbb{Z}_2$ indices differ by a $R \wedge F$ term with $\Phi(0) = 2\pi$.

Importantly, the value of $\Phi(0)$ has a direct physical interpretation when switching from periodic boundaries to open boundaries in the z-direction. We show below that a disclination with open boundaries has charge $Q_{\mathrm{disc}} = 0 \mod (2\frac{\Theta_F}{\pi})$ when $\Phi(0) = 0$, and charge $\frac{\Theta_F}{\pi} \mod (2\frac{\Theta_F}{\pi})$ when $\Phi(0) = 2\pi$. We refer to the quantity $Q_{\mathrm{disc}} \mod (2\frac{\Theta_F}{\pi})$ as the *disclination charge parity*. The disclination charge parity is a natural quantity to consider for inversion-symmetric systems with open boundary conditions, as purely 2D boundary effects can change the disclination charge by at most an integer multiple of $2\frac{\Theta_F}{\pi}$, provided they respect inversion symmetry. The charge parity is therefore a physical observable that determines the $\mathbb{Z}_2$ classification.

To show why the value of $\Phi(0)$ determines the disclination charge parity, let us consider a system of length L_z with periodic boundaries in the z-direction and use local perturbations to "cut" the system and generate open boundaries at $z = \pm L_z/2$. We assume that the resulting open boundary system satisfies the following four conditions:

1. Changing from periodic to open boundary conditions preserves inversion symmetry around $z = 0$.
2. The system with open boundaries is gapped, such that $\Phi(z)$ can be defined over the entire system.
3. The value of Φ at the inversion center, $\Phi(0)$ remains constant when changing from periodic to open boundaries. This condition is satisfied if the gap at the inversion center remains open when switching

the boundary conditions.

4. At the boundaries of the system, Φ vanishes (i.e., $\Phi(z) = 0$ for $|z| \geq L_z/2$). This choice of boundary conditions is equivalent to requiring that the $R \wedge F$ term fully vanishes outside the boundaries of the system.

Consider adding a disclination to the system with open boundary conditions. Using Eq. 5.18, the total charge bound to the disclination is

$$\begin{aligned} Q_{\text{disc}} &= \frac{\Theta_F}{2\pi}\frac{1}{2\pi}\int_{-L_z/2}^{L_z/2}\partial_z\Phi(z)dz \\ &= \frac{\Phi(0)}{\pi}\frac{\Theta_F}{2\pi} + 2n\frac{\Theta_F}{\pi}, \end{aligned} \tag{5.23}$$

where $n \in \mathbb{Z}$ is the number of times Φ fully winds by 4π between 0 and $L_z/2$. Here we have used the facts that $\Phi(z) = -\Phi(-z)$ and $\Phi(L_z/2) = 0$. This equation reflects that Φ must wind by an integer multiple of 4π between 0 and $L_z/2$ if $\Phi(0) = \Phi(L_z/2) = 0$, while if Φ must instead wind by a half-integer integer multiple of 4π if $\Phi(0) = 2\pi$ and $\Phi(L_z/2) = 0$. This is illustrated in Fig. 5.3b, and two representative configurations of $\Phi(z)$ are shown in Fig. 5.5, where $n = 3$. We therefore find that

$$Q_{\text{disc}} = \frac{\Phi(0)}{\pi}\frac{\Theta_F}{2\pi} \mod (2\frac{\Theta_F}{\pi}). \tag{5.24}$$

The difference between the $\Phi(0) = 0$ and $\Phi(0) = 2\pi$ insulators is therefore manifest in the value of Q_{disc} mod $(2\frac{\Theta_F}{\pi})$ when open boundaries are present. Specifically $Q_{\text{disc}} = 0 \mod (2\frac{\Theta_F}{\pi})$ and $\frac{\Theta_F}{\pi} \mod (2\frac{\Theta_F}{\pi})$ for $\Phi(0) = 0$ and 2π, respectively. We also find that $Q_{\text{disc}} = 0 \mod (2\frac{\Theta_F}{\pi})$ for $\Phi(0) = 4\pi$, in agreement with Φ being 4π periodic.

The $R \wedge F$ term with discrete translation and inversion symmetry

If an insulator has both inversion symmetry and T^z discrete translation symmetry ($z \to z + a_z$), then the values of $\Phi(0)$ and $\mathcal{S}_{3\text{D}}$ from Eq. 5.21 lead to a $\mathbb{Z}_4 \times \mathbb{Z}_2$ classification based on the phenomena associated to the $R \wedge F$ term. We stress that this classification is not exhaustive, but it is sufficient to characterize the Dirac-CDW insulators we discuss in the following sections.

If two insulators have the same 3D dWZ response (i.e., the same value of $\mathcal{S}_{3\text{D}}$ in Eq. 5.21), but different values of $\Phi(0)$, the polarization of disclination lines *differ* by $\frac{\delta\Phi(0)}{2\pi}\frac{\Theta_F}{2\pi}$, where the difference between the value of $\Phi(0)$ between the two insulators, $\delta\Phi(0)$, is equal to either 0 or 2π based on our previous discussions.

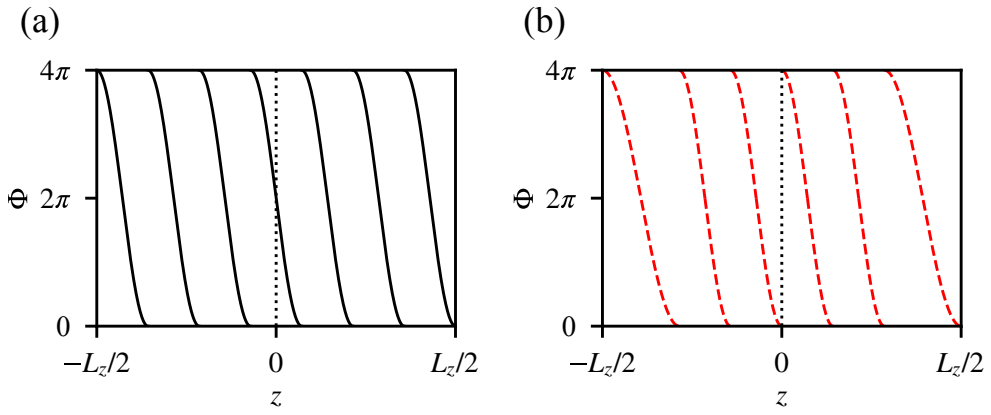

Figure 5.5: The disclination charge parity of inversion-symmetric insulators is determined by the value of $\Phi(z)$ at the inversion center (the $z = 0$ plane here). Figures (a) and (b) show two windings of $\Phi(z)$ with $n = 3$ but different values of $\Phi(0)$. Figure (a) has $\Phi(0) = 2\pi$ and thus winds a total of seven times, producing an odd disclination charge parity. Figure (b) has $\Phi(0) = 0$ and therefore winds only six times, yielding an even disclination charge parity.

To show why different values of $\Phi(0)$ lead to a difference in polarization, we take a given $\Phi(z)$ that is invariant under T^z discrete translation and inversion symmetry, and define an adiabatic evolution where $\Phi(z)$ increases by 2π over a time T, $\Phi(z) \to \Phi(z) + 2\pi t/T$. Inversion symmetry is broken for $0 < t < T$ but is restored at $t = T$. During this process, $\Phi(0)$ changes by 2π, and $\int_0^{a_z} dz \partial_z \Phi(z)$ remains constant (i.e., $\mathcal{S}_{3D}$ remains constant). Based on Eq. 5.18, and 5.19 the polarization of a disclination line changes by $\frac{\Theta_F}{2\pi}$ during this process. Recall that disclinations of insulators with a non-zero $\mathcal{S}_{3D}$ have a finite charge per length. Therefore, the polarization of a disclination is not strictly well-defined for insulators with finite $\mathcal{S}_{3D}$. However, the difference in the polarization of disclinations between insulators with the same $\mathcal{S}_{3D}$ is well-defined. This is analogous to discussions of polarization in Chern insulators [194], [195].

For insulators with $\mathcal{S}_{3D} = 2$, the two classes of inversion-symmetric insulators are related to each other by a half-translation $z \to z + a_z/2$. For $\mathcal{S}_{3D} = 2$, this is clear if we set $\Phi(z) = 2G_z z$, for which $\Phi(0) = 0$. Translating the system by $a_z/2$ shifts $\Phi(z) \to 2\pi + 2G_z z$, for which $\Phi(0) = 2\pi$. This relationship can be naturally understood if we treat the 3D dWZ response as arising from a stacking of 2D systems with $\mathcal{S}_{2D} = 2$. In order to preserve inversion symmetry around $z = 0$, the 2D systems must be centered at either $z = na_z$ or $z = na_z + a_z/2$ with $n \in \mathbb{Z}$. A disclination line of such a system has charge Θ_F/π centered at $z = na_z$ or $z = na_z + a_z/2$, respectively. This is the same charge configurations that are realized by the two topologically distinct phases of the 1D inversion symmetric Su–Schrieffer–Heeger (SSH) model [22], [23], if we set the electron charge to be Θ_F/π instead of 1 in the SSH model.

We similarly have that the two insulators with $\mathcal{S}_{3D} = 6$ are related by a half-translation. This can be understood using that $\mathcal{S}_{3D} = 6 = -2 \mod (8)$, and hence the $\mathcal{S}_{3D} = 6$ dWZ response is captured by

$\Phi(z) = -2G_z z$. A half translation then shifts $\Phi(0) \to \Phi(0) - 2\pi = \Phi(0) + 2\pi \mod (4\pi)$. We can also invoke a similar stacking argument to the one used above, but instead stacking 2D systems with $\mathcal{S}_{\text{2D}} = -2$.

The two inversion symmetric insulators having $\mathcal{S}_{\text{3D}} = 4$ are related to each other by a quarter translation, $z \to z + a_z/4$. Here, we can imagine the 3D dWZ response as arising from having *two* 2D systems between $z = na_z$ and $z = (n+1)a_z$, each with $\mathcal{S}_{\text{2D}} = 2$. To preserve inversion symmetry, these 2D systems must be stacked in one of two classes of configurations. In the first class of stacking configurations, one insulator is at $z = na_z + \delta_z$ and one is at $z = (n+1)a_z - \delta_z$ for each $n \in \mathbb{Z}$, where $\delta_z \in [0, a_z)$ is a constant offset. Since inversion symmetry is preserved for all δ_z here, stacking configurations having different values of δ_z are adiabatically connected. In the second class of stacking configurations, one insulator is at $z = na_z$ and one is at $z = na_z + a_z/2$. It can be directly confirmed that the second stacking configuration is distinct from the first stacking configuration for any value of δ_z. Furthermore, if we take the second stacking configuration and perform a quarter translation, we arrive at the first stacking configuration with $\delta_z = a_z/4$.

The value of $\Phi(0)$ determines the disclination charge parity for a system with open boundaries. However, as we discuss in Appendix B.1, the absolute disclination charge parity is not a practical quantity to consider since it can depend on the choice of inversion center. For insulators with T^z discrete translation symmetry, a more useful quantity to consider is the *difference* in the value of the disclination bound charge Q_{disc} mod $(2\frac{\Theta_F}{\pi})$ between a system with open boundaries and a system of the same size with periodic boundaries. For a system of size $L_z = a_z N_z$, the difference in charge is

$$Q_{\text{FA}} = \frac{\Theta_F}{2\pi}\left[\frac{\Phi(0)}{\pi} - \mathcal{S}_{\text{3D}} N_z\right] \mod (2\frac{\Theta_F}{\pi}). \tag{5.25}$$

Since $\mathcal{S}_{\text{3D}}$ is an even integer for spin-1/2 insulators with TRS, $Q_{\text{FA}} = 0$ or $\frac{\Theta_F}{\pi}$ are the distinct values. When Q_{FA} is non-zero, we will refer to the system as having a *disclination filling anomaly*. The usual filling anomaly reflects an inability to symmetrically deform from periodic to open boundary conditions while keeping the charge in the system constant [161], [162], [196], [197]. Here, the disclination filling anomaly reflects an inability to change from periodic to open boundary conditions while keeping both inversion symmetry and the charge on disclination lines constant.

In Appendix B.1 we argue that the disclination line filling anomaly necessarily vanishes for any layered insulator. Here we specifically define a layered insulator as an insulator where electrons from different unit cells in the z-direction are fully decoupled. Cutting a layered system to change from periodic to open boundary conditions is a trivial procedure under this definition. Hence, insulators that exhibit a disclination filling anomaly are not layered in this way.

In summary, the $R \wedge F$ term characterizes both the 3D dWZ response and the disclination filling anomaly

of rotation-symmetric insulators. The response phenomena lead to a $\mathbb{Z}_4 \times \mathbb{Z}_2$ classification for insulators with T^z discrete translation symmetry and inversion symmetry. On the one hand, the $\mathbb{Z}_4$ index is determined by calculating the disclination charge per length for a system with periodic boundary conditions. On the other, the $\mathbb{Z}_2$ index is determined by calculating and comparing the total disinclination charge for a given system with periodic boundary conditions and with open boundary conditions.

For systems that do not have translation symmetry, the value of $\Phi(0)$ remains quantized, since its quantization requires only inversion symmetry. This means that there should be two distinct insulators characterized by $\Phi(0) = 0$ and $\Phi(0) = 2\pi$, respectively, for systems with only inversion symmetry. For open boundary conditions, the two classes of insulators will have different disclination charge parities. However, without translation symmetry, it is not possible to define the disclination filling anomaly. The disclination charge parity is therefore be significant when considering DSMs with an incommensurate CDW, which lack any form of translation symmetry.

5.4 Gapping a Dirac Semimetal with a Charge Density Wave

The gapless nodes of the DSM are protected by translation, rotation, and U(1) charge conservation symmetries. By spontaneously breaking one of these symmetries it is possible to drive the system into a gapped phase with charge density wave (CDW), nematic, or superconducting order, respectively. Here we consider the gapped insulating phase that is generated by breaking translation symmetry using CDW order (see Ref. [179] for a discussion of the instabilities of a DSM to CDW formation). We pay special attention to inversion symmetry and show that there are two distinct classes of inversion-symmetric Dirac-CDW insulators. The differences between these two classes of insulators is further discussed in Sec. 5.5.

To consider the effects of a CDW distortion on the low-energy degrees of freedom, we start with a DSM with two Dirac nodes at $\pm\mathbf{k}_{DN}$, and expand the fermion annihilation operators around the two Dirac points, as

$$c_{\mathbf{r}} \approx \sum_{\boldsymbol{q}} e^{i\mathbf{r}\cdot\boldsymbol{q}+ir_z\mathcal{K}} c_{\boldsymbol{q},R} + e^{i\mathbf{r}\cdot\boldsymbol{q}-ir_z\mathcal{K}} c_{\boldsymbol{q},L}, \tag{5.26}$$

and introduce a new set of Pauli matrices $\boldsymbol{\tau}$, where $\tau^z = +1$ (-1) for the fermions in the R (L) valley. In terms of the R and L fermions, the 8×8 low-energy Hamiltonian for the DSM is

$$\mathcal{H} = q_x a_x \Gamma_1 + q_y a_y \Gamma_2 + q_z a_z \sin(\mathcal{K} a_x)\Gamma_3 \tau^z. \tag{5.27}$$

The crystalline symmetries act on the low-energy Hamiltonian as follows: The C_{4z} rotation symmetry

acts as

$$R_4 = \exp\left(-i\frac{\pi}{4}[\sigma^z s^z - 2s^z]\right). \tag{5.28}$$

As discussed previously, there are two possible inversion symmetries, site-centered and bond-centered. The site-centered inversion symmetry acts on the low-energy Hamiltonian as

$$\mathcal{I}_s = \sigma^z \tau^x = \Gamma_3 \tau^x. \tag{5.29}$$

The bond-centered inversion symmetry can be similarly written as

$$\mathcal{I}_b = \mathcal{I}_s e^{iq_z a_z + i\mathcal{K} a_z \tau^z}. \tag{5.30}$$

This expression can be simplified by performing a unitary transformation, $U = \exp(-i\mathcal{K} a_z \tau^z)$, which leaves the Hamiltonian unaffected but reduces the bond-centered inversion symmetry to

$$\mathcal{I}_b = \mathcal{I}_s e^{iq_z a_z}. \tag{5.31}$$

This unitary transformation simplifies our later discussions, and so we implicitly assume such a unitary transformation has been performed when discussing continuum models with bond-centered inversion symmetry.

A CDW can be dynamically generated through interactions, as discussed in Ref. [179]. In the mean field limit, a CDW order corresponds to a translation symmetry breaking term. We consider two possible types of translation symmetry breaking terms here. First is an onsite term that is given in terms of the original lattice model by

$$\hat{H}_{\text{site}} = \sum_{\mathbf{r}} |\Delta_s| \cos(2\mathcal{K} r_z + \theta_s)[c^\dagger_{\mathbf{r}} \Gamma_3 c_{\mathbf{r}}], \tag{5.32}$$

where $|\Delta_s|$ and θ_s are the amplitude and phase of the onsite CDW, respectively. Second is a bond-order term in the z-direction that modulates the hopping terms as

$$\hat{H}_{\text{bond}} = \sum_{\mathbf{r}} |\Delta_b| \cos(2\mathcal{K} r_z + \theta_b)[c^\dagger_{\mathbf{r}} \Gamma_3 c_{\mathbf{r}+\mathbf{z}}] + \text{H.c.}, \tag{5.33}$$

where $|\Delta_b|$ and θ_b are the amplitude and phase of the bond-order CDW, respectively. Note that we explicitly choose terms that carry momentum equal to the separation of the Dirac nodes ($2\mathcal{K}$). This nesting condition allows the mean field term to couple the low-energy degrees of freedom at the two Dirac nodes. We also could have chosen different Γ-matrix structure in Eqs. 5.32,5.33, but our choice of Γ_3 ensures that these

terms can open a mass gap in the continuum Hamiltonian.

Returning to the low-energy theory, Eq. 5.27, the CDW mean field terms in Eq. 5.32 and 5.33 induce the following terms in the continuum Hamiltonian

$$\mathcal{H}_{\text{mass}} = M(\boldsymbol{q})\Gamma_3\tau^x + M'(\boldsymbol{q})\Gamma_3\tau^y. \tag{5.34}$$

The two mass terms are off-diagonal in τ and, hence, couple the two Dirac nodes. The spectrum of the continuum Hamiltonian with the M and M' terms is 4-fold degenerate with energy eigenvalues

$$E_{\pm}(\boldsymbol{q}) = \pm\Big[(q_x a_x)^2 + (q_y a_y)^2 + (q_z a_z \sin(\mathcal{K}a_z))^2 + M(\boldsymbol{q})^2 + M'(\boldsymbol{q})^2\Big]^{1/2}. \tag{5.35}$$

We are interested in the situation where the CDW is weak and tangibly affects only the low-energy modes along the $k_x = k_y = 0$ high-symmetry line. In terms of the original lattice model, this leads to the requirement that $|\Delta_{s/b}| \ll b_{xy}$ (recall that b_{xy} determines the gap away from $k_x = k_y = 0$).

Now let us consider the effects of inversion symmetry. By comparing Eq. 5.31 and 5.29 to Eq. 5.34, we find that M and M' must be an even and odd functions of $\boldsymbol{q}$ in presence of inversion, respectively. Therefore $M'(\boldsymbol{q})$ must vanish at the Dirac point, $\boldsymbol{q} = 0$ in inversion-symmetric systems. This leads to two distinct inversion-symmetric insulators, one with and $M'(0) = 0$ and $M(0) > 0$, and one with $M'(0) = 0$ and $M(0) < 0$. We now wish to relate the values of the M and M' to the microscopic mean-field CDW parameters, $|\Delta_s|$, $|\Delta_b|$, θ_s and θ_b. Recall that we are implicitly using a unitary transformation when considering bond-centered inversion symmetry, such that the inversion operation takes on the simple form in Eq. 5.31. Because of this, we have to consider the site-centered and bond-centered cases (i.e. those with and without the unitary transformation) separately when relating M and M' to the mean-field parameters. Plugging Eq. 5.26 into Eq. 5.32 and 5.33, we find that symmetry M and M' are related to the mean-field terms for site-centered inversion as

$$\begin{aligned} M(0) &= |\Delta_s|\cos(\theta_s) + |\Delta_b|\cos(\theta_b - \mathcal{K}a_z), \\ M'(0) &= |\Delta_s|\sin(\theta_s) + |\Delta_b|\sin(\theta_b - \mathcal{K}a_z). \end{aligned} \tag{5.36}$$

To be compatible with inversion symmetry we need $M'(0)$ to vanish, hence, the onsite term is compatible with site-centered inversion symmetry when $\theta_s = 0$, or π, and the hopping term is compatible with site-centered inversion symmetry when $\theta_b = \mathcal{K}a_z$, or $\mathcal{K}a_z + \pi$. Similarly, for bond-centered inversion symmetry

(using the unitary transformation discussed above) M and M' are related to the mean-field terms as

$$\begin{aligned} M(0) &= |\Delta_s| \cos(\theta_s + \mathcal{K} a_z) + |\Delta_b| \cos(\theta_b), \\ M'(0) &= |\Delta_s| \sin(\theta_s + \mathcal{K} a_z) + |\Delta_b| \sin(\theta_b). \end{aligned} \tag{5.37}$$

Hence, the onsite term is compatible with bond-centered inversion symmetry when $\theta_s = -\mathcal{K} a_z$, or $-\mathcal{K} a_z + \pi$, and the hopping term is compatible with bond-centered inversion when $\theta_b = 0, \pi$.

We note that the commensurate CDW with period 2 ($\mathcal{K} = \pi/2a_z$) is a special case, since the corresponding onsite term is compatible with site centered inversion symmetry for all values of θ_s, while the hopping term is not compatible with site-centered inversion symmetry for any value of θ_b. Similarly, the hopping term is compatible with bond-centered inversion symmetry for all θ_b, while the onsite term is never compatible with bond-centered inversion symmetry. This can be confirmed by direct inspection of Eq. 5.32 and 5.33.

The two inversion-symmetric Dirac-CDW insulators ($M(0) \lessgtr 0$, $M'(0) = 0$) are anisotropic topological crystalline insulators (TCI). As we show in the next section, they have different $\mathbb{Z}_2$ indices under the classification scheme discussed in Sec. 5.3. Although they have different crystalline-electromagnetic responses, both classes of insulators share many important physical properties. Namely, both classes of insulators have symmetry-protected gapless surface states on boundaries normal to the x and y directions. This can be understood by noting that the Dirac-CDW insulator is adiabatically connected to two TRS-related copies of the Weyl-CDW insulator. Since the Weyl-CDW insulators have gapless 1D chiral surface modes on the x and y surfaces that circulate around the z-axis [174], the Dirac-CDW insulator has helical surface modes that counter-propagate around the z-axis [179]. These edge modes match those that are found in a stack of 2D quantum spin Hall (QSH) layers. The helical surface modes also indicate that edge and screw dislocations of the CDW bind helical modes [179]. The helical modes of the Dirac-CDW insulator are interesting in their own right, but they do not have an immediate impact on our discussion of the disclination responses of the Dirac-CDW insulator, provided that disclinations are far away from any boundaries normal to the x or y directions. We note that while the surfaces normal to the x and y directions are gapless due to time-reversal symmetry, surfaces normal to the z direction can be gapped while preserving all relevant symmetries.

5.5 Crystalline-electromagnetic responses of the Dirac-CDW insulator

We now turn our attention to the topological responses of Dirac-CDW insulators. The usual topological electromagnetic responses, namely the 3D Hall response and axion electrodynamics, are trivial for a Dirac-CDW

insulator since such an insulator is essentially two time-reversal symmetry related, Weyl-CDW insulators. However, even though Dirac-CDW insulators have trivial electromagnetic responses, they can host non-trivial crystalline-electromagnetic responses. The exact nature of these responses depends on if the CDW preserves a subgroup of the T^z discrete translation symmetry of the lattice (i.e., if the CDW is commensurate with the lattice) and if the CDW preserves inversion symmetry.

Below we will show the following results. If the CDW is commensurate, the Dirac-CDW insulators have a quantized 3D dWZ response. If the CDW preserves inversion symmetry but is incommensurate, we find there are two distinct inversion-symmetric Dirac-CDW insulators that differ by a $\Phi = 2\pi\ R \wedge F$ term. Based on our previous arguments, two insulators differing by an $R \wedge F$ term will have different disclination charge parities. If the CDW is both commensurate and preserves inversion symmetry, we find that there are two distinct inversion-symmetric Dirac-CDW insulators that have the same 3D dWZ response, but differ by a $\Phi = 2\pi\ R \wedge F$ term. One of these insulators has a disclination filling anomaly, while the other does not. We will establish these results analytically, and confirm them through explicit numerical lattice model calculations.

The 3D discrete Wen-Zee response of the Dirac-CDW insulator

We show in this subsection that the Dirac-CDW insulator realizes the 3D dWZ response when the CDW is commensurate. Such a response cannot occur for an incommensurate CDW, as a well-defined 3D dWZ response requires discrete translation symmetry. To this end, let us consider a Dirac-CDW insulator generated by a commensurate CDW with a period $\frac{p}{q}a_z$, where a_z is lattice constant along the z-direction ($\mathcal{K} = \frac{q}{p}\frac{\pi}{a_z}$ in Eq. 5.1). Such a system has an enlarged unit cell of length $\tilde{a}_z = pa_z$, and a reduced T^z discrete translation symmetry $z \to z + pa_z$. The 3D dWZ response of such a system can be written analogously to Eq. 5.14 as

$$\mathcal{L}_{\text{3D-WZ CDW}} = \mathcal{S}_{\text{3D}} \frac{\tilde{G}_z}{4\pi^2} \epsilon^{ijk} \omega_i \partial_j A_k, \tag{5.38}$$

where $\tilde{G}_z = 2\pi/pa_z$ is the reciprocal lattice vector along the z-direction with respect to the enlarged lattice and $\mathcal{S}_{\text{3D}} = 2q$. This response indicates that a disclination line of a system of size $L_z = a_z N_z$ binds charge

$$\begin{aligned} Q_{\text{disc}} &= \mathcal{S}_{\text{3D}} \frac{\Theta_F}{2\pi} N_z/p \mod (2N_z/p), \\ &= 2\frac{q}{p}\frac{\Theta_F}{2\pi} N_z \mod (2N_z/p), \end{aligned} \tag{5.39}$$

where the mod $(2N_z/p)$ ambiguity comes from adding a local Kramers degenerate pair of electrons to each enlarged unit cell. Note that we assume N_z is a multiple of p in order for the system to be invariant under

the reduced translation symmetry.

We can arrive at Eq. 5.38 by starting with the anomaly equation of the DSM, Eq. 5.7, and enlarging the unit cell,

$$\begin{aligned} a_z &\to \tilde{a}_z = p a_z, \\ G_z &\to \tilde{G}_z = G_z/p \end{aligned} \tag{5.40}$$

Using that $\nu = q/p$, we then arrive at Eq. 5.38. Note that after this redefinition of the unit cell, Eq. 5.7 has an integer coefficient and is therefore gauge invariant and anomaly free. The system no longer needs to have gapless degrees of freedom to compensate. Indeed, the Dirac nodes can be gapped out by the CDW order as discussed previously. The 3D dWZ response of the Dirac-CDW insulator is therefore the descendant of the anomalous DSM response when the anomaly is removed by breaking translation symmetry.

We can also argue that the commensurate Dirac-CDW insulator realizes the response in Eq. 5.38 by treating the DSM (without a CDW) as a family of 2D insulators that are parameterized by k_z. We recall from above that the 2D insulators with $|k_z| < \mathcal{K}$ are QSH insulators with $\mathcal{S}_{2\mathrm{D}} = 2$ and the insulators with $|k_z| > \mathcal{K}$ are trivial ($\mathcal{S}_{2\mathrm{D}} = 0$) in this interpretation. The total charge on a disclination in the DSM is simply the sum of contributions coming from the QSH insulators and the gapless degrees of freedom at $k_z = \pm\mathcal{K}$. Turning on the CDW couples the 2D system indexed by k_z to the 2D system indexed by $k_z + 2\mathcal{K}$. If the magnitude of the CDW is small, the coupling will affect only the gapless systems at $k_z = \pm\mathcal{K}$. The effect of the CDW on the gapped states that are initially indexed $|k_z| < \mathcal{K}$ and $|k_z| > \mathcal{K}$ will be negligible and therefore not affect the topological responses of these states. In particular, at weak coupling the topological responses of the $|k_z| < \mathcal{K}$ (i.e., the QSH insulators) will not be affected. Therefore, if we add a disclination to the system, each of the $|k_z| < \mathcal{K}$ insulators will still bind charge $\frac{\Theta_F}{\pi}$. Additionally, a direct calculation shows that the two hybridized states at $k_z = \pm\mathcal{K}$ bind a net charge of $\frac{\Theta_F}{\pi}$. The states for $|k_z| > \mathcal{K}$ correspond to trivial 2D insulators and therefore do not bind any charge. For a system of size $L_z = a_z N_z$, where k_z is quantized as a multiple of $2\pi/N_z$ (assuming periodic boundary conditions), there will be a total of $\frac{q}{p}N_z - 1$ states with $|k_z| < \mathcal{K}$ (recall that N_z must be a multiple of q). A disclination therefore binds a total charge of $2\frac{q}{p}\frac{\Theta_F}{2\pi}N_z$, in agreement with Eq. 5.39.

The disclination filling anomaly of the Dirac semimetal-charge density wave insulator

In Sec. 5.4 we showed that there are two distinct inversion-symmetric Dirac-CDW insulators for a given $\mathcal{K}$. In this section we show that the effective response theories for these insulators differ by an $R \wedge F$ term with

$\Phi = 2\pi$. If the CDW is commensurate such that the system has T^z discrete translation symmetry, one of these insulators will have a disclination filling anomaly and the other will not (see Sec. 5.3). More generally, i.e., for incommensurate CDWs as well, the difference in the $R \wedge F$ term indicates that the disclination charges of the two insulators will differ by $\Theta_F/\pi \mod (2\Theta_F/\pi)$ when open boundaries are present.

To show that the two inversion-symmetric insulators differ by a $\Phi = 2\pi$ $R \wedge F$ term, we consider the low-energy Lagrangian for the DSM subject to a mean-field CDW term (see Sec. 5.4 and Eq. 5.34), and minimally couple the Dirac fermions to the U(1) charge and C_{4z} rotation gauge fields,

$$\begin{aligned} \mathcal{L} &= \bar{\Psi}[i\bar{\Gamma}^\mu D_\mu + M + M'\bar{\Gamma}^5]\Psi, \\ D_\mu &= \partial_\mu - iA_\mu - i\omega_\mu \left[\frac{1}{2}\sigma^z s^z - s^z\right], \end{aligned} \tag{5.41}$$

where Ψ is an 8 component spinor, $\bar{\Psi} = \Psi^\dagger \bar{\Gamma}^0$, and

$$\bar{\Gamma}^x = \sigma^y s^z \tau^x, \quad \bar{\Gamma}^y = \sigma^x \tau^x, \quad \bar{\Gamma}^z = \tau^y, \bar{\Gamma}^0 = \sigma^z \tau^x, \quad \bar{\Gamma}^5 = \tau^z. \tag{5.42}$$

The covariant derivative D_μ minimally couples the low-energy fermions to the U(1) gauge field, A_μ, and the C_{4z} gauge field, ω_μ. The latter couples via the C_{4z} angular momentum operator, $\frac{1}{2}\sigma^z s^z - s^z$ [83]. In this minimal coupling procedure, we are treating ω as a continuous gauge field with fluxes that are quantized in multiples of $\pi/2$ as discussed before. Compared to Eq. 5.34, we are suppressing any momentum dependence of the CDW mass terms M and M', as it is either irrelevant at this order, or can be absorbed into a redefinition of the Fermi velocity.

We are interested in the difference between the topological response of the two gapped inversion-symmetric phases, i.e., inversion symmetry sets $M' = 0$, and we want to compare the insulators having $M > 0$ or $M < 0$. To this end, we set $M = \bar{M}\cos(\theta)$ and $M' = \bar{M}\sin(\theta)$, and consider a process where θ is smoothly increased from 0 to π. The fermions remain gapped during this process (Eq. 5.35), and the effective response theory (treated as a function of θ) is found by integrating out the massive fermions. The resulting effective response theory contains the topological term,

$$\mathcal{L}_{\text{top}}[\theta] = \frac{\theta}{2\pi^2}\epsilon^{\mu\nu\lambda\eta}\partial_\mu\omega_\nu\partial_\lambda A_\eta \quad , \tag{5.43}$$

which arises from a triangle diagram with external legs A_μ, ω_μ, and θ. The $\theta = 0$ and $\theta = \pi$ inversion-symmetric insulators therefore differ by a $\Phi = 2\pi$ $R \wedge F$ term (Eq. 5.16).

Based on this, and our discussions in Sec. 5.3 and 5.5, we therefore conclude that the two distinct

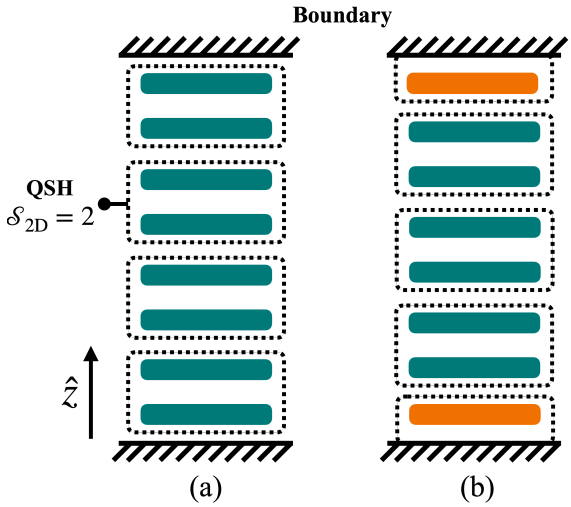

Figure 5.6: Layered construction of the period-2 Dirac-CDW insulators, where a two adjacent z-layers (teal) pair up to form a QSH insulator (dashed box) with $\mathcal{S}_{3D} = 2$. For a system of length $L_z = a_z N_z$ with open boundaries, this stacking can be done such that there are $N_z/2$ QSH insulators (a) or $N_z/2-1$ QSH insulator layers (b). This describes Eq. 5.51 with $|\Delta_b| = 1$, and $\theta_b = 0$ and π respectively. When there $N_z/2-1$ QSH insulator layers, there are a pair of decoupled z-layers on the top and bottom surfaces (orange).

inversion-symmetric Dirac-CDW insulators differ by a $\Phi = 2\pi\ R \wedge F$ term. For commensurate CDWs, this difference is related to the presence or absence of a disclination filling anomaly. For incommensurate CDWs, the difference in $R \wedge F$ term indicates that the two insulators have different disclination charge parities.

Analytic solution for the period 2 charge density wave

To demonstrate the Dirac-CDW insulator responses we will first consider the insulators that form when a DSM with $\mathcal{K} = \pi/2a_z$ is driven into a insulating phase by a period-2 CDW with inversion symmetry. As noted in Sec. 5.2, there are two types of inversion symmetries to consider, the site-centered inversion symmetry that sends $z \to -z$, and the bond-centered inversion symmetry that sends $z \to -z + a_z$. For a system with open boundaries, the site-centered inversion symmetry requires an odd number of sites, while the bond-centered inversion symmetry requires an even number of sites. For an insulator with a period-2 CDW, it is natural to require an even number of sites for commensurability, and so we will consider a lattice model with bond-centered inversion symmetry.

The mean field limit of the DSM (Eq. 5.1) with a period-2 CDW hopping term (Eq. 5.33) is

$$H_{\text{DSM-CDW}} = \begin{bmatrix} H^{xy} & H^{z} \\ H^{z\dagger} & H^{xy} \end{bmatrix} \tag{5.44}$$

$$H^{xy} = \sin(k_x a_x)\Gamma_1 + \sin(k_y a_y)\Gamma_2 - b_{xy}(2 - \cos(k_x a_x) - \cos(k_y a_y))\Gamma_3 \tag{5.45}$$

$$H^z = (1 + |\Delta_b| \cos(\theta_b))\Gamma_3 + e^{i\tilde{k}_z \tilde{a}_z}(1 - |\Delta_b| \cos(\theta_b))\Gamma_3 \tag{5.46}$$

where $\tilde{k}_z = k_z/2$ is the momentum of the folded Brillouin zone with conjugate position, $\tilde{z} = 2z$. The unit cells indexed by $\tilde{z}$ are twice as large as in the gapless DSM, and have length $\tilde{a}_z = 2a_z$. We consider a weak CDW where $|\Delta_b| \ll b_{xy}$. The bond-centered inversion symmetry acts on $H_{\text{DSM-CDW}}$ as

$$\mathcal{I}_b = \sigma^z t^x, \tag{5.47}$$

where the $\boldsymbol{t}$ Pauli matrices act on the 4×4 blocks that make up $H_{\text{DSM-CDW}}$. The even-z (odd-z) sublattices of Eq. 5.1 correspond to $t^z = +1(-1)$ in Eq. 5.44. The $\boldsymbol{t}$ Pauli matrices should not to be confused with the $\boldsymbol{\tau}$ Pauli matrices that differentiate the two Dirac nodes in the low-energy Hamiltonian, Eq. 5.27.

There are two inversion-symmetric gapped phases to consider, $\cos(\theta_b) > 0$ and $\cos(\theta_b) < 0$. For simplicity, we restrict our attention to the cases where $\theta_b = 0$ or $\theta_b = \pi$. For the period-2 CDW, other values of θ_b are equivalent to one of these two values by a redefinition of $|\Delta_b|$. To demonstrate that the $\theta_b = 0$ and $\theta_b = \pi$ insulators differ by a $\Phi = 2\pi\ R \wedge F$ term we can add an inversion symmetry breaking onsite term

$$H' = 2\Delta' \Gamma_3 t^z \tag{5.48}$$

which is simply the onsite CDW term, Eq. 5.32 with $\Delta' = |\Delta_s| \cos(\theta_s)$. Indeed, $H_{\text{DSM-CDW}} + H'$ is equivalent to Eq. 5.41 in the continuum limit with $M \propto |\Delta_b| \cos(\theta_b)$ and $M' \propto \Delta'$. Hence, based on Sec. 5.5 the $\theta_b = 0$ and $\theta_b = \pi$ phases differ by a $\Phi = 2\pi\ R \wedge F$ term.

To analyze the full lattice model, it is useful to consider $|\Delta_b| = 1$ and $\theta_b = 0$ where the Hamiltonian is independent of $\tilde{k}_z$, and can be treated as a stack of 2D insulating layers. The $t^x = \pm 1$ sectors of each layer are equivalent to QSH Hamiltonians, Eq. 5.12, with masses $m = 2 \mp \frac{2}{b_{xy}}$ respectively. Recalling that we have set $b_{xy} \gg |\Delta_b| = 1$, the $t^x = -1$ sector is in the QSH phase, while the $t^x = +1$ sector is in the trivial phase. We can therefore conclude that for $|\Delta_b| = 1$ and $\theta_b = 0$ each CDW period hosts a single 2D QSH insulator, in agreement with our earlier arguments.

To determine the 3D dWZ response in this layered limit, let us consider adding a disclination to a lattice of length $L_z = a_z N_z$ with periodic boundary conditions. In order for the system to preserve the reduced translation symmetry, $z \to z + 2a_z$, N_z must be an even integer such that there are $N_z/2$ CDW periods. Since each CDW period contains a single QSH insulator which has a $\mathcal{S}_{\text{2D}} = 2$ 2D dWZ response, the charge bound to a disclination is

$$Q_{\text{disc}} = \frac{1}{2}\frac{\Theta_F}{\pi} N_z \mod (N_z). \tag{5.49}$$

Comparing this to Eq. 5.39, we find that the full 3D system has a 3D dWZ response with $\mathcal{S}_{\text{3D}} = 2$, as expected for a layered system.

Next let us consider the $|\Delta_b| = 1$ and $\theta_b = \pi$ insulator. This insulator is related to the $\theta_b = 0$ insulating phase by a translation in the z-direction by half of the doubled unit cell (i.e., translation by one unit cell of the original DSM lattice model)

$$T_{z-1/2} = \begin{bmatrix} 0 & e^{ik_z} \\ 1 & 0 \end{bmatrix}. \tag{5.50}$$

The $|\Delta_b| = 1$ and $\theta_b = \pi$ insulator can therefore also be treated as a stack of 2D insulating layers. The 2D insulators equally occupy the $t^z = +1$ sublattice of layer $\tilde{z}$ and the $t^z = -1$ sublattice of layer $\tilde{z}+1$. Based on our previous results, the bulk of the $|\Delta_b| = 1$ and $\theta_b = \pi$ insulator also hosts a single 2D QSH insulator per CDW period, and therefore has $\mathcal{S}_{\text{3D}} = 2$. Hence, both the $|\Delta_b| = 1$ and $\theta_b = 0, \pi$ insulators have an identical 3D dWZ response with $\mathcal{S}_{\text{3D}} = 2$. Since the 3D dWZ response is quantized for insulators with rotation symmetry and charge conservation, we conclude that all insulating phases of our model with $b_{xy} \gg |\Delta_b| \neq 0$ have this response.

While these phases are not distinguished by their dWZ response, based our previous discussions in Sec. 5.3, we expect two distinct classes of inversion-symmetric insulators can be distinguished by another response. In fact, we have shown that the effective response theories for these insulators differ by a $\Phi = 2\pi$ $R \wedge F$ term. Based on our results from Sec. 5.5, the $\theta_b = 0$, and $\theta_b = \pi$ insulators should fall into different classes, and one of these insulators should have a disclination filling anomaly, while the other should not. As we show below, the $\theta_b = \pi$ insulator has a disclination filling anomaly, while the $\theta_b = 0$ insulator does not.

To show this, let us consider a system described by Eq. 5.44 of length $L_z = aN_z$ (N_z even) with open boundaries in the z-direction. Using position space in the z-direction and momentum space in the x and y-directions, the Hamiltonian is

$$\begin{aligned} \hat{H}_{\text{DSM-CDW}} = \sum_{\tilde{z}=1}^{N_z/2} \Big[& c^\dagger_{k_x,k_y,\tilde{z}} H^{xy} c_{k_x,k_y,\tilde{z}} \\ & + (1 + |\Delta_b| \cos(\theta_b)) c^\dagger_{k_x,k_y,\tilde{z}} \Gamma_3 t^x c_{k_x,k_y,\tilde{z}} \\ & + (1 - |\Delta_b| \cos(\theta_b)) c^\dagger_{k_x,k_y,\tilde{z}} \Gamma_3 t^x c_{k_x,k_y,\tilde{z}+1} \Big], \end{aligned} \tag{5.51}$$

where $\tilde{z} = 2z$ labels the doubled unit cells along the z-direction. As before, we consider the representative insulators with $|\Delta_b| = 1$ and $\theta_b = 0$ or π.

For $|\Delta_b| = 1$ and $\theta_b = 0$, the spectrum is fully gapped, and different $\tilde{z}$-layers are fully decoupled. Furthermore, each of these layers has $\mathcal{S}_{\text{2D}} = 2$, and constitutes a QSH insulator, i.e. one non-trivial QSH

per $\tilde{z}$. This stacking configuration is shown in Fig. 5.6(a). If we add a $\pi/2$ disclination-line to the insulator, each $\tilde{z}$-layer will bind charge Θ_F/π. For a system of length $L_z = a_z N_z$, the total charge on the disclination line is the sum of the charges on the 2D layers,

$$Q_{\text{disc}} = \frac{1}{2}\frac{\Theta_F}{\pi} N_z \mod (2\frac{\Theta_F}{\pi}), \tag{5.52}$$

where the $2\Theta_F/\pi$ ambiguity comes from the ability to add 2D insulators having $\mathcal{S}_{\text{2D}} \in 2\mathbb{Z}$ to the top and bottom surfaces while preserving inversion symmetry (recall that $\mathcal{S}_{\text{2D}}$ is an even integer for spin-1/2 insulators with TRS). Comparing Eq. 5.52 and 5.49, we find that the disclination charge of the $|\Delta_b| = 1$ and $\theta_b = 0$ insulator changes by $0 \mod (2\Theta_F/\pi)$ when changing boundary conditions, indicating that this system does not have a disclination filling anomaly.

We can similarly find the charge on the disclination line when $|\Delta_b| = 1$ and $\theta_b = \pi$. For open boundaries, the $t^z = -1$ sublattice of the $\tilde{z} = 1$ layer is fully decoupled. The Hamiltonian for the fermions in this sublattice/layer sector is just H^{xy} from Eq. 5.44, which has a gapless point at $k_x = k_y = 0$. The fermions on the $t^z = +1$ sublattice of the $\tilde{z} = N_z/2$ layer at the top are also decoupled from the other layers/sublattices and are gapless. These sectors can be gapped out, with inversion symmetry preserving mass terms $\propto \Gamma^3$. When such a perturbation has been applied we can determine the charge distribution on a $\pi/2$-disclination line. As noted previously, the bulk of the $|\Delta_b| = 1$, $\theta_b = \pi$ insulator is composed of layers of QSH insulators having $\mathcal{S}_{\text{2D}} = 2$. These insulators have equal weight on the $t^z = +1$ sublattice of $\tilde{z}$ and the $t^z = -1$ sublattice of $\tilde{z}+1$. Since these QSH insulators live *between* $\tilde{z}$ layers, a system of length $L_z = aN_z$ with open boundaries in the z-direction will have $N_z/2 - 1$ QSH layers. This stacking configuration is shown in Fig. 5.6(b). To compute the disclination charge we also note that the gapping perturbation on the surfaces can generate boundary insulators that also have 2D dWZ responses with $\mathcal{S}_{\text{2D-bnd}} \in 2\mathbb{Z}$. However, the discrete Wen-Zee shift of the boundary insulators at the top and bottom must be the same because of inversion symmetry. Counting up the contributions from the bulk QSH layers and the boundary insulating layers, the total charge on the disclination line is

$$Q_{\text{disc}} = \frac{1}{2}\frac{\Theta_F}{\pi}(N_z - 2 + 2\mathcal{S}_{\text{2D-bnd}}) \mod (2\frac{\Theta_F}{\pi}). \tag{5.53}$$

Using Eqs. 5.53 and 5.49, we find that the charge on the disclination lines of the $|\Delta_b| = 1$, $\theta_b = \pi$ insulator changes by $\Theta_F/\pi \mod (2\Theta_F/\pi)$ when changing boundary conditions. The $\theta_b = \pi$ insulator therefore has a disclination filling anomaly. Physically, the difference in charge can be traced back to the fact that if we place the QSH insulators between $\tilde{z}$ layers (as we did for the $\theta_b = \pi$ insulator), there will be one less QSH

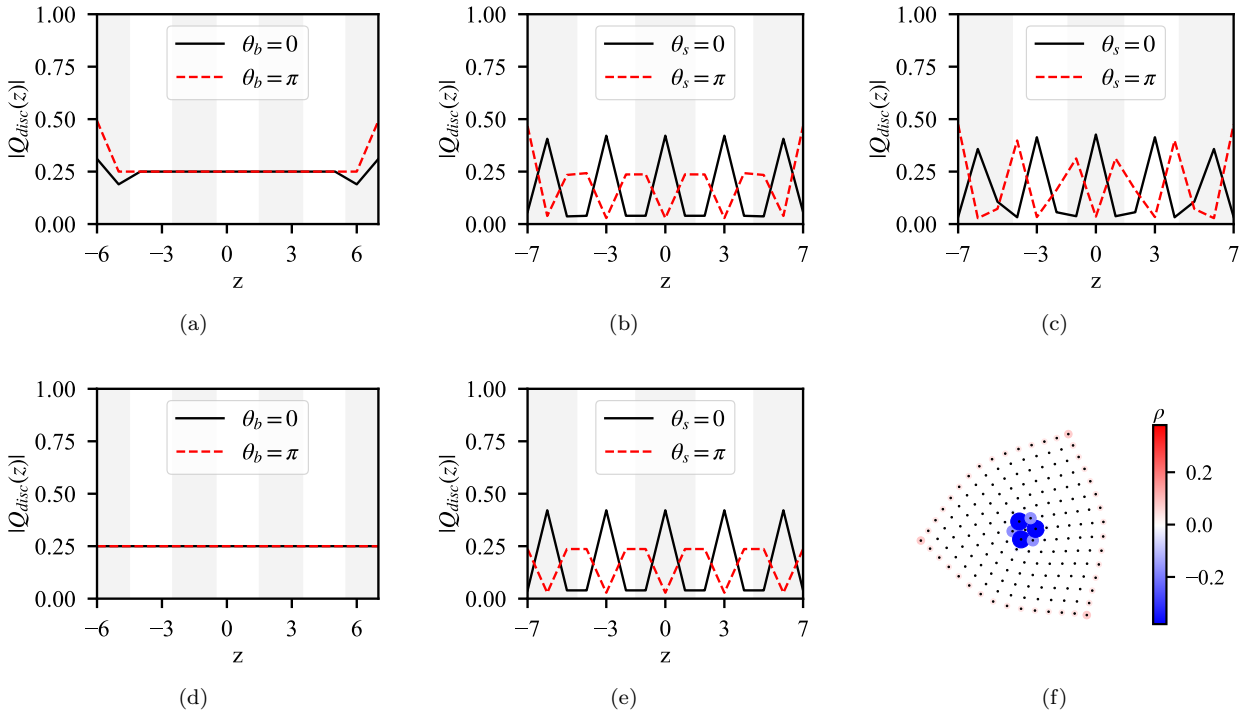

Figure 5.7: (a, b) The charge bound to a disclination as a function of z for $\mathcal{K} = \pi/2a_z$, $\Delta_s = 0$, $\Delta_b = 0.5$, $n_x = 15$, and $n_z = 14$ with (a) open and (d) periodic boundary conditions. (b, e) The charge bound to a disclination as a function of z for $\mathcal{K} = \pi/3a_z$, $\Delta_s = 0.5$, $\Delta_b = 0$, $n_x = 15$, and $n_z = 15$ with (b) open and (e) periodic boundary conditions. (c) The charge bound to a disclination as a function of z for $\mathcal{K} = \sqrt{2}\pi/4$, $\Delta_s = 0.5$, $\Delta_b = 0$, $n_x = 15$, and $n_z = 15$ with open boundary conditions. In all cases we set $b_{xy} = 1.0$ and $\Delta_{\text{surf}} = 0.25$. The solid black and dashed red lines indicate $\theta_{b/s} = 0$ and $\theta_{b/s} = \pi$, respectively. The alternating gray and white shading indicates unit cells of the CDWs. (f) The charge density around a disclination summed over the z-direction with $\mathcal{K} = \pi/2a_z$, $\theta_b = \pi$, $\Delta_s = 0$, $\Delta_b = 0.5$, $b_{xy} = 1.0$, $\Delta_{\text{surf}} = 0.25$, $n_x = 15$, and $n_z = 12$. The charge distribution is qualitatively identical for all other cases considered in this work.

insulator than if we place the QSH insulators on the $\tilde{z}$ layers (as we did for the $\theta_b = 0$ insulator). Boundary effects can add a QSH insulator to the top and bottom layers. But even with the effect, the parity of the number of QSH insulators is fixed in each stacking configuration. This leads to the quantized difference in disclination charge found above.

In summary, we find two distinct inversion-symmetric insulators can arise from the coupling a $\mathcal{K} = \pi/2a_z$ DSM to a CDW. As expected, both insulators have a $\mathcal{S}_{3D} = 2$ 3D dWZ response, and one has a disclination filling anomaly while the other does not.

Numeric analysis

In this subsection, we numerically calculate the crystalline-electromagnetic responses for the inversion-symmetric Dirac-CDW insulators that form when a DSM is coupled to: a commensurate $\mathcal{K} = \pi/2a_z$ (period

$\mathcal{K}a_z$	$\lvert\Delta_s\rvert$	$\lvert\Delta_b\rvert$	$\theta_{s/b}$	N_z	Q_{disc} OBC	Q_{disc} PBC	DL Filling Anomaly
$\pi/2$	0	1/2	0	14	7/2	7/2	No
$\pi/2$	0	1/2	π	14	4	7/2	Yes
$\pi/3$	1/2	0	0	15	5/2	5/2	No
$\pi/3$	1/2	0	π	15	3	5/2	Yes
$\pi/2\sqrt{2}$	1/2	0	0	15	5/2	N/A	N/A
$\pi/2\sqrt{2}$	1/2	0	π	15	3	N/A	N/A

Table 5.1: Summary of the numerical analysis of the crystalline-electromagnetic responses of the Dirac-CDW insulator. The Hamiltonian for the DSM is given by Eq. 5.1 with Dirac nodes at $\boldsymbol{k} = (0, 0, \pm\mathcal{K})$ and $b_{xy} = 1$. The CDW is included at the via either an inversion-symmetric onsite potential ($\hat{H}_s$ in Eq. 5.32 with $\theta_s = 0$ or π) or an inversion-symmetric hopping amplitude ($\hat{H}_b$ in Eq. 5.33 with $\theta_b = 0$ or π) with period $\pi/\mathcal{K}$. For the commensurate values of $\mathcal{K} = \pi/2$ and $\pi/3$) the total charge bound to a disclination is calculated for periodic and open and boundary conditions, the difference of which gives the disclination filling anomaly, defined in Sec. 5.3. However, periodic boundary conditions are not compatible with the incommensurate value of $\mathcal{K} = \pi/2\sqrt{2}$, precluding the calculation of the disclination filling anomaly.

2) CDW, a commensurate $\mathcal{K} = \pi/3a_z$ (period 3) CDW, and an incommensurate $\mathcal{K} = \pi/2\sqrt{2}a_z$ CDW. These calculations are performed using the DSM Hamiltonian in Eq. 5.1 with $b_{xy} = 1$. The $\mathcal{K} = \pi/2a_z$ CDW is implemented via the hopping mean field term in Eq. 5.33 with $|\Delta_b| = 1/2$ and either $\theta_b = 0$ or π, both of which preserve bond-centered inversion symmetry. The $\mathcal{K} = \pi/3a_z$ CDW is implemented via the onsite mean field term in Eq. 5.32 with $|\Delta_s| = 1/2$ and either $\theta_s = 0$ or π, preserving the site-centered inversion symmetry. The $\mathcal{K} = \pi/2\sqrt{2}a_z$ CDW is similarly implemented with the onsite mean field term in Eq. 5.32 with $|\Delta_s| = 1/2$ and either $\theta_s = 0$ or π, also preserving site-centered inversion symmetry.

For each system, we evaluate the Hamiltonian on a lattice with open boundary conditions and a $\Theta_F = \pi/2$ disclination line. The disclination line is located at the center of the lattice and stretches straight along the z-direction. To reduce the impact of finite size effects, we also add an inversion-preserving perturbation of the form $H'_{\text{surf}} = \Delta_{\text{surf}}\Gamma_3$ ($\Delta_{\text{surf}} = 1/4$ on both the top and bottom layers and vanishes elsewhere) to increase the gap on the z-normal surfaces. Then we calculate the disclination charge by summing the charge density over all sites within some radial distance from the disclination core. To further reduce the impact of finite size effects, we perform these calculations over a range of system sizes and extrapolate to the infinite-size limit. The details of how the integration radius is determined and how the extrapolations are performed, are provided in Appendix B.2.

As expected from our analysis in previous sections, we find that charge is bound to the disclination line for all Dirac-CDW insulators, as shown in Fig. 5.7f. Specifically, in Fig. 5.7 we plot the layer-resolved disclination charge for each insulator at the largest accessible system size. For the commensurate CDWs, $\mathcal{K} = \pi/2a_z$ and $\mathcal{K} = \pi/3a_z$, we find that the charge distribution oscillates with a period matching the CDW

period, with deviations at open boundaries. There is no notable periodicity for the $\mathcal{K} = \pi/2\sqrt{2}a_z$ CDW, as it is incommensurate with the lattice. The total disclination charges for each of these insulators extrapolated to the infinite-size limit are enumerated in Table 5.1.

For $\mathcal{K} = \pi/2a_z$, the total charge bound to the disclination with open boundary conditions differs by 1/2 between the $\theta_b = 0$ and $\theta_b = \pi$ Dirac-CDW insulators. This difference in disclination charge is a direct manifestation of the difference in the coefficient of the $R \wedge F$ term between the two Dirac-CDW insulators. Similarly, the disclination charge differs by 1/2 between the $\theta_s = 0$ and $\theta_s = \pi$ Dirac-CDW insulators with $\mathcal{K} = \pi/3a_z$, and $\mathcal{K} = \pi/2\sqrt{2}a_z$. We therefore find that the two distinct inversion-symmetric Dirac-CDW insulators for each CDW wavevector have different disclination charge parities, matching our analytic predictions.

For the commensurate $\mathcal{K} = \pi/2a_z$ and $\mathcal{K} = \pi/3a_z$ CDWs, it is also possible to have periodic boundary conditions in the z-direction. Hence in these cases we can determine the 3D dWZ response of the Dirac-CDW insulators and whether or not the insulators host a disclination filling anomaly. We find that for periodic boundaries, both the $\theta_b = 0$ and π insulators with $\mathcal{K} = \pi/2a_z$ bind charge 1/2 per CDW period (1/4 per original lattice layer). The $\theta_b = 0$ and π insulators with $\mathcal{K} = \pi/3a_z$ also bind charge 1/2 per CDW period (1/6 per original lattice layer). This is exactly the 3D dWZ response that we have previously discussed. Furthermore, we find that the disclination charges differ by 1/2 with periodic and open boundary conditions for the $\mathcal{K} = \pi/2a_z$, $\theta_b = \pi$ and $\mathcal{K} = \pi/3a_z$, $\theta_s = \pi$ insulators, indicating disclination filling anomalies. The presence of the disclination filling anomaly can also be observed in the charge density profiles plotted in Fig. 5.7, in which it manifests as a deviation at the boundaries of the disclination charge per CDW period. The disclination charges for open and periodic boundary conditions are identical for the $\mathcal{K} = \pi/2a_z$, $\theta_b = 0$ and $\mathcal{K} = \pi/3a_z$, $\theta_s = 0$ insulators, marking the absence of disclination filling anomalies. These results agree with the analytic calculations presented in Sec. 5.5. As discussed in Sec. 5.3, the disclination filling anomaly is ill-defined for insulators with incommensurate $\mathcal{K}$, like the $\mathcal{K} = \pi/2\sqrt{2}a_z$ Dirac-CDW insulators, since they are incompatible with periodic boundaries.

5.6 Discussion

In this chapter we considered the topological responses of the insulating state that arises from coupling a 3D DSM to a CDW. Unlike the related Weyl-CDW insulators, the Dirac-CDW insulators do not display a Hall effect or axion electrodynamics. Rather, the Dirac-CDW insulators display novel crystalline-electromagnetic responses wherein charge is bound to disclination defects of the lattice. These crystalline-electromagnetic responses are encoded in a 3D discrete Wen-Zee term and an $R \wedge F$ term. Due to the inversion symmetry

of the DSM, there are two classes of insulating states where $\Phi = 0$ and $\Phi = 2\pi$ respectively. These two insulating phases can be differentiated by considering the total charge bound to disclination lines. These responses naturally arise from the combination of topology and spatial symmetries that stabilize the DSMs.

In terms of real materials, a potential material candidate for realizing the Dirac-CDW insulator is $TaTe_4$, a DSM that develops commensurate CDW order at finite temperature [198]. The CDW momentum matches the momentum space separation for a pair of Dirac points. Despite this, the CDW phase of $TaTe_4$ is not insulating, but rather has an 8-fold degenerate doubled Dirac point in the folded Brillouin zone. Additionally, $TaTe_4$ has Dirac points at other momenta that do not strongly couple to the CDW, and are expected to remain gapless. The gapless Dirac points prevent $TaTe_4$ from realizing the quantized crystalline-electromagnetic responses discussed, but it does indicate that the combination of Dirac and CDW physics can occur in real materials.

There is also a much broader family of topological semimetals protected by non-symmorphic crystal symmetries, for which there are many candidate host materials and some experimentally confirmed examples [125], [199]. Understanding the mixed crystalline-electromagnetic response of non-symmorphic topological semimetals is an open question for future work, as the structure of non-symmorphic symmetry fluxes is not currently understood. In addition, it would be interesting to consider the crystalline-electromagnetic responses of rotation-symmetric higher order Dirac semimetals, both with and without interactions. Previous studies of higher order semimetals [94], [102], [103], [137], [138] have already revealed novel behavior not found in their first order counterparts, but a full understanding of the topological responses of higher order semimetals remains incomplete, even for symmorphic symmetries.

Appendix A

Supplementary information for Chapter 2

This chapter is adapted from Mark R. Hirsbrunner, Oleg Dubinkin, Fiona J. Burnell, and Taylor Hughes, arXiv preprint arXiv:2309.10840.

A.1 Translation gauge fields derived from the teleparallel prescription

In this section we provide a derivation of the translation gauge field $\mathfrak{e}^{\mu}_{\nu}$ and its' coupling prescription that follow directly from gauging the translational symmetry group, which can be done in a similar fashion to gauging the ordinary electromagnetic $U(1)$ symmetry. Consider a translation transformation

$$r^{\mu} \to r^{\mu} + a^{\mu}, \tag{A.1}$$

which is generated by corresponding operators $\hat{P}_{\mu} = -i\hbar\partial_{\mu}$. Under such an infinitesimal translation the wave function changes by $\delta\psi = ia^{\mu}(\hat{P}_{\mu}/\hbar)\psi$. Promoting the transformation to a local one, $a^{\mu} \to a^{\mu}(r)$, we find that the derivative of ψ does not transform covariantly anymore:

$$\hbar\delta(\partial_{\nu}\psi) = ia^{\mu}(r)\partial_{\nu}(\hat{P}_{\mu}\psi) + i\hat{P}_{\mu}\psi\partial_{\nu}a^{\mu}(r). \tag{A.2}$$

We can compensate the second term by introducing an additional gauge potential B^μ_ν that obeys the gauge transformation rules $B^\mu_\nu \to B^\mu_\nu - \partial_\nu a^\mu(r)$. This allows us to define a covariant derivative:

$$D_\nu \psi = \partial_\nu \psi + i B^\mu_\nu (\hat{P}_\mu/\hbar)\psi. \tag{A.3}$$

Now it is straightforward to check that the covariant derivative transforms as expected:

$$\hbar\delta(D_\nu \psi) = i a^\mu(t,x) D_\nu(\hat{P}_\mu \psi) \tag{A.4}$$

We can re-express the partial derivative in Eq. A.3 as a momentum operator to write down:

$$D_\nu \psi = i\mathfrak{e}^\mu_\nu \hat{P}_\mu/\hbar \tag{A.5}$$

where $\mathfrak{e}^\mu_\nu = \delta^\mu_\nu + B^\mu_\nu$ is a translation gauge field that inherits its gauge transformations from the gauge potential B^μ_ν:

$$\mathfrak{e}^\mu_\nu \to \mathfrak{e}^\mu_\nu - \partial_\nu a^\mu(r). \tag{A.6}$$

A.2 Gradient expansion

In this appendix we provide a quick review of the gradient expansion procedure. As we are interested in responses involving both electromagnetic and translation gauge fields, we need to consider how the electron wave vector gets shifted in the presence of spatially-varying gauge fields $A_\mu(r)$ and $\mathfrak{e}^\lambda_\mu(r) = \delta^\lambda_\mu + B^\lambda_\mu(r)$ (see Appendix A.1):

$$k_\mu \to k_\mu + \frac{e}{\hbar} A_\mu(r) + k_\lambda B^\lambda_\mu(r). \tag{A.7}$$

For small gauge fields, we can obtain a simple form of the resulting single-particle Green's functions by performing a Taylor expansion:

$$\begin{aligned} G_0(k)^{-1} \to G^{-1}_{AB}(k,r) &= G_0^{-1}\left(k_\mu + \frac{e}{\hbar}A_\mu(r) + k_\lambda B^\lambda_\mu(r)\right) \\ &\approx G_0^{-1}(k) + \frac{e}{\hbar}A_\mu(r)\frac{\partial G_0^{-1}}{\partial k_\mu} + k_\lambda B^\lambda_\mu(r)\frac{\partial G_0^{-1}}{\partial k_\mu}(k) + ... \\ &\approx G_0^{-1}(k) + \left(\frac{e}{\hbar}A_\mu(r) + k_\lambda \mathfrak{e}^\lambda_\mu(r) - k_\mu\right)\frac{\partial G_0^{-1}}{\partial k_\mu}(k) + ... \end{aligned} \tag{A.8}$$

We then follow the standard procedure to derive the effective action:

$$\begin{aligned}\frac{i}{\hbar}S &= \log\left(\frac{Z_{AB}}{Z_0}\right) = \log\left(\frac{\mathrm{Det}G_{AB}^{-1}}{\mathrm{Det}G_0^{-1}}\right) \\ &\approx \mathrm{Tr}\log\left(I + G_0\Sigma\right)\end{aligned} \tag{A.9}$$

where

$$\Sigma = \left(\frac{e}{\hbar}A_\mu(r) + k_\lambda \mathfrak{e}_\mu^\lambda(r) - k_\mu\right)\frac{\partial G_0^{-1}}{\partial k_\mu}(k) + ... \tag{A.10}$$

Expanding the trace of logarithm we get

$$\begin{aligned}\frac{i}{\hbar}S &\approx \mathrm{Tr}\log\left(I + G_0\Sigma\right) \\ &\approx \mathrm{Tr}\left(G_0\Sigma\right) - \frac{1}{2}\mathrm{Tr}\left(G_0\Sigma G_0\Sigma\right) \\ &+ \frac{1}{3}\mathrm{Tr}\left(G_0\Sigma G_0\Sigma G_0\Sigma\right) - ...\end{aligned} \tag{A.11}$$

The RHS of this equation is a sum of integrals over the entire phase space and the products under functional traces are convolutions. Therefore we need to use the Moyal product formula, expanding each $G_0\Sigma$ term as:

$$G_0 \star \Sigma \approx G_0\Sigma + \frac{i}{2}\{G_0, \Sigma\} + ... \tag{A.12}$$

where $\star$ is the Moyal product operator and $\{\cdot,\cdot\}$ are the Poisson brackets for the r^μ and k_μ variables. The RHS of the last equation contains ordinary products of G_0 and Σ that are subsequently integrated over the phase-space. For example, in d space-time dimensions we get for the $\mathrm{Tr}\left(G_0\Sigma\right)$ term in the 0-th order of the Moyal product expansion:

$$\int d^d r \frac{d^d k}{(2\pi)^d}\left(\frac{e}{\hbar}A_\mu + k_\lambda B_\mu^\lambda\right)\mathrm{tr}\left(G_0\frac{\partial G_0^{-1}}{\partial k_\mu}\right). \tag{A.13}$$

where 'tr' denotes the ordinary trace over orbital and spin degrees of freedom.

A.3 Electric polarization as a Berry curvature dipole

Let us consider the expression for the polarization of a 2D system with a single filled band,

$$P_e^y = \frac{e\Omega}{(2\pi)^2} i\int_{BZ} d^2\mathbf{k}\langle u_\mathbf{k}|\partial_{k_y}u_\mathbf{k}\rangle \equiv \frac{e\Omega}{(2\pi)^2} iP, \tag{A.14}$$

where Ω is the area of the unit cell. We rewrite the last integral denoted as 'P' as a first moment of the Berry curvature, $\mathcal{F}^{xy} = i\langle\partial_{k_x} u_{\mathbf{k}}|\partial_{k_y} u_{\mathbf{k}}\rangle - i\langle\partial_{k_y} u_{\mathbf{k}}|\partial_{k_x} u_{\mathbf{k}}\rangle$. Consider the following quantity:

$$\begin{aligned} F &= -i\int_{BZ} d^2\mathbf{k}\; k_x \mathcal{F}^{xy} \\ &= \int_{BZ} d^2\mathbf{k}\; k_x \left[\langle\partial_{k_x} u_{\mathbf{k}}|\partial_{k_y} u_{\mathbf{k}}\rangle - \langle\partial_{k_y} u_{\mathbf{k}}|\partial_{k_x} u_{\mathbf{k}}\rangle\right], \end{aligned} \tag{A.15}$$

where we assume $\mathcal{F}^{xy}$ to be smooth and integrable in the Brillouin zone spanning $k_x \in [-\pi/a_x, \pi/a_x)$ and $k_y \in [-\pi/a_y, \pi/a_y)$. Clearly, the integrand jumps in value at the $k_x = \pi/a_x$ boundary of the Brillouin zone and so we will treat the k_x direction as open. Integrating by parts with respect to k_x we find:

$$\begin{aligned} F = &-i\frac{4\pi}{a_x}\oint dk_y \mathcal{A}^y(k_x = \pi/a_x, k_y) \\ &- \int_{BZ} d^2\mathbf{k}\big(\langle u_{\mathbf{k}}|\partial_{k_y} u_{\mathbf{k}}\rangle - \langle\partial_{k_y} u_{\mathbf{k}}|u_{\mathbf{k}}\rangle\big) \\ &- \int_{BZ} d^2\mathbf{k}\; k_x\langle u_{\mathbf{k}}|\partial_{k_x}\partial_{k_y} u_{\mathbf{k}}\rangle \\ &+ \int_{BZ} d^2\mathbf{k}\; k_x\langle\partial_{k_x}\partial_{k_y} u_{\mathbf{k}}|u_{\mathbf{k}}\rangle, \end{aligned} \tag{A.16}$$

where $\mathcal{A}^\mu(\mathbf{k}) = i\langle u_{\mathbf{k}}|\partial_{k_\mu} u_{\mathbf{k}}\rangle$ is the Berry connection. The first term is proportional to a Wilson loop $W^y(k_x = \pi/a_x)$ along the $k_x = \pi/a_x$ line. It is easy to recognize that the second term is twice the integral of interest, $-2P$. Integrating the third and fourth terms by parts with respect to k_y we find:

$$\begin{aligned} &- \int_{BZ} d^2\mathbf{k}\; k_x\big(\langle u_{\mathbf{k}}|\partial_{k_x}\partial_{k_y} u_{\mathbf{k}}\rangle - \langle\partial_{k_x}\partial_{k_y} u_{\mathbf{k}}|u_{\mathbf{k}}\rangle\big) \\ &= \int_{BZ} d^2\mathbf{k}\; k_x\big(\langle\partial_{k_y} u_{\mathbf{k}}|\partial_{k_x} u_{\mathbf{k}}\rangle - \langle\partial_{k_x} u_{\mathbf{k}}|\partial_{k_y} u_{\mathbf{k}}\rangle\big) \\ &= -i\int d^2\mathbf{k}\; k_x \mathcal{F}^{yx} = -F \end{aligned} \tag{A.17}$$

Summing up, we have:

$$\begin{aligned} F &= -i\frac{4\pi}{a_x} W^y - 2P - F \\ &\Downarrow \\ P &= -F - i\frac{2\pi}{a_x} W^y \end{aligned} \tag{A.18}$$

and the polarization is therefore given by

$$\begin{aligned} P_e^y = &-\frac{e\Omega}{(2\pi)^2}\int_{BZ} d^2\mathbf{k}\; k_x \mathcal{F}^{xy} \\ &+ \frac{ea_y}{2\pi}\oint dk_y \mathcal{A}^y(k_x = \pi/a_x, k_y). \end{aligned} \tag{A.19}$$

Performing a similar calculation for P_e^x, we find the general formula

$$P_e^i = \frac{e\Omega}{(2\pi)^2}\varepsilon^{ij}\int d^2\mathbf{k}\; k_j \mathcal{F}^{xy} + ea_i W^i. \tag{A.20}$$

In the case when the system has inversion symmetry, the Wilson loop taken along a high-symmetry line satisfies $W^i(k_j = \pi/a_j) = -W^i(k_j = \pi/a_j)$ and $W^i(k_j = 0) = -W^i(k_j = 0)$ for $i \neq j$ and we find that the non-quantized part of the polarization is accounted for entirely by the Berry curvature's dipole moment.

A.4 Momentum polarization as a Berry curvature quadrupole

Let us consider the following expression for the k_x momentum polarization in the $\hat{y}$ direction of a 2D system with a single filled band:

$$P_{k_x}^y = \frac{\Omega}{(2\pi)^2} i\int_{BZ} d^2\mathbf{k}\; k_x \langle u_\mathbf{k}|\partial_{k_y} u_\mathbf{k}\rangle \equiv \frac{\Omega}{(2\pi)^2} iQ, \tag{A.21}$$

which is just a natural extension of the analogous expression for the charge polarization. We can rewrite the integral denoted as 'Q' as a second moment of the Berry curvature, as we now show. Consider the following quantity:

$$\begin{aligned} F &= -\frac{i}{2}\int_{BZ} d^2\mathbf{k}\; k_x^2 \mathcal{F}^{xy} \\ &= \frac{1}{2}\int_{BZ} d^2\mathbf{k}\; k_x^2 \langle \partial_{k_x} u_\mathbf{k}|\partial_{k_y} u_\mathbf{k}\rangle \\ &\quad - \frac{1}{2}\int_{BZ} d^2\mathbf{k}\; k_x^2 \langle \partial_{k_y} u_\mathbf{k}|\partial_{k_x} u_\mathbf{k}\rangle \end{aligned} \tag{A.22}$$

where we once again assume $\mathcal{F}^{xy}$ to be smooth and integrable in the Brillouin zone spanned by $k_x \in [-\pi/a_x, \pi/a_x)$ and $k_y \in [-\pi/a_y, \pi/a_y)$. Treating the k_x direction of the BZ as open, we integrate by parts with respect to k_x to find:

$$\begin{aligned} F &= -\int_{BZ} d^2\mathbf{k}\; k_x \big(\langle u_\mathbf{k}|\partial_{k_y} u_\mathbf{k}\rangle - \langle \partial_{k_y} u_\mathbf{k}|u_\mathbf{k}\rangle\big) \\ &\quad - \frac{1}{2}\int_{BZ} d^2\mathbf{k}\; k_x^2 \langle u_\mathbf{k}|\partial_{k_x}\partial_{k_y} u_\mathbf{k}\rangle \\ &\quad + \frac{1}{2}\int_{BZ} d^2\mathbf{k}\; k_x^2 \langle \partial_{k_x}\partial_{k_y} u_\mathbf{k}|u_\mathbf{k}\rangle \end{aligned} \tag{A.23}$$

Note the absence of the Wilson loop contribution we found in the previous section, which is a result of the symmetric nature of the function k_x^2. We see again that the first term is twice the integral of interest, $-2Q$.

Integrating the third and fourth terms by parts with respect to k_y we find:

$$\begin{aligned}
&-\frac{1}{2}\int_{BZ} d^2\mathbf{k}\; k_x^2\big(\langle u_\mathbf{k}|\partial_{k_x}\partial_{k_y}u_\mathbf{k}\rangle - \langle\partial_{k_x}\partial_{k_y}u_\mathbf{k}|u_\mathbf{k}\rangle\big)\\
&=\frac{1}{2}\int_{BZ} d^2\mathbf{k}\; k_x^2\big(\langle\partial_{k_y}u_\mathbf{k}|\partial_{k_x}u_\mathbf{k}\rangle - \langle\partial_{k_x}u_\mathbf{k}|\partial_{k_y}u_\mathbf{k}\rangle\big)\\
&=-\frac{i}{2}\int d^2\mathbf{k}\; k_x^2\mathcal{F}^{yx} = \frac{i}{2}\int d^2\mathbf{k}\; k_x^2\mathcal{F}^{xy} = -F
\end{aligned} \tag{A.24}$$

Summing up, we have:

$$\begin{gathered}
F = -2Q - F\\
\Downarrow\\
Q = -F
\end{gathered} \tag{A.25}$$

and we find the polarization to be:

$$P^y_{k_x} = -\frac{\Omega}{8\pi^2}\int_{BZ} d^2\mathbf{k}\; k_x^2\mathcal{F}^{xy}. \tag{A.26}$$

Performing a similar calculation for $P^x_{k_y}$, we find the general relation:

$$P^x_{k_y} = \frac{\Omega}{8\pi^2}\int_{BZ} d^2\mathbf{k}\; k_y^2\mathcal{F}^{xy}. \tag{A.27}$$

A.5 Responses for 1D systems

Here we discuss responses of isolated one-dimensional metals with a fixed number of electrons N_e. For the cases we consider, the Fermi surface consists of an even integer number N_F of Fermi points with chiralities $\chi_a = \text{sgn}\, v_a$, where v_a is the Fermi velocity of the a-th Fermi point. From the Fermion doubling theorem [200] the total chirality vanishes, $\chi = \sum_{a=1}^{N_F}\chi_a = 0$. We wish to define three more quantities besides χ that characterize 1D metals:

$$\mathcal{P}_x = \sum_{a=1}^{N_F}\chi_a k_{Fx}^{(a)} \tag{A.28}$$

$$\mathcal{Q}_{xx} = \sum_{a=1}^{N_F}\chi_a\left(k_{Fx}^{(a)}\right)^2 \tag{A.29}$$

$$\mathcal{O}_{xxx} = \sum_{a=1}^{N_F}\chi_a\left(k_{Fx}^{(a)}\right)^3. \tag{A.30}$$

These three quantities represent the momentum space dipole, quadrupole, and octupole moments of the Fermi-points, respectively (see Fig. 2.3(a), (b), (c)). We could go beyond the octupole moment to any higher

moment, but for brevity we stop at this order. Importantly, these momentum moments are related to the ground state properties of the metal. The total charge is proportional to the dipole moment,

$$Q = \frac{eL}{2\pi}\mathcal{P}_x, \tag{A.31}$$

the total momentum $\langle \hbar k_x \rangle$ is proportional to the quadrupole moment,

$$P_x = \frac{1}{2}\frac{\hbar L}{2\pi}\mathcal{Q}_{xx}, \tag{A.32}$$

the total momentum squared $\langle (\hbar k_x)^2 \rangle$ is proportional to the octupole moment,

$$P_{xx} = \frac{1}{3}\frac{\hbar^2 L}{2\pi}\mathcal{O}_{xxx}, \tag{A.33}$$

and so on for higher moments. From this we see that each of the momentum-space moments determines the density of higher and higher powers of momentum, starting at zeroth order where the charge is proportional to the momentum dipole. There are two important caveats to note: (i) in order for the n-th moment and its associated physical quantity to be independent of the origin of the BZ, all lower moments must vanish, and (ii) these results hold only up to constants independent of the set of $k_{Fx}^{(a)}$ which result from contributions of filled bands.

Here we consider a family of anomalous responses to various gauge fields in 1D metals. We have already considered some of these anomalies in Sec. 2.4, and we go into more detail in this Appendix. To proceed, we introduce a family of gauge fields $\mathfrak{e}, \mathfrak{e}^{\alpha}, \mathfrak{e}^{\alpha\beta}, \mathfrak{e}^{\alpha\beta\gamma}, \ldots$. Each of these fields couples to charges that are powers of momentum. The field $\mathfrak{e}$ we identify with the family of electromagnetic gauge field one-forms $\frac{e}{\hbar}A$, as it couples to zero powers of momentum. The field $\mathfrak{e}^{\alpha}$ is the translation gauge field we have extensively discussed, and it couples linearly to momentum k_α. In general the fields $\mathfrak{e}^{\alpha\beta\gamma\ldots\zeta}$ couple to the momentum charges $k_\alpha k_\beta k_\gamma \ldots k_\zeta$. Since we consider momentum-space moments only up to the octupole moment $\mathcal{O}_{xxx}$, we consider gauge fields only up to $\mathfrak{e}^{\alpha\beta\gamma}$.

Using these gauge fields we can consider the following set of actions

$$S_\chi = \frac{e^2\chi}{2\pi\hbar}\int dxdt\, A_0 A_x \tag{A.34}$$

$$S_{\mathcal{P}} = \frac{e}{2\pi}\int dxdt\, \mathcal{P}_x(\mathfrak{e}_0^x A_x - \mathfrak{e}_x^x A_0) \tag{A.35}$$

$$S_{\mathcal{Q}} = \frac{\hbar}{2\pi}\int dxdt\, \mathcal{Q}_{xx}\left[\tfrac{1}{2}\mathfrak{e}_0^x\mathfrak{e}_x^x + e(\mathfrak{e}_0^{xx}A_x - \mathfrak{e}_x^{xx}A_0)\right] \tag{A.36}$$

$$S_{\mathcal{O}} = \frac{\hbar^2}{2\pi}\int dxdt\, \mathcal{O}_{xxx}\left[\tfrac{1}{3}(\mathfrak{e}_0^x\mathfrak{e}_x^{xx} - \mathfrak{e}_x^x\mathfrak{e}_0^{xx}) + e(\mathfrak{e}_0^{xxx}A_x - \mathfrak{e}_x^{xxx}A_0)\right]. \tag{A.37}$$

These actions capture two important phenomena associated to each of the momentum moments: (i) the connection to the assiociated ground state quantity, i.e., Q, P_x, and P_{xx}, and (ii) the shift in Q, P_x, P_{xx}, and P_{xxx} when an electric field is turned on. As a first example let us consider S_χ. We can calculate the electromagnetic charge density and current to find $\rho = \frac{e^2\chi}{h}A_x$ and $j^x = \frac{e^2\chi}{h}A_0$. If we use these results to calculate the conservation law we find

$$\partial_\mu j^\mu = \frac{e^2\chi}{h}E_x, \tag{A.38}$$

which is just the usual $U(1)$ anomaly of a chiral fermion. The fact that $\chi = 0$ for any lattice model has two immediate consequences: (i) the $U(1)$ charge anomaly above vanishes for lattice systems, and (ii) the momentum dipole moment $\mathcal{P}_x$ is well-defined and independent of the choice of momentum space origin. Just as for conventional electric or magnetic multipole moments, in order for the n-th moment to be well-defined, all of the lower moments must vanish. As such, the action $S_{\mathcal{Q}}$ is well-defined only if $\chi = \mathcal{P}_x = 0$. Similarly, for $S_{\mathcal{O}}$ to be well-defined we must have $\chi = \mathcal{P}_x = \mathcal{Q}_{xx} = 0$.

Now let us consider each of the remaining actions in turn. We begin with $S_{\mathcal{P}}$. As mentioned in Sec. 2.4, $\mathcal{P}_x$ is related to the charge density of a 1D metal via $\rho = -\frac{e}{2\pi}\mathcal{P}_x\mathfrak{e}_x^x$, and the momentum density via $\mathcal{J}_x^0 = \frac{e}{2\pi}\mathcal{P}_x A_x$ [36]. Assuming that our system is translation invariant, let us consider stretching our system via a time-dependent $\mathfrak{e}_x^x$. During this process the total number of electrons cannot change. Working from the charge density we find

$$\partial_t\rho = -\frac{e}{2\pi}\partial_t(\mathcal{P}_x\mathfrak{e}_x^x). \tag{A.39}$$

Naively we are just changing $\mathfrak{e}_x^x$, however if we stretch the system at fixed particle number the Fermi momenta will change inversely. We therefore have $\partial_t\mathcal{P}_x = -\frac{\mathcal{P}_x}{\mathfrak{e}_x^x}\partial_t\mathfrak{e}_x^x$. Inserting this into Eq. A.39 we find

$$\partial_t\rho = -\frac{e}{2\pi}\left(-\mathfrak{e}_x^x\frac{\mathcal{P}_x}{\mathfrak{e}_x^x}\partial_t\mathfrak{e}_x^x + \mathcal{P}_x\partial_t\mathfrak{e}_x^x\right) = 0. \tag{A.40}$$

Using this equation we find

$$\Delta Q = \int dt \int dx\, \partial_t \rho = 0 \tag{A.41}$$

as we expect for a fixed number of electrons.

To be self-contained, let us reiterate our argument from the main text. At a fixed particle number we know the total charge cannot change. Intuitively we might expect that the density should decrease if we stretch the system. However, the quantity ρ above, which is defined as $\frac{\delta S}{\delta A_0}$ is not a scalar density. For general geometries the scalar charge density would be defined as

$$\bar{\rho} = \frac{1}{\mathfrak{e}^x_x} \frac{\delta S}{\delta A_0}. \tag{A.42}$$

To calculate the total charge we would then use

$$Q = \int dx\, \mathfrak{e}^x_x \bar{\rho} = \int dx\, \rho. \tag{A.43}$$

Indeed, the scalar charge density $\bar{\rho}$ will decrease as the system is stretched since $\partial_t \bar{\rho} \propto \partial_t \mathcal{P}_x$, which decreases as the system size increases at fixed electron number.

Next, we can see that another consequence of a non-vanishing $\mathcal{P}_x$ is a mixed crystalline-electromagnetic anomaly. To illustrate this, let us consider the change in momentum-density in an applied electric field generated by a change in A_x. We find

$$\partial_t \mathcal{J}^x_0 = \frac{e}{2\pi} \partial_t (\mathcal{P}_x A_x). \tag{A.44}$$

Unlike the previous case, when we turn on a non-vanishing A_x the dipole $\mathcal{P}_x$ does not change. Hence we find the anomalous conservation law

$$\partial_\mu \mathcal{J}^\mu_x \quad = \quad \frac{e\mathcal{P}_x}{2\pi} E_x. \tag{A.45}$$

Moving on, let us discuss the action $S_{\mathcal{Q}}$. To have a well-defined quadrupole moment $\mathcal{Q}_{xx}$ we need $\mathcal{P}_x = 0$. This scenario can happen non-trivially in systems with more than one occupied band near the Fermi-level, as shown in Fig. 2.3(b). As long as any perturbations we apply keep χ and $\mathcal{P}_x$ fixed to zero, then the phenomena associated to $\mathcal{Q}_{xx}$ are physically meaningful. From this action we can derive three separate

conservation laws:

$$\partial_t \rho = \frac{e}{2\pi}\partial_t(\mathcal{Q}_{xx}\mathfrak{e}_x^{xx}) \tag{A.46}$$

$$\partial_t \mathcal{J}_x^0 = \frac{\hbar}{4\pi}\partial_t(\mathcal{Q}_{xx}\mathfrak{e}_x^{x}) \tag{A.47}$$

$$\partial_t \mathcal{J}_{xx}^0 = -\frac{e}{2\pi}\partial_t(\mathcal{Q}_{xx}A_x), \tag{A.48}$$

where the quantities P_x and P_{xx} in Eqs. A.32 and A.33 are determined by $P_x = \int \mathcal{J}_x^0 dx, P_{xx} = \int \mathcal{J}_{xx}^0 dx$. The first and third equations generate a kind of mixed anomaly, so let us discuss those first. For fixed electron number we know that $\partial_t \rho$ must vanish, which implies that $\partial_t \mathcal{Q}_{xx} = -\frac{\mathcal{Q}_{xx}}{\mathfrak{e}_x^{xx}}\partial_t \mathfrak{e}_x^{xx}$. Thus the first equation is simply $\partial_t \rho = 0$. For the third equation, since changing A_x while keeping $\chi = \mathcal{P}_x = 0$ does not change $\mathcal{Q}_{xx}$, we have

$$\partial_\mu \mathcal{J}_{xx}^\mu = \frac{e\mathcal{Q}_{xx}}{2\pi}E_x. \tag{A.49}$$

This implies that if we insert flux into the system, then the momentum quadrupole moment changes, i.e., the expectation value of the momentum squared in the resulting excited state changes while the total charge and momentum remain fixed.

Returning to the middle equation, we consider the change in momentum as we stretch the system. Crucially we use the relationship $\partial_t \mathcal{Q}_{xx} = -2\frac{\mathcal{Q}_{xx}}{\mathfrak{e}_x^x}\partial_t \mathfrak{e}_x^x$ (heuristically, this comes from the fact that quadratic powers of momentum are proportional to L^{-2}). Inserting this in Eq. A.47 we find

$$\partial_t \mathcal{J}_x^0 = -\frac{\hbar\mathcal{Q}_{xx}}{2\pi}\partial_t \mathfrak{e}_x^x + \frac{\hbar\mathcal{Q}_{xx}}{4\pi}\partial_t \mathfrak{e}_x^x = -\frac{\hbar\mathcal{Q}_{xx}}{4\pi}\partial_t \mathfrak{e}_x^x. \tag{A.50}$$

We can interpret the first contribution in the middle section of the above equation as coming from the change in the Fermi points $k_{Fx}^{(a)}$ induced by changing $\mathfrak{e}_x^x$. The second contribution arises from the existence of a non-vanishing ground state momentum density when the length of the system is changed. Note that while the coefficient of the final result is the same magnitude as Eq. A.47, the sign is opposite. The full conservation law becomes

$$\partial_\mu \mathcal{J}_x^\mu = \frac{\hbar\mathcal{Q}_{xx}}{4\pi}\mathcal{E}_x^x. \tag{A.51}$$

Finally, if we have a scenario where $\chi, \mathcal{P}_x$, and $\mathcal{Q}_{xx}$ are all vanishing, and remain vanishing after applying any gauge fields, then the phenomena associated to $\mathcal{O}_{xxx}$ become physically relevant. Such a scenario can exist in a 1D metal where four bands appear at the Fermi surface (see Fig. 2.3(c)). Just as above, let us

consider the conservation laws we can derive from $S_{\mathcal{O}}$:

$$\partial_t \rho = -\frac{e\hbar^2}{2\pi}\partial_t(\mathcal{O}_{xxx}\mathfrak{e}_x^{xxx}) \tag{A.52}$$

$$\partial_t \mathcal{J}_x^0 = \frac{\hbar^2}{6\pi}\partial_t(\mathcal{O}_{xxx}\mathfrak{e}_x^{xx}) \tag{A.53}$$

$$\partial_t \mathcal{J}_{xx}^0 = -\frac{\hbar^2}{6\pi}\partial_t(\mathcal{O}_{xxx}\mathfrak{e}_x^{x}) \tag{A.54}$$

$$\partial_t \mathcal{J}_{xxx}^0 = \frac{e\hbar^2}{2\pi}\partial_t(\mathcal{O}_{xxx}A_x). \tag{A.55}$$

We can use identical arguments as above to determine that $\partial_t \mathcal{O}_{xxx} = -\frac{\mathcal{O}_{xxx}}{\mathfrak{e}_x^{xxx}}\partial_t \mathfrak{e}_x^{xxx}$ so that the total charge remains fixed. Under a change of A_x we have $\partial_t \mathcal{O}_{xxx} = 0$, and under a change in $\mathfrak{e}_x^x$ we can determine that $\partial_t \mathcal{O}_{xxx} = -3\frac{\mathcal{O}_{xxx}}{\mathfrak{e}_x^x}\partial_t \mathfrak{e}_x^x$. Using these relationships we can reduce three of the conservation laws to find

$$\partial_\mu j^\mu = 0 \tag{A.56}$$

$$\partial_\mu \mathcal{J}_{xx}^\mu = -\frac{\hbar^2 \mathcal{O}_{xxx}}{3\pi}\mathcal{E}_x^x \tag{A.57}$$

$$\partial_\mu \mathcal{J}_{xxx}^\mu = -\frac{e\hbar^2 \mathcal{O}_{xxx}}{2\pi}E_x. \tag{A.58}$$

To get the final conservation law we need to determine how $\mathcal{O}_{xxx}$ changes when $\mathfrak{e}_x^{xx}$ changes. From counting powers of length we find $\partial_t \mathcal{O}_{xxx} = -\frac{3}{2}\frac{\mathcal{O}_{xxx}}{\mathfrak{e}_x^{xx}}\partial_t \mathfrak{e}_x^{xx}$. Inserting this into the conservation law for ρ^x generates

$$\partial_\mu \mathcal{J}_x^\mu = \frac{\hbar^2 \mathcal{O}_{xxx}}{12\pi}\mathcal{E}_x^{xx}. \tag{A.59}$$

In summary, while the anomalous responses we have written in this section are formally correct, it is impossible to uniquely determine the coefficients $\mathcal{P}_x, \mathcal{Q}_{xx}$, or $\mathcal{O}_{xxx}$ unless all lower moments vanish (starting with the chirality χ). Additionally, even if the lower moments are initially vanishing, turning on gauge fields may generate these moments anomalously and hence invalidate the higher moments. We expect that under the assumptions of vanishing lower moments that the highest moment will generate the physical responses described above.

Appendix B

Supplementary information for Chapter 5

This chapter is adapted from Julian May-Mann, Mark R. Hirsbrunner, Lei Gioia, and Taylor Hughes, arXiv preprint arXiv:2403.00055.

B.1 Disclination charge parity and the disclination filling anomaly in layered systems

In this Appendix we discuss why the disclination charge parity is not a meaningful quantity for inversion-symmetric insulators, as it depends on the choice of inversion center for systems with open boundaries. However, the difference between the disclination charge parity for open and periodic boundary conditions (referred to in the main text as the disclination filling anomaly) does not depend on the inversion center, and is therefore a physically meaningful quantity. We establish this by considering layered insulators. Although we are only considering specific systems, the dependence of the disclination charge parity on the choice of inversion center is general. We recall from the main text that what we mean by a layered insulator is one that is adiabatically connected to a limit of decoupled layers where electrons are not hybrdized between different unit cells in the z-direction.

To this end, let us consider an inversion-symmetric 3D insulator composed of N_z layers of 2D insulators, stacked along the z-direction. We further take the system to have open boundary conditions in the z-direction. For such a system, there are two choices of inversion symmetry that differ with respect to their inversion center. First, there is inversion symmetry where the inversion center is in a given layer, such that

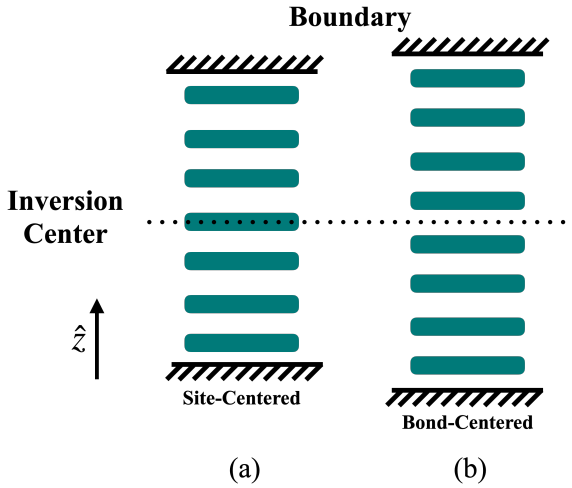

Figure B.1: An inversion-symmetric stack of 2D layers (green) for site-centered inversion symmetry (a) and bond-centered inversion symmetry (b). For site-centered inversion symmetry, one layer maps onto itself under inversion symmetry, while other layers map onto a partner, such that the total number of layers, N_z is odd. For bond-centered inversion symmetry, all layers map onto a partner, such that the total number of layers, N_z is even.

this layer maps to itself under inversion symmetry. This was referred to as site-centered inversion symmetry in the main text. Second, there is inversion symmetry where the inversion center is in-between two adjacent layers. This was referred to as bond-centered inversion symmetry in the main text. For site-centered inversion symmetry and open boundaries, N_z must be odd, since under inversion symmetry, one layer maps to itself, while all other layers must map onto an inversion symmetry related partner. Similarly, for bond-centered inversion symmetry, N_z must be even, since all layers map onto an inversion symmetry related partner. The two inversion-symmetric stacking configurations are shown in Fig. B.1(a),(b).

Consider the disclination response of the layered insulator. For a 3D layered insulator, the disclination response of the full system is simply the sum of responses of the 2D layers. Each 2D layer is described by a 2D dWZ term, with discrete shift $\mathcal{S}_{\text{2D}}$. For spin-1/2 fermions with TRS, $\mathcal{S}_{\text{2D}}$ is quantized as an even integer. Because of the 2D dWZ response, a Θ_F disclination line binds charge $Q_{\text{disc-2D}} = \mathcal{S}_{\text{2D}} \frac{\Theta_F}{2\pi}$ mod (2) on each layer, where the mod (2) factor reflects that it is possible to locally add a Kramers degenerate pair of electrons to the disclination core. The total disclination charge of the full 3D system is then $Q_{\text{disc-3D}} = N\mathcal{S}_{\text{2D}} \frac{\Theta_F}{2\pi}$ mod (2). For a finite size system of spin-1/2 fermions with time-reversal symmetry (TRS), the disclination charge parity is equal to the total charge on disclination line mod$(2\frac{\Theta_F}{\pi})$,

$$Q_{\text{disc-3D}} \bmod \left(2\frac{\Theta_F}{\pi}\right) = \mathcal{S}_{\text{2D}} N_z \frac{\Theta_F}{2\pi} \bmod \left(2\frac{\Theta_F}{\pi}\right), \tag{B.1}$$

where we have used the fact that Θ_F is a multiple of $2\pi/n$ for C_n symmetric insulators. The disclination

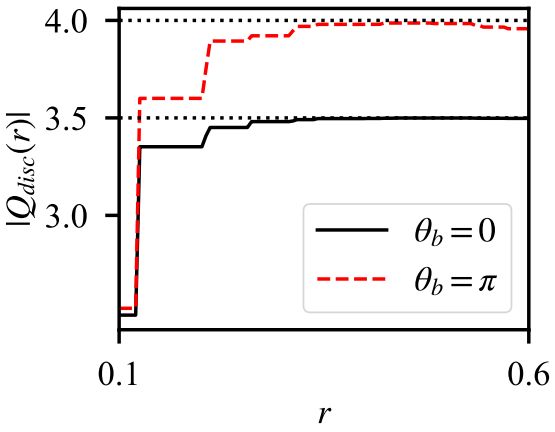

Figure B.2: The charge bound to a $\Theta_F = \pi/2$ disclination for a Dirac-CDW insulator as a function of the integration radius distance r with $Q = \pi/2$, $b_{xy} = 1$, $\Delta_{\text{surf}} = 0.25$, $\Delta_s = 0$, $\Delta_b = 0.5$, $N_x = 15$, and $N_z = 14$. The radius r is scaled such that the farthest point from the disclination core is at $r = 1$. Note that the r-axis only extends from 0.1 to 0.6.

charge parity is therefore zero when $N_z\mathcal{S}_{2D}/2$ is even, and non-zero when $N_z\mathcal{S}_{2D}/2$ is odd. From this, we can conclude the following: when $\mathcal{S}_{2D}/2$ is even, the disclination charge parity always vanishes, but when $\mathcal{S}_{2D}/2$ is odd, the disclination charge parity vanishes when N_z is even and is non-zero when N_z is odd. So when $\mathcal{S}_{2D}/2$ is odd, the disclination charge parity always vanishes for bond centered inversion symmetry, and is always non-zero for site-centered inversion symmetry. This occurs for an insulator composed of quantum spin Hall layers, each of which have $\mathcal{S}_{2D} = 2$.

Having established that the disclination charge parity depends on the choice of inversion center, let us now consider the disclination filling anomaly. To do this, we will take the layered system and "sew" the top and bottom layers to one another such that the system has periodic boundaries in the z-direction. For a layered system, the sewing procedure is trivial by definition and will not change the total disclination charge, or, by extension, the disclination charge parity. The disclination filling anomaly will therefore necessarily vanish for all layered systems, regardless of the choice of inversion center or the value of $\mathcal{S}_{2D}$.

B.2 Details of the numerics

Here we discuss the details of how we calculate the charge bound to a disclination and the extrapolations in system size that we performed. To calculate the charge bound to a disclination, we sum the charge on all lattice sites in each layer that are within some radius from the disclination core. In Fig. B.2 we plot the charge bound to a disclination as a function of the integration radius for a Dirac-CDW insulator

with $Q = \pi/2$, $N_x = 15$, $N_z = 14$, $b_{xy} = 1$, $\Delta_{\text{surf}} = 0.25$, $\Delta_s = 0$, $\Delta_b = 0.5$, and both $\theta_b = 0$ and $\theta_b = \pi$. The radius r is scaled such that the farthest point from the disclination core in the lattice is at $r = 1$. The disclination charges approach the theoretical predictions, marked by dashed horizontal lines, for roughly $r > 0.3$, indicating the exponential localization of the disclination charge. The disclination charge approaches zero for both small and large r, and the largest values of the disclination charge generally approach the theoretical predictions, except for very small system sizes. However, the integration radius at which the disclination charge most closely obtains the theoretical prediction varies significantly as a function of system size and other parameters. As such, we always calculate the disclination charge using a range of integration radius and report the maximal absolute value.

To diminish the impact of finite-size effects, we calculated the charges for each case enumerated in Table 5.1 over a range of system sizes and extrapolated to the infinite system-size limit. We found that effects arising from the finite extent of the lattice in the z-direction were minimal, so for each calculation we fixed N_z and varied N_x, the side length of the disclinated lattice. In Table B.1 we plot the disclination charges as a function of N_x along with fits to a decaying exponential, $|Q_{\text{disc}}(N_x)| = Q_\infty + be^{-cN_x}$. We plot the infinite system size limit, Q_∞, with red dashed lines and report the values and uncertainties in the insets. The values reported in Table 5.1 are the values of Q_∞ rounded to the nearest half integer, which produces less than a 1% error in all cases.

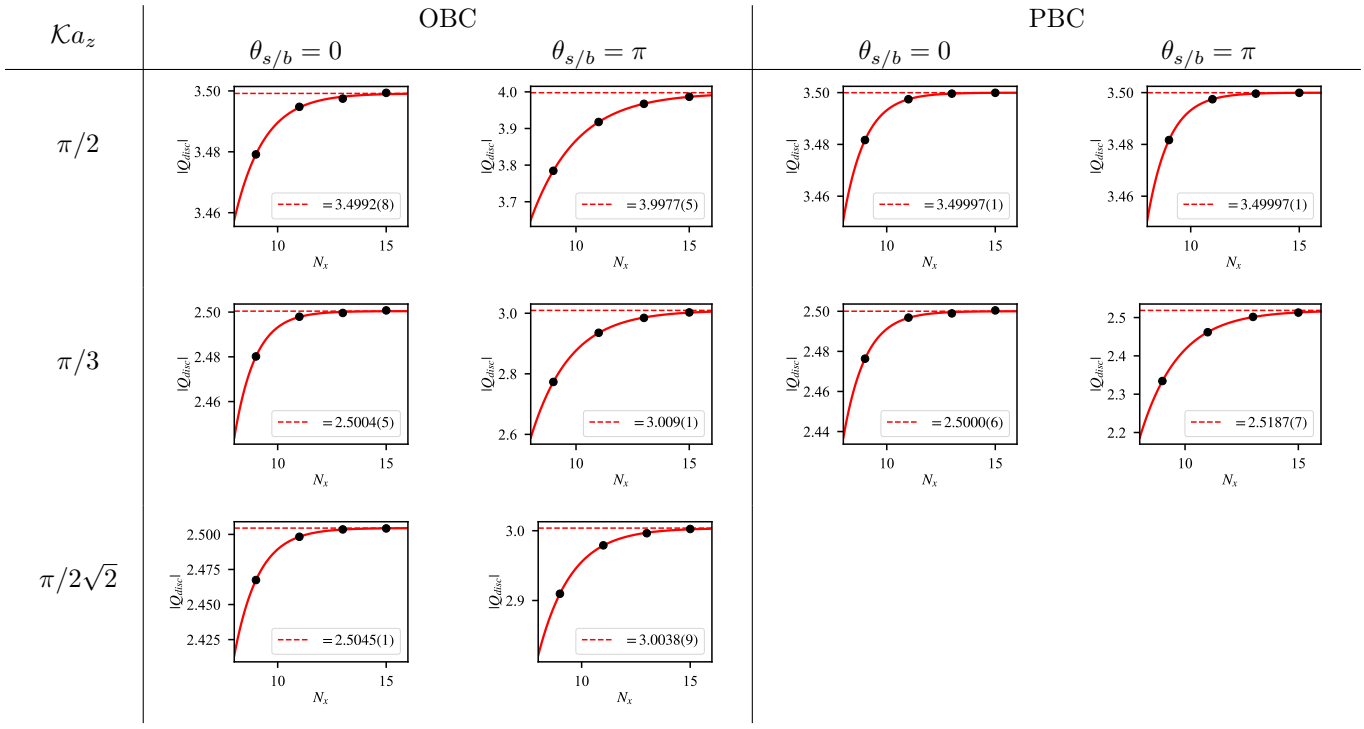

Table B.1: System size extrapolations of the charge bound to a $\Theta_F = \pi/2$ disclination for $\mathcal{K} = \pi/2$, $\pi/3$, and $\pi/2\sqrt{2}$ with $\theta_{s/b} = 0$ and π for both open and periodic boundary conditions. For each calculation we used $b_{xy} = 1$, $\Delta_{\text{surf}} = 0.25$, and $\Delta_s = 0$. The system size along the disclination was set to $N_z = 14$ for $\mathcal{K} = \pi/2$ and $N_z = 15$ for $\mathcal{K} = \pi/3$ and $\pi/2\sqrt{2}$. The solid red lines are fits to a decaying exponential, $|Q_{\text{disc}}(N_x) = Q_\infty + be^{-cN_x}$. The value and uncertainty of the large-N_x limit, Q_∞, is reported in the legend and plotted with a red dashed line.

References

[1] K. v. Klitzing, G. Dorda, and M. Pepper, "New method for high-accuracy determination of the fine-structure constant based on quantized hall resistance," *Phys. Rev. Lett.*, vol. 45, pp. 494–497, 6 Aug. 1980. DOI: 10.1103/PhysRevLett.45.494. [Online]. Available: https://link.aps.org/doi/10.1103/PhysRevLett.45.494.

[2] B. I. Halperin, "Quantized hall conductance, current-carrying edge states, and the existence of extended states in a two-dimensional disordered potential," *Phys. Rev. B*, vol. 25, pp. 2185–2190, 4 Feb. 1982. DOI: 10.1103/PhysRevB.25.2185.

[3] R. B. Laughlin, "Quantized hall conductivity in two dimensions," *Phys. Rev. B*, vol. 23, pp. 5632–5633, 10 May 1981. DOI: 10.1103/PhysRevB.23.5632.

[4] D. J. Thouless, M. Kohmoto, M. P. Nightingale, and M. den Nijs, "Quantized hall conductance in a two-dimensional periodic potential," *Phys. Rev. Lett.*, vol. 49, pp. 405–408, 6 Aug. 1982. DOI: 10.1103/PhysRevLett.49.405.

[5] D. J. Thouless, "Quantization of particle transport," *Phys. Rev. B*, vol. 27, pp. 6083–6087, 10 May 1983. DOI: 10.1103/PhysRevB.27.6083.

[6] D. C. Tsui, H. L. Stormer, and A. C. Gossard, "Two-dimensional magnetotransport in the extreme quantum limit," *Phys. Rev. Lett.*, vol. 48, pp. 1559–1562, 22 May 1982. DOI: 10.1103/PhysRevLett.48.1559. [Online]. Available: https://link.aps.org/doi/10.1103/PhysRevLett.48.1559.

[7] A. P. Schnyder, S. Ryu, A. Furusaki, and A. W. W. Ludwig, "Classification of topological insulators and superconductors in three spatial dimensions," *Phys. Rev. B*, vol. 78, p. 195 125, 19 Nov. 2008. DOI: 10.1103/PhysRevB.78.195125.

[8] Z.-C. Gu and X.-G. Wen, "Tensor-entanglement-filtering renormalization approach and symmetry-protected topological order," *Phys. Rev. B*, vol. 80, p. 155 131, 15 Oct. 2009. DOI: 10.1103/PhysRevB.80.155131.

[9] M. Z. Hasan and C. L. Kane, "Colloquium: Topological insulators," *Rev. Mod. Phys.*, vol. 82, pp. 3045–3067, 4 Nov. 2010. DOI: 10.1103/RevModPhys.82.3045.

[10] X.-L. Qi and S.-C. Zhang, "Topological insulators and superconductors," *Rev. Mod. Phys.*, vol. 83, pp. 1057–1110, 4 Oct. 2011. DOI: 10.1103/RevModPhys.83.1057.

[11] M. Z. Hasan and J. E. Moore, "Three-dimensional topological insulators," *Annual Review of Condensed Matter Physics*, vol. 2, no. Volume 2, 2011, pp. 55–78, 2011. DOI: https://doi.org/10.1146/annurev-conmatphys-062910-140432.

[12] F. Pollmann, E. Berg, A. M. Turner, and M. Oshikawa, "Symmetry protection of topological phases in one-dimensional quantum spin systems," *Phys. Rev. B*, vol. 85, p. 075 125, 7 Feb. 2012. DOI: 10.1103/PhysRevB.85.075125.

[13] B. A. Bernevig, *Topological insulators and topological superconductors*. Princeton, NJ: Princeton University Press, Apr. 2013.

[14] X. Chen, Z.-C. Gu, Z.-X. Liu, and X.-G. Wen, "Symmetry protected topological orders and the group cohomology of their symmetry group," *Phys. Rev. B*, vol. 87, p. 155 114, 15 Apr. 2013. DOI: 10.1103/PhysRevB.87.155114.

[15] T. Senthil, "Symmetry-protected topological phases of quantum matter," *Annual Review of Condensed Matter Physics*, vol. 6, no. Volume 6, 2015, pp. 299–324, 2015. DOI: https://doi.org/10.1146/annurev-conmatphys-031214-014740.

[16] C.-K. Chiu, J. C. Y. Teo, A. P. Schnyder, and S. Ryu, "Classification of topological quantum matter with symmetries," *Rev. Mod. Phys.*, vol. 88, p. 035 005, 3 Aug. 2016. DOI: 10.1103/RevModPhys.88.035005.

[17] M. Sato and Y. Ando, "Topological superconductors: A review," *Reports on Progress in Physics*, vol. 80, no. 7, p. 076 501, 2017. DOI: 10.1088/1361-6633/aa6ac7.

[18] X. G. WEN, "Topological orders in rigid states," *International Journal of Modern Physics B*, vol. 04, no. 02, pp. 239–271, 1990. DOI: 10.1142/S0217979290000139.

[19] X. Chen, Z.-C. Gu, and X.-G. Wen, "Local unitary transformation, long-range quantum entanglement, wave function renormalization, and topological order," *Phys. Rev. B*, vol. 82, p. 155 138, 15 Oct. 2010. DOI: 10.1103/PhysRevB.82.155138.

[20] X.-G. Wen, "Topological order: From long-range entangled quantum matter to a unified origin of light and electrons," *International Scholarly Research Notices*, vol. 2013, 2013. DOI: 10.1155/2013/198710.

[21] X.-G. Wen, "Colloquium: Zoo of quantum-topological phases of matter," *Rev. Mod. Phys.*, vol. 89, p. 041 004, 4 Dec. 2017. DOI: 10.1103/RevModPhys.89.041004.

[22] W. P. Su, J. R. Schrieffer, and A. J. Heeger, "Solitons in polyacetylene," *Phys. Rev. Lett.*, vol. 42, pp. 1698–1701, 25 Jun. 1979. DOI: 10.1103/PhysRevLett.42.1698.

[23] W. P. Su, J. R. Schrieffer, and A. J. Heeger, "Soliton excitations in polyacetylene," *Phys. Rev. B*, vol. 22, pp. 2099–2111, 4 Aug. 1980. DOI: 10.1103/PhysRevB.22.2099. [Online]. Available: https://link.aps.org/doi/10.1103/PhysRevB.22.2099.

[24] J. K. Asbóth, L. Oroszlány, and A. Pályi, "A short course on topological insulators," *Lecture notes in physics*, vol. 919, p. 166, 2016.

[25] F. Wilczek, "Two applications of axion electrodynamics," *Phys. Rev. Lett.*, vol. 58, pp. 1799–1802, 18 May 1987. DOI: 10.1103/PhysRevLett.58.1799.

[26] X.-L. Qi, T. L. Hughes, and S.-C. Zhang, "Topological field theory of time-reversal invariant insulators," *Phys. Rev. B*, vol. 78, p. 195 424, 19 Nov. 2008. DOI: 10.1103/PhysRevB.78.195424.

[27] A. M. Essin, J. E. Moore, and D. Vanderbilt, "Magnetoelectric Polarizability and Axion Electrodynamics in Crystalline Insulators," *Phys. Rev. Lett.*, vol. 102, no. 14, Apr. 2009. DOI: 10.1103/PhysRevLett.102.146805.

[28] N. P. Armitage and L. Wu, "On the matter of topological insulators as magnetoelectrics," *SciPost Physics*, vol. 6, no. 4, p. 046, 2019. DOI: 10.21468/SciPostPhys.6.4.046.

[29] P. Streda, "Theory of quantised Hall conductivity in two dimensions," *Journal of Physics C: Solid State Physics*, vol. 15, no. 22, p. L717, 1982. DOI: 10.1088/0022-3719/15/22/005.

[30] P. Streda, "Quantised hall effect in a two-dimensional periodic potential," *Journal of Physics C: Solid State Physics*, vol. 15, no. 36, p. L1299, 1982. DOI: 10.1088/0022-3719/15/36/006.

[31] B. A. Bernevig and S.-C. Zhang, "Quantum spin hall effect," *Phys. Rev. Lett.*, vol. 96, p. 106 802, 10 Mar. 2006. DOI: 10.1103/PhysRevLett.96.106802.

[32] F. D. M. Haldane, "Berry curvature on the fermi surface: Anomalous hall effect as a topological fermi-liquid property," *Phys. Rev. Lett.*, vol. 93, p. 206 602, 20 Nov. 2004. DOI: 10.1103/PhysRevLett.93.206602.

[33] A. Burkov and L. Balents, "Weyl semimetal in a topological insulator multilayer," *Phys. Rev. Lett.*, vol. 107, no. 12, p. 127 205, 2011. DOI: 10.1103/PhysRevLett.107.127205.

[34] X. Wan, A. M. Turner, A. Vishwanath, and S. Y. Savrasov, "Topological semimetal and fermi-arc surface states in the electronic structure of pyrochlore iridates," *Phys. Rev. B*, vol. 83, no. 20, p. 205 101, 2011. DOI: 10.1103/PhysRevB.83.205101.

[35] A. A. Zyuzin and A. A. Burkov, "Topological response in Weyl semimetals and the chiral anomaly," *Phys. Rev. B*, vol. 86, no. 11, p. 115 133, Sep. 2012. DOI: 10.1103/PhysRevB.86.115133.

[36] S. T. Ramamurthy and T. L. Hughes, "Patterns of electromagnetic response in topological semimetals," *Phys. Rev. B*, vol. 92, no. 8, p. 085 105, Aug. 2015. DOI: 10.1103/PhysRevB.92.085105.

[37] S. T. Ramamurthy and T. L. Hughes, "Quasitopological electromagnetic response of line-node semimetals," *Phys. Rev. B*, vol. 95, p. 075 138, 7 Feb. 2017. DOI: 10.1103/PhysRevB.95.075138.

[38] B. I. Halperin, "Possible states for a three-dimensional electron gas in a strong magnetic field," *Jpn. J. Appl. Phys. Suppl.*, vol. 26, no. S3-3, p. 1913, 1987. DOI: 10.7567/JJAPS.26S3.1913.

[39] L. Fu, C. L. Kane, and E. J. Mele, "Topological insulators in three dimensions," *Phys. Rev. Lett.*, vol. 98, no. 10, p. 106 803, 2007. DOI: 10.1103/PhysRevLett.98.106803.

[40] Y. Ran, Y. Zhang, and A. Vishwanath, "One-dimensional topologically protected modes in topological insulators with lattice dislocations," *Nature Physics*, vol. 5, no. 4, pp. 298–303, 2009. DOI: 10.1038/nphys1220.

[41] A. Kitaev, "Periodic table for topological insulators and superconductors," *AIP Conference Proceedings*, vol. 1134, no. 1, pp. 22–30, May 2009. DOI: 10.1063/1.3149495.

[42] S. Ryu, A. P. Schnyder, A. Furusaki, and A. W. Ludwig, "Topological insulators and superconductors: Tenfold way and dimensional hierarchy," *New Journal of Physics*, vol. 12, no. 6, p. 065 010, 2010. DOI: 10.1088/1367-2630/12/6/065010.

[43] L. Fu, "Topological crystalline insulators," *Phys. Rev. Lett.*, vol. 106, p. 106 802, 10 Mar. 2011. DOI: 10.1103/PhysRevLett.106.106802.

[44] T. L. Hughes, E. Prodan, and B. A. Bernevig, "Inversion-symmetric topological insulators," *Phys. Rev. B*, vol. 83, p. 245 132, 24 Jun. 2011. DOI: 10.1103/PhysRevB.83.245132.

[45] C.-K. Chiu, H. Yao, and S. Ryu, "Classification of topological insulators and superconductors in the presence of reflection symmetry," *Phys. Rev. B*, vol. 88, p. 075 142, 7 Aug. 2013. DOI: 10.1103/PhysRevB.88.075142.

[46] T. Morimoto and A. Furusaki, "Topological classification with additional symmetries from clifford algebras," *Phys. Rev. B*, vol. 88, p. 125 129, 12 Sep. 2013. DOI: 10.1103/PhysRevB.88.125129.

[47] K. Shiozaki and M. Sato, "Topology of crystalline insulators and superconductors," *Phys. Rev. B*, vol. 90, p. 165 114, 16 Oct. 2014. DOI: 10.1103/PhysRevB.90.165114.

[48] B. Bradlyn, L. Elcoro, J. Cano, *et al.*, "Topological quantum chemistry," *Nature*, vol. 547, no. 7663, pp. 298–305, 2017. DOI: 10.1038/nature23268.

[49] M. Vergniory, L. Elcoro, Z. Wang, *et al.*, "Graph theory data for topological quantum chemistry," *Phys. Rev. E*, vol. 96, no. 2, p. 023 310, 2017. DOI: 10.1103/PhysRevE.96.023310.

[50] B. Bradlyn, L. Elcoro, M. G. Vergniory, *et al.*, "Band connectivity for topological quantum chemistry: Band structures as a graph theory problem," *Phys. Rev. B*, vol. 97, p. 035 138, 3 Jan. 2018. DOI: 10.1103/PhysRevB.97.035138.

[51] J. Cano, B. Bradlyn, Z. Wang, *et al.*, "Building blocks of topological quantum chemistry: Elementary band representations," *Phys. Rev. B*, vol. 97, no. 3, p. 035 139, 2018. DOI: 10.1103/PhysRevB.97.035139.

[52] J. Cano, B. Bradlyn, Z. Wang, *et al.*, "Topology of disconnected elementary band representations," *Phys. Rev. Lett.*, vol. 120, p. 266 401, 26 Jun. 2018. DOI: 10.1103/PhysRevLett.120.266401.

[53] L. Elcoro, B. J. Wieder, Z. Song, Y. Xu, B. Bradlyn, and B. A. Bernevig, "Magnetic topological quantum chemistry," *Nat commun*, vol. 12, no. 1, p. 5965, 2021. DOI: 10.1038/s41467-021-26241-8.

[54] H. C. Po, A. Vishwanath, and H. Watanabe, "Symmetry-based indicators of band topology in the 230 space groups," *Nature communications*, vol. 8, no. 1, p. 50, 2017. DOI: 10.1038/s41467-017-00133-2.

[55] E. Khalaf, H. C. Po, A. Vishwanath, and H. Watanabe, "Symmetry indicators and anomalous surface states of topological crystalline insulators," *Phys. Rev. X*, vol. 8, p. 031 070, 3 Sep. 2018. DOI: 10.1103/PhysRevX.8.031070.

[56] F. Tang, H. C. Po, A. Vishwanath, and X. Wan, "Comprehensive search for topological materials using symmetry indicators," *Nature*, vol. 566, no. 7745, pp. 486–489, 2019. DOI: 10.1038/s41586-019-0937-5.

[57] H. C. Po, "Symmetry indicators of band topology," *Journal of Physics: Condensed Matter*, vol. 32, no. 26, p. 263 001, 2020. DOI: 10.1088/1361-648X/ab7adb.

[58] R. Thorngren and D. V. Else, "Gauging spatial symmetries and the classification of topological crystalline phases," *Phys. Rev. X*, vol. 8, p. 011 040, 1 Mar. 2018. DOI: 10.1103/PhysRevX.8.011040.

[59] B. Han, H. Wang, and P. Ye, "Generalized wen-zee terms," *Phys. Rev. B*, vol. 99, p. 205 120, 20 May 2019. DOI: 10.1103/PhysRevB.99.205120.

[60] S. Liu, A. Vishwanath, and E. Khalaf, "Shift insulators: Rotation-protected two-dimensional topological crystalline insulators," *Phys. Rev. X*, vol. 9, p. 031 003, 3 Jul. 2019. DOI: 10.1103/PhysRevX.9.031003.

[61] Y. Zhang, N. Manjunath, G. Nambiar, and M. Barkeshli, "Fractional disclination charge and discrete shift in the hofstadter butterfly," *Phys. Rev. Lett.*, vol. 129, p. 275 301, 27 Dec. 2022. DOI: 10.1103/PhysRevLett.129.275301.

[62] N. Manjunath and M. Barkeshli, "Crystalline gauge fields and quantized discrete geometric response for abelian topological phases with lattice symmetry," *Phys. Rev. Res.*, vol. 3, p. 013 040, 1 Jan. 2021. DOI: 10.1103/PhysRevResearch.3.013040.

[63] L. Gioia, C. Wang, and A. A. Burkov, "Unquantized anomalies in topological semimetals," *Phys. Rev. Res.*, vol. 3, no. 4, p. 043 067, Oct. 2021. DOI: 10.1103/PhysRevResearch.3.043067.

[64] J. May-Mann and T. L. Hughes, "Crystalline responses for rotation-invariant higher-order topological insulators," *Phys. Rev. B*, vol. 106, no. 24, p. L241113, 2022. DOI: 10.1103/PhysRevB.106.L241113.

[65] Y. Zhang, N. Manjunath, R. Kobayashi, and M. Barkeshli, "Complete crystalline topological invariants from partial rotations in $(2+1)$D invertible fermionic states and hofstadter's butterfly," *Phys. Rev. Lett.*, vol. 131, p. 176 501, 17 Oct. 2023. DOI: 10.1103/PhysRevLett.131.176501.

[66] N. Manjunath, A. Prem, and Y.-M. Lu, "Rotational symmetry protected edge and corner states in abelian topological phases," *Phys. Rev. B*, vol. 107, p. 195 130, 19 May 2023. DOI: 10.1103/PhysRevB.107.195130.

[67] N. Manjunath, V. Calvera, and M. Barkeshli, "Characterization and classification of interacting (2+1)-dimensional topological crystalline insulators with orientation-preserving wallpaper groups," *Phys. Rev. B*, vol. 109, p. 035 168, 3 Jan. 2024. DOI: 10.1103/PhysRevB.109.035168.

[68] J. C. Teo and T. L. Hughes, "Topological Defects in Symmetry-Protected Topological Phases," *Annual Review of Condensed Matter Physics*, vol. 8, no. 1, pp. 211–237, Mar. 2017. DOI: 10.1146/annurev-conmatphys-031016-025154.

[69] J. E. Avron, R. Seiler, and P. G. Zograf, "Viscosity of quantum hall fluids," *Phys. Rev. Lett.*, vol. 75, pp. 697–700, 4 Jul. 1995. DOI: 10.1103/PhysRevLett.75.697.

[70] N. Read, "Non-abelian adiabatic statistics and hall viscosity in quantum hall states and p_x+ip_y paired superfluids," *Phys. Rev. B*, vol. 79, p. 045 308, 4 Jan. 2009. DOI: 10.1103/PhysRevB.79.045308.

[71] M. Sherafati, A. Principi, and G. Vignale, "Hall viscosity and electromagnetic response of electrons in graphene," *Phys. Rev. B*, vol. 94, p. 125 427, 12 Sep. 2016. DOI: 10.1103/PhysRevB.94.125427.

[72] T. L. Hughes, R. G. Leigh, and E. Fradkin, "Torsional response and dissipationless viscosity in topological insulators," *Phys. Rev. Lett.*, vol. 107, p. 075 502, 7 Aug. 2011. DOI: 10.1103/PhysRevLett.107.075502.

[73] Y. You, G. Y. Cho, and T. L. Hughes, "Response properties of axion insulators and weyl semimetals driven by screw dislocations and dynamical axion strings," *Phys. Rev. B*, vol. 94, p. 085 102, 8 Aug. 2016. DOI: 10.1103/PhysRevB.94.085102.

[74] H. Sumiyoshi and S. Fujimoto, "Torsional chiral magnetic effect in a weyl semimetal with a topological defect," *Phys. Rev. Lett.*, vol. 116, p. 166 601, 16 Apr. 2016. DOI: 10.1103/PhysRevLett.116.166601.

[75] R. Soto-Garrido, E. Muñoz, and V. Juri či ć, "Dislocation defect as a bulk probe of monopole charge of multi-weyl semimetals," *Phys. Rev. Res.*, vol. 2, p. 012 043, 1 Feb. 2020. DOI: 10.1103/PhysRevResearch.2.012043.

[76] S. Laurila and J. Nissinen, "Torsional landau levels and geometric anomalies in condensed matter weyl systems," *Phys. Rev. B*, vol. 102, p. 235 163, 23 Dec. 2020. DOI: 10.1103/PhysRevB.102.235163.

[77] O. Dubinkin, F. J. Burnell, and T. L. Hughes, "Higher rank chiral fermions in three-dimensional weyl semimetals," *Phys. Rev. B*, vol. 109, p. 115 146, 11 Mar. 2024. DOI: 10.1103/PhysRevB.109.115146.

[78] C. Wang, A. Hickey, X. Ying, and A. A. Burkov, "Emergent anomalies and generalized Luttinger theorems in metals and semimetals," *Phys. Rev. B*, vol. 104, no. 23, p. 235 113, Dec. 2021. DOI: 10.1103/PhysRevB.104.235113.

[79] J. Nissinen, T. T. Heikkilä, and G. E. Volovik, "Topological polarization, dual invariants, and surface flat bands in crystalline insulators," *Phys. Rev. B*, vol. 103, no. 24, p. 245 115, Jun. 2021. DOI: 10.1103/PhysRevB.103.245115.

[80] L.-L. Gao, S. Kaushik, D. E. Kharzeev, and E. J. Philip, "Chiral kinetic theory of anomalous transport induced by torsion," *Phys. Rev. B*, vol. 104, p. 064 307, 6 Aug. 2021. DOI: 10.1103/PhysRevB.104.064307.

[81] Y. You, J. Bibo, F. Pollmann, and T. L. Hughes, "Fracton critical point at a higher-order topological phase transition," *Phys. Rev. B*, vol. 106, no. 23, p. 235 130, Dec. 2022. DOI: 10.1103/PhysRevB.106.235130.

[82] T. Amitani and Y. Nishida, "Torsion-induced chiral magnetic current in equilibrium," *Annals of Physics*, vol. 448, p. 169 181, 2023. DOI: 10.1016/j.aop.2022.169181.

[83] J. May-Mann, M. R. Hirsbrunner, X. Cao, and T. L. Hughes, "Topological field theories of three-dimensional rotation symmetric insulators: Coupling curvature and electromagnetism," *Phys. Rev. B*, vol. 107, p. 205 149, 20 May 2023. DOI: 10.1103/PhysRevB.107.205149.

[84] N. Manjunath and M. Barkeshli, *Classification of fractional quantum hall states with spatial symmetries*, 2020. arXiv: 2012.11603 [cond-mat.str-el].

[85] L. D. Landau, L. P. Pitaevskii, E. M. Lifshitz, and A. M. Kosevich, *Theory of Elasticity*, 3rd ed. Butterworth-Heinemann, 1986, ISBN: 075062633X.

[86] D. I. Pikulin, A. Chen, and M. Franz, "Chiral anomaly from strain-induced gauge fields in dirac and weyl semimetals," *Phys. Rev. X*, vol. 6, p. 041 021, 4 Oct. 2016. DOI: 10.1103/PhysRevX.6.041021.

[87] A. G. Grushin, J. W. F. Venderbos, A. Vishwanath, and R. Ilan, "Inhomogeneous weyl and dirac semimetals: Transport in axial magnetic fields and fermi arc surface states from pseudo-landau levels," *Phys. Rev. X*, vol. 6, p. 041 046, 4 Dec. 2016. DOI: 10.1103/PhysRevX.6.041046.

[88] T. Matsushita, S. Fujimoto, and A. P. Schnyder, "Topological piezoelectric effect and parity anomaly in nodal line semimetals," *Phys. Rev. Res.*, vol. 2, p. 043 311, 4 Dec. 2020. DOI: 10.1103/PhysRevResearch.2.043311.

[89] X.-Y. Song, Y.-C. He, A. Vishwanath, and C. Wang, "Electric polarization as a nonquantized topological response and boundary Luttinger theorem," *Phys. Rev. Res.*, vol. 3, no. 2, p. 023 011, Apr. 2021. DOI: 10.1103/PhysRevResearch.3.023011.

[90] T. Kaluza, "Zum Unitätsproblem der Physik," *Sitzungsber. Preuss. Akad. Wiss. Berlin (Math. Phys.)*, vol. 1921, pp. 966–972, 1921. DOI: 10.1142/S0218271818700017.

[91] O. Klein, "Quantentheorie und fünfdimensionale relativitätstheorie," *Zeitschrift für Physik*, vol. 37, no. 12, pp. 895–906, 1926. DOI: 10.1007/BF01397481.

[92] W. A. Benalcazar, B. A. Bernevig, and T. L. Hughes, "Quantized electric multipole insulators," *Science*, vol. 357, no. 6346, pp. 61–66, Jul. 2017. DOI: 10.1126/science.aah6442.

[93] W. A. Benalcazar, B. A. Bernevig, and T. L. Hughes, "Electric multipole moments, topological multipole moment pumping, and chiral hinge states in crystalline insulators," *Phys. Rev. B*, vol. 96, no. 24, p. 245 115, Dec. 2017. DOI: 10.1103/PhysRevB.96.245115.

[94] M. R. Hirsbrunner, A. D. Gray, and T. L. Hughes, "Crystalline electromagnetic responses of higher-order topological semimetals," *Phys. Rev. B*, vol. 109, p. 075 169, 7 Feb. 2024. DOI: 10.1103/PhysRevB.109.075169.

[95] O. Parrikar, T. L. Hughes, and R. G. Leigh, "Torsion, parity-odd response, and anomalies in topological states," *Phys. Rev. D*, vol. 90, p. 105 004, 10 Nov. 2014. DOI: 10.1103/PhysRevD.90.105004.

[96] T. L. Hughes, R. G. Leigh, and O. Parrikar, "Torsional anomalies, hall viscosity, and bulk-boundary correspondence in topological states," *Phys. Rev. D*, vol. 88, p. 025 040, 2 Jul. 2013. DOI: 10.1103/PhysRevD.88.025040.

[97] B. Bradlyn and N. Read, "Low-energy effective theory in the bulk for transport in a topological phase," *Phys. Rev. B*, vol. 91, no. 12, p. 125 303, 2015. DOI: 10.1103/PhysRevB.91.125303.

[98] P. Rao and B. Bradlyn, "Hall viscosity in quantum systems with discrete symmetry: Point group and lattice anisotropy," *Phys. Rev. X*, vol. 10, p. 021 005, 2 Apr. 2020. DOI: 10.1103/PhysRevX.10.021005.

[99] Z. Wang and S.-C. Zhang, "Simplified topological invariants for interacting insulators," *Phys. Rev. X*, vol. 2, p. 031 008, 3 Aug. 2012. DOI: 10.1103/PhysRevX.2.031008.

[100] D. Vanderbilt and R. D. King-Smith, "Electric polarization as a bulk quantity and its relation to surface charge," *Phys. Rev. B*, vol. 48, pp. 4442–4455, 7 Aug. 1993. DOI: 10.1103/PhysRevB.48.4442.

[101] A. M. Turner, Y. Zhang, R. S. K. Mong, and A. Vishwanath, "Quantized response and topology of magnetic insulators with inversion symmetry," *Phys. Rev. B*, vol. 85, p. 165 120, 16 Apr. 2012. DOI: 10.1103/PhysRevB.85.165120.

[102] M. Lin and T. L. Hughes, "Topological quadrupolar semimetals," *Phys. Rev. B*, vol. 98, no. 24, Dec. 2018. DOI: 10.1103/PhysRevB.98.241103.

[103] B. J. Wieder, Z. Wang, J. Cano, *et al.*, "Strong and fragile topological dirac semimetals with higher-order fermi arcs," *Nat commun*, vol. 11, no. 1, pp. 1–13, 2020. DOI: 10.1038/s41467-020-14443-5.

[104] K. Kodama and Y. Takane, "Persistent current due to a screw dislocation in weyl semimetals: Role of one-dimensional chiral states," *Journal of the Physical Society of Japan*, vol. 88, no. 5, p. 054 715, 2019. DOI: 10.7566/JPSJ.88.054715.

[105] Z.-M. Huang, L. Li, J. Zhou, and H.-H. Zhang, "Torsional response and liouville anomaly in weyl semimetals with dislocations," *Phys. Rev. B*, vol. 99, p. 155 152, 15 Apr. 2019. DOI: 10.1103/PhysRevB.99.155152.

[106] Z.-M. Huang, B. Han, and M. Stone, "Nieh-yan anomaly: Torsional landau levels, central charge, and anomalous thermal hall effect," *Phys. Rev. B*, vol. 101, p. 125 201, 12 Mar. 2020. DOI: 10.1103/PhysRevB.101.125201.

[107] Z.-M. Huang and B. Han, *Torsional anomalies and bulk-dislocation correspondence in weyl systems*, 2020. arXiv: 2003.04853 [cond-mat.mes-hall].

[108] L. Liang and T. Ojanen, "Topological magnetotorsional effect in weyl semimetals," *Phys. Rev. Research*, vol. 2, p. 022 016, 2 Apr. 2020. DOI: 10.1103/PhysRevResearch.2.022016.

[109] J. Nissinen and G. Volovik, "Tetrads in solids: From elasticity theory to topological quantum hall systems and weyl fermions," *Journal of Experimental and Theoretical Physics*, vol. 127, pp. 948–957, 2018. DOI: 10.1134/S1063776118110080.

[110] J. Nissinen and G. E. Volovik, "Elasticity tetrads, mixed axial-gravitational anomalies, and $(3+1)$-d quantum hall effect," *Phys. Rev. Res.*, vol. 1, p. 023 007, 2 Sep. 2019. DOI: 10.1103/PhysRevResearch.1.023007.

[111] Y. Ferreiros, Y. Kedem, E. J. Bergholtz, and J. H. Bardarson, "Mixed axial-torsional anomaly in weyl semimetals," *Phys. Rev. Lett.*, vol. 122, no. 5, p. 056 601, 2019. DOI: 10.1103/PhysRevLett.122.056601.

[112] C.-S. Chu and R.-X. Miao, "Chiral current induced by torsional weyl anomaly," *Phys. Rev. B*, vol. 107, no. 20, p. 205 410, 2023. DOI: 10.1103/PhysRevB.107.205410.

[113] P. Zhu, X.-Q. Sun, T. L. Hughes, and G. Bahl, "Higher rank chirality and non-hermitian skin effect in a topolectrical circuit," *Nat. Comms.*, vol. 14, no. 1, p. 720, 2023. DOI: 10.1038/s41467-023-36130-x.

[114] M.-C. Chang and Q. Niu, "Berry phase, hyperorbits, and the hofstadter spectrum," *Phys. Rev. Lett.*, vol. 75, no. 7, p. 1348, 1995.

[115] M.-C. Chang and Q. Niu, "Berry phase, hyperorbits, and the hofstadter spectrum: Semiclassical dynamics in magnetic bloch bands," *Phys. Rev. B*, vol. 53, no. 11, p. 7010, 1996. DOI: 10.1103/PhysRevLett.75.1348.

[116] J. Zak, "Berry's phase for energy bands in solids," *Phys. Rev. Lett.*, vol. 62, pp. 2747–2750, 23 Jun. 1989. DOI: 10.1103/PhysRevLett.62.2747.

[117] A. Burkov, "Weyl metals," *Annual Review of Condensed Matter Physics*, vol. 9, no. 1, pp. 359–378, 2018. DOI: 10.1146/annurev-conmatphys-033117-054129.

[118] J. Nissinen and G. E. Volovik, "Thermal nieh-yan anomaly in weyl superfluids," *Phys. Rev. Research*, vol. 2, p. 033 269, 3 Aug. 2020. DOI: 10.1103/PhysRevResearch.2.033269.

[119] C. Callan and J. Harvey, "Anomalies and fermion zero modes on strings and domain walls," *Nuclear Physics B*, vol. 250, no. 1, pp. 427–436, 1985. DOI: 10.1016/0550-3213(85)90489-4.

[120] S. G. Naculich, "Axionic strings: Covariant anomalies and bosonization of chiral zero modes," *Nucl. Phys. B*, vol. 296, no. 4, pp. 837–867, 1988. DOI: 10.1016/0550-3213(88)90400-2.

[121] M. Stone, "Gravitational anomalies and thermal hall effect in topological insulators," *Phys. Rev. B*, vol. 85, no. 18, p. 184 503, 2012. DOI: 10.1103/PhysRevB.85.184503.

[122] B. Yan and C. Felser, "Topological Materials: Weyl Semimetals," *Annual Review of Condensed Matter Physics*, vol. 8, no. 1, pp. 337–354, 2017. DOI: 10.1146/annurev-conmatphys-031016-025458.

[123] N. P. Armitage, E. J. Mele, and A. Vishwanath, "Weyl and Dirac semimetals in three-dimensional solids," *Rev. Mod. Phys.*, vol. 90, no. 1, p. 015 001, Jan. 2018. DOI: 10.1103/RevModPhys.90.015001.

[124] A. Bernevig, H. Weng, Z. Fang, and X. Dai, "Recent Progress in the Study of Topological Semimetals," *Journal of the Physical Society of Japan*, vol. 87, no. 4, p. 041 001, Apr. 2018. DOI: 10.7566/JPSJ.87.041001.

[125] B. Q. Lv, T. Qian, and H. Ding, "Experimental perspective on three-dimensional topological semimetals," *Rev. Mod. Phys.*, vol. 93, no. 2, p. 025 002, Apr. 2021, Publisher: American Physical Society. DOI: 10.1103/RevModPhys.93.025002.

[126] H. Gao, J. W. Venderbos, Y. Kim, and A. M. Rappe, "Topological Semimetals from First Principles," *Annual Review of Materials Research*, vol. 49, no. 1, pp. 153–183, 2019. DOI: 10.1146/annurev-matsci-070218-010049.

[127] J. Hu, S.-Y. Xu, N. Ni, and Z. Mao, "Transport of Topological Semimetals," *Annual Review of Materials Research*, vol. 49, no. 1, pp. 207–252, 2019. DOI: 10.1146/annurev-matsci-070218-010023.

[128] S. Wang, B.-C. Lin, A.-Q. Wang, D.-P. Yu, and Z.-M. Liao, "Quantum transport in Dirac and Weyl semimetals: A review," *Advances in Physics: X*, vol. 2, no. 3, pp. 518–544, May 2017. DOI: 10.1080/23746149.2017.1327329.

[129] Y. Fang and J. Cano, "Classification of Dirac points with higher-order Fermi arcs," *Phys. Rev. B*, vol. 104, no. 24, p. 245 101, Dec. 2021. DOI: 10.1103/PhysRevB.104.245101.

[130] M. Ezawa, "Higher-order topological insulators and semimetals on the breathing kagome and pyrochlore lattices," *Phys. Rev. Lett.*, vol. 120, p. 026 801, 2 Jan. 2018. DOI: 10.1103/PhysRevLett.120.026801.

[131] Q.-B. Zeng, Y.-B. Yang, and Y. Xu, "Higher-order topological insulators and semimetals in generalized aubry-andré-harper models," *Phys. Rev. B*, vol. 101, p. 241 104, 24 Jun. 2020. DOI: 10.1103/PhysRevB.101.241104.

[132] Z. Wang, B. J. Wieder, J. Li, B. Yan, and B. A. Bernevig, "Higher-order topology, monopole nodal lines, and the origin of large fermi arcs in transition metal dichalcogenides $X\mathrm{Te}_2$ (X = Mo, W)," *Phys. Rev. Lett.*, vol. 123, p. 186 401, 18 Oct. 2019. DOI: 10.1103/PhysRevLett.123.186401.

[133] A. L. Szabó and B. Roy, "Dirty higher-order Dirac semimetal: Quantum criticality and bulk-boundary correspondence," *Phys. Rev. Res.*, vol. 2, no. 4, p. 043 197, Nov. 2020. DOI: 10.1103/PhysRevResearch.2.043197.

[134] C.-Z. Li, A.-Q. Wang, C. Li, *et al.*, "Reducing Electronic Transport Dimension to Topological Hinge States by Increasing Geometry Size of Dirac Semimetal Josephson Junctions," *Phys. Rev. Lett.*, vol. 124, no. 15, p. 156 601, Apr. 2020. DOI: 10.1103/PhysRevLett.124.156601.

[135] M. Ezawa, "Second-order topological insulators and loop-nodal semimetals in Transition Metal Dichalcogenides XTe2 (X = Mo, W)," *Scientific Reports*, vol. 9, no. 1, p. 5286, Mar. 2019. DOI: 10.1038/s41598-019-41746-5.

[136] D. Călugăru, V. Juričić, and B. Roy, "Higher-order topological phases: A general principle of construction," *Phys. Rev. B*, vol. 99, no. 4, p. 041 301, Jan. 2019. DOI: 10.1103/PhysRevB.99.041301.

[137] S. A. A. Ghorashi, T. Li, and T. L. Hughes, "Higher-Order Weyl Semimetals," *Phys. Rev. Lett.*, vol. 125, no. 26, p. 266 804, Dec. 2020. DOI: 10.1103/PhysRevLett.125.266804.

[138] H.-X. Wang, Z.-K. Lin, B. Jiang, G.-Y. Guo, and J.-H. Jiang, "Higher-Order Weyl Semimetals," *Phys. Rev. Lett.*, vol. 125, no. 14, p. 146 401, Sep. 2020. DOI: 10.1103/PhysRevLett.125.146401.

[139] Y. Tanaka, R. Takahashi, R. Okugawa, and S. Murakami, "Rotoinversion-symmetric bulk-hinge correspondence and its applications to higher-order Weyl semimetals," *Phys. Rev. B*, vol. 105, no. 11, p. 115 119, Mar. 2022. DOI: 10.1103/PhysRevB.105.115119.

[140] W. B. Rui, Z. Zheng, M. M. Hirschmann, S.-B. Zhang, C. Wang, and Z. D. Wang, "Intertwined Weyl phases emergent from higher-order topology and unconventional Weyl fermions via crystalline symmetry," *npj Quantum Materials*, vol. 7, no. 1, pp. 1–7, Jan. 2022. DOI: 10.1038/s41535-022-00422-0.

[141] L. Song, H. Yang, Y. Cao, and P. Yan, "Square-root higher-order Weyl semimetals," *Nat commun*, vol. 13, no. 1, p. 5601, Sep. 2022. DOI: 10.1038/s41467-022-33306-9.

[142] K. Wang, J.-X. Dai, L. B. Shao, S. A. Yang, and Y. X. Zhao, "Boundary criticality of $\mathcal{PT}$-invariant topology and second-order nodal-line semimetals," *Phys. Rev. Lett.*, vol. 125, p. 126 403, 12 Sep. 2020. DOI: 10.1103/PhysRevLett.125.126403.

[143] S. A. A. Ghorashi, X. Hu, T. L. Hughes, and E. Rossi, "Second-order dirac superconductors and magnetic field induced majorana hinge modes," *Phys. Rev. B*, vol. 100, no. 2, p. 020 509, 2019. DOI: 10.1103/PhysRevB.100.020509.

[144] W. B. Rui, S.-B. Zhang, M. M. Hirschmann, *et al.*, "Higher-order weyl superconductors with anisotropic weyl-point connectivity," *Phys. Rev. B*, vol. 103, p. 184 510, 18 May 2021. DOI: 10.1103/PhysRevB.103.184510.

[145] Z. Wu and Y. Wang, "Nodal higher-order topological superconductivity from a $\mathcal{C}_4$-symmetric dirac semimetal," *Phys. Rev. B*, vol. 106, p. 214 510, 21 Dec. 2022. DOI: 10.1103/PhysRevB.106.214510.

[146] S. Simon, M. Geier, and P. W. Brouwer, "Higher-order topological semimetals and nodal superconductors with an order-two crystalline symmetry," *Phys. Rev. B*, vol. 106, no. 3, p. 035 105, Jul. 2022. DOI: 10.1103/PhysRevB.106.035105.

[147] S. A. A. Ghorashi, T. Li, M. Sato, and T. L. Hughes, "Non-hermitian higher-order dirac semimetals," *Phys. Rev. B*, vol. 104, no. 16, p. L161116, 2021. DOI: 10.1103/PhysRevB.104.L161116.

[148] S. A. A. Ghorashi, T. Li, and M. Sato, "Non-hermitian higher-order weyl semimetals," *Phys. Rev. B*, vol. 104, no. 16, p. L161117, 2021. DOI: 10.1103/PhysRevB.104.L161117.

[149] T. Liu, J. J. He, Z. Yang, and F. Nori, "Higher-order weyl-exceptional-ring semimetals," *Phys. Rev. Lett.*, vol. 127, no. 19, p. 196 801, 2021. DOI: 10.1103/PhysRevLett.127.196801.

[150] S. Bid, G. K. Dash, and M. Thakurathi, "Non-hermitian higher-order weyl semimetal with surface diabolic points," *Phys. Rev. B*, vol. 107, p. 165 120, 16 Apr. 2023. DOI: 10.1103/PhysRevB.107.165120.

[151] W. Zhu, M. Umer, and J. Gong, "Floquet higher-order Weyl and nexus semimetals," *Phys. Rev. Res.*, vol. 3, no. 3, p. L032026, Jul. 2021. DOI: 10.1103/PhysRevResearch.3.L032026.

[152] H. Wu and J.-H. An, "Hybrid-order topological odd-parity superconductors via floquet engineering," *Phys. Rev. B*, vol. 107, p. 235 132, 23 Jun. 2023. DOI: 10.1103/PhysRevB.107.235132.

[153] Z.-M. Wang, R. Wang, J.-H. Sun, T.-Y. Chen, and D.-H. Xu, "Floquet weyl semimetal phases in light-irradiated higher-order topological dirac semimetals," *Phys. Rev. B*, vol. 107, p. L121407, 12 Mar. 2023. DOI: 10.1103/PhysRevB.107.L121407.

[154] S. Ghosh, K. Saha, and K. Sengupta, "Hinge-mode dynamics of periodically driven higher-order Weyl semimetals," *Phys. Rev. B*, vol. 105, no. 22, p. 224 312, Jun. 2022. DOI: 10.1103/PhysRevB.105.224312.

[155] X.-L. Du, R. Chen, R. Wang, and D.-H. Xu, "Weyl nodes with higher-order topology in an optically driven nodal-line semimetal," *Phys. Rev. B*, vol. 105, no. 8, p. L081102, Feb. 2022. DOI: 10.1103/PhysRevB.105.L081102.

[156] M. R. Hirsbrunner, O. Dubinkin, F. J. Burnell, and T. L. Hughes, *Anomalous crystalline-electromagnetic responses in semimetals*, 2023. arXiv: 2309.10840 [cond-mat.mes-hall].

[157] Y. Peng, Y. Bao, and F. von Oppen, "Boundary green functions of topological insulators and superconductors," *Phys. Rev. B*, vol. 95, p. 235 143, 23 Jun. 2017. DOI: 10.1103/PhysRevB.95.235143.

[158] Z. Song, Z. Fang, and C. Fang, "$(d-2)$-dimensional edge states of rotation symmetry protected topological states," *Phys. Rev. Lett.*, vol. 119, p. 246 402, 24 Dec. 2017. DOI: 10.1103/PhysRevLett.119.246402.

[159] F. Schindler, A. M. Cook, M. G. Vergniory, *et al.*, "Higher-order topological insulators," *Science Advances*, vol. 4, no. 6, eaat0346, 2018. DOI: 10.1126/sciadv.aat0346.

[160] J. Langbehn, Y. Peng, L. Trifunovic, F. von Oppen, and P. W. Brouwer, "Reflection-symmetric second-order topological insulators and superconductors," *Phys. Rev. Lett.*, vol. 119, p. 246 401, 24 Dec. 2017. DOI: 10.1103/PhysRevLett.119.246401.

[161] W. A. Benalcazar, T. Li, and T. L. Hughes, "Quantization of fractional corner charge in C_n-symmetric higher-order topological crystalline insulators," *Phys. Rev. B*, vol. 99, p. 245 151, 24 Jun. 2019. DOI: 10.1103/PhysRevB.99.245151.

[162] E. Khalaf, W. A. Benalcazar, T. L. Hughes, and R. Queiroz, "Boundary-obstructed topological phases," *Phys. Rev. Res.*, vol. 3, p. 013 239, 1 Mar. 2021. DOI: 10.1103/PhysRevResearch.3.013239.

[163] M. Ezawa, "Edge-corner correspondence: Boundary-obstructed topological phases with chiral symmetry," *Phys. Rev. B*, vol. 102, p. 121 405, 12 Sep. 2020. DOI: 10.1103/PhysRevB.102.121405.

[164] K. Asaga and T. Fukui, "Boundary-obstructed topological phases of a massive dirac fermion in a magnetic field," *Phys. Rev. B*, vol. 102, p. 155 102, 15 Oct. 2020. DOI: 10.1103/PhysRevB.102.155102.

[165] W. A. Benalcazar and A. Cerjan, "Chiral-symmetric higher-order topological phases of matter," *Phys. Rev. Lett.*, vol. 128, p. 127 601, 12 Mar. 2022. DOI: 10.1103/PhysRevLett.128.127601.

[166] A. Tiwari, A. Jahin, and Y. Wang, "Chiral dirac superconductors: Second-order and boundary-obstructed topology," *Phys. Rev. Res.*, vol. 2, p. 043 300, 4 Dec. 2020. DOI: 10.1103/PhysRevResearch.2.043300.

[167] L. Lu, Z. Wang, D. Ye, *et al.*, "Experimental observation of weyl points," *Science*, vol. 349, no. 6248, pp. 622–624, 2015. DOI: 10.1126/science.aaa927.

[168] M. Serra-Garcia, V. Peri, R. Süsstrunk, *et al.*, "Observation of a phononic quadrupole topological insulator," *Nature*, vol. 555, no. 7696, pp. 342–345, 2018. DOI: 10.1038/nature25156.

[169] C. W. Peterson, W. A. Benalcazar, T. L. Hughes, and G. Bahl, "A quantized microwave quadrupole insulator with topologically protected corner states," *Nature*, vol. 555, no. 7696, pp. 346–350, 2018. DOI: 10.1038/nature25777.

[170] S. Imhof, C. Berger, F. Bayer, *et al.*, "Topolectrical-circuit realization of topological corner modes," *Nature Physics*, vol. 14, no. 9, pp. 925–929, 2018. DOI: 10.1038/s41567-018-0246-1.

[171] A. C. Potter, I. Kimchi, and A. Vishwanath, "Quantum oscillations from surface fermi arcs in weyl and dirac semimetals," *Nat commun*, vol. 5, no. 1, p. 5161, 2014. DOI: 10.1038/ncomms6161.

[172] Z. Wang and S.-C. Zhang, "Chiral anomaly, charge density waves, and axion strings from weyl semimetals," *Phys. Rev. B*, vol. 87, no. 16, p. 161 107, 2013. DOI: 10.1103/PhysRevB.87.161107.

[173] J. Maciejko and R. Nandkishore, "Weyl semimetals with short-range interactions," *Phys. Rev. B*, vol. 90, no. 3, p. 035 126, 2014. DOI: 10.1103/PhysRevB.90.035126.

[174] B. J. Wieder, K.-S. Lin, and B. Bradlyn, "Axionic band topology in inversion-symmetric weyl-charge-density waves," *Phys. Rev. Res.*, vol. 2, no. 4, p. 042 010, 2020. DOI: 10.1103/PhysRevResearch.2.042010.

[175] E. Witten, "Fermion path integrals and topological phases," *Rev. Mod. Phys.*, vol. 88, no. 3, p. 035 001, 2016. DOI: 10.1103/RevModPhys.88.035001.

[176] N. Varnava and D. Vanderbilt, "Surfaces of axion insulators," *Phys. Rev. B*, vol. 98, no. 24, p. 245 117, 2018. DOI: 10.1103/PhysRevB.98.245117.

[177] B. J. Wieder and B. A. Bernevig, *The axion insulator as a pump of fragile topology*, 2018. arXiv: 1810.02373 [cond-mat.mes-hall].

[178] M. Kohmoto, B. I. Halperin, and Y.-S. Wu, "Diophantine equation for the three-dimensional quantum hall effect," *Phys. Rev. B*, vol. 45, no. 23, p. 13 488, 1992. DOI: 10.1103/PhysRevB.45.13488.

[179] R.-X. Zhang, J. A. Hutasoit, Y. Sun, B. Yan, C. Xu, and C.-X. Liu, "Topological nematic phase in dirac semimetals," *Phys. Rev. B*, vol. 93, no. 4, p. 041 108, 2016. DOI: 10.1103/PhysRevB.93.041108.

[180] S. M. Young, S. Zaheer, J. C. Teo, C. L. Kane, E. J. Mele, and A. M. Rappe, "Dirac semimetal in three dimensions," *Phys. Rev. Lett.*, vol. 108, no. 14, p. 140 405, 2012. DOI: 10.1103/PhysRevLett.108.140405.

[181] Z. Wang, Y. Sun, X.-Q. Chen, *et al.*, "Dirac semimetal and topological phase transitions in a 3 bi (a= na, k, rb)," *Phys. Rev. B*, vol. 85, no. 19, p. 195 320, 2012. DOI: 10.1103/PhysRevB.85.195320.

[182] J. C. Teo and T. L. Hughes, "Existence of majorana-fermion bound states on disclinations and the classification of topological crystalline superconductors in two dimensions," *Phys. Rev. Lett.*, vol. 111, no. 4, p. 047 006, 2013. DOI: 10.1103/PhysRevLett.111.047006.

[183] S. Gopalakrishnan, J. C. Teo, and T. L. Hughes, "Disclination classes, fractional excitations, and the melting of quantum liquid crystals," *Phys. Rev. Lett.*, vol. 111, no. 2, p. 025 304, 2013. DOI: 10.1103/PhysRevLett.111.025304.

[184] W. A. Benalcazar, J. C. Teo, and T. L. Hughes, "Classification of two-dimensional topological crystalline superconductors and majorana bound states at disclinations," *Phys. Rev. B*, vol. 89, no. 22, p. 224 503, 2014. DOI: 10.1103/PhysRevB.89.224503.

[185] T. Li, P. Zhu, W. A. Benalcazar, and T. L. Hughes, "Fractional disclination charge in two-dimensional c n-symmetric topological crystalline insulators," *Phys. Rev. B*, vol. 101, no. 11, p. 115 115, 2020. DOI: 10.1103/PhysRevB.101.115115.

[186] X.-g. Wen and A. Zee, "Shift and spin vector: New topological quantum numbers for the hall fluids," *Phys. Rev. Lett.*, vol. 69, no. 6, p. 953, 1992. DOI: 10.1103/PhysRevLett.69.953.

[187] A. Rüegg and C. Lin, "Bound states of conical singularities in graphene-based topological insulators," *Phys. Rev. Lett.*, vol. 110, no. 4, p. 046 401, 2013. DOI: 10.1103/PhysRevLett.110.046401.

[188] A. Rüegg, S. Coh, and J. E. Moore, "Corner states of topological fullerenes," *Phys. Rev. B*, vol. 88, no. 15, p. 155 127, 2013. DOI: 10.1103/PhysRevB.88.155127.

[189] C. W. Peterson, T. Li, W. Jiang, T. L. Hughes, and G. Bahl, "Trapped fractional charges at bulk defects in topological insulators," *Nature*, vol. 589, no. 7842, pp. 376–380, 2021. DOI: 10.1038/s41586-020-03117-3.

[190] B.-J. Yang and N. Nagaosa, "Classification of stable three-dimensional dirac semimetals with nontrivial topology," *Nat commun*, vol. 5, no. 1, p. 4898, 2014. DOI: 10.1038/ncomms5898.

[191] L. Gioia and C. Wang, "Nonzero momentum requires long-range entanglement," *Phys. Rev. X*, vol. 12, p. 031 007, 3 Jul. 2022. DOI: 10.1103/PhysRevX.12.031007.

[192] C. L. Kane and E. J. Mele, "Quantum spin hall effect in graphene," *Phys. Rev. Lett.*, vol. 95, no. 22, p. 226 801, 2005. DOI: 10.1103/PhysRevLett.95.226801.

[193] E. Lieb, T. Schultz, and D. Mattis, "Two soluble models of an antiferromagnetic chain," *Annals of Physics*, vol. 16, no. 3, pp. 407–466, 1961. DOI: 10.1016/0003-4916(61)90115-4.

[194] S. Coh and D. Vanderbilt, "Electric polarization in a chern insulator," *Phys. Rev. Lett.*, vol. 102, no. 10, p. 107 603, 2009. DOI: 10.1103/PhysRevLett.102.107603.

[195] S. Vaidya, M. C. Rechtsman, and W. A. Benalcazar, *Response to polarization and weak topology in chern insulators*, 2023. arXiv: 2304.13118 [cond-mat.mes-hall].

[196] Y. Fang and J. Cano, "Filling anomaly for general two-and three-dimensional c 4 symmetric lattices," *Phys. Rev. B*, vol. 103, no. 16, p. 165 109, 2021. DOI: 10.1103/PhysRevB.103.165109.

[197] P. Rao and B. Bradlyn, "Effective action approach to the filling anomaly in crystalline topological matter," *Phys. Rev. B*, vol. 107, no. 19, p. 195 153, 2023. DOI: 10.1103/PhysRevB.107.195153.

[198] X. Zhang, Q. Gu, H. Sun, *et al.*, "Eightfold fermionic excitation in a charge density wave compound," *Phys. Rev. B*, vol. 102, no. 3, p. 035 125, 2020. DOI: 10.1103/PhysRevB.102.035125.

[199] B. Bradlyn, J. Cano, Z. Wang, *et al.*, "Beyond dirac and weyl fermions: Unconventional quasiparticles in conventional crystals," *Science*, vol. 353, no. 6299, aaf5037, 2016. DOI: 10.1126/science.aaf5037.

[200] H. Nielsen and M. Ninomiya, "A no-go theorem for regularizing chiral fermions," *Physics Letters B*, vol. 105, no. 2, pp. 219–223, 1981. DOI: 10.1016/0370-2693(81)91026-1.